HYSTERESIS AND MODE COMPETITION IN FARADAY WAVES

Stephen Paul Decent

A Thesis Submitted for the Degree of PhD
at the
University of St Andrews

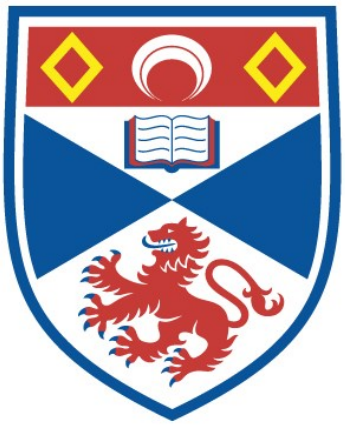

1996

HYSTERESIS AND MODE COMPETITION IN FARADAY WAVES

STEPHEN PAUL DECENT

THESIS SUBMITTED IN MAY 1995 FOR THE DEGREE OF DOCTOR OF PHILOSOPHY OF THE UNIVERSITY OF ST ANDREWS

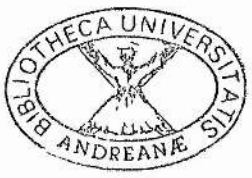

Abstract

Faraday waves arise on the surface of a liquid in a container that is undergoing vertical periodic oscillations. We investigate two-dimensional Faraday waves in a long rectangular container, both theoretically and experimentally.

Hysteresis occurs when both finite amplitude solutions and the flat surface solution are available. We derive a nonlinear model of a standing wave, extending the Lagrangian method of Miles (1976). The model is used to investigate hysteresis. It is found necessary to retain cubic damping, cubic forcing and the fifth-order conservative term in order to achieve agreement with experiments. The fifth-order conservative term was omitted from all previous studies of Faraday waves.

Stable limit cycles are found to arise from this single-mode equation. We examine the structure of this new solution in detail, both analytically and numerically. We describe local bifurcations using a multiple time scales analysis and global bifurcations using Melnikov's method.

The coefficients of linear and cubic damping are derived for a standing wave in a rectangular container by considering energy dissipation in the main body of the fluid (due to potential flow and streaming) and in boundary layers at the sidewalls and at the surface. Surface contamination, due to the presence of a thin viscoelastic surface film, creates a boundary layer at the surface which causes enhanced dissipation comparable to, or greater than, that caused by the boundary layers at the walls of the container.

Three-mode interaction equations are used to model intermittency and complex modulations which are found to arise from a sideband instability mechanism similar to that of Eckhaus (1963) and Benjamin & Feir (1967). The role of cubic and fifth-order nonlinear terms on this instability mechanism is examined. Theoretical results are found to compare quite favourably with experimental data.

DECLARATION

I, S. P. Decent, hereby certify that this thesis, which is approximately 40 000 words in length, has been written by me, that it is the record of work carried out by me and that it has not been submitted in any previous application for a higher degree.

21.5.95

date signature of candidate

POSTGRADUATE CAREER

I was admitted as a research student in October 1992 and as a candidate for the degree of Doctor of Philosophy in the same month; the higher study for which this is a record was carried out in the University of St. Andrews between 1992 and 1995.

22.5.95

date signature of candidate

CERTIFICATE

I hereby certify that the candidate has fulfilled the conditions of the Resolution and Regulations appropriate for the degree of Doctor of Philosophy in the University of St. Andrews and that the candidate is qualified to submit this thesis in application for that degree.

date 22/5/95 signature of supervisor

COPYRIGHT

In submitting this thesis to the University of St. Andrews I understand that I am giving permission for it to be made available for use in accordance with the regulations of the University Library for the time being in force, subject to any copyright vested in the work not being affected thereby. I also understand that the title and abstract will be published, and that a copy of the work may be made and supplied to any bona fide library or research worker.

22-5-95

date signature of candidate

Acknowledgements

I would like to thank my supervisor Professor Alex Craik for his continual guidance, patience and encouragement during my time at St. Andrews.

I am also grateful to Professor J. W. Miles for an enlightening discussion at the University of California at San Diego in October 1993, and to Professor N. Riley for a useful discussion at the 1995 B.A.M.C. at the University of Birmingham.

Thanks too to staff and fellow students in the Mathematical Institute and in the Department of Physics and Astronomy; in particular, I would like to thank Mr Jonathan Armitage for supervising me during my time in the laboratory. Also, thanks to Mr Graham Forster, Mr David Sterratt and Dr Darren McDonald for helpful discussions during my research.

I am also grateful to the Department of Physics and Astronomy for providing the experimental equipment used in this thesis.

I would like to thank the Engineering and Physical Sciences Research Council for their support by an earmarked studentship.

Finally, I would like to thank all my friends in St. Andrews for making my time here so enjoyable.

CONTENTS

IV Limit cycles

V Theoretical determination of the damping coefficients

A note on nomenclature

Equations, Figures and Tables are not numbered with reference to the Chapter they appear in. For example, there is an equation (1.1) in Chapter III and a (different) equation (1.1) in Chapter IV. Whenever an equation, Figure or Table is referenced, it should be taken that we mean the Chapter currently being read, unless otherwise stated.

Also, Figures are not placed in the text, but are located at the end of Chapters.

CHAPTER I

Introduction

1. Surface water waves

Surface water waves continue to provide a challenge to experimental and theoretical scientists. The 'classical' linear theory, which enables the application of attractive mathematics such as Fourier-series and complex-variable techniques, is described in numerous books, though the treatises of Lamb (1895, 1932) and Rayleigh (1896) remain influential. The linear theory is however very limited in its validity, since the equations of motion of fluid dynamics are nonlinear. The weakly nonlinear theory of water waves, in which linear theory is used as a first approximation, was first proposed by Stokes (1847), though it was not until the 1960's that nonlinear theories began to dominate the literature. A fascinating variety of surface wave phenomena have been described theoretically as a result of nonlinear analysis, including modulations, solitons and low-dimensional chaos.

The theory of resonant wave interactions, pioneered by Phillips (1960), has become a central theme. The mutual interaction of several wave modes is modelled using coupled nonlinear ordinary differential equations which describe the slow evolution of the amplitude of each wave mode. The simplest cases are three-wave and four-wave resonance, in which the coupling of the amplitude equations is via quadratic and cubic nonlinear terms respectively. There are several reviews of this subject: Phillips (1977, 1981), Yuen & Lake (1980), Craik (1985) and Hammack & Henderson (1993).

For wave modes which vary slowly over both space and time, nonlinear partial differential equations are needed to describe the evolution of the wave amplitude. There are many different scenarios. In certain situations, two-dimensional weakly

nonlinear wave-packets can be modelled using a nonlinear Schrödinger equation, while three-dimensional wave-packets can be described by the Davey-Stewartson equations. For long inviscid gravity waves in shallow water, the Korteweg-de Vries equation is used. Craik (1985) reviews the evolution of such nonlinear wave-trains.

2. Faraday waves

Faraday resonance is a particularly interesting nonlinear surface-wave phenomenon. (Miles & Henderson 1990 reviews the subject). In 1831, Michael Faraday reported on a series of observations of waves resulting on the surface of a liquid when its container is vibrated vertically. He examined mercury, ink, water, alcohol, turpentine, milk and egg white, and observed what have now become known as Faraday waves. In his paper (Faraday 1831), he reported that the free surface oscillated at half the oscillation frequency of the vessel. This was later disputed by Matthiessen (1868), who observed a synchronous response, though Lord Rayleigh (1883a and b) carried out further experiments and found a subharmonic response, in agreement with Faraday.

Faraday waves are an example of a parametrically driven system. This is where a parameter in the equations of motion varies periodically in time and thereby acts as an energy feed source. See Lord Rayleigh (1883a) and Nayfeh & Mook (1979) for examples of parametric excitation in mechanics, and Locherer & Brandt (1982) for examples in electronics.

The first theoretical work on Faraday resonance was carried out by Benjamin & Ursell (1954). They derived an infinite set of Mathieu's equations from the linearized equations of irrotational motion for an ideal fluid. From this they showed that wave modes of frequency $\omega, 2\omega, 3\omega, 4\omega, 5\omega, \ldots$ result from an excitation with frequency 2ω. The principal wave mode which is excited is the subharmonic with frequency ω,

thus confirming the observations of Faraday and Lord Rayleigh (see the following section for further details).

Ockendon & Ockendon (1973) developed a nonlinear model of Faraday waves, extending the work of Benjamin & Ursell to small but finite wave amplitudes. However, they did not explicitly calculate the coefficient of the nonlinear cubic interaction term in their equations. Miles (1976) first successfully determined a nonlinear model complete with an expression for the cubic coefficient. His derivation developed the variational methods for water waves proposed by Whitham (1965) and developed by Whitham (1967, 1970), Luke (1967), Simmons (1969), Miles (1967) and Milder (1967), with damping being introduced via a dissipation function. Miles (1976) also examined the internal resonance $\omega_2 \approx 2\omega_1$, where ω_1 is the frequency of the primary mode and ω_2 is the frequency of its second harmonic. Miles (1984) continued this work, showing errors in Dodge et al. (1965) and Henstock & Sani (1974).

Experiments have been carried out by Benjamin & Ursell (1954), Dodge et al. (1965), Keolian et al. (1981), Gollub & Meyer (1983), Ciliberto & Gollub (1985), Ezerskii et al. (1986), Douady & Fauve (1988), Virnig et al. (1988), Simonelli & Gollub (1989), Feng & Sethna (1989), Douady (1990), Henderson & Miles (1990), Ciliberto, Douady & Fauve (1991), Fauve, Kumar & Laroche (1992), Edwards & Fauve (1992, 1993, 1994) and Craik & Armitage (1995). Gollub & Meyer (1983) reported chaos arising from complex mode interactions in a circular tank. They identified the chaos as resulting from a series of symmetry-breaking bifurcations which led to quasi-periodic motion and eventually chaos. Ciliberto & Gollub (1985) observed periodic and chaotic solutions in a circular tank and reconstructed the chaotic attractor in phase space. From this they showed that the attractor has fractional dimension (they measured the dimension to be approximately 2.2) with at least one positive Lyapunov exponent, so that nearby trajectories diverge from each other exponentially.

Simonelli & Gollub (1989) studied the interaction of two modes that are degenerate in a square basin but non-degenerate in a 'slightly rectangular' basin (by this we mean a basin where the length and breadth of the rectangle are approximately equal). They experimentally determined the sinks, sources and saddles, and examined their bifurcation structure. In most parameter regimes they identified multiple attractors and repellors (up to 16), giving rise to pure and mixed modes i.e. standing waves that correspond to a single mode (pure) or a mixture of modes (mixed). They found that the symmetry of the basin was crucial to the dynamics of the system. The square container gave only standing waves (pure and mixed modes) and the authors were able to describe the observed dynamics theoretically in terms of cubic interaction equations (similar those of Miles 1976, 1984, though for several modes). In the slightly rectangular basin (where the frequencies of the two modes are separated by about 1%), time-dependent periodic and chaotic solutions were observed, resulting from mode competition. They also observed hysteresis: this is when surface waves can be sustained at smaller values of the forcing than that required for the onset of waves from the flat surface. Intermittency was also seen in their experiment, with quiescent periods of up to two hours, separated by periods of wave activity lasting for about a minute. The authors suggested that introducing fifth-order terms into their theoretical model would enable a full theoretical description of their experimental observations. Silber & Knobloch (1989) produced a theoretical description of Simonelli & Gollub's experiment and also suggested that the inclusion of fifth-order terms would significantly improve the agreement between theoretical and experimental results. This is a formidable task and has yet to be done (as far as we are aware), though this thesis includes a fifth-order theoretical analysis of a single mode, and a fifth-order analysis of the sideband instability which occurs with three neighbouring modes.

Feng & Sethna (1989) studied a slightly rectangular container both experimentally and theoretically (they use a normal form analysis to derive their equations). There are many things in common between this study and the one of Simonelli & Gollub

(1989), however Feng & Sethna observed a mixed travelling wave state, not observed by Simonelli & Gollub. Also, Feng & Sethna's theoretical calculations predicted two different types of stationary mixed wave states (in agreement with the theoretical calculations of Umeki 1991), while Simonelli & Gollub observed only one mixed wave in their square container and no mixed wave states in their slightly rectangular container. However, it is difficult to compare the two papers because Feng & Sethna's dimensionless parameters do not directly compare to Simonelli & Gollub's experiment.

Douady (1990) studied capillary waves in a square basin experimentally. He found the stability boundary, wave amplitudes and time of decay of unforced waves to be in agreement with the existing theory. He also found that the meniscus is excited by the vertical oscillation, causing an isochronous surface wave to be emitted from the boundary. This wave mode interferes with the parametric wave modes.

Henderson & Miles (1990) studied Faraday waves in a rectangular container and a circular container experimentally. Theoretical predictions of the resonant frequency of a single mode and of the threshold forcing for its excitation (calculated from a model which included a linear boundary layer) were found to agree well with observations. Theoretical predictions of wave amplitudes were found to be in reasonable agreement with experimental data in the case of the circular tank.

Fauve, Kumar & Laroche (1992) experimentally studied the liquid-vapour interface of carbon-dioxide close to its critical temperature subject to vertical forcing. Edwards & Fauve (1994) reported on a small-depth large-aspect-ratio experimental system. The vertical forcing they used had two simultaneous frequencies, instead of the single frequency more normally associated with these experiments. The small depth was designed to suppress long-wavelength instabilities which, when present, make it difficult to obtain stable homogenous patterns over wide parameter ranges. They observed parallel lines, squares and hexagons. With high viscosity fluids (100cS) they found that the standing waves observed did not exhibit strong sidewall influence, and found regular patterns in various irregularly shaped containers (including one of the

shape of the map of France!). They found that many of their experimental phenomena could be modelled by appropriate cubic interaction equations.

They also found 'quasi-patterns' (see also Edwards & Fauve 1992, 1993) which exhibited twelve-fold symmetry. They define the term 'quasi-pattern' to be "a pattern with long-range orientational order but no spatial periodicity, thus analogous to a quasi-crystal, but arising spontaneously in a nonlinear continuum-mechanical system having the symmetries of a (horizontal) plane". The existence of this structure demonstrates that quasi-crystalline order can arise in a purely continuum-mechanical system where spatially localised objects such as atoms or tiles do not appear to be a necessary aspect of the theoretical treatment. Analogous theoretical advances have been made by Kumar & Tuckerman (1994) and Tuckerman, Kumar & Edwards (1994).

Craik & Armitage (1995) reported on a long rectangular tank (see Chapter II for a full discussion of this and related experiments). They observed standing waves, travelling waves, intermittency and hysteresis. The qualitative behaviour of the surface waves was found to depend strongly on the ambient water depth.

Meron & Procaccia (1986) derived cubic amplitude equations appropriate for an analysis of the experiment of Ciliberto & Gollub (1985). They expressed their nonlinear coefficients in terms of correlation integrals, but did not evaluate them. Miles (1989) pointed out that Meron & Procaccia's equations were in error, since they do not lead to the canonical formulations. Ciliberto & Gollub's experiment was re-examined by Umeki & Kambe (1989) and Kambe & Umeki (1990), using an extension of Miles' (1976, 1984) formulation. Umeki (1989) discussed the relationship between the parameters in the Hamiltonian function and the symmetry of the shape of the container. Using Umeki & Kambe (1989) and Umeki (1991), the controversy between Meron & Procaccia (1986) and Miles (1989) can be clarified (see also Miles & Henderson 1990 and Meron & Procaccia 1989).

Meron (1987) took a general approach to parametric excitation of a multimode dissipative system, calculating normal form equations. (For further details of normal

forms see Velhulst 1979, Guckenheimer & Holmes 1983, Golubitsky & Stewart 1985, 1986 and Crawford 1991). With a reduction of the flow to a lower dimensionality, he predicted that the onset of waves in Faraday excitation can be smooth or hysteretic. Meron & Procaccia (1987) showed that the system of parametrically excited surface waves falls into the category of *critical flows* whose dynamics and transition to chaos can be understood from first-return maps derived in the vicinity of one saddle point phase space. They identified a parameter regime in which the onset of chaos is via a series of gluing bifurcations intermingled with period-doubling bifurcations. (A gluing bifurcation is when two limit cycles with period s and t approach a saddle point and then *glue* together to produce a single limit cycle of period $s+t$). For further discussion of gluing bifurcations see Arneodo, Coullet & Tresser (1981), Gambaudo, Procaccia, Thomae & Tresser (1986), Procaccia, Thomae, Tresser (1987).

Gu & Sethna (1987) (see also Gu, Sethna & Narain 1988) carried out a theoretical analysis of a rectangular container, when the frequencies of two modes are in the ratio 1:2. They found sufficient conditions for the two modes to dominate the motion. They also proved that chaos is present in certain parameter ranges in their model, using a theorem of Silnikov (1970) and verified this by numerical computations. This is in contrast to Holmes (1986) who proved that homoclinic chaos is present in the equations for the 2:1:2 external-internal resonance problem, though only in a system which is perturbed from a completely integrable Hamiltonian system.

Kambe & Umeki (1990) and Craik (1993) emphasise the distinction between Hamiltonian chaos and dissipative chaos. Hamiltonian chaos usually collapses onto stable equilibrium states on the addition of a small dissipative term. In contrast, dissipative chaos is robust to changes in the dissipation parameters.

Umeki (1991) derived the cubic amplitude equations for two modes in a rectangular container, using the variational method of Miles (1976, 1984), Umeki & Kambe (1989) and Umeki (1989), incorporating surface tension. He showed the presence of periodic and chaotic solutions, and carried out a full theoretical analysis of the experiment of Simonelli & Gollub (1989). He also gave a proof of homoclinic chaos

under the rather limited assumption that forcing and damping form small perturbations to the completely integrable Hamiltonian system. This proof therefore does not apply to the strongly dissipative systems observed in experiments. Umeki (1991) also points out two advantages of using the variational method to derive the amplitude equations: (i) the explicit Hamiltonian structure of the mode interactions is obtained and (ii) an extension of the equations to more than two modes appears easier if the variational method is used rather than any other method.

Nagata (1989) analysed a square container of length a and breadth b theoretically, concentrating on the two completely degenerate modes $\cos\frac{\pi x}{a}$ and $\cos\frac{\pi y}{b}$ (in the cartesian $x-y$ plane) occurring at the same frequency, and identified five different parameter regimes. He also found that both pure and mixed modes are stable in some parameter ranges, with complex (probably fractal) basins of attraction. He also found chaotic solutions, which are discussed further in Nagata (1991).

Crawford, Knobloch & Riecke (1990) theoretically examined the circular tank experiment of Ciliberto & Gollub (1985) using a normal form approach. Normal form analysis, which utilises the symmetries of the system, provides a very different approach from the more 'traditional' methods deriving from hydrodynamics. Crawford et al. (1990) emphasised differences between their results and those of Umeki & Kambe (1989), who derived their equations from hydrodynamics. Crawford (1991) derived normal form equations for the square symmetry.

Crawford, Gollub & Lane (1993) identify 'hidden' translational and rotational symmetries in square containers. These symmetries constrain the linear and nonlinear behaviour of the liquid causing unexpected degeneracies among the linear wave frequencies, resulting in unexpected branches of nonlinear solutions in the bifurcation equations. They remove the hidden symmetries by deforming the (previously straight) sidewalls of the container (without disturbing the square symmetry). These deformations are studied theoretically and experimentally. With curved sidewalls (that is, without hidden symmetries) standing wave patterns are observed to break the symmetry in a period-doubling bifurcation, in agreement with the generic behaviour.

However, if the container has straight sidewalls, the bifurcations of standing waves is observed to be inconsistent with the generic behaviour, unless the hidden symmetries are included in the bifurcation theory.

The first papers to include nonlinear terms in the amplitude expansion equations, other than the nonlinear cubic conservative terms, were Douady (1990) and Milner (1991), who both included a cubic damping term. Miles (1993, 1994) retained cubic forcing and cubic damping terms in addition to the linear terms and the cubic conservative terms. Miles (1993) derives the evolution equation for square (three-dimensional) standing (capillary-gravity) waves, and Miles (1994) analysed the pattern selection process for the mode competition between square waves and rolls, in a square container.

Theoretical calculations of the coefficients of the damping terms in the amplitude expansion equations have been attempted, but only the calculation of the coefficient of linear damping has been completed successfully. Miles (1967) determines the linear damping of surface waves in a container, taking into account dissipation due to (i) the main body of the liquid, (ii) the boundary layers at the walls of the container, (iii) the surface boundary layer (resulting from surface contamination) and (iv) capillary hysteresis, resulting from the meniscus. Milner (1991) and Miles (1993, 1994) have estimated the coefficient of cubic damping theoretically, though they only considered dissipation due to the main body of the liquid, neglecting the other three effects. See Chapter V for a theoretical calculation which improves on Miles (1993, 1994).

Knobloch & de Luca (1990) describe spatio-temporal "blinking states" in which the direction of propagation of a travelling wave reverses more or less periodically in time (resembling those seen in the experiments of Craik & Armitage 1995, described in Chapter II), and "confined" states in which a travelling wave fills only part of the container (though they do not incorporate parametric forcing into their model). They show these phenomena in partial differential equations, as opposed to the amplitude expansion equations (which are ordinary differential equations) used by Miles (1976,

1984, 1993, 1994), Umeki (1991), Simonelli & Gollub (1989), Craik & Armitage (1995) and several other authors. They show that the coupled complex Ginzburg-Landau equations have a limited range of validity, and go on to derive equations valid over a greater range of parameter values. Pierce & Knobloch (1994) use these evolution equations to study the stability of trains of standing waves with respect to longitudinal and transverse perturbations.

Riecke (1990) studied parametrically excited standing waves in large-aspect-ratio systems theoretically. He found that the Eckhaus-stable (see Eckhaus 1963) band of wave numbers can split into two sub-bands which are separated by a region of unstable wave numbers. Waves in the unstable regime are approximately described by a Ginzburg-Landau equation.

Hughes & Proctor (1990 a, b) investigated three-wave resonant coupling (without parametric forcing), and found bursts of activity followed by long calm periods. Though their evolution equations do not describe Faraday excitation, their results have some similarities with the intermittency observed in the experiments of Craik & Armitage (1995) and Simonelli & Gollub (1989). They found that their solution trajectory sometimes lingers near to a saddle point at the origin, where it is very susceptible to noise, destroying the periodicity of the behaviour.

Solitary standing waves have also been studied theoretically and experimentally in Faraday resonance. Wu et al. (1984) contains a description of an experimental observation. See also Larraza & Putterman (1984) and Wu & Rudnick (1985).

Faraday resonance has also been studied at the interface of two liquids. See Kumar & Tuckerman (1994) and Generalis & Nagata (1995).

The surface waves resulting from the horizontal oscillation of a tank, rather than vertical oscillation, have also received theoretical and experimental attention. Notable papers include Miles (1985), Nobili et al. (1988) and Funakoshi & Inoue (1988, 1992a, 1992b).

Other related work includes nonlinear convection studies, especially Rayleigh-Bénard convection. Here thermally-driven convective instabilities arise in a horizontal

fluid layer heated uniformly from below, resulting in mode competition processes similar to those in Faraday waves. However, there are several important differences between Rayleigh-Bénard convection and Faraday waves, particularly the frequency detuning aspect of Faraday waves which is absent in Rayleigh-Bénard convection. There are several reviews of this subject, including Craik (1985) and Busse (1981). More recent work includes Jones & Proctor (1987) and Chen (1992).

Finally, the study of Faraday waves utilises the modern theories of nonlinear dynamical systems and chaos theory. Informal introductions into this subject are given by Gleick (1986) and Stewart (1989). Scientific and mathematical texts include Guckenheimer & Holmes (1983), Hao Bai-Lin (1982), MacKay & Meiss (1987), Devaney (1989) and Perko (1991).

3. Mathematical Overview

We will now discuss in more detail some of the early theoretical results, starting with the linear theory of Benjamin & Ursell (1954), which we summarise for two-dimensional waves. We consider surface waves on an ideal fluid of ambient depth d in a cylindrical tank subjected to vertical oscillations with acceleration $f\cos 2\omega t$. Let (x,z) be the coordinates in a reference frame fixed in the container, with the bottom being identified as the plane $z=-d$. The inviscid equations of irrotational motion are

$$\begin{aligned}
&\nabla^2\phi = 0,\\
&\phi_z = 0 \text{ on } z=-d,\\
&\phi_x = 0 \text{ on the tank walls } x=0,l,\\
&\text{and on the surface } z=\eta,\\
&\phi_t + (g + f\cos 2\omega t)\eta + \frac{1}{2}|\nabla\phi|^2 = 0,\\
&\phi_z = \eta_t + \phi_x\eta_x + \phi_z\eta_z,
\end{aligned} \tag{3.1}$$

where ϕ is the velocity potential (so that the velocity field $\mathbf{u}=\nabla\phi$) and $z=\eta$ is the vertical displacement of the surface. Equations (3.1) are linearized by omitting squares and products of ϕ and η. The linear problem has the solution

$$\phi = \sum_{i=1}^{\infty} \frac{\cosh[k_i(z+d)]}{k_i \sinh(k_i d)} \frac{da_i(t)}{dt} S_i(x), \tag{3.2}$$

where k_i and S_i are the spatial eigenvalues and eigenfunctions here given by

$$S_i(x) = \cos(k_i x),\ k_i = i\pi / l. \tag{3.3}$$

The natural frequencies of the modes are

$$\omega_i = \left\{ g k_i \tanh(k_i d) \right\}^{1/2} \tag{3.4}$$

and

$$\frac{d^2 a_i}{dt^2} + (p_i - 2q_i \cos 2T) a_i = 0, \tag{3.5}$$

where $p_i = g k_i \tanh(k_i d) / \omega^2$, $q_i = k_i f \tanh(k_i d) / 2\omega^2$ and $T = \omega t$.

Equation (3.5) is Mathieu's equation (see Nayfeh & Mook 1979 for a full discussion of the properties of this equation) and the zero solution of equation (3.5) is unstable in certain regions of the p_i, q_i plane. It is in these regions that Faraday waves occur and a nonlinear analysis is necessary to determine the nature of the waves.

The p_i, q_i plane consists of *tongues* of instability, each corresponding to one of the resonant frequencies $\omega, 2\omega, 3\omega, 4\omega, 5\omega, \ldots$. When linear damping is added to Mathieu's equations (equivalent to adding the term $\upsilon\, da_i/dt$ to the left-hand side of (3.5), where υ measures the damping) then the tongues only exist for large values of f, except for the tongue corresponding to the wave with frequency ω (see Douady 1990 for more details of the damped Mathieu's equation). This confirms the observation of Faraday (1831) that the surface waves have frequency ω, and it is this resonance about which the weakly nonlinear theories are based.

Miles (1976, 1984) derived, through an ε scaling,

$$\frac{dA}{d\tau} = -\mu A + i\Omega A + iFA^* + i\Pi |A|^2 A, \tag{3.6}$$

for the slowly varying complex wave amplitude $A(\tau) = p(\tau) + iq(\tau)$ of a single mode (that is, a standing wave), where the slow timescale $\tau = \varepsilon^2 \omega t$, μ is the coefficient of linear damping, Ω measures the frequency detuning from resonance, F is a measure of the forcing and Π is the (nonlinear) cubic conservative coefficient

(which is a function of ambient water depth, tank geometry and surface tension). The surface elevation is given by

$$\eta = \frac{\sqrt{2}\varepsilon\cos(kx)}{k\tanh(kd)}\left[p(\tau)\cos(\omega t) + q(\tau)\sin(\omega t)\right] + O\left(\varepsilon^2\right), \tag{3.7}$$

where k is the wavenumber and ε is a small parameter.

A linear stability analysis of the zero (flat surface) solution of equation (3.6) can be carried out as follows. If we consider small disturbances $B = B_r + iB_i$ of the stationary point $A = 0$ then

$$\frac{d}{dt}\begin{pmatrix} B_r \\ B_i \end{pmatrix} = \begin{pmatrix} -\mu & F-\Omega \\ F+\Omega & -\mu \end{pmatrix}\begin{pmatrix} B_r \\ B_i \end{pmatrix} \tag{3.8}$$

upon linearization. Seeking eigenvalues of the matrix gives

$$F_n^2 \equiv F^2 = \mu^2 + \Omega^2 \tag{3.9}$$

for the neutral stability boundary. For values of the forcing $F < F_n$, the flat surface is stable, and for values $F > F_n$, the flat surface is unstable. The behaviour of evolution equations such as (3.6) are best described in terms of the frequency-forcing plane (Ω, F), in which (3.9) is a hyperbola.

Finite-amplitude stationary solutions $A = re^{i\theta}$ of equation (3.6) are given by

$$\begin{aligned} r^2 &= \frac{-\Omega \pm \left(F^2 - \mu^2\right)^{1/2}}{\Pi}, \\ \cos 2\theta &= \frac{\pm\left(F^2 - \mu^2\right)^{1/2}}{-F}, \\ \sin 2\theta &= \frac{\mu}{F}, \end{aligned} \tag{3.10}$$

which are obtained by solving (3.6) with $\frac{dA}{d\tau} = 0$.

If $\Pi > 0$ then the + solution of r is real for $F > F_n$. Also, for $\mu < F < F_n$ and $\Omega < 0$, both the + and - solutions of r are real. If $\Pi < 0$ then the - solution is real for $F > F_n$. Also, for $\mu < F < F_n$ and $\Omega > 0$, both the + and - solutions are real.

A stability analysis similar to that shown above for the flat surface reveals that the + solution is always a sink (attractor) and the - solution is always a saddle for $\Pi > 0$. For $\Pi < 0$, the - solution is found to be a sink while the + solution is a saddle. Therefore, for $\mu < F < \left(\mu^2 + \Omega^2\right)$ and $\Omega < 0$ when $\Pi > 0$, both the flat surface and a

finite amplitude stationary solution are stable. This is the hysteresis region in this case. Similarly, for $\mu < F < \left(\mu^2 + \Omega^2\right)$ and $\Omega > 0$ when $\Pi < 0$.

Equation (3.6) is the simplest nonlinear model of Faraday waves, though it is unsuitable for describing most experimental observations. It will be seen that the hysteresis region observed in experiments is very different to that predicted by (3.6); in Chapter III we show that this is due to higher-order nonlinear terms which are neglected in (3.6). Moreover, (3.6) only describes standing waves: when more than one mode is 'active' then interaction equations, nonlinear coupled complex differential equations, are needed to described the resulting mode competition; we discuss interaction equations in Chapter VI.

4. Outline of the thesis

This thesis was originally motivated by the experimental observations of Craik & Armitage (1995) of two-dimensional Faraday waves in a long rectangular tank. This experiment and their observations are described in detail in Chapter II, along with some new experiments.

In Chapter III, we derive a nonlinear model of a parametrically driven standing wave, extending the Lagrangian method of Miles (1976). The model is used to investigate hysteresis and the theoretical results are compared to experimental data. It is found necessary to retain damping and forcing terms up to third-order in wave amplitude, and also the fifth-order conservative frequency shift, in order to achieve even broad agreement with experiments. The latter fifth-order term was omitted from all previous studies of Faraday waves. The lower hysteresis boundary in forcing-frequency space is found, in most cases, to be defined by the lower boundary above which non-trivial stationary points exist. However the stability of stationary points and the existence of stable limit cycles are also found to be factors in determining the lower hysteresis boundary. Our results also suggest an indirect method for estimating

the coefficient of cubic damping, which is difficult to obtain either experimentally or theoretically.

The stable limit cycles correspond to the amplitude and phase of the standing wave experiencing a slow periodic modulation, in addition to its fast basic periodicity. In Chapter IV, we examine the structure of this new solution in detail, both analytically and numerically. We describe local bifurcations using a multiple time scales analysis, and global bifurcations using Melnikov's method.

In Chapter V, the coefficients of linear and cubic damping are derived for a standing wave in a rectangular container by considering energy dissipation in the main body of the fluid and in boundary layers at the sidewalls and at the surface. Surface contamination due to the presence of a thin viscoelastic surface film creates a boundary layer at the surface which causes enhanced dissipation comparable to, or greater than, that caused by the boundary layers at the walls of the container. The linear analysis was carried out by Miles (1967), and is extended here to a weakly nonlinear theory for infinite depth. Second order mean velocity fields are found to arise in the boundary layers, which cause significant dissipation. These mean fields are found to give rise to streaming, as in Longuet-Higgins (1953), though here modified by the surface contamination. The effect of changes in the coefficient of cubic damping on hysteresis and mode competition in Faraday waves is discussed.

In Chapter VI, three-mode interaction equations are used to model Faraday waves with complex spatial structure, including travelling waves. Intermittency and complex modulations are found to arise from a sideband instability mechanism similar to that of Eckhaus (1963) and Benjamin & Feir (1967). The role of cubic and fifth-order nonlinear terms on this instability mechanism is examined. Theoretical results are found to compare quite favourably with experimental data.

Chapter VII contains a discussion of the conclusions of this thesis. Appendix A contains a discussion of two-mode competition, demonstrating the significance of cubic damping terms. Appendix B gives a numerical example of the derivation of (3.22) from Chapter III.

CHAPTER II

Experiment

1. Introduction

Experiments have been conducted using the same long rectangular tank as in Craik & Armitage (1995) to examine Faraday waves for an ambient water depth of 1.3cm (Craik & Armitage studied ambient water depths of 1cm and 2cm). For each value of the acceleration of forcing and frequency of oscillation of the tank, three different qualitative types of behaviour were found in the experiment of Craik & Armitage (1995): (i) the flat surface, (ii) waves (standing waves or travelling waves) and (iii) hysteresis, where both the flat surface and waves are possible. If the forcing and frequency of the vibration of the tank were chosen for a value corresponding to (i), then any waves already present would eventually decay to the flat surface. If the forcing and frequency of the tank were chosen for a value corresponding to (ii), then if the flat surface was initially present, waves would eventually appear. If the forcing and frequency of the tank were chosen for a value corresponding to (iii) then any waves initially present would persist, and the flat surface, if initially present, would persist. In practice, hysteresis is usually observed by slowly increasing the forcing of the tank (holding the frequency of forcing constant) until the flat surface destablizes, resulting in waves. The forcing is then slowly decreased until the waves disappear. This difference in the level of forcing for the onset and disappearance of waves corresponds to hysteresis.

The apparatus is described in section 2, and the experimental method and hysteresis results (for the 1.3cm ambient depth observations) are discussed in section 3. In section 4, the experimental results of Craik & Armitage (1995) are discussed. Their

experimental observations were more detailed, including observations of modulations and intermittency.

2. Apparatus

The experiment was carried out in a perspex tank of length 69.9 cm, width 2.82 cm and depth 7.7 cm which was suspended from two flat springs, allowing only vertical motion. The tank was driven by two vibrators, one near each end, connected in a series circuit. The circuit also contained a control box for the vibrators (setting frequency and acceleration of forcing), a counter to measure the frequency of oscillation and resistors to balance the two vibrators. A plate accelerometer was used to measure the r.m.s. forcing.

The depth of water used was 1.352 cm (measured using a vernier scale telescope to an accuracy of 0.001 cm). Fine controls on the legs of the base of the apparatus allowed the tank to be levelled. Distilled water was used with Kodak Photoflow wetting agent (proportion of wetting agent to water approximately 1:393) to reduce capillary hysteresis effects on the perspex walls and to avoid problems with inadvertent contamination of the surface. To reduce evaporation, a lid was added. The accelerometer was used in conjunction with the resistors to balance the vibrators by measuring the acceleration of the tank at each end when no waves were present; the output of the accelerometer could also be examined on an oscilloscope to check that the motion of the tank was sinusoidal.

3. Experimental method and hysteresis results

Standing waves of 21,22 and 23 half-wavelengths were examined experimentally. A frequency of oscillation would be chosen with an initial acceleration that was too small

to generate waves on a flat surface. The forcing was then gradually increased with an increment of about 0.01 ms^{-2}, with this being maintained for at least ten minutes each time before making a further change. When the forcing crossed over the neutral stability boundary, then it took about ten minutes for the standing waves to slowly build up from the flat surface. As in Craik & Armitage (1995), frequencies were chosen so that three-dimensional waves that vary across the width of the tank were avoided. Once a standing wave was obtained, the forcing was slowly decreased again until the wave disappeared. This whole process was repeated for a range of frequencies. (Note that the period of the oscillation was controllable to within 0.05%.)

Also a particular standing wave mode could be followed by slowly changing the frequency of oscillation. In this way, the lower hysteresis boundaries were found to extend beneath the neutral stability curves of neighbouring wave modes. As the frequency was further altered, the standing wave would suddenly jump to another mode with one less half-wavelength.

Figure 1 shows the experimental results for 21, 22 and 23 half-wavelengths. The upper curves show the onset of waves and the lower curves shows the disappearance of waves, with the hysteresis region between the two sets of curves. These are similar to the experimental results of Craik & Armitage (1995) for their 2.075 cm depth case, but unlike the results of their 1.060 cm depth case.

4. Summary of the experimental results of Craik & Armitage (1995) [1]

Craik & Armitage (1995) carried out experiments for ambient water depths of 1.060cm and 2.075cm. They carried out hysteresis observations and examined the nature of time-dependent surface waves.

---

[1] Figures 3, 4 and 8 appeared in Craik & Armitage (1995). Figures 2, 5, 6, 7, 9, 10 and 11 were produced during the same experimental set of observations, though were not published in Craik & Armitage (1995). All diagrams were kindly provided by Professor A. D. D. Craik, and are reproduced here with permission.

Their hysteresis results are shown (for three neighbouring modes) in Figures 2 and 3 for water depths of 1.060cm and 2.075cm respectively. It can be seen that Figure 3 is similar to Figure 1, but Figure 2 shows a qualitatively different hysteresis region. Note that the increment of the r.m.s. acceleration used in Figure 3 was 0.01 ms^{-2}, as for Figure 1. However, for Figure 2, the increment was 0.02 ms^{-2}.

(i) Nature of waves at an ambient water depth of 1.060 cm

For the 1.060 cm depth observations, standing waves always occurred initially, though strong modulations often set in shortly after onset. The onset and disappearance of modulations are shown in Figure 4 for a single mode: points marked (●) signify the onset of stable standing waves (from a flat surface), and points marked (■) signify the onset of modulations. The disappearance of modulations, resulting in stable standing waves, is denoted by points marked (□); therefore, the small region between the onset and disappearance of modulations is apparently a hysteresis region for the modulations. The disappearance of standing waves, resulting in a flat surface is denoted by points marked (○). The upper curve is the linear onset curve and the lower curve is the lower hysteresis boundary. It can be seen that for some frequencies, modulations are marked on the linear onset curve, while for other frequencies, there is an intermediate stable standing wave region between the linear onset curve and the points denoting the onset of modulations.

The modulations were described using a chart recorder. It was found that the r.m.s. acceleration of the tank was somewhat affected by the level and type of wave activity present (the waves exert a pressure on the bottom of the tank which interferes with the sinusoidal forcing of the tank; see Douady 1990 for a similar effect). As a result, the accelerometer detected modulations in the wave activity, and the signal from the accelerometer was fed into the chart recorder.

The modulations at this depth were characterised by two timescales: a dominant fast timescale of about 3 to 5 seconds, which was always present when modulations occurred, and a long timescale which was sometimes present for the 1.060 cm depth

modulations, but never present for the 2.075 cm depth modulations. Figure 5 shows a series of traces at T = 114ms with increasing r.m.s. accelerations. The first trace shows almost sinusoidal modulations with a period of about 17 seconds. The next two traces show modulations with the same period, but of a more complicated nature. The fourth trace shows a long period amplitude variation of about 57 seconds. The fifth trace shows complex behaviour, with periods of intense wave activity interspersed with intervals of very small waves. In all five traces there is also a shorter period of about 5 seconds, though this is not always clearly visible in the graphs.

The most interesting feature is the intermittency: periods of near calm interspersed with periods of intense wave activity. Figure 6 shows two good examples of this. In both cases, there was a virtually flat surface for about 3 minutes. Then a standing wave gradually appeared, started to modulate and then decayed again to zero in about 30 seconds, followed again by another 3 minute period of near calm.

Figure 7 shows a particularly intriguing case of intermittency for T = 111ms with a mean acceleration of 0.88 ms^{-2}. Here the calm periods are separated by unpredictable time intervals that vary from 55 to 100 seconds.

(ii) Nature of waves at an ambient water depth of 2.075 cm

For the 2.075 cm depth observations, modulations set in at r.m.s. accelerations considerably above that for the onset of standing waves (see Figure 8, which shows three neighbouring modes). The solid symbols denote the onset of modulations and the open symbols denote the disappearance of modulations. The curves denote the lower hysteresis boundaries. There is again a region where modulations or standing waves may occur, this time larger than the equivalent region for the 1.060 cm depth observations.

The nature of the modulations for this depth are quite different from the previous case, with no intermittency found at all. Figure 9 shows an almost continuous record over 28 minutes at T = 98.5 ms. The first trace begins with an r.m.s. acceleration of 0.85 ms^{-2}, showing standing waves. These standing waves start to modulate with a period

of 3.6 s. (The break in the trace shows where the chart recorder was set to a smaller scale.) The first arrow denotes an increase in the r.m.s. acceleration of about 20%. This can be seen to have increased the amplitude of the trace. The following arrow denotes a further increase of 10% in the r.m.s. acceleration. This can be seen to produce a second time-scale, of about 31.5 s, in addition to the 3.6 s modulations. The final arrow denotes a further increase in the r.m.s. acceleration, giving rise to rather peculiar modulations. Craik & Armitage report that these waves were no longer two-dimensional: spanwise-periodic disturbances could now be seen to appear and disappear in competition with the previously two-dimensional waves.

Figure 10 is the trace for T = 99.5 ms with the r.m.s. acceleration initially at 0.74 ms^{-2}, showing modulations with a period of about 3.4 s. The first arrow denotes an increase in the r.m.s. acceleration of about 15%, which causes the period to double to about 6.6 s. The second arrow shows a further small increase in the acceleration, which has little effect. The next arrow shows a further increase of 10% in the r.m.s acceleration, giving an additional modulation with period 24 s.

Figure 11 shows the trace for T = 102 ms. At first periodic modulations can be seen, before the acceleration is increased. After the signal has settled down, there are signs of period-doubling plus an additional slow modulation with a period of about 107 s. The modulations are irregular, though there is a dominant period of 6.6 s.

Finally, we discuss the limitations of the apparatus described in this Chapter. The resonant frequency of the tank was about 11.4 Hz, which is rather close to the frequency of oscillation which was about 10 Hz. As mentioned earlier in this section, the waves exerted a periodic force on the bottom of the tank, resulting in a considerable tank response: Craik & Armitage (1995) report decreases in the r.m.s. acceleration of up to 25% in response to the onset of waves, though usually the value was much less. It is desirable to minimise this tank response. The apparatus has recently been modified by Mr D. Sterratt, which resulted in the resonant frequency of the tank increasing to about 20.1 Hz, and therefore reducing the tank response. Preliminary experiments show results similar to those desribed here (see Sterratt 1995).

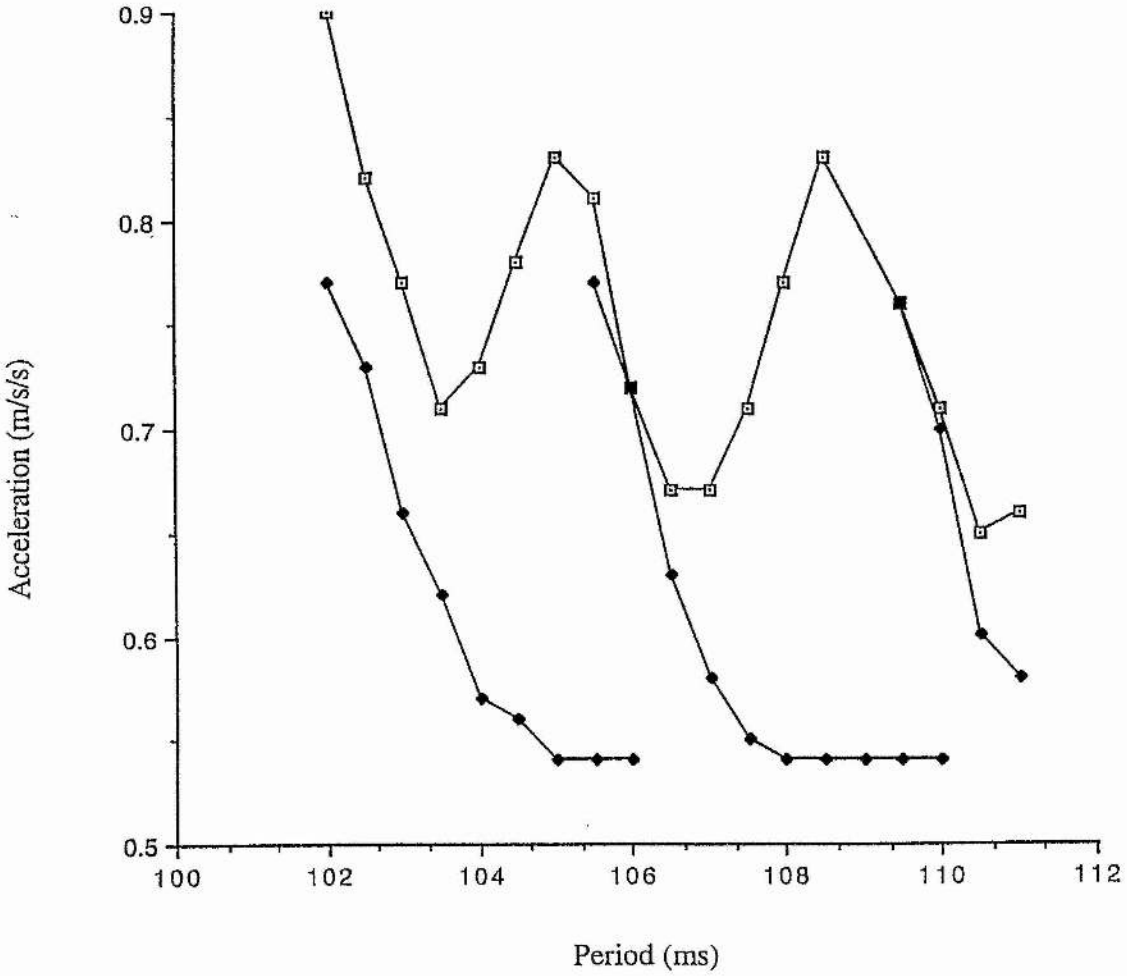

Figure 1. Experimental hysteresis results showing acceleration (ms^{-2}) against period (ms) for three neighbouring modes of 21, 22 and 23 half-wavelengths in a rectangular tank of length 70cm with a water depth of 1.3cm.

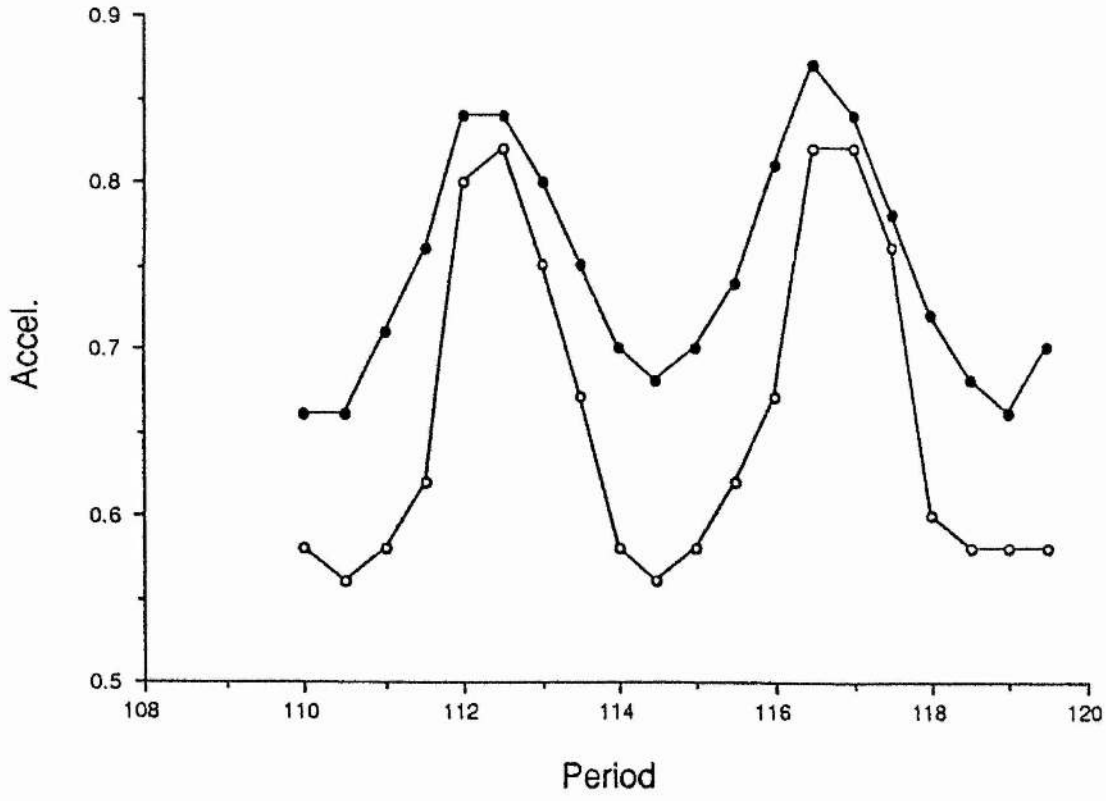

Figure 2. Experimental hysteresis results for three neighbouring modes of 21, 22 and 23 half-wavelengths for a water depth of 1cm.

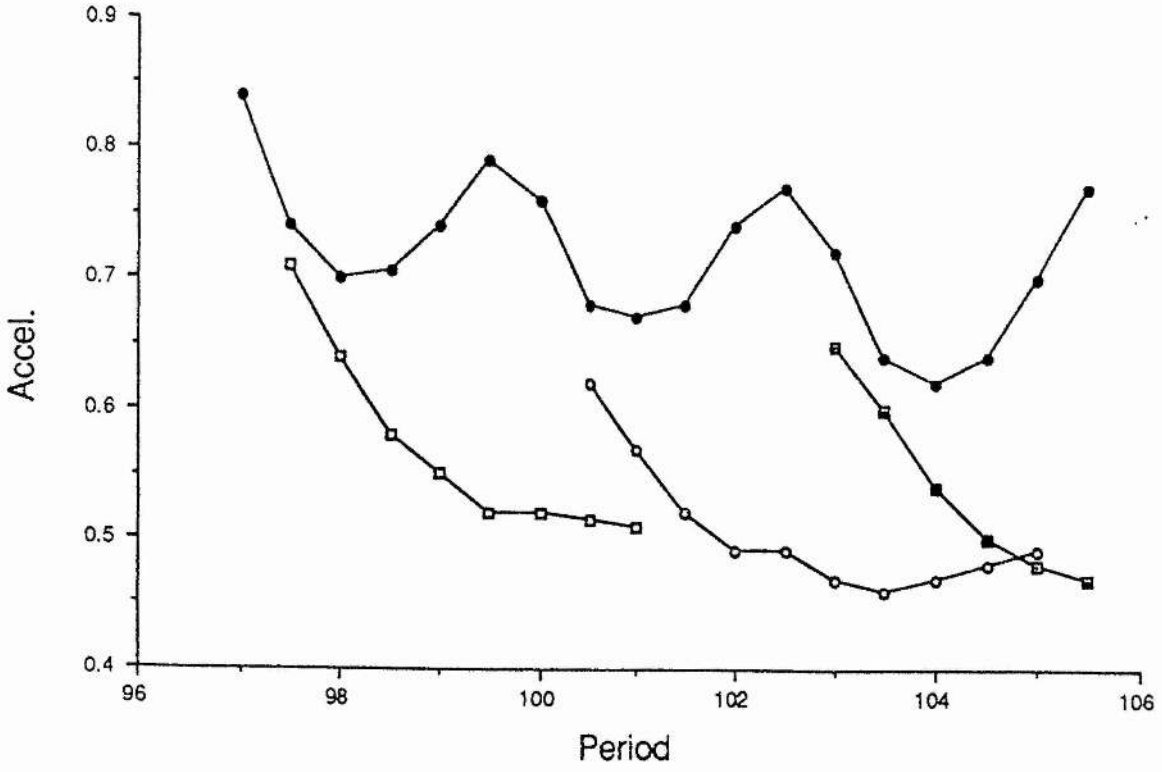

Figure 3. Experimental hysteresis results for three neighbouring modes of 21, 22 and 23 half-wavelengths for a water depth of 2cm.

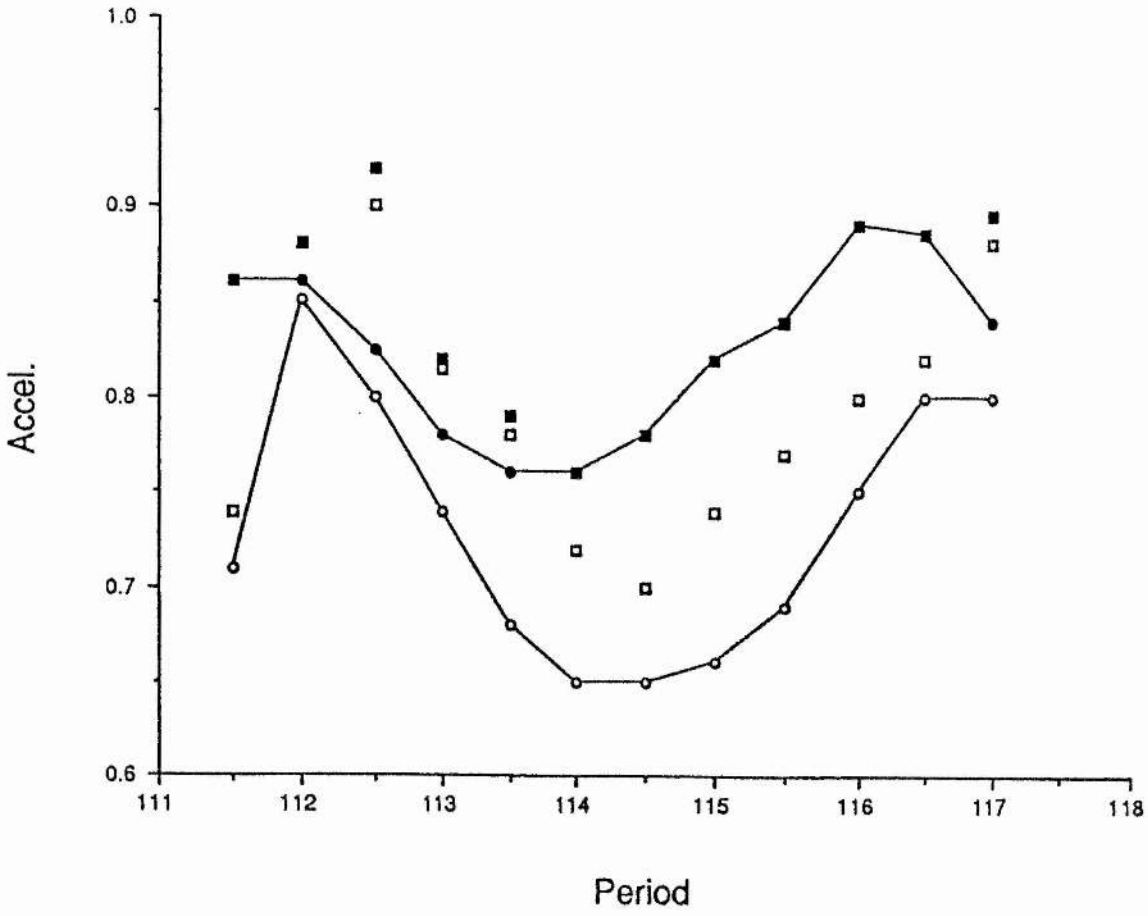

Figure 4. Experimental results for the onset and offset of standing waves and modulations for the 22 half-wavelength mode at a water depth of 1cm. Points marked (•) signify the onset of standing waves and points marked (■) signify the onset of modulations. The offset of modulations is denoted by (□) and the offset of standing waves is denoted by points marked (○).

Figure 5. Series of traces for T = 114 ms with increasing r.m.s. accelerations for a water depth of 1cm.

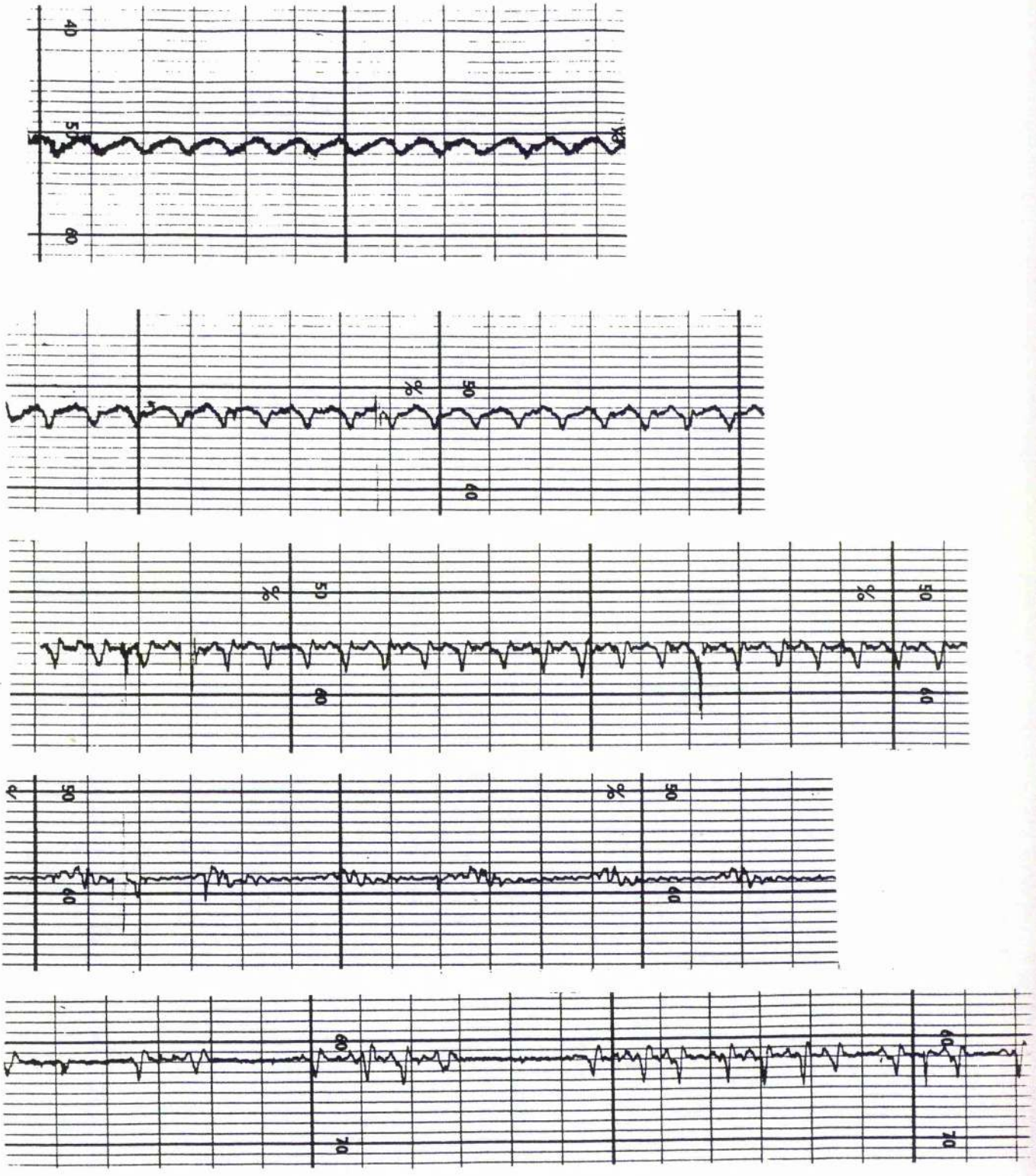

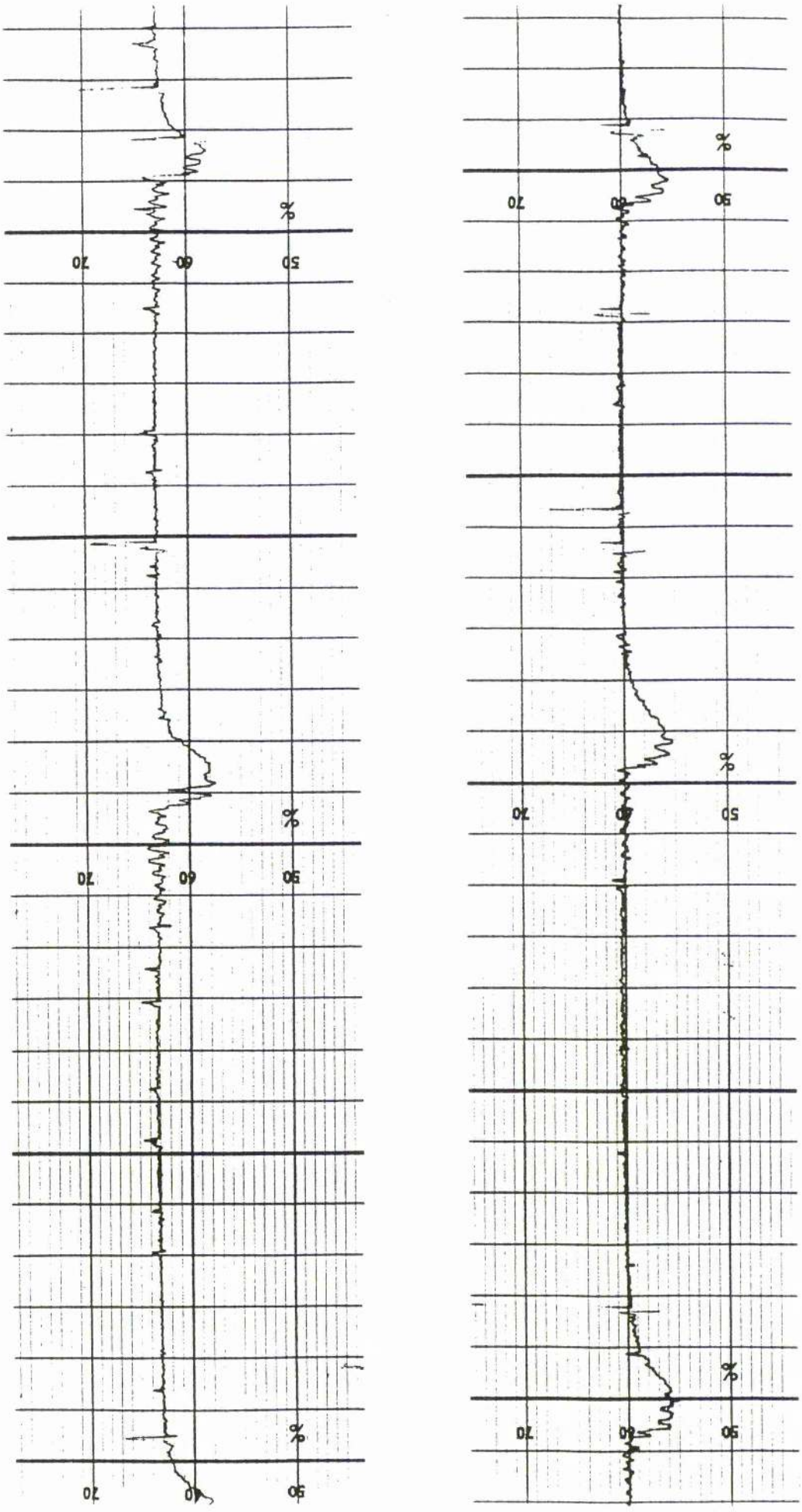

Figure 6. Two examples of intermittency for a water depth of 1cm.

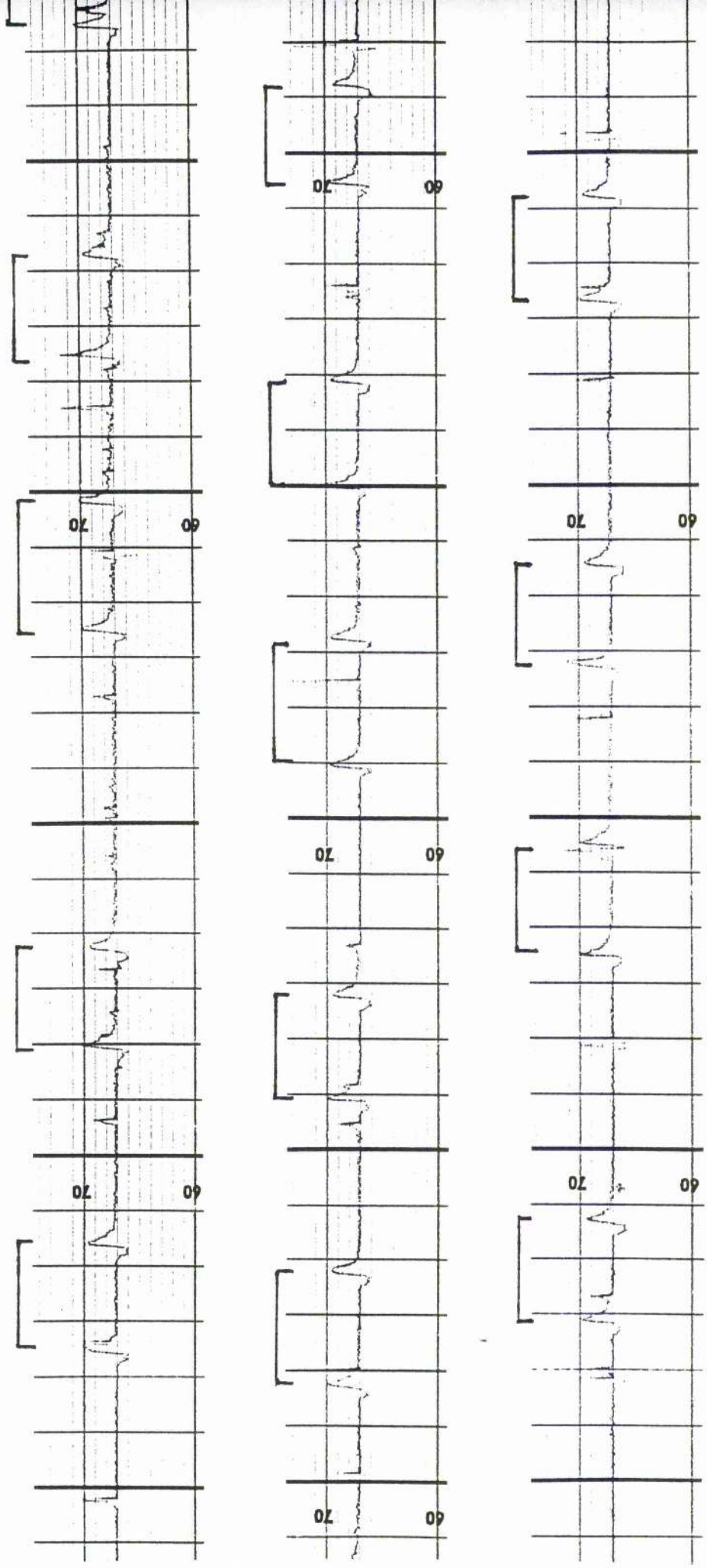

Figure 7. Intermittency for a water depth of 1cm for T = 111ms.

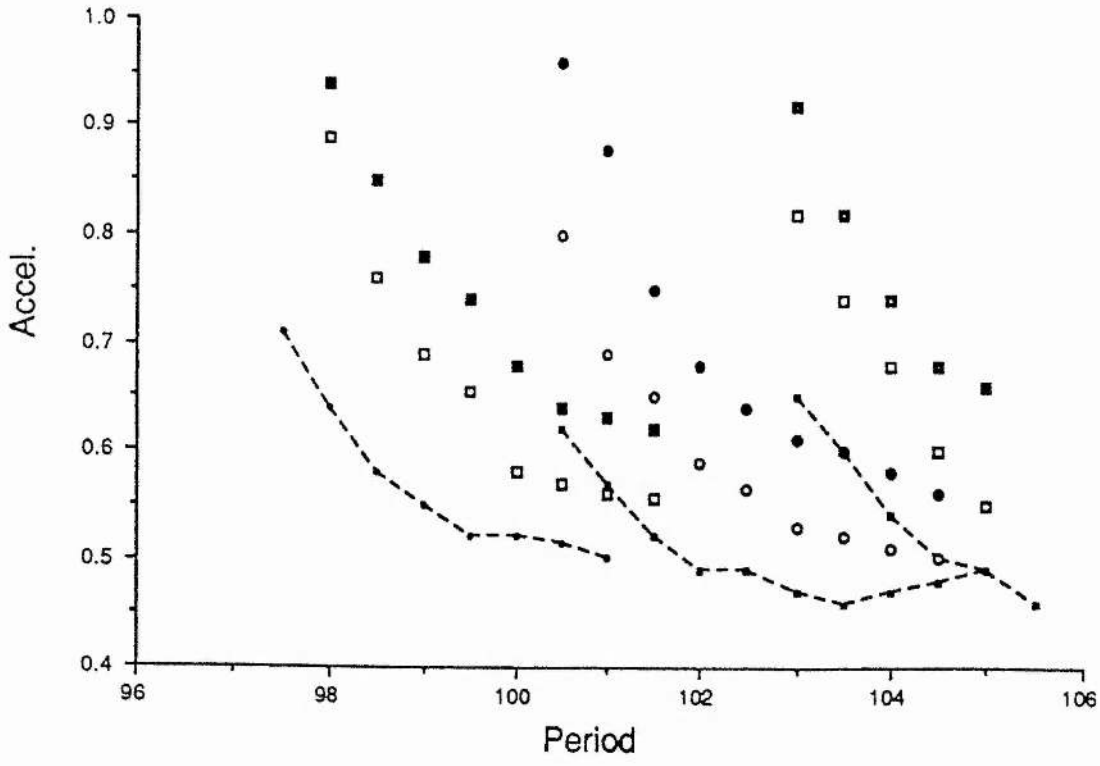

Figure 8. Experimental results for the onset and offset of modulations for three neighbouring modes of 21, 22 and 23 half-wavelengths for a water depth of 2cm. The solid symbols denote the onset of modulations and the open symbols denote the offset of modulations. The curves denote the lower hysteresis boundaries for the three modes.

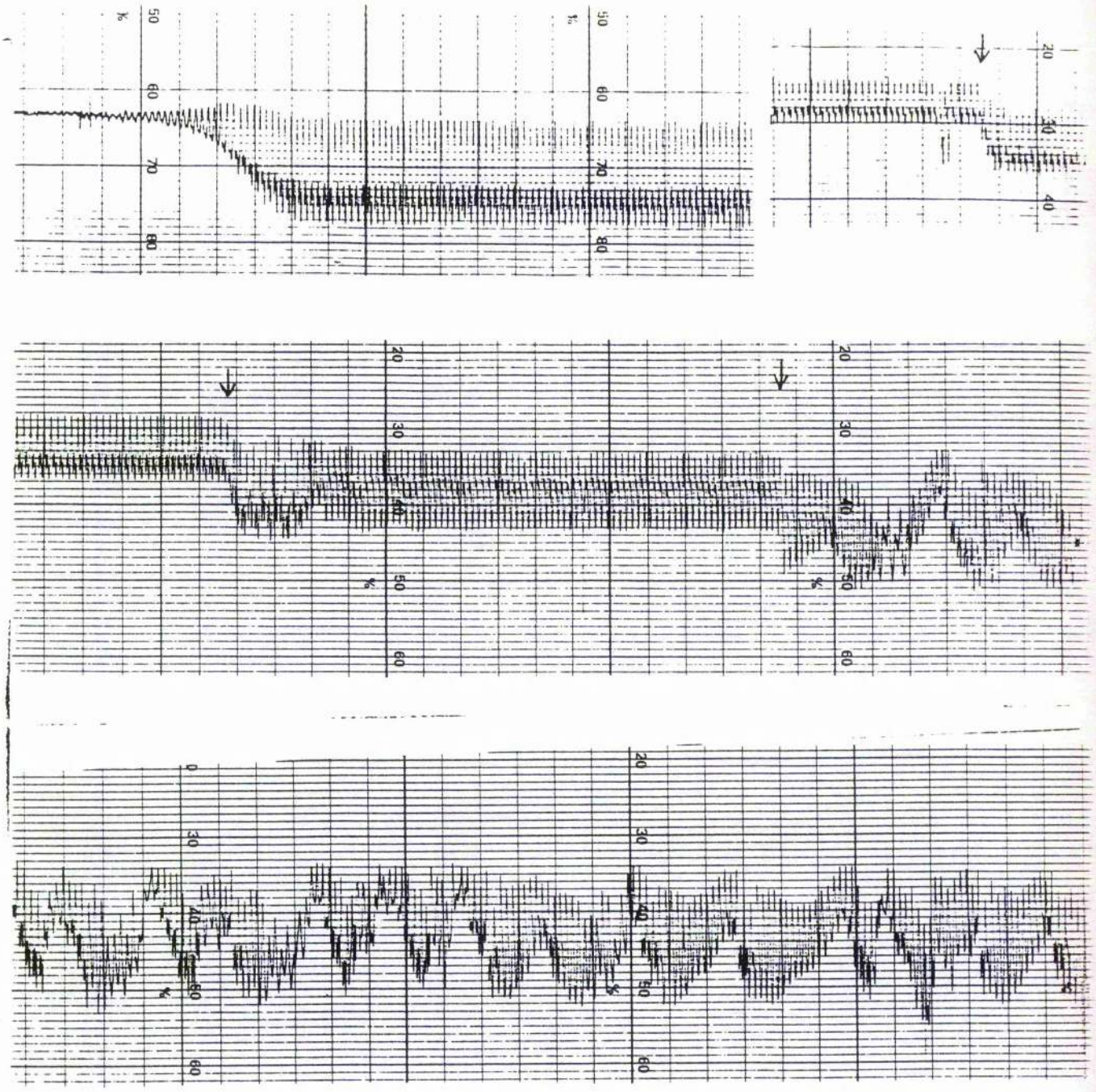

Figure 9. Modulations for a water depth of 2cm at T = 98.5 ms over a period of 28 minutes. The break in the trace shows where the chart recorder was set to a smaller scale. Each arrows denotes an increase in the r.m.s. acceleration of forcing.

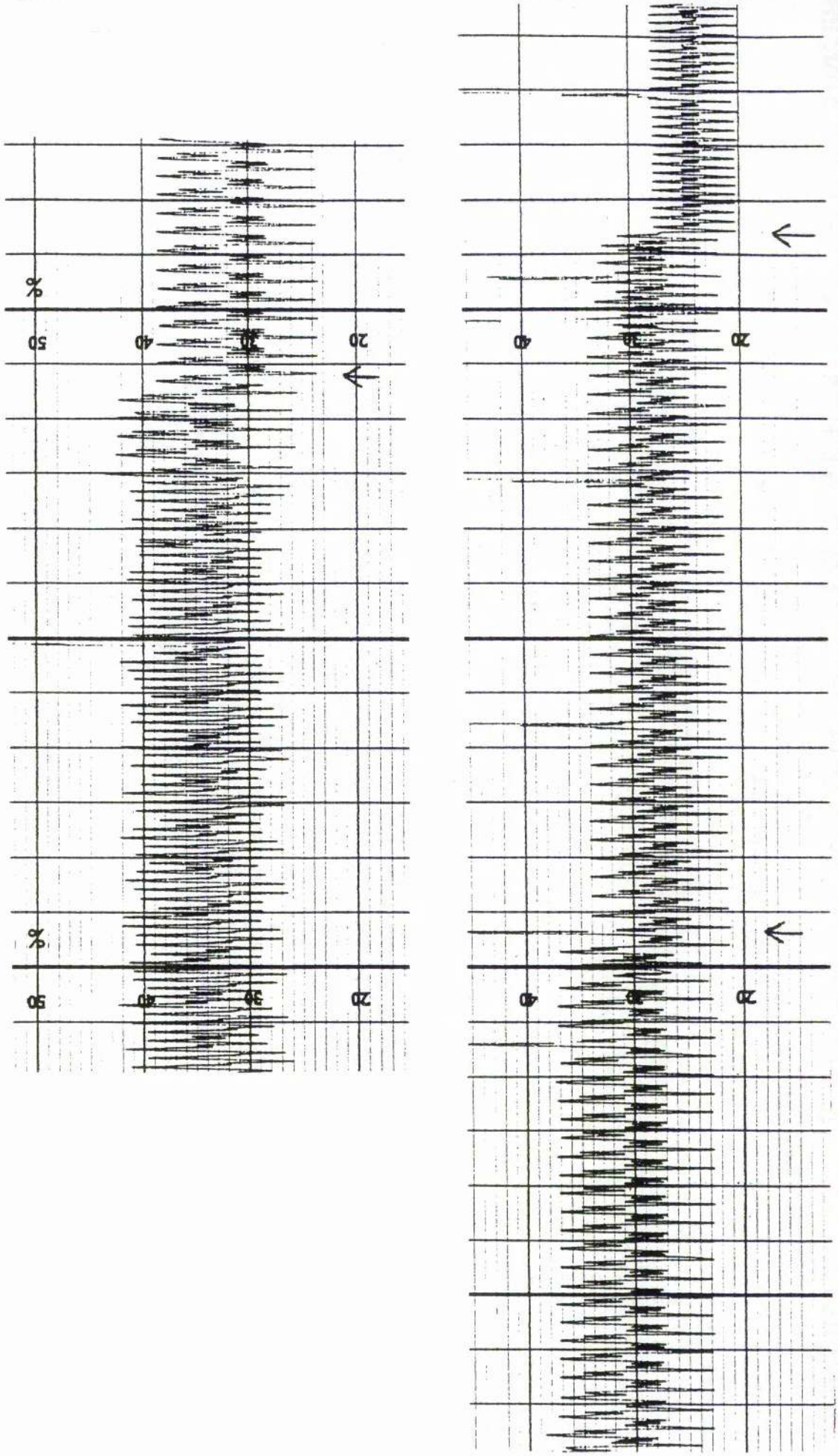

Figure 10. Trace for a water depth of 2cm for T = 99.5 ms. Each arrow indicates an increase in the acceleration of forcing.

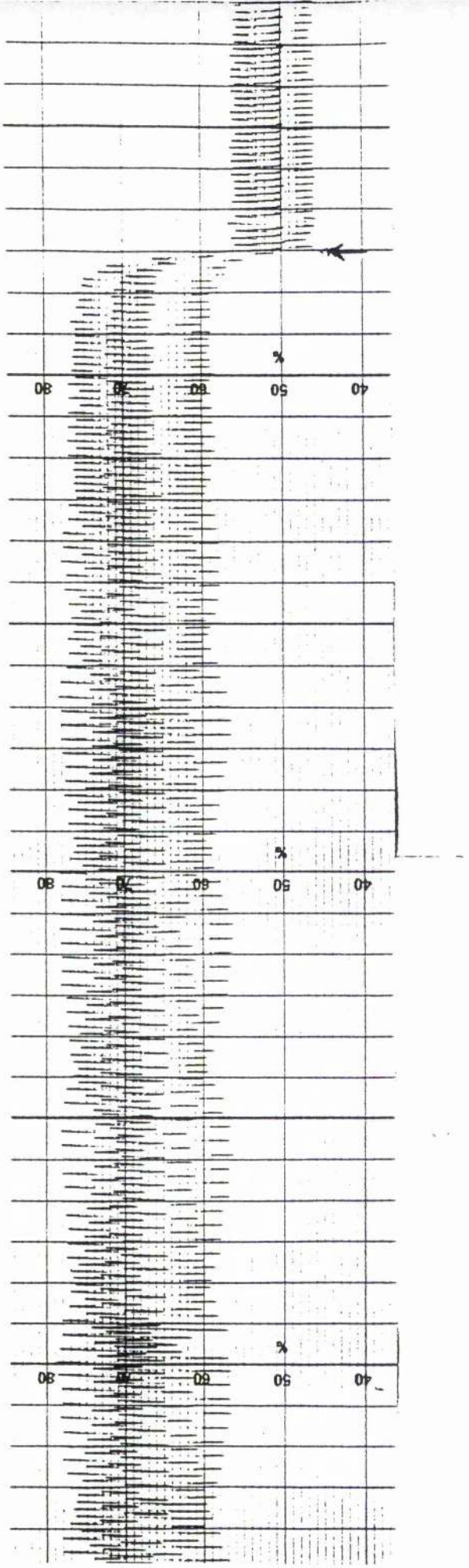

Figure 11. Trace for a water depth of 2cm for T = 102 ms. The arrow indicates an increase in the r.m.s. acceleration of forcing.

CHAPTER III

Hysteresis [2]

1. Introduction

Hysteresis occurs when constant finite-amplitude solutions and the flat surface solution are both available for a particular frequency and amplitude of sinusoidal forcing, with the observed behaviour being dependent upon the initial conditions. Both the linear stability boundary of the flat surface solution and the lower hysteresis boundary depend on the frequency and the amplitude of the forcing. In the frequency-amplitude plane, the stability boundary has a hyperbolic shape with its minimum (in amplitude) at the resonant frequency equal to *twice* that of the natural water wave frequency. In this plane, the hysteresis region is the area between the two boundaries.

A mathematical model of Faraday resonance is derived here which captures the essential features of hysteresis that have been observed in some experiments (Simonelli & Gollub (1989), Douady (1990), Craik & Armitage (1995) and the experiments described in Chapter II). Hysteresis has often been observed for values of forcing below the minimum value at which the flat surface solution is unstable. The lower hysteresis boundary sometimes bifurcates from this neutral stability curve at a point away from the minimum and the hysteresis lower boundary is generally curved (Figure 1, Chapter II shows the linear stability boundary and the lower hysteresis boundary, for three neighbouring modes in a long rectangular tank). The simple nonlinear theoretical model of a single mode by Miles (1976, 1984) has none of these features, in that it bifurcates from the minimum of the neutral stability curve, has no

[2] This Chapter will appear in Decent & Craik 1995 Hysteresis in Faraday resonance. *J. Fluid Mech.* **293**, *237-268.*

hysteresis below the minimum, and is a horizontal straight line (see Figure 1(a) discussed below). Later models by Douady (1990) and Milner (1991) better describe the bifurcation of the hysteresis boundary from the linear stability boundary and allow hysteresis below the minimum; but the boundary remains straight and, if extended sufficiently, would meet the zero forcing axis (see Figure 1(b) discussed below).

Craik & Armitage (1995) investigated theoretically and experimentally the hysteresis of two-dimensional Faraday waves in a long rectangular tank. Their theoretical model yields a variety of more realistic-looking hysteresis regions, though certain terms neglected (a fifth-order, in wave amplitude, conservative frequency shift, and one of the third-order forcing terms) in their model are likely to be of comparable size to those retained. Further, they did not calculate the coefficients of the terms in their equations for particular experimental configurations but considered instead the general form of the equations. Accordingly, they did not investigate the dependence of hysteresis upon depth, surface tension, wavelength, tank dimensions etc.

This Chapter, which follows on from Craik & Armitage (1995), calculates the various coefficients and provides a more rational derivation of the governing evolution equation which leads to the retention of the previously omitted fifth-order conservative frequency shift. We find that this fifth-order conservative term, a third-order forcing term, and a third-order damping term all combine to yield hysteresis regions similar to those observed in experiments.

The simplest nonlinear model of Faraday resonance is provided by the equation

$$\dot{A} = -\mu A + i\Omega A + iFA^{*} + i\Pi|A|^{2}A \tag{1.1}$$

(see Miles (1976, 1984)) where A is the slowly-varying complex wave amplitude; the overdot denotes a time-derivative, the real constants μ, Ω, F represent non-dimensionalised linear damping, frequency detuning from resonance, and the amplitude of the imposed vibrations, and Π represents the cubic coefficient of nonlinear (Stokes) frequency modification. Equilibrium solutions with $\dot{A} = 0$ give hysteresis as shown in Figure 1(a), with the linear stability criterion $F \geq \left(\Omega^{2} + \mu^{2}\right)^{1/2}$

and the lower hysteresis boundary $F = \mu$ on the left of the neutral stability boundary if Π is positive, and on the right if Π is negative.

Douady (1990) and Milner (1991) instead proposed

$$\dot{A} = -\mu A + i\Omega A + iFA^* + i\Pi|A|^2 A + d|A|^2 A \tag{1.2}$$

which retains a cubic correction to the damping with real coefficient d. However they ignore cubic forcing and the fifth-order conservative frequency shift that can be of the same order of magnitude (see later). This produces hysteresis diagrams of the form shown in Figure 1(b) corresponding to d positive and negative respectively. In the experiments by Simonelli & Gollub (1989) and Craik & Armitage (1995) hysteresis diagrams somewhat similar to Figure 1(b) (line a) were found, but the lower hysteresis boundary turned upwards before reaching the line $F = 0$ and was curved rather than straight. Douady (1990) interpreted his observations in terms of Figure 1(b) (line b) (in fact, he observed no hysteresis in his experiment).

If $d < 0$, then the cubic correction to the damping in (1.2) acts to enhance dissipation; if it is positive then it will act in opposition to the linear damping term, reducing dissipation. In the latter case, so long as $d|A|^2$ is sufficiently small, the combined effect of the two terms is dissipative; however if $d|A|^2$ exceeds μ then the model clearly breaks down. The coefficient d is difficult to calculate or to measure experimentally. Milner (1991) and Miles (1993, 1994) give expressions for d that are based upon the assumptions of large depth and small wavelength and waveslope, and that the surface is uncontaminated. However this is often not the case; in particular, in the experiments described here and in Craik & Armitage (1995) these assumptions do not hold. Even the *linear* damping coefficient μ is rather difficult to calculate or to measure experimentally. Both damping coefficients, μ and d will depend upon viscous boundary layers at the sidewalls and the bottom of the tank, surface contamination etc: see Miles (1967). But μ and d may be estimated indirectly by comparison of theoretical and experimental data, as described in section 5.

Miles (1993) and Craik & Armitage (1995) both proposed a model equation that incorporates third-order forcing and third-order damping terms, namely

$$\dot{A} = -\mu A + i\Omega A + iFA^* + i\Pi|A|^2 A + d|A|^2 A + i\overline{F}\left(A^3 + 3|A|^2 A^*\right) \qquad (1.3)$$

and this produces hysteresis somewhat like those in Figure 1(b) if $\overline{F}$ is chosen to be constant with respect to variations in F (note that an overbar does *not* denote complex conjugate). However the coefficient of cubic-forcing $\overline{F}$ is proportional to F and so does not remain constant as F varies. Craik & Armitage (1995) showed that (1.3) can produce qualitatively all the observed effects of hysteresis. However, we here argue that a fifth-order conservative frequency shift may well be of comparable size to the cubic damping and cubic forcing terms, and so the inclusion of cubic damping and/or cubic forcing cannot be justified rationally without also retaining a fifth-order conservative term in $|A|^4 A$. Here, as in Miles (1976,1984), Umeki (1991) and Umeki & Kambe (1989), a rational theory is developed in terms of a small parameter ε which orders the terms in the governing equations. The cubic corrections to damping and forcing then appear formally at the same order in ε as an $|A|^4 A$ conservative term.

Craik & Armitage (1995) mainly investigate a simplified version of (1.3) with the $i\overline{F}A^3$ term neglected. This still produces hysteresis qualitatively similar to observations, while permitting precise analytic description. Miles (1993) mainly considered pattern selection and did not explicitly obtain the hysteresis boundary.

Miles (1993) gives a formula for the coefficient of cubic forcing $\overline{F}$ in terms of depth, wavelength, surface tension and tank geometry, but the equivalent formula calculated here is not in agreement with this. In fact, Miles omitted the effect of the third harmonic of the dominant mode and we find that this contributes to the cubic forcing term. Our result and Miles' are often, but not always, close numerically.

In Chapter II, hysteresis was described experimentally for water depths of 1cm, 1.3cm and 2cm. The results for 1.3cm resemble those for 2cm, but are unlike those at 1cm. One reason for this is that the coefficient Π changes sign at a depth between 1cm and 1.3cm.

Our mathematical model is derived using the variational method due to Miles (1976, 1984, 1993), Umeki and Kambe (1989) and Umeki (1991). Along the way, the

Lagrangian is calculated up to sixth-order in the generalised co-ordinate for any discrete set of wave modes in an arbitrary cylinder of cross-section S undergoing vertical oscillations; previously only fourth-order expansions have been derived (Miles 1976). The initial generality of this derivation potentially allows the fifth-order conservative terms to be incorporated into other (future) Faraday wave problems (e.g. mode competition and pattern selection). Here a single two-dimensional mode is considered, but this restriction is made only towards the end of section 2. Examination of a different geometry or multiple wave interactions up to fifth-order could be done by using the general Lagrangian given in section 2 as the starting point.

The derivation of the evolution equations is described in section 3. This was algebraically very demanding and made extensive use of the symbolic manipulation computer package MAPLE. The nonlinear evolution equations are arrived at in the form

$$\begin{aligned} \frac{\partial A}{\partial \tau_1} &= -\mu A + i\Omega A + iFA^* + i\Pi|A|^2 A \\ \frac{\partial A}{\partial \tau_2} &= N|A|^2 A + i\bar{F}\left(A^3 + 3|A|^2 A^*\right) - ih|A|^4 A \end{aligned} \tag{1.4}$$

where τ_1 and τ_2 are separate slow and very slow time scales. The lower hysteresis boundary is investigated analytically in section 4 and computationally in section 5, by considering the existence of finite-amplitude stationary solutions. This allows a comparison between experimental and theoretical results. Numerical lower hysteresis boundaries from our model can be directly compared both to experimental observations and to the corresponding boundaries produced using the simpler model (1.3). This clearly shows that our model produces lower hysteresis boundaries that are quantitatively and qualitatively closer to observations than the previous 'best' model. Unfortunately the experiment of Simonelli & Gollub (1989) cannot be described by our model since they observed three-dimensional waves and we have only considered two-dimensional waves here, though broad qualitative agreement is obtained. However, we anticipate that quantitative agreement can be achieved with a three-dimensional model similar to that of (1.4).

The numerical solutions also indirectly give estimates for the coefficient of cubic damping. This is achieved by choosing the coefficient so that the experimental and theoretical lower hysteresis boundaries are as close as possible (described later).

The stability of finite amplitude solutions is investigated in section 6. In some cases this leads to a revised theoretical prediction of the lower hysteresis boundary. Also time-dependent solutions of the evolution equation are briefly discussed. It is found that for the 2cm depth experiment, the hysteresis region contains small stable limit cycles as well as stable stationary points: these limit cycles represent standing waves with amplitudes that experience a (small) slow oscillation on top of the fast sinusoidal oscillation at the basic frequency. This modulation of the wave amplitude would be difficult to observe experimentally with the present apparatus because the amplitude of the slow oscillation is never more than 10-20% of the amplitude of the fast oscillation, and the latter amplitude is only a few millimetres. Further experimental work is needed with more accurate equipment to investigate these stable limit cycles.

Finally a word on terminology. The *lower hysteresis boundary* is the theoretical lower boundary above which non-trivial solutions (stationary or time-oscillatory) exist and are stable. We will show that this usually coincides with the boundary above which non-trivial stationary points exist, since these stationary points are normally, but not invariably, stable. Sections 4 and 5 are concerned with calculating this boundary. However, as discussed in section 6, the boundary above which non-trivial stationary points are stable is sometimes distinct from the boundary above which non-trivial stationary points exist, and in this case, *the lower stability boundary* is the appropriate lower hysteresis boundary.

2. Derivation of generalised Lagrangian

Consider capillary-gravity surface waves of an inviscid liquid of density ρ in a closed cylindrical container of cross-section S and depth d. Let (x,y,z) be the co-

ordinates in a reference frame fixed in the container, with the bottom being identified as the plane $z=-d$, and S being independent of z. Let $\mathbf{n}$ be the outward normal to the fluid boundary, and let the free surface be denoted by $z=\eta(x,y,t)$. Assuming that the fluid motion is irrotational, it may be represented by the velocity potential $\phi(x,y,z,t)$ where $\nabla\phi$ is the fluid velocity.

Following Miles (1976), the governing evolution equations can be derived using the Lagrangian method by applying the variational principle. The dynamic boundary condition is not explicitly used, but is instead incorporated intrinsically as part of the variational principle. The kinematical boundary-value problem is

$$\begin{aligned} &\nabla^2\phi=0, \quad (x,y)\in S, -d<z<\eta, \\ &\mathbf{n}.\nabla\phi=0 \text{ on container}, \quad \phi_z-\nabla\eta.\nabla\phi=\eta_t \text{ on } z=\eta. \end{aligned} \tag{2.1}$$

This can be derived from the variational problem

$$SI=\frac{1}{2}\iiint(\nabla\phi)^2 dSdz-\iint(\phi)_{z=\eta}\eta_t dS \tag{2.2}$$

with respect to variations $\delta\phi$ of ϕ for given η.

Now take

$$\eta(x,y,t)=\eta_n(t)\psi_n(x,y), \quad \phi(x,y,z,t)=\phi_n(t)\chi_n(x,y,z), \tag{2.3}$$

where η_n and ϕ_n are generalised co-ordinates, $\{k_n\}$ are the eigenvalues and $\{\psi_n\}$ and $\{\chi_n\}$ are the eigenfunctions from

$$\begin{aligned} &(\nabla^2+k_n^2)\psi_n=0, \quad \mathbf{n}.\nabla\psi_n=0 \text{ on } \partial S, \\ &\iint\psi_m\psi_n dS=\delta_{mn}S, \quad k_n=|\mathbf{k}_n|, \\ &\chi_n(x,y,z)=\psi_n(x,y)\sec h(k_n d)\cosh\{k_n(z+d)\}, \quad \text{n not summed}, \end{aligned} \tag{2.4}$$

and δ_{mn} is the Kronecker delta function.

Repeated indices are summed over the set of eigenfunctions except where stated.

Substituting (2.3) into (2.2) gives

$$I=\frac{1}{2}j_{mn}\phi_m\phi_n-d_{mn}\dot{\eta}_m\phi_n, \tag{2.5}$$

where

$$d_{mn}=S^{-1}\iint(\chi_n)_{z=\eta}\psi_m dS, \quad j_{mn}=S^{-1}\iint dS\int_{-d}^{\eta}\nabla\chi_m.\nabla\chi_n dz. \tag{2.6}$$

Applying the variational principle to (2.5) (by making I stationary with respect to variations in ϕ) gives

$$\phi_n = l_{nm}\dot{\eta}_m, \tag{2.7}$$

where

$$l_{nm} = d_{nl}j_{lm}^{-1}. \tag{2.8}$$

Substituting (2.3 a) and (2.4 e) into (2.6) and expanding about $z=0$ using Taylor's theorem gives (see appendix of Miles (1976))

$$\begin{aligned} d_{mn} = \delta_{mn} + C_{lmn}j_n\eta_l + \frac{1}{2}C_{jlmn}k_n^2\eta_j\eta_l + \frac{1}{6}C_{ijlmn}j_nk_n^2\eta_i\ \eta_j\eta_l \\ + \frac{1}{24}C_{hijlmn}k_n^4\eta_h\eta_i\eta_j\eta_l + \ldots, \end{aligned} \tag{2.9}$$

$$\begin{aligned} j_{mn} = \delta_{mn}j_m + \left(C_{lmn}j_mj_n + D_{lmn}\right)\eta_l + \frac{1}{2}\left[C_{jlmn}\left(j_mk_n^2 + j_nk_m^2\right) + D_{jlmn}\left(j_m + j_n\right)\right]\eta_j\eta_l \\ + \frac{1}{6}\left[C_{ijlmn}\left(j_mj_nk_m^2 + j_mj_nk_n^2 + 2k_m^2k_n^2\right) + D_{ijlmn}\left(k_m^2 + k_n^2 + 2j_mj_n\right)\right]\eta_i\eta_j\eta_l \\ + \frac{1}{24}\left[C_{hijlmn}\left(j_nk_m^4 + 3j_mk_n^2k_m^2 + 3j_nk_n^2k_m^2 + j_mk_n^4\right)\right. \\ \left. + D_{hijlmn}\left(j_mk_m^2 + 3j_nk_m^2 + 3j_mk_n^2 + j_nk_n^2\right)\right]\eta_h\eta_i\eta_j\eta_l + \ldots, \end{aligned} \tag{2.10}$$

where

$$\begin{aligned} j_n &= k_n\tanh(k_nd), \\ C_{lmn} &= S^{-1}\iint \psi_l\psi_m\psi_n dS, \qquad C_{jlmn} = S^{-1}\iint \psi_j\psi_l\psi_m\psi_n dS \quad \text{etc.} \\ D_{lmn} &= S^{-1}\iint \psi_l\nabla\psi_m.\nabla\psi_n dS, \quad D_{jlmn} = S^{-1}\iint \psi_j\psi_l\nabla\psi_m.\nabla\psi_n dS \quad \text{etc.} \end{aligned} \tag{2.11}$$

This now allows l_{mn} to be calculated explicitly up to the term in $\eta_h\eta_i\eta_j\eta_l$ from (2.8), though the result is very complicated and is not given here.

The dynamical problem is now considered by constructing the Lagrangian. The kinetic energy of the fluid is described by

$$T = \frac{1}{2}\rho\iiint\left(\nabla\phi\right)^2 dSdz = \frac{1}{2}\rho Sj_{mn}\phi_m\phi_n = \frac{1}{2}\rho Sa_{mn}\dot{\eta}_m\dot{\eta}_n, \tag{2.12}$$

where

$$a_{mn} = d_{mj}l_{jn}. \tag{2.13}$$

Substituting (2.9) and the expression for l_{mn} into (2.13) gives

$$a_{mn} = \delta_{mn}a_m + a_{lmn}\eta_l + \frac{1}{2}a_{jlmn}\eta_j\eta_l + \frac{1}{6}a_{ijlmn}\eta_i\eta_j\eta_l + \frac{1}{24}a_{hijlmn}\eta_h\eta_i\eta_j\eta_l + \ldots, \tag{2.14}$$

where

$$a_n = j_n^{-1}, \tag{2.15}$$

$$a_{lmn} = C_{lmn} - D_{lmn}a_ma_n, \tag{2.16}$$

$$a_{jlmn} = -D_{jlmn}\left(a_m + a_n\right) + 2D_{jmg}D_{\ln g}a_g a_m a_n, \tag{2.17}$$

$$\begin{aligned} a_{ijlmn} = &-2C_{ijlmn}k_n^2 k_m^2 a_m a_n - D_{ijlmn}\left\{\left(k_m^2 + k_n^2\right)a_m a_n + 2\right\} \\ &+ 3D_{ijmg}D_{\lg n}a_n\left(a_g + a_m\right) + 3D_{j\lg n}D_{img}a_m\left(a_g + a_n\right) \\ &+ 3C_{j\lg n}D_{img}k_n^2 a_m a_n + 3C_{jlmg}D_{ign}k_m^2 a_m a_n \\ &- 6\mathbf{D}_{\ln f}D_{img}a_m a_n\left(a_g a_f D_{jgf} + C_{fjg}\right). \end{aligned} \tag{2.18}$$

$$\begin{aligned} a_{hijlmn} = &-4C_{hijme}D_{len}k_e^2 a_n \\ &+\left\{4C_{ijlen}k_n^2\left(1 + 2k_e^2 a_n a_e\right) + 4D_{ijlen}\left(\left(k_e^2 + k_n^2\right)a_n a_e + 2\right)\right. \\ &-12D_{\lg n}D_{ijeg}a_n\left(a_g + a_e\right) - 12D_{\lg n}C_{ijeg}a_n\left(a_g k_g^2 + a_e k_e^2\right) \\ &\left.-12\left[C_{j\lg n}a_e a_n k_n^2 + D_{j\lg n}a_e\left(a_g + a_n\right) - 2D_{\ln f}a_n a_e\left(a_f a_g D_{jgf} + C_{fjg}\right)\right]D_{ieg}\right\} \\ &-12\left[C_{j\lg n}a_n j_g k_n^2 + D_{j\lg n}\left(1 + a_n j_g\right) - 2D_{\ln f}a_n\left(a_f D_{jgf} + C_{fjg}j_g\right)\right]C_{ieg}\left\{\left(D_{hme}\ a_m + C_{hme}j_e\right)\right. \\ &-6\left\{D_{himg}\left(1 + a_m j_g\right) + C_{himg}\left(k_g^2 + a_m j_g k_m^2\right)\right\}\times \\ &\left\{-C_{j\lg n}a_n k_n^2 - D_{j\lg n}\left(a_g + a_n\right) + 2D_{\ln f}a_n\left(C_{fjg} + D_{jgf}a_g a_f\right)\right\} \\ &+4D_{\lg n}a_n\left\{D_{hijmg}\left(a_g a_m\left[k_m^2 + k_g^2\right] + 2\right) + C_{hijmg}\left(k_m^2 + k_g^2 + 2a_m a_g k_m^2 k_g^2\right)\right\} \\ &-D_{hijlmn}\left(a_n k_m^2 + 3a_m k_m^2 + 3a_n k_n^2 + a_m k_n^2\right) - C_{hijlmn}3k_n^2 k_m^2\left[a_m + a_n\right] \\ &+6C_{hime}k_e^2\left\{-C_{jlen}a_n k_n^2 - D_{jlen}\left(a_e + a_n\right) + 2D_{\ln g}\left(C_{gje} + D_{jeg}a_g a_e\right)a_n\right\} \\ &+4C_{hmd}j_d\left\{-C_{ijldn}\left(k_n^2 + 2k_n^2 k_d^2 a_n a_d\right) - D_{ijldn}\left[\left(k_d^2 + k_n^2\right)a_n a_d + 2\right]\right. \\ &+3D_{\lg n}C_{ijdg}a_n\left(a_g k_g^2 + a_d k_d^2\right) + 3D_{\lg n}D_{ijdg}a_n\left(a_g + a_d\right) \\ &+3\left[C_{j\lg n}a_n j_g k_n^2 + D_{j\lg n}\left(1 + a_n j_g\right) - 2D_{\ln f}a_n\left(a_f D_{jgf} + C_{fjg}j_g\right)\right]C_{idg} \\ &\left.+3\left[C_{j\lg n}a_d a_n k_n^2 + D_{j\lg n}a_d\left(a_g + a_n\right) - 2D_{\ln f}a_n a_d\left(a_f a_g D_{jgf} + C_{fjg}\right)\right]D_{idg}\right\}. \end{aligned} \tag{2.19}$$

The summing convention may at first appear complicated, but is quite straightforward. For example in (2.19), h,i,j,l,m and n (which appear on the left-hand side) are not summed, while d,e,f and g (which do not) are summed over the set of participating modes.

In section 3, where a single primary two-dimensional mode will be considered (along with its second and third harmonics), these considerably simplify using eigenfunctions and eigenvectors given by (3.13) and (3.14) respectively. The required non-trivial constants will then be

$$a_{112}=a_{121}=\frac{1}{\sqrt{2}}\left(1-2k_1^2a_1a_2\right),\quad a_{211}=\frac{1}{\sqrt{2}}\left(1+k_1^2a_1^2\right),$$
$$a_{123}=a_{132}=\frac{1}{\sqrt{2}}\left(1-6k_1^2a_2a_3\right),\quad a_{231}=a_{213}=\frac{1}{\sqrt{2}}\left(1-3k_1^2a_1a_3\right),\tag{2.20}$$
$$a_{321}=a_{312}=\frac{1}{\sqrt{2}}\left(1+2k_1^2a_1a_2\right),$$

$$a_{1111}=k_1^2a_1\left(4k_1^2a_1a_2-1\right),\quad a_{1122}=4k_1^2a_2\left(k_1^2a_1a_2-2+9k_1^2a_2a_3\right),$$
$$a_{2211}=k_1^2a_1\left(k_1^2a_1^2-2+9k_1^2a_1a_3\right),\quad a_{2112}=a_{1221}=18k_1^4a_1a_2a_3-2k_1^4a_1^2a_2,$$
$$a_{1113}=a_{1131}=12k_1^4a_1a_2a_3-\frac{3}{2}k_1^2\left(a_1+a_3\right),\tag{2.21}$$
$$a_{1311}=a_{3111}=k_1^2a_1\left(1-4k_1^2a_1a_2\right),$$

$$a_{11112}=a_{11121}=-\frac{1}{\sqrt{2}}k_1^2\left(4-49k_1^2a_1a_2+24k_1^4a_1^2a_2^2-27k_1^2a_2a_3+216k_1^4a_1a_2^2a_3\right),$$
$$a_{11211}=\sqrt{2}k_1^4a_1\left(\frac{13}{4}a_1+\frac{27}{4}a_3+6k_1^2a_1^2a_2-54k_1^2a_1a_2a_3\right),\tag{2.22}$$
$$a_{12111}=4\sqrt{2}k_1^4a_1^2,$$
$$a_{21111}=\sqrt{2}k_1^4a_1\left(-\frac{11}{4}a_1+\frac{27}{4}a_3+6k_1^2a_1^2a_2-54k_1^2a_1a_2a_3\right),$$

$$a_{111111}=\frac{205}{2}k_1^4a_1-\frac{81}{2}k_1^4a_3-9\frac{k_1^2}{a_2}-200k_1^6a_1^2a_2$$
$$+216k_1^6a_1a_2a_3+96k_1^8a_1^3a_2^2+864k_1^8a_1^2a_2^2a_3.\tag{2.23}$$

The potential energy due to the free-surface displacement is

$$V_A=\rho\iint dS\int_0^{\eta}\left(g+\ddot{z}_0\right)zdz=\frac{1}{2}\rho S\left(g+\ddot{z}_0\right)\eta_n\eta_n,\tag{2.24}$$

where ρ is the density of the liquid, g is the acceleration due to gravity and $\ddot{z}_0$ is the vertical acceleration of the container. The potential energy due to the surface tension is given by

$$V_B=\gamma\iint\left(\left(1+\left(\nabla\eta\right)^2\right)^{1/2}-1\right)dS,\tag{2.25}$$

where γ is the coefficient of surface tension.

This gives

$$V_B=\rho Sc_{mn}\eta_m\eta_n,\tag{2.26}$$

where

$$c_{mn}=\frac{\gamma}{2\rho}\left(\delta_{mn}k_n^2-\frac{1}{4}E_{jlmn}\eta_j\eta_l+\frac{1}{8}E_{hijlmn}\eta_h\eta_i\eta_j\eta_l-\ldots\right),\tag{2.27}$$

$$E_{jlmn} = S^{-1}\iint(\nabla\psi_j.\nabla\psi_l)(\nabla\psi_m.\nabla\psi_n)dS,$$
$$E_{hijlmn} = S^{-1}\iint(\nabla\psi_h.\nabla\psi_i)(\nabla\psi_j.\nabla\psi_l)(\nabla\psi_m.\nabla\psi_n)dS. \tag{2.28}$$

The Lagrangian is given by

$$L = (\rho S)^{-1}(T - V_A - V_B). \tag{2.29}$$

By defining

$$\omega_n^2 \equiv gk_n \tanh(k_n d)(1+\lambda^2 k_n^2), \tag{2.30}$$

where ω_n is just the natural (linearised) frequency of the nth normal mode, d is the depth and $\lambda = (\gamma/\rho g)^{1/2}$ is the capillary length, the Lagrangian can be rearranged into

$$\begin{aligned} L = {} & \frac{1}{2}a_n\left(\dot{\eta}_n^2 - \omega_n^2\eta_n^2\right) - \frac{1}{2}\ddot{z}_0\,\eta_n\eta_n + \frac{1}{2}a_{lmn}\eta_l\dot{\eta}_m\dot{\eta}_n + \frac{1}{4}a_{jlmn}\eta_j\eta_l\dot{\eta}_m\dot{\eta}_n \\ & + \frac{1}{12}a_{ijlmn}\eta_i\eta_j\eta_l\dot{\eta}_m\dot{\eta}_n + \frac{1}{48}a_{hijlmn}\eta_h\eta_i\eta_j\eta_l\dot{\eta}_m\dot{\eta}_n + \frac{\gamma}{8\rho}E_{jlmn}\eta_j\eta_l\eta_m\eta_n \\ & - \frac{\gamma}{16\rho}E_{hijlmn}\eta_h\eta_i\eta_j\eta_l\eta_m\eta_n + \ldots \end{aligned} \tag{2.31}$$

The higher-order terms in a_{ijlmn}, a_{hijlmn}, and E_{hijlmn} were not retained in the previous work of Miles (1976,1984, 1993), Umeki and Kambe (1989) and Umeki (1991). At lower orders, the formulations are in agreement.

3. Derivation of evolution equation

The evolution equation for a single principal two-dimensional mode (along with its associated harmonics) will now be found, where there are no internal resonances.

The container oscillates as

$$z_0 = \varepsilon^2 f \cos 2\omega t \qquad \left(\varepsilon^2 \omega^2 |f| << g\right), \tag{3.1}$$

where $0 < \varepsilon << 1$ is a small parameter.

It will be found useful to put

$$f = f_0 + \varepsilon^2 f_1 + O(\varepsilon^4), \tag{3.2}$$

where f_0 arises in the $O(\varepsilon^4)$ equation and the perturbation f_1 from this value arises in the $O(\varepsilon^6)$ equation.

The generalized co-ordinate of the n'th mode is written as (with n not summed)

$$\begin{aligned}\eta_n(t) &= \delta_{1n}\varepsilon a_n\left(p(\tau_1,\tau_2,\varepsilon)\cos(\omega t) + q(\tau_1,\tau_2,\varepsilon)\sin(\omega t)\right)\\ &+\varepsilon^2 a_n\left(A_n(\tau_1,\tau_2)\cos(2\omega t) + B_n(\tau_1,\tau_2)\sin(2\omega t) + C_n(\tau_1,\tau_2)\right)\\ &+\varepsilon^3 a_n\left(D_n(\tau_1,\tau_2)\cos(3\omega t) + E_n(\tau_1,\tau_2)\sin(3\omega t) + F_n(\tau_1,\tau_2)\right) + O(\varepsilon^4),\end{aligned} \tag{3.3}$$

where the terms in p and q arise only for the principal resonant mode ($n=1$), $\tau_1 \equiv \varepsilon^2\omega t, \tau_2 \equiv \varepsilon^4 \omega t$ are dimensionless slow time variables, taken to be independent,, $a_n = 1/k_n \tanh(k_n d)$ and $\delta_{1n} = \begin{cases}1, n=1\\ 0, n\neq 1\end{cases}$. Only $n=1,2$ and 3 need to be considered here. Later (see equation (4.1)) p and q will be expanded in a series in ε^2 to emphasize the multiple time scales present in the problem.

Substituting (3.1),(3.2) and (3.3) into (2.31), and averaging over a $\frac{2\pi}{\omega}$ interval of t, gives

$$\langle L\rangle = a_1^3\omega^2\varepsilon^4\left[\frac{1}{2}\left(\frac{\partial p}{\partial\tau_1}q-\frac{\partial q}{\partial\tau_1}p\right)+\frac{1}{4\varepsilon^2}\left(1-\frac{\omega_1^2}{\omega^2}\right)\left(p^2+q^2\right)+\frac{f_0}{2\varepsilon^2 a_1}\left(p^2-q^2\right)\right]$$
$$+a_n^3\omega^2\varepsilon^4\left[\left(1-\frac{\omega_n^2}{4\omega^2}\right)\left(A_n^2+B_n^2\right)-\frac{\omega_n^2}{2\omega^2}C_n^2\right]+\frac{1}{32}\omega^2\varepsilon^4 a_1^4 a_{1111}\left(p^2+q^2\right)^2$$
$$+\frac{1}{2}\omega^2\varepsilon^4 a_1^2 a_n\left[\left(a_{11n}-\frac{1}{4}a_{n11}\right)\left\{A_n\left(p^2-q^2\right)+2B_n pq\right\}+\frac{1}{2}a_{n11}\left(p^2+q^2\right)C_n\right]$$
$$+\frac{1}{2}a_1^3\omega^2\varepsilon^6\left[\frac{\partial p}{\partial\tau_2}q-\frac{\partial q}{\partial\tau_2}p+\frac{f_1}{\varepsilon^2 a_1}\left(p^2-q^2\right)\right]+\frac{3\gamma}{64\rho}\varepsilon^4 a_1^4 E_{1111}\left(p^2+q^2\right)^2$$
$$+\varepsilon^6 \mathrm{X}\left(\begin{array}{l} p,q,f_0,\omega,\{\omega_n,a_n\}_{n=1,2,3},\{A_n,B_n,C_n\}_{n=1,2,3},\{D_n,E_n,F_n\}_{n=1,2,3} \\ \{a_{lmn},a_{jlmn}\}_{j,l,m,n=1,2,3},a_{11112},a_{11121},a_{11211},a_{12111},a_{21111},a_{111111} \\ \rho,\gamma,g,E_{1111},E_{1113},E_{1122},E_{111111},\dfrac{\partial p}{\partial\tau_1},\dfrac{\partial q}{\partial\tau_1},\dfrac{\partial p}{\partial\tau_2},\dfrac{\partial q}{\partial\tau_2} \end{array}\right)+O(\varepsilon^8), \tag{3.4}$$

where repeated indices are summed over the set of participating modes and X is a highly complicated $O(1)$ expression that occupies many pages in MAPLE and which is omitted here for brevity. The ordering in (3.4) is based upon $\dfrac{\omega^2-\omega_1^2}{2\omega^2}=O(\varepsilon^2)$

which selects the single principal mode being considered from this point onwards. In (3.4) there is summing over $n=1,2,3$. From Hamilton's principle, < L > must be stationary with respect to variations of A_n,B_n,C_n,D_n,E_n,F_n . At $O(\varepsilon^4)$ the averaged Lagrangian is made stationary with respect to variations in A_n,B_n,C_n (e.g. by solving $\dfrac{\partial\langle L\rangle}{\partial A_n}=0$ for A_n). This gives (with n not summed)

$$\begin{aligned}\left(A_n,B_n\right)&=-\frac{a_1^2}{4a_n^2}\left(1-\frac{\omega_n^2}{4\omega^2}\right)^{-1}\left(a_{11n}-\frac{1}{4}a_{n11}\right)\left(p^2-q^2,2pq\right)\\ C_n&=\frac{a_1^2\omega^2 a_{n11}}{4a_n^2\omega_n^2}\left(p^2+q^2\right).\end{aligned} \tag{3.5}$$

Equations (3.5) are then substituted into < L >. At $O(\varepsilon^4)$ < L > can then be made stationary with respect to variations in p and q, which gives evolution equations in p and q for τ_1 variations. These are the same equations as derived by Miles (1976, 1984), namely

$$\frac{\partial A}{\partial\tau_1}=-\mu A+i\Omega A+iF_0A^*+i\Pi|A|^2A, \tag{3.6}$$

where $A = p + iq$, and μ is the coefficient of linear damping (artificially introduced at this stage) on the timescale τ_1. Also,

$$\Pi = -\frac{1}{4}a_1^2k_1^2 + a_1^3a_2k_1^4 + \frac{a_1\omega_1^2}{8a_2\omega_2^2}\left\{1 + a_1^2k_1^2\right\}^2 + \frac{9\lambda^2a_1gk_1^4}{16\omega_1^2}$$
$$-\frac{a_1}{4a_2}\left(1 - \frac{\omega_2^2}{4\omega_1^2}\right)^{-1}\left\{\frac{3}{4} - 2a_1a_2k_1^2 - \frac{1}{4}a_1^2k_1^2\right\}^2 \tag{3.7}$$

is the coefficient of the cubic (Stokes) frequency modification (in agreement with Miles (1984)) and

$$\Omega = \frac{1}{\varepsilon^2}\left(1 - \frac{\omega_1^2}{\omega^2}\right),\ F_0 = \frac{2f_0}{a_1}. \tag{3.8}$$

(Note that the introduction of the linear damping term in (3.6) can be explained by using an appropriate dissipation function: see Milner 1991 and Miles 1993).

Trivial and non-trivial equilibrium solutions of this can be found, and their local stability analysed (see for example Nagata (1989)). Hysteresis is found as shown in Figure 1(a) for $\Pi > 0$. When $\Pi < 0$ the lower hysteresis boundary is to the right, not to the left, of the neutral stability curve. Clearly, no non-trivial equilibrium exists for

$$F_0 < \mu, \tag{3.9}$$

a result sometimes at odds with experimental evidence, as already mentioned.

The above equilibrium is found by putting

$$p + iq = ae^{i\theta}, \tag{3.10}$$

which gives

$$\cos 2\theta = \frac{\pm\left(F_0^2 - \mu^2\right)^{1/2}}{-F_0},\ \sin 2\theta = \frac{\mu}{F_0}$$
$$a^2 = \frac{-\Omega \pm \left(F_0^2 - \mu^2\right)^{1/2}}{\Pi} \tag{3.11}$$

for the non-trivial solution. In section 4(a) we shall perturb about this equilibrium on the line in forcing-frequency parameter space given by

$$F_0 = \mu,\ \omega \le \omega_1. \tag{3.12}$$

That is, we shall take (3.11) and (3.12) as the basic solution about which perturbations will be made.

The three eigenfunctions that must be taken into account are

$$\psi_1 = \sqrt{2}\cos\frac{m\pi x}{l},\ \psi_2 = \sqrt{2}\cos\frac{2m\pi x}{l},\ \psi_3 = \sqrt{2}\cos\frac{3m\pi x}{l}, \tag{3.13}$$

corresponding to spatial eigenvalues (i.e. wavenumbers)

$$k_1 = \frac{m\pi}{l},\ k_2 = \frac{2m\pi}{l},\ k_3 = \frac{3m\pi}{l}, \tag{3.14}$$

where l is the length of the container. These correspond to the two-dimensional primary near-resonant mode with m half-wavelengths within the channel length and its second and third forced harmonics.

The averaged Lagrangian is now made stationary with respect to variations in D_n, E_n, F_n giving

$$\begin{aligned} D_1 = &-\frac{2\omega^2 p f_0 + \frac{1}{4}\omega^2 a_{1111} a_1^2 p\left(p^2 - 3q^2\right)}{a_1\left(9\omega^2 - \omega_1^2\right)} \\ &+\frac{\omega^4 a_1 p\left(p^2 - 3q^2\right)}{8a_2\left(4\omega^2 - \omega_2^2\right)\left(9\omega^2 - \omega_1^2\right)}\left[16a_{112}^2 + 8a_{112}a_{211} - 3a_{211}^2\right] \\ &-\frac{\gamma E_{1111} a_1 p\left(p^2 - 3q^2\right)}{8\rho\left(9\omega^2 - \omega_1^2\right)}, \end{aligned} \tag{3.15}$$

$$D_2 = 0, \tag{3.16}$$

$$\begin{aligned} D_3 = &\frac{a_1^3\omega^2 p\left(p^2 - 3q^2\right)}{16a_3^2\left(9\omega^2 - \omega_3^2\right)}\left\{a_{3111} + a_{1311} - 3a_{1131} - 3a_{1113}\right\} \\ &-\frac{\omega^4 a_1^3 p\left(p^2 - 3q^2\right)}{8a_2 a_3^2\left(4\omega^2 - \omega_2^2\right)\left(9\omega^2 - \omega_3^2\right)}\left(4a_{112} - a_{211}\right)\left(2a_{321} - 6a_{123} - 3a_{231}\right) \\ &-\frac{\gamma E_{1113} a_1^3 p\left(p^2 - 3q^2\right)}{8\rho a_3^2\left(9\omega^2 - \omega_3^2\right)}, \end{aligned} \tag{3.17}$$

$$E_1 = -\frac{2\omega^2 q f_0 + \frac{1}{4}\omega^2 a_{1111} a_1^2 q\left(3p^2 - q^2\right)}{a_1\left(9\omega^2 - \omega_1^2\right)}$$
$$+\frac{\omega^4 a_1 q\left(3p^2 - q^2\right)}{8a_2\left(4\omega^2 - \omega_2^2\right)\left(9\omega^2 - \omega_1^2\right)}\left[16a_{112}^2 + 8a_{112}a_{211} - 3a_{211}^2\right] \tag{3.18}$$
$$-\frac{\gamma E_{1111} a_1 q\left(3p^2 - q^2\right)}{8\rho\left(9\omega^2 - \omega_1^2\right)},$$

$$E_2 = 0, \tag{3.19}$$

$$E_3 = \frac{a_1^3\omega^2 q\left(3p^2 - q^2\right)}{16a_3^2\left(9\omega^2 - \omega_3^2\right)}\left\{a_{3111} + a_{1311} - 3a_{1131} - 3a_{1113}\right\}$$
$$-\frac{\omega^4 a_1^3 q\left(3p^2 - q^2\right)}{8a_2 a_3^2\left(4\omega^2 - \omega_2^2\right)\left(9\omega^2 - \omega_3^2\right)}\left(4a_{112} - a_{211}\right)\left(2a_{321} - 6a_{123} - 3a_{231}\right) \tag{3.20}$$
$$-\frac{\gamma E_{1113} a_1^3 q\left(3p^2 - q^2\right)}{8\rho a_3^2\left(9\omega^2 - \omega_3^2\right)},$$

$$F_1 = F_2 = F_3 = 0. \tag{3.21}$$

It should be noted that (3.15) and (3.18) have dependence upon the forcing. It is these terms in f_0 that result in differences between the coefficient of cubic forcing found here and that given by Miles (1993), who omitted third harmonics.

It is now possible to make < L > stationary with respect to variations in p and q at $O(\varepsilon^6)$. This gives a second evolution equation

$$\frac{\partial A}{\partial \tau_2} \equiv \frac{\partial}{\partial \tau_2}(p + iq) = i\overline{F}_1 A^* - \frac{1}{8}i\mu^2 A + NA|A|^2$$
$$+i\tilde{F}_0\left(A^3 + 3|A|^2 A^*\right) - ihA|A|^4. \tag{3.22}$$

which must be made compatible with (3.6).

Here

$$\frac{\tilde{F}_0}{f_0} = -\frac{a_{1111}}{4} - \frac{3k_1^4\gamma}{16\rho\omega_1^2} + \frac{2\omega_1^2 a_{112}^2}{a_2\left(4\omega_1^2 - \omega_2^2\right)}$$
$$+\frac{a_{211}^2\omega_1^4}{a_2\left(4\omega_1^2 - \omega_2^2\right)}\left(-\frac{3}{8\omega_1^2} + \frac{a_1}{a_2\omega_2^2}\right) \tag{3.23}$$
$$+\frac{4a_{112}a_{211}\omega_1^4}{a_2\left(4\omega_1^2 - \omega_2^2\right)}\left(\frac{2}{8\omega_1^2} - \frac{a_1}{a_2\omega_2^2}\right)$$

is the coefficient of cubic forcing, $\overline{F}_1 = \frac{2f_1}{a_1}$ is a small correction to the linear forcing coefficient, h is the fifth-order conservative nonlinear frequency shift, and N is a coefficient of cubic damping (as in Miles (1993), Douady (1990) and Milner (1991)); this cubic damping term is introduced artificially, as it is absent from the Lagrangian formulation; however, the introduction of damping terms into the model could be done *a priori* by the inclusion of a dissipation function, as in Milner (1991) and Miles (1993). The form of the amplitude-dependence of the cubic forcing term is in agreement with Miles (1993), though the coefficient (3.23) differs from Miles' (1993) coefficient (B3); this is because Miles only considered the first and second harmonics in his calculation, while we also considered the third harmonic. See section 7 for a comparison between our cubic forcing and that of Miles.

The inclusion of the third harmonic also resulted in our retaining the $-iA\frac{\mu^2}{8}$ term which Miles did not derive; this is a small correction to the linear frequency shift term. This term is numerically very small and can be neglected in (3.22) by including it instead in (3.6). This results in the linear frequency detuning coefficient being replaced by $\Omega - \frac{\varepsilon^2\mu^2}{8}$ which is equivalent to a very small change in the origin.

The coefficient h, which derives from the expression X in (3.4), has been calculated using MAPLE for the general case but is too lengthy to be given here, as it occupies several pages of text. However h simplifies in two limiting cases, namely zero surface tension and infinite depth. For zero surface tension we find that

$$h = \frac{3\kappa^2 R(\kappa)}{2048\left(\kappa^2-1\right)^7\left(2\kappa^2-1\right)\left(4\kappa^2-1\right)}, \tag{3.24}$$

where

$$\begin{aligned} R(\kappa) &= 64 - 66\kappa^2 - 4687\kappa^4 + 33170\kappa^6 - 101256\kappa^8 \\ &+162208\kappa^{10} - 139584\kappa^{12} + 61248\kappa^{14} - 10368\kappa^{16}, \\ \kappa &= \cosh(k_1 d). \end{aligned} \tag{3.25}$$

For infinite depth we find that

$$h = \frac{9S(\varsigma)}{2048(1+4\varsigma)^2(-1+2\varsigma)^2(-1+3\varsigma)(1+\varsigma)^2} \tag{3.26}$$

where

$$S(\varsigma) = 432 + 1360\varsigma - 12663\varsigma^2 - 34495\varsigma^3$$
$$+16144\varsigma^4 - 12444\varsigma^5 - 98272\varsigma^6 - 47808\varsigma^7, \qquad (3.27)$$
$$\varsigma = \frac{\gamma k_1^2}{\rho g}.$$

In (3.26) the denominator is singular, as expected, at the second- and third-harmonic resonant frequencies $\varsigma = ½$ and $⅓$ (where this theory will break down). Notice that as the depth tends towards infinity in (3.24), and as the surface tension tends towards zero in (3.26) then $h \to -\frac{243}{128}$.

Figure 2 demonstrates how the full expression for h depends on depth, surface tension and the wavenumber parameter m as defined in (3.13) for a particular example. In Figure 2(c), the missing parts of the graph correspond to second and third harmonic resonances where $|h|$ becomes very large and the ordering breaks down. Figure 2(d) shows a 'close-up' view of the part of Figure 2(c) which is encountered in the experiments discussed in section 5.

We now examine the compatibility of the two evolution equations (3.6) and (3.22), and so determine the region of hysteresis.

4. The lower hysteresis boundary

This section estimates the lower hysteresis boundary by analytically determining the curve above which finite-amplitude stationary solutions exist. The next section investigates this boundary computationally.

(a) Solution near $F = \mu$

For steady solutions $\frac{\partial A}{\partial \tau_1} + \varepsilon^2 \frac{\partial A}{\partial \tau_2} = 0$, it is useful to apply the expansion

$$p + iq = u + iv + \varepsilon^2(r + is) + O(\varepsilon^4). \qquad (4.1)$$

Combining (3.6), (3.22) and applying (4.1) gives at O(1)

$$-\mu C + i\Omega C + iF_0 C^* + i\Pi|C|^2 C = 0, \text{ where } C = u + iv \tag{4.2}$$

which results in constant equilibrium values for u,v (which are just those of (3.10) and (3.11)). At $O(\varepsilon^2)$, (3.6), (3.22) and (4.1) give

$$\begin{aligned} &-\mu B + \Omega iB + F_0 iB^* + i\Pi\left\{2(ru+sv)C + |C|^2 B\right\} \\ &+i\bar{F}_1 C^* + i\tilde{F}_0\left(C^3 + 3|C|^2 C^*\right) + NC|C|^2 - ihC|C|^4 = 0, \end{aligned} \tag{4.3}$$

where $B = r + is$ and C is given by (4.2).

At leading order, the lower boundary of the hysteresis region is given by (3.12), on which the amplitude C is

$$|C|^2 = -\frac{\Omega}{\Pi}, \quad \text{phase}(C) = \frac{\pi}{4}\left(\text{or } \frac{5\pi}{4}\right). \tag{4.4}$$

Substituting (4.4) into (4.3) and looking for equilibrium solutions gives rise to consistency conditions of the form

$$\begin{pmatrix} \Omega - \mu & \Omega + \mu \\ -\Omega + \mu & -\Omega - \mu \end{pmatrix}\begin{pmatrix} r \\ s \end{pmatrix} = \begin{pmatrix} c \\ d \end{pmatrix}, \tag{4.5}$$

where c and d are given by

$$c + id \equiv i\bar{F}_1 C^* + i\tilde{F}_0\left(C^3 + 3|C|^2 C^*\right) + NC|C|^2 - ihC|C|^4, \tag{4.6}$$

with $C = \pm(-\Omega/\Pi)^{1/2} e^{i\pi/4}$ from (4.4).

Clearly, for (4.5) to have a solution it is necessary that $c = -d$. This gives rise to

$$\frac{\bar{F}_1 a_1}{2} \equiv f_1 = \frac{a_1 \Omega}{2\Pi}\left(N + 2\tilde{F}_0\right), \tag{4.7}$$

which is valid for $\omega \le \omega_1$ (for $\Pi > 0$). Notice that the h term does not contibute here because $ph(C) = \pi/4, 5\pi/4$; accordingly, this result is exactly the same as that obtained from (1.3). Equations (3.2), (3.8b), (3.12) and (4.7) together give the lower boundary of the hysteresis region as

$$F = \mu + \frac{\varepsilon^2 \Omega}{\Pi}\left(N + 2\tilde{F}_0\right) + O(\varepsilon^4). \tag{4.8}$$

This gives hysteresis below $F = \mu$ (for $\Omega < 0$ when $\Pi > 0$, and for $\Omega > 0$ when $\Pi < 0$) whenever $N + 2\tilde{F}_0 > 0$, but it gives the lower hysteresis boundary above $F = \mu$ whenever $N + 2\tilde{F}_0 < 0$.

(b) The bending of the lower hysteresis boundary by the fifth-order conservative term

It will be seen in section 5 that the fifth-order conservative term is found to bend the lower hysteresis boundary in computational studies of the evolution equation (5.1). Here the local analysis of section 4(a), which gave an expansion for the lower hysteresis boundary (4.8), will be extended in order to demonstrate this effect analytically.

Evolution equations (3.6) and (3.22) have already been determined. If one is justified in neglecting the fifth-order damping and forcing terms as well as the seventh-order conservative term (which we do for simplicity), then the next evolution equation in this sequence is

$$\frac{\partial A}{\partial \tau_3} = i\bar{F}_2 A^* + i\tilde{F}_1(A^3 + 3|A|^2 A^*), \tag{4.9}$$

where $\bar{F}_2 = \frac{2}{a_1} f_2$ and $\tilde{F}_1 = f_1 \frac{\tilde{F}_0}{f_0}$ are small corrections to the linear and cubic forcing coefficients respectively, with the forcing now expanded as

$$f = f_0 + \varepsilon^2 f_1 + \varepsilon^4 f_2 + O(\varepsilon^6). \tag{4.10}$$

Note that a third slow time $\tau_3 \equiv \varepsilon^6 \omega t$ has been introduced.

Now we perturb about (3.12) and (4.8). Equation (4.1) is extended to

$$p + iq = u + iv + \varepsilon^2(r + is) + \varepsilon^4(R + iS) + O(\varepsilon^6). \tag{4.11}$$

Again $C = u + iv, B = r + is$ and $G = R + iS$ giving (4.2) to (4.8). At the highest order the system of equations takes the form

$$\begin{pmatrix} \Omega - \mu & \Omega + \mu \\ -\Omega + \mu & -\Omega - \mu \end{pmatrix} \begin{pmatrix} R \\ S \end{pmatrix} = \begin{pmatrix} P \\ Q \end{pmatrix}, \tag{4.12}$$

where P and Q are known functions of (u,v,r,s).

From (4.5),

$$r = \frac{c - (\Omega + \mu)s}{\Omega - \mu} \quad (\Omega \neq \mu). \tag{4.13}$$

Putting (4.7) into (4.6) gives

$$c = -d = \pm \frac{h\Omega^2}{2\Pi^2} \left(\frac{-2\Omega}{\Pi} \right)^{1/2}. \tag{4.14}$$

For (4.12) to be consistent, we require that $P + Q = 0$. This is however a single equation in two unknowns, namely $\bar{F}_2$ and s, if (4.13) and (4.14) are substituted into

$P+Q=0$. We require to find $\bar{F}_2$, but clearly we cannot do so while s remains unknown.

Now we can write

$$r+is=b_1e^{-i\frac{\pi}{4}}+b_2e^{i\frac{\pi}{4}}. \tag{4.15}$$

The second component of (4.15) lies along $u+iv$ since $phase(u+iv)=\frac{\pi}{4}$. Therefore b_2 contributes only to an infinitesimal change in $|C|=\left(-\frac{\Omega}{\Pi}\right)^{1/2}$ and so an infinitesimal change in Ω. So, we may choose to set $b_2=0$, effectively without loss, to obtain

$$-r=s=\frac{c}{2\mu}=\pm\frac{h\Omega^2}{4\mu\Pi^2}\left(\frac{-2\Omega}{\Pi}\right)^{1/2}. \tag{4.16}$$

Then, $phase(r+is)=-\frac{\pi}{4}$, the component b_1 being orthogonal to $u+iv$.

The calculation is readily completed, using

$$\tilde{F}_1=\frac{\tilde{F}_0\Omega}{\mu\Pi}\left(N+2\tilde{F}_0\right) \tag{4.17}$$

which comes from (3.8), (3.12) and (4.8). The lower hysteresis boundary is

$$F=\mu+\varepsilon^2\frac{\Omega}{\Pi}\left(N+2\tilde{F}_0\right)+\varepsilon^4\frac{\Omega^2}{4\mu\Pi^4}\left(8\tilde{F}_0\Pi^2\left(N+2\tilde{F}_0\right)+2h^2\Omega^2\right)+O(\varepsilon^6). \tag{4.18}$$

Clearly, the fifth-order conservative term is responsible for bending the lower hysteresis boundary through the $h^2\Omega^4$ term. Although this calculation is only valid near to the line $F=\mu$, it supports the computational results of section 5.

(c) Solution near minimum of neutral stability curve

The lower hysteresis boundary has often been observed to bifurcate from the neutral stability curve at a point away from the minimum, and for there to be hysteresis beneath the minimum of the neutral stability curve at $\Omega=0$. Clearly (4.8) and (4.18) do not model this behaviour, since the bifurcation from the neutral stability curve ($F^2=\mu^2+\Omega^2$) appears to occur at $\Omega=0$, but the scalings break down when $\Omega\sim O(\varepsilon^2)$. With a change of scalings however, these features can be found in our evolution equations. We now rescale so that

$$\Omega=\varepsilon\Omega_1,\Pi=\varepsilon\Pi_1,F=\mu+\varepsilon^2F_1 \tag{4.19}$$

and replace (4.1) with

$$p+iq=u+iv+\varepsilon(r+is)+\varepsilon^2(U+iV)+O(\varepsilon^3). \tag{4.20}$$

These changes correspond to an analysis near to the minimum of the neutral stability curve. Note that (3.6) gives equilibrium solutions

$$|A|^2=\frac{-\Omega\pm\left(F^2-\mu^2\right)^{1/2}}{\Pi}=\frac{\varepsilon\left(-\Omega_1\pm\left(2\mu F_1\right)^{1/2}\right)}{\Pi}, \tag{4.21}$$

so that the rescaling of Π ensures that A (and hence C) remains $O(1)$.

Applying the above scalings to our evolution equations and supposing that $dA/dt=0$, giand replace (4.1) with

ves

$$\begin{aligned}
&O(1):\quad 0=-\mu C+i\mu C^*,\\
&O(\varepsilon):\quad 0=i\Omega_1 C+i\Pi_1|C|^2C-\mu B+i\mu B^*,\\
&O(\varepsilon^2):\quad 0=N|C|^2C+i\tilde{F}_0\left(C^3+3|C|^2C^*\right)-ih|C|^4C+iF_1C^*\\
&\qquad -\mu D+i\mu D^*+i\Omega_1 B+i\Pi_1|C|^2B+2i\Pi_1 C(\mathrm{Re}\,B\,\mathrm{Re}\,C+\mathrm{Im}\,B\,\mathrm{Im}\,C),
\end{aligned} \tag{4.22}$$

where $C=u+iv, B=r+is, D=U+iV$.

At *O(1)* we have that $phase(C)=\frac{\pi}{4},-\frac{3\pi}{4}$ as in (4.4), though the amplitude of C is left undetermined. At $O(\varepsilon)$ we have

$$\mu(r-s)=-u(\Omega_1+2\Pi_1u^2). \tag{4.23}$$

At $O(\varepsilon^2)$ we have

$$\begin{pmatrix}-\mu & \mu\\ \mu & -\mu\end{pmatrix}\begin{pmatrix}U\\ V\end{pmatrix}=\begin{pmatrix}-2Nu^3-4\tilde{F}_0u^3-4hu^5+\Omega_1s+2\Pi_1u^2(r+2s)-F_1u\\ -2Nu^3-4\tilde{F}_0u^3+4hu^5-\Omega_1r-2\Pi_1u^2(2r+s)-F_1u\end{pmatrix}. \tag{4.24}$$

The consistency condition on (4.24) along with equation (4.23) gives

$$u\left[4\Pi_1^2u^4+4u^2\left(\Pi_1\Omega_1-\mu\left(N+2\tilde{F}_0\right)\right)+\Omega_1^2-2F_1\mu\right]=0. \tag{4.25}$$

The non-trivial roots of (4.25) coalesce when

$$F_1=\frac{\left(N+2\tilde{F}_0\right)}{\Pi_1}\left(\Omega_1-\frac{\mu\left(N+2\tilde{F}_0\right)}{2\Pi_1}\right), \tag{4.26}$$

which is the lower hysteresis boundary. For (4.25) to have real non-trivial roots it is also necessary that

$$\Omega_1 < \frac{\mu\left(N+2\tilde{F}_0\right)}{\Pi_1} \text{ for } \Pi_1 > 0, \text{ or}$$
$$\Omega_1 > \frac{\mu\left(N+2\tilde{F}_0\right)}{\Pi_1} \text{ for } \Pi_1 < 0. \tag{4.27}$$

The equation for the neutral stability curve under these scalings is

$$F_1 = \frac{\Omega_1^2}{2\mu}. \tag{4.28}$$

Solving (4.26) with (4.28) gives the point of bifurcation of the lower hysteresis boundary from the neutral stability curve. This is

$$\Omega_1 = \frac{\mu\left(N+2\tilde{F}_0\right)}{\Pi_1}. \tag{4.29}$$

Equation (4.26) gives rise to a lower hysteresis boundary similar to (4.8), but shifted slightly; this correctly gives rise to a tangential bifurcation from the neutral stability curve, whereas (4.8) incorrectly meets the neutral curve at an angle at $\Omega_1 = 0$. This bifurcation point agrees with the corresponding result of Craik & Armitage (1995).

(d) Solutions close to neutral curve for $\Omega \sim O(1)$

We now assume that $\Pi = \varepsilon^2\hat{\Pi}$ where $\hat{\Pi}$ is $O(1)$.

Applying the above rescaling and (4.1) to our stationary evolution equation gives

$$\begin{aligned} O(1): &\quad -\mu C + i\Omega C + iF_0 C^* = 0, \\ O(\varepsilon^2): &\quad -\mu B + i\Omega B + iF_0 B^* + i\hat{\Pi}|C|^2 C + iF_1 C^* \\ &\quad + N|C|^2 C + iF_0\Gamma\left(C^3 + 3|C|^2 C^*\right) - ih|C|^4 C = 0, \end{aligned} \tag{4.30}$$

where $C = u + iv, B = r + is$. Note that the coefficient of cubic forcing is now taken to be $F\Gamma = F_0\Gamma + O\left(\varepsilon^2\right)$, in line with Craik & Armitage (1995).

From the O(1) equations we have

$$\begin{aligned} &F_0 = \left(\mu^2 + \Omega^2\right)^{1/2} \text{ and} \\ &phase(C) = \theta \text{ where } e^{-2i\theta} = \frac{\mu - i\Omega}{iF_0}. \end{aligned} \tag{4.31}$$

The $O(\varepsilon^2)$ equations give

$$\begin{pmatrix} -\mu & -\Omega + F_0 \\ \Omega + F_0 & -\mu \end{pmatrix}\begin{pmatrix} r \\ s \end{pmatrix} = \begin{pmatrix} \mathrm{Re}Q \\ \mathrm{Im}Q \end{pmatrix}, \tag{4.32}$$

where

$$Q = -\left[i\hat{\Pi}|C|^2 C + iF_1 C^* + N|C|^2 C + iF_0\Gamma\left(C^3 + 3|C|^2 C^*\right) - ih|C|^4 C\right] \tag{4.33}$$

and *ph(C)* is known from (4.31).

As the determinant of (4.32) is zero, we need

$$\left(\Omega + F_0\right)\mathrm{Re}\,Q + \mu\,\mathrm{Im}\,Q = 0, \tag{4.34}$$

which is equivalent to

$$\mathrm{Re}\left[\left(1 - e^{2i\theta}\right)Q\right] = 0, \tag{4.35}$$

using (4.31).

This gives the trivial solution and also a quadratic equation in $|C|^2$ which has roots

$$|C|^2 = \frac{\Lambda \pm \left(\Lambda^2 - 4h\Omega F_1\left(\mu^2 + \Omega^2\right)^{1/2}\right)^{1/2}}{2h\Omega}, \tag{4.36}$$

where $\Lambda = \Omega\hat{\Pi} - \mu N - 2\Gamma\left(2\Omega^2 + \mu^2\right)$.

The roots of (4.36) coalesce at the lower hysteresis boundary, where

$$F_1 = \frac{\left(\Omega\hat{\Pi} - \mu N - 2\Gamma\left(2\Omega^2 + \mu^2\right)\right)^2}{4h\Omega\left(\mu^2 + \Omega^2\right)^{1/2}}. \tag{4.37}$$

It should be noted that for hysteresis it is necessary that $F_1 < 0$ which implies that $h\Omega < 0$.

It is also necessary that the right-hand side of (4.36) must be positive. If $h\Omega < 0$ then it is necessary that $\Omega < \Omega_-$ or $\Omega > \Omega_+$ where

$$\Omega_\pm \equiv \frac{\hat{\Pi} \pm \left(\hat{\Pi}^2 - 16\Gamma\mu\left(N + 2\mu\Gamma\right)\right)^{1/2}}{8\Gamma}, \tag{4.38}$$

assuming $\Gamma > 0$ (which is generally true - see section 3). Solving (4.37) together with the expression for the neutral curve shows that both Ω_- and Ω_+ correspond to bifurcation points. Substituting $\hat{\Pi} = \dfrac{\Pi}{\varepsilon^2}$ into these bifurcation points and expanding in a Taylor series gives

$$\Omega_- = \frac{\varepsilon^2\mu}{\Pi}\left(N + 2\mu\Gamma\right) = \frac{\varepsilon^2\mu}{\Pi}\left(N + 2\tilde{F}_0\right), \tag{4.39}$$

which is identical to (4.29), and $\Omega_+ = O\left(\dfrac{1}{\varepsilon^2}\right)$ which is probably spurious.

The behaviour of the lower hysteresis boundary near to the bifurcation point can be examined by putting $\Omega = \Omega_{bif} + \Delta$ in (4.37), where Ω_{bif} is the frequency offset corresponding to the bifurcation, and $|\Delta| << |\Omega_{bif}|$. Then

$$F_1 = \frac{\Delta^2(\hat{\Pi} - 8\Gamma\Omega_{bif})^2}{4h\Omega_{bif}\left(\mu^2 + \Omega_{bif}^2\right)^{1/2}} + O(\Delta^3). \tag{4.40}$$

Therefore as $|h|$ decreases, the lower hysteresis boundary will move more quickly away from the neutral curve. This result seems paradoxical; but since the scaling requires h to be *O(1)*, no singularity is expected as $|h| \to 0$.

Equation (4.40) is significant because it shows the fifth-order conservative term appearing in an expression for the lower hysteresis boundary at the lowest possible order, and this expression describes the lower hysteresis boundary at a point that is near to the neutral curve. So the fifth-order conservative term is playing an important role even close to the bifurcation point. It will be seen in the next section that the fifth-order conservative term also has large effects on the lower hysteresis boundary far from the neutral stability curve.

Figure 3 shows possible hysteresis diagrams produced from (4.40) near to the bifurcation point. It can be seen that increasing $|h|$ again causes an increase in the upwards curvature of the lower hysteresis boundary, though not for the same reason as in (4.9). Note that $|h| << 1$ would give downwards bending, but sufficiently small h values are ruled out by scaling assumptions. (Though (4.36) has simple poles at both $\Omega = 0$ and $h = 0$, this subsection has assumed that Ω and h are $O(1)$).

5. Numerical work

Equations (3.6) and (3.22) give the composite equation

$$\begin{aligned}\frac{dA}{dt} &= \varepsilon^2\omega\left(\frac{\partial A}{\partial \tau_1}+\varepsilon^2\frac{\partial A}{\partial \tau_2}\right)\\ &= \varepsilon^2\omega\left(-\mu A+i\Omega A+iFA^*+i\Pi|A|^2A\right)\\ &+\varepsilon^4\omega\left(N|A|^2A+i\tilde{F}\left(A^3+3|A|^2A^*\right)-ih|A|^4A\right)=0,\end{aligned} \tag{5.1}$$

where the forcing expansion (3.2) has *not* been applied, and the small shift in the origin caused by the linear frequency detuning term in (3.22) has been ignored. Equation (5.1) has been examined computationally using a FORTRAN NAG routine. The model equation (1.3), previously discussed by Craik & Armitage (1995), which omits the h-term, has also been investigated numerically.

In order to compare theory with experiments, it is necessary to determine the scaling parameter ε^2 and to estimate N. Using (3.1), the r.m.s. acceleration is given by

$$\left(\frac{\omega}{2\pi}\int_0^{2\pi/\omega}\left(4\omega^2\varepsilon^2 f\right)^2\cos^2 2\omega t dt\right)^{1/2}=2\sqrt{2}\omega^2\varepsilon^2 f. \tag{5.2}$$

At the minimum of the neutral stability curve $F\equiv\dfrac{2f}{a_1}=\mu$. Therefore

$$\varepsilon^2\mu\approx\frac{\alpha}{\sqrt{2}a_1\omega_1^2}, \tag{5.3}$$

where α is the experimentally observed r.m.s. acceleration at the minimum of the neutral stability curve. Without loss of generality, we choose $\mu=1$, so that (5.3) gives ε^2. For the experimental observations shown in Figure 1 (Chapter II), this gives $\varepsilon^2=0.047$ for the 22 half-wavelength mode. (The choice of $\mu=1$ is equivalent to expanding the evolution equation in terms of a linear dissipation parameter $\varepsilon^2\mu$).

Equations (5.1) and (1.3) were each solved numerically by searching for the value of the forcing F that corresponds to the disappearance of finite-amplitude equilibrium solutions, for various chosen frequencies Ω. A comparison of the hysteresis diagrams resulting from three different models is shown in Figure 4. There are two possible choices for the coefficient of cubic forcing, namely

$$\text{(i) } \tilde{F}_1=f\Gamma \text{ or (ii) } \tilde{F}_2=f_0\Gamma, \tag{5.4}$$

where Γ is the expression in square brackets in equation (3.23). Cubic forcing coefficient $\tilde{F}_1$ is likely to be the physically more realistic case where it is taken to be proportional to the actual linear forcing *f*, rather than its fixed value $f_0 = \frac{\mu a_1}{2}$ at the minimum of the neutral stability curve. Figure 4 shows four lower hysteresis boundaries, for *(a)* equation (5.1) with cubic forcing given by $\tilde{F}_1$, *(b)* equation (5.1) with cubic forcing given by $\tilde{F}_2$,*(c)* equation (1.3) with cubic forcing given by $\tilde{F}_1$ and *(d)* equation (1.3) with cubic forcing given by $\tilde{F}_1$ but with the coefficient of cubic damping chosen so that the boundary coincides with *(a)* vertically beneath the minimum of the neutral curve.

It can be seen that the effect of the fifth-order conservative term in (5.1) is to bend the lower hysteresis boundary and to shift the minimum in the lower hysteresis boundary to smaller values of the frequency Ω. Bending of the lower hysteresis boundary also was seen in sections 4(a) and 4(c), again caused by the fifth-order conservative term. Craik & Armitage (1995) pointed out that choosing the coefficient of cubic forcing to be $\tilde{F}_1$ rather than $\tilde{F}_2$ (see (5.4)) will cause the lower hysteresis boundary to bend. Comparing the three lower hysteresis boundaries in Figure 4, it can be seen for this example that the presence of the fifth-order conservative term curves the lower hysteresis boundary far more than the effect produced by using $\tilde{F}_1$ instead of $\tilde{F}_2$.

The effect of varying the coefficient of cubic damping *N* is shown in Figure 5 for a depth of 1.3cm. These graphs show our model (5.1) along with $\tilde{F}_1$ (from (5.4)) for six different values of *N*. The line for $N = -5$ shows the type of diagram that Douady (1990) used to explained his observations, where hysteresis was not found, while the lines with $N > 0$ show hysteresis similar to that observed by Simonelli & Gollub (1989) and Craik & Armitage (1995).

Figure 6 shows the effect on the lower hysteresis boundary of varying ε^2. As expected, as ε^2 tends towards zero, the hysteresis boundary approaches the horizontal line $F = \mu$.

Figure 7 shows the experimental data plotted on the same diagram as the lower hysteresis boundaries predicted by our model (5.1) with $\tilde{F}_1$, for a variety of values of

the coefficient of cubic damping N, where the other coefficients have been chosen to match the experimental situation at depth 1.3cm. This allows a value of N to be selected which gives the best agreement between theory and experiment, and hopefully this gives a good estimate of the parameter. (Milner (1991) and Miles (1993) offer analytical expressions for N, but both rely upon assumptions that do not hold in our case). However it can be seen that there is not a unique theoretical curve which best agrees with the experimental results, and the choice is subjective.

The ultimate test of this Chapter is whether our model gives significantly better agreement with experimental results than the previously most accurate model. A comparison is made, here and in section 6, between our model (5.1) (with cubic forcing given by $\tilde{F}_1$) and with experimental results, for all three depths for which observations are available. The results are shown in Figures 8 and 9. For both models, and for each depth, the coefficient of cubic damping N used in the computations was selected to give the 'best' agreement between that model and experimental results. The criterion used for this selection (except in Figure 9(c) - see section 6) was to choose the value of N which fixes the theoretical lower hysteresis boundary at the same point as the experimental boundary when $\Omega = 0$ i.e.vertically beneath the minimum of the neutral stability curve. Obviously other criteria could have been adopted.

Figure 8 shows the comparison between theory and experiment for the 1cm depth case. The experimental results for Figure 8 come from Craik & Armitage (1995) (22 half-wavelengths). Two things should be noted about the 1cm depth case. Firstly, the coefficient Π has changed sign from the 1.3cm depth experiment, and this results in a qualitative difference. Secondly, the minimum observed in the lower hysteresis boundary (see Figures 4,5 and 6) has been shifted into frequencies Ω where it is observed physically.

Figures 9(a) and 9(b) show the comparisons for water depths of 1.3cm and 2cm (the 2cm depth experimental results come from the 22 half-wavelength observations of Craik & Armitage (1995)). The two graphs show the boundaries computed from (5.1) by considering the existence of stationary points. Figure 4 shows that for the 1.3cm

depth experiment, the lower hysteresis boundary calculated from (5.1) (line *a*) lies above the boundary calculated from (1.3) (line *d*), in the experimental frequency range. So we can see from Figure 9(a) that (5.1) gives better agreement with the experiment than equation (1.3). The extra bending of the lower hysteresis boundary caused by the fifth-order conservative term is the main cause of this improvement. Similarly, the 2cm depth observations are closer to the boundary given by (5.1) than the boundary given by (1.3).

Agreement between theory and experiment is satisfactory, but not spectacularly good. In particular, the trend of the experimental results at the greatest periods (for the two larger depths) is not well captured theoretically. The work of the next section suggests why this is so.

6. Stability of finite-amplitude solutions

Stability of the finite-amplitude wave solutions will now be considered. If A_0 is a stationary solution of (5.1), and $A = A_0 + B$ where B is small, then the combined evolution equation becomes, upon linearization with respect to B,

$$\begin{aligned}
&\dot{B} = -\mu B + i\Omega B + iFB^* + i\Pi|A_0|^2 B \\
&+2i\Pi A_0(\mathrm{Re}\,A_0\,\mathrm{Re}\,B + \mathrm{Im}\,A_0\,\mathrm{Im}\,B) + 3i\varepsilon^2 F\Gamma A_0^2 B \\
&+\varepsilon^2 N|A_0|^2 B + 2\varepsilon^2 N A_0(\mathrm{Re}\,A_0\,\mathrm{Re}\,B + \mathrm{Im}\,A_0\,\mathrm{Im}\,B) \\
&+3i\varepsilon^2 F\Gamma|A_0|^2 B^* + 6i\varepsilon^2 F\Gamma A_0^*(\mathrm{Re}\,A_0\,\mathrm{Re}\,B + \mathrm{Im}\,A_0\,\mathrm{Im}\,B) \\
&-i\varepsilon^2 h|A_0|^4 B - 4i\varepsilon^2 h A_0|A_0|^2(\mathrm{Re}\,A_0\,\mathrm{Re}\,B + \mathrm{Im}\,A_0\,\mathrm{Im}\,B).
\end{aligned} \tag{6.1}$$

Expressing B in (6.1) in terms of real and imaginary parts as $B = B_r + iB_i$ gives two real equations. These can be rewritten in the form

$$\begin{pmatrix} \dot{B}_r \\ \dot{B}_i \end{pmatrix} = M \begin{pmatrix} B_r \\ B_i \end{pmatrix}, \tag{6.2}$$

where M is a two-dimensional real matrix. The characterestic equation of M is

$$\begin{aligned}
&\sigma^2 + 2\sigma\left\{\mu - 2\varepsilon^2 N|A_0|^2\right\} \\
&+\mu^2 + \Omega^2 - F^2 + 3(\varepsilon^4 N^2 + \Pi^2 - 6\varepsilon^4\Gamma^2 F^2)|A_0|^4 \\
&+4(\Pi\Omega - \mu\varepsilon^2 N - 3\varepsilon^2\Gamma F^2)|A_0|^2 + 2F|A_0|^2\cos 2\phi(6\varepsilon^2\Omega\Gamma - \Pi) \\
&-2F\varepsilon^2 N|A_0|^2\sin 2\phi + 4\varepsilon^2 F\cos 2\phi|A_0|^4(h + 3\Pi\Gamma) \\
&-12\varepsilon^4 F\Gamma h|A_0|^6\cos 2\phi + 18\varepsilon^4 F^2\Gamma^2|A_0|^4\cos 4\phi \\
&-12\varepsilon^4 NF\Gamma|A_0|^4\sin 2\phi - 6\varepsilon^2\Omega h|A_0|^4 - 8\varepsilon^2\Pi h|A_0|^6 + 5\varepsilon^4 h^2|A_0|^8 = 0,
\end{aligned} \tag{6.3}$$

where σ is an eigenvalue so that B_r and B_i are both proportional to $\mathrm{Re}\,e^{\sigma t}$. This allows the stability of finite-amplitude solutions A_0 to be investigated, using the following algorithm.

For a given value of the forcing F and frequency Ω, all stationary solutions A_0 are found numerically (see section 5). Each of these in turn is substituted into (6.3), resulting in a quadratic equation in σ, for each stationary point. The stability of each stationary point is determined by solving the corresponding quadratic equation and examining the real part of the eigenvalues. If any of the available stationary points is stable then the point (Ω, F) can be labelled as a stable point in parameter space. This is

repeated over a fine grid of (Ω, F) points, giving a stability diagram in the forcing-frequency plane.

Figure 9(a) shows the results for the 1.3cm depth experiment. Two regions are identified: one region indicates the existence of stable finite amplitude stationary solutions (corresponding to self-stable standing waves); the other region describes where the finite amplitude stationary solutions are all unstable. The dashed line gives the boundary between these two regions (this line is labelled the *stability boundary*). This line bifurcates from the lower hysteresis boundary calculated in section 5 near to the point $\Omega = -0.5, F = 0.76$. Remarkably, the experimental lower hysteresis boundary almost coincides with this theoretical stability boundary. Accordingly, here there is very good agreement between theoretical and experimental results, when the stability of equilibrium points, as well as their existence, is taken into account.

For the 1cm depth observations, all finite-amplitude stationary points were found to be stable. (This is because the estimated coefficient of cubic damping is negative in this case). Therefore taking stability into consideration does not give an improved theoretical prediction for the lower hysteresis boundary calculated in section 5, for this depth.

Figure 9(b) shows the stability diagram for the 2cm depth experiment. Here the agreement is not so good, with the experimental points following the lower stability boundary, but continuing out of the stable region into the unstable region. However, if the coefficient of cubic damping (which as explained in the previous section was chosen in a rather ad hoc fashion) is chosen differently, then better overall agreement with the stability calculation can be achieved. Figure 9(c) shows the stability diagram for $N = 3.7$ (as opposed to $N = 6.4$ for Figure 9(b)). Here the lower hysteresis boundary calculated in section 5 coincides with the lower stationary point stability boundary. In this case, limit cycles were investigated as well as fixed points. This was done by numerically solving the evolution equation (5.1) with a Runge-Kutta scheme, for a variety of initial conditions. Figure 9(c) suggests that some of the standing waves observed in the experiment were stable limit cycles, rather than stable stationary points.

An example of stable limit cycles is given in Figure 10, which shows a phase plane diagram for $\Omega = -1.5, F = 0.7$. Physically a stable limit cycle corresponds to a standing wave where the amplitude experiences a slow oscillation on top of the fast sinusoidal oscillation of the wave motion. It can be seen that the limit cycles are relatively small compared with the amplitude $|A| = \left(p^2 + q^2\right)^{1/2}$, so this small modulation would not be easily observed in an experiment.

7. Conclusions

In Chapters II and III, we have examined, both theoretically and experimentally, the hysteresis region within which a flat surface or standing waves may occur, with Faraday excitation. We have confirmed the important roles of nonlinear cubic forcing and damping terms, previously incorporated into theoretical models by Miles (1993, 1994) and Craik & Armitage (1995); but we also find that a fifth-order conservative frequency shift must not be neglected.

The variational method due to Miles (1976) has been extended to allow the coefficient of this term to be calculated. This involved a significant use of symbolic computation. The Lagrangian given in section 2 can be used in future to calculate the coefficient of the fifth-order conservative term for different geometries and for multiple wave interaction problems. We suggest that the fifth-order conservative term may also be important in other fields of interest in Faraday resonance, for example, pattern selection processes.

The cubic forcing coefficient calculated in Miles (1993, 1994) differs from the one calculated here (3.23) because Miles considered the first and second harmonics, but not the third harmonic. We find that there are two contributions to the cubic forcing: a cubic interaction between the first and second harmonics and the forcing (which Miles (1993, 1994) included), and a quadratic interaction between the third harmonic and the forcing (which Miles (1993, 1994) omitted). (However it should be pointed out that the extra work in calculating the quadratic interaction between the third harmonic and the forcing is considerable, and if Miles had carried out this calculation then he would have been in a position to calculate the fifth-order conservative term as well if he had chosen).

We can rewrite our expression in terms of depth, surface tension and wavenumber parameters, so as to enable comparison with Miles' (B3) expression. In the limiting case of zero surface tension, we get for our expression

$$\tilde{F} = f k_1 \frac{\left(4\cosh^2(k_1 d)+3\right)\left(4\cosh^2(k_1 d)-1\right)}{16\tanh(k_1 d)\left(\cosh^2(k_1 d)-1\right)^2} \tag{7.1}$$

and for Miles' coefficient

$$\tilde{F}_{Miles} = fk_1 \frac{\tanh(k_1 d)(4\cosh^4(k_1 d) - 1)}{4\cosh^2(k_1 d)\left(\cosh^2(k_1 d) - 1\right)}. \tag{7.2}$$

For the limiting case of infinite depth, we get

$$\tilde{F} = fk_1 \frac{16g^3 + 9g^2 y k_1^2 + 6g y^2 k_1^4 + 40 y^3 k_1^6}{16\left(g + k_1^2 y\right)\left(g - 2k_1^2 y\right)\left(g + 4k_1^2 y\right)} \tag{7.3}$$

while for Miles' coefficient

$$\tilde{F}_{Miles} = fk_1 \frac{\left(g + y k_1^2\right)^2}{\left(g + 4y k_1^2\right)\left(g - 2y k_1^2\right)} \tag{7.4}$$

where $y = \gamma/\rho$.

Notice that as the depth tends towards infinity in (7.1) and (7.2), and as the surface tension tends towards zero in (7.3) and (7.4), then all four of the above expressions tend towards fk_1. Figure 11 shows how our coefficient compares to Miles' coefficient over a range of depths and surface tensions.

We have not calculated the damping coefficients theoretically. However, we show how the coefficients of linear and of cubic damping can be estimated from the experimental data: but the latter estimate remains a rather subjective one. For depths 1.3cm and 2cm, our estimates show the cubic damping coefficient to be positive, and so opposite in sign to linear damping; but both damping coefficients appear to have the same sign for the 1cm depth. (A purely theoretical determination of the cubic damping coefficient is carried out in Milner 1991, Miles 1993, 1994 and in Chapter V).

The lower hysteresis boundary is normally the boundary above which *any* finite-amplitude stationary points exist, since locally-stable stationary points are then usually present. However, in some cases, these stationary points may all be unstable; then the lower hysteresis boundary should correspond to the boundary of stability of the stationary points. We have obtained local analytical results for the hysteresis boundary in sections 4 a,b,c and d. Global numerical results for a composite evolution equation are given in section 5 and questions of stability are treated in section 6.

Good agreement between theory and experiment is achieved for our 1.3cm water depth case, when stationary point stability is taken into account. Agreement with the

1cm and 2cm depth observations of Craik & Armitage (1995) is also quite good: but, for the latter, we conjecture that some observations may have corresponded to stable limit cycles, predicted by our model, rather than to stable stationary points.

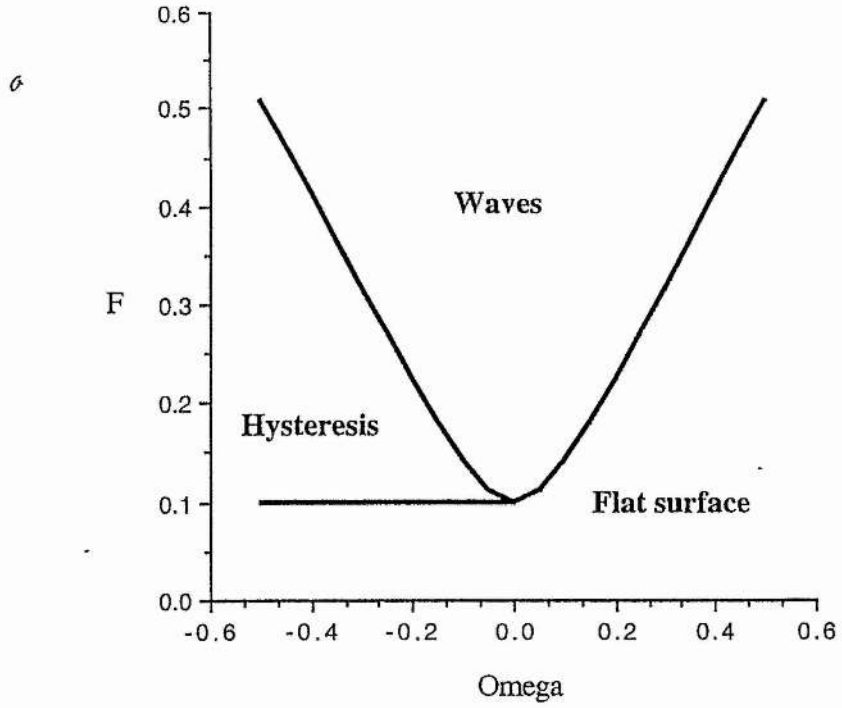

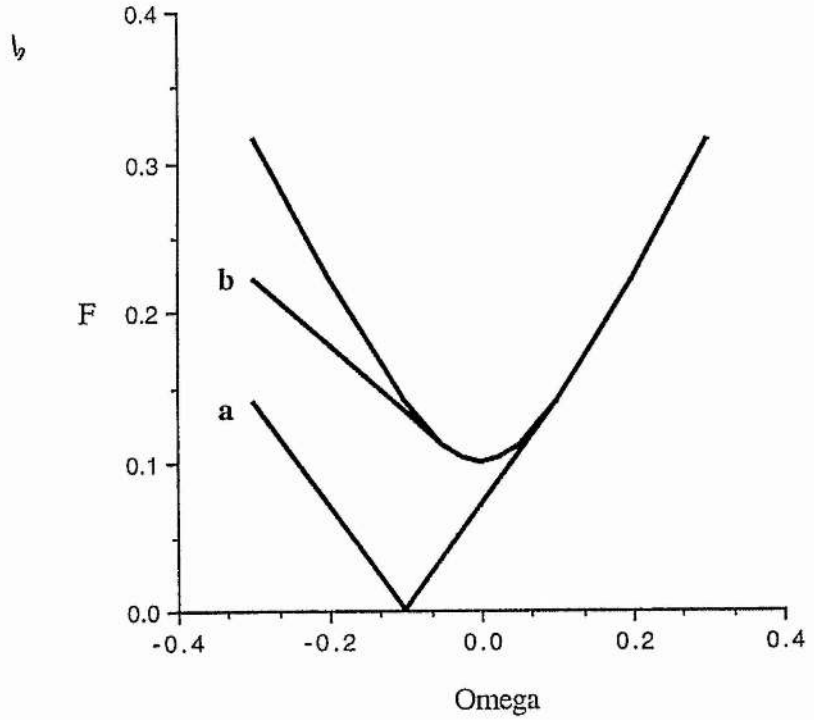

Figure 1. (a) Hysteresis diagram resulting from (1.1). (b) Hysteresis diagrams resulting from (1.2).

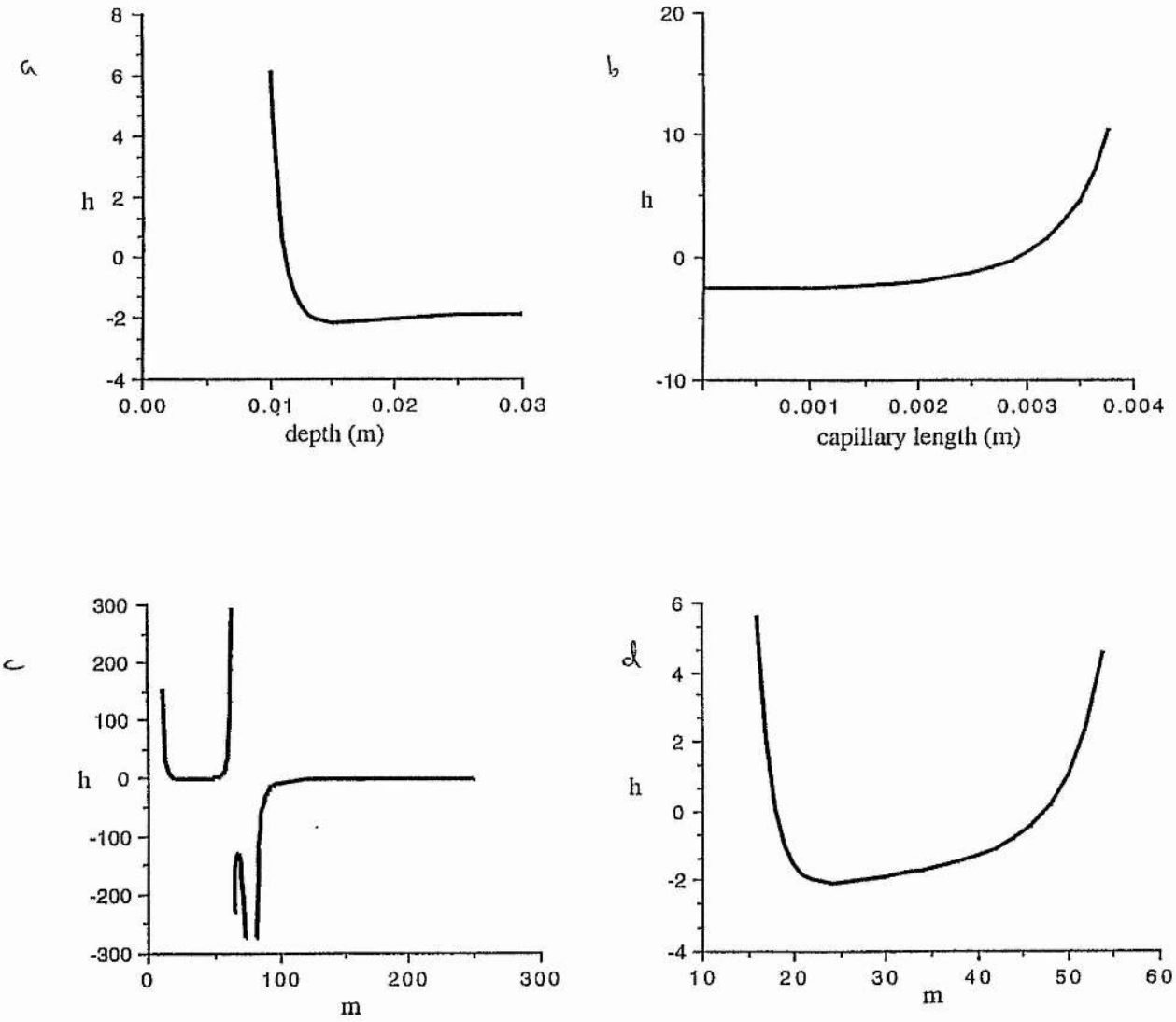

Figure 2. (a) h vs deptn for $m = 23, l = 0.7, \lambda = 0.02$. (b) h vs capillary length for $m = 23, l = 0.7, d = 0.01352$. (c) h vs m for $d = 0.01352, l = 0.7, \lambda = 0.02$. (d) Closer view of (c)

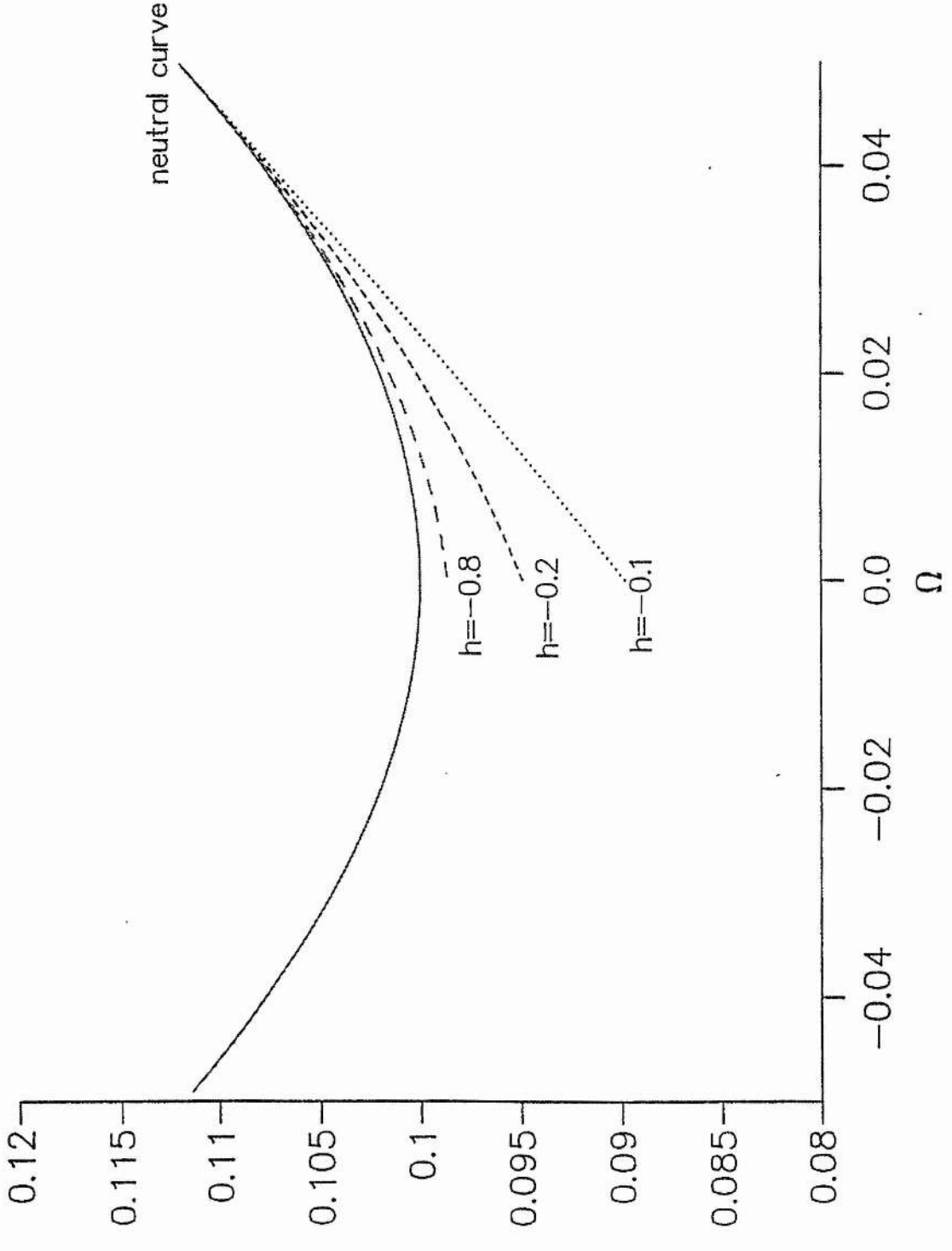

Figure 3. Lower hysteresis boundaries predicted by (4.30). Parameters $\mu = 0.1, \Gamma = 1.1, \varepsilon^2 = 0.047, \Omega_{bif} = 0.05, h = -0.1, -0.2, -0.8$.

Figure 4. Existence of finite amplitude fixed points for four different models: (a) our model (5.1) with $\tilde{F}_1$, (b) our model (5.1) with $\tilde{F}_2$, and (c) equation (1.3) with $\tilde{F}_1$ and (d) equation (1.3) with $\tilde{F}_1$ for $N = 1.57$.

Parameters are $m = 22, l = 0.7, d = 0.01352, \lambda = 0.02, \mu = 1, N = 2.43, \varepsilon^2 = 0.047$, $h = -2.1, \Pi = 0.25, \Gamma = 1.1$.

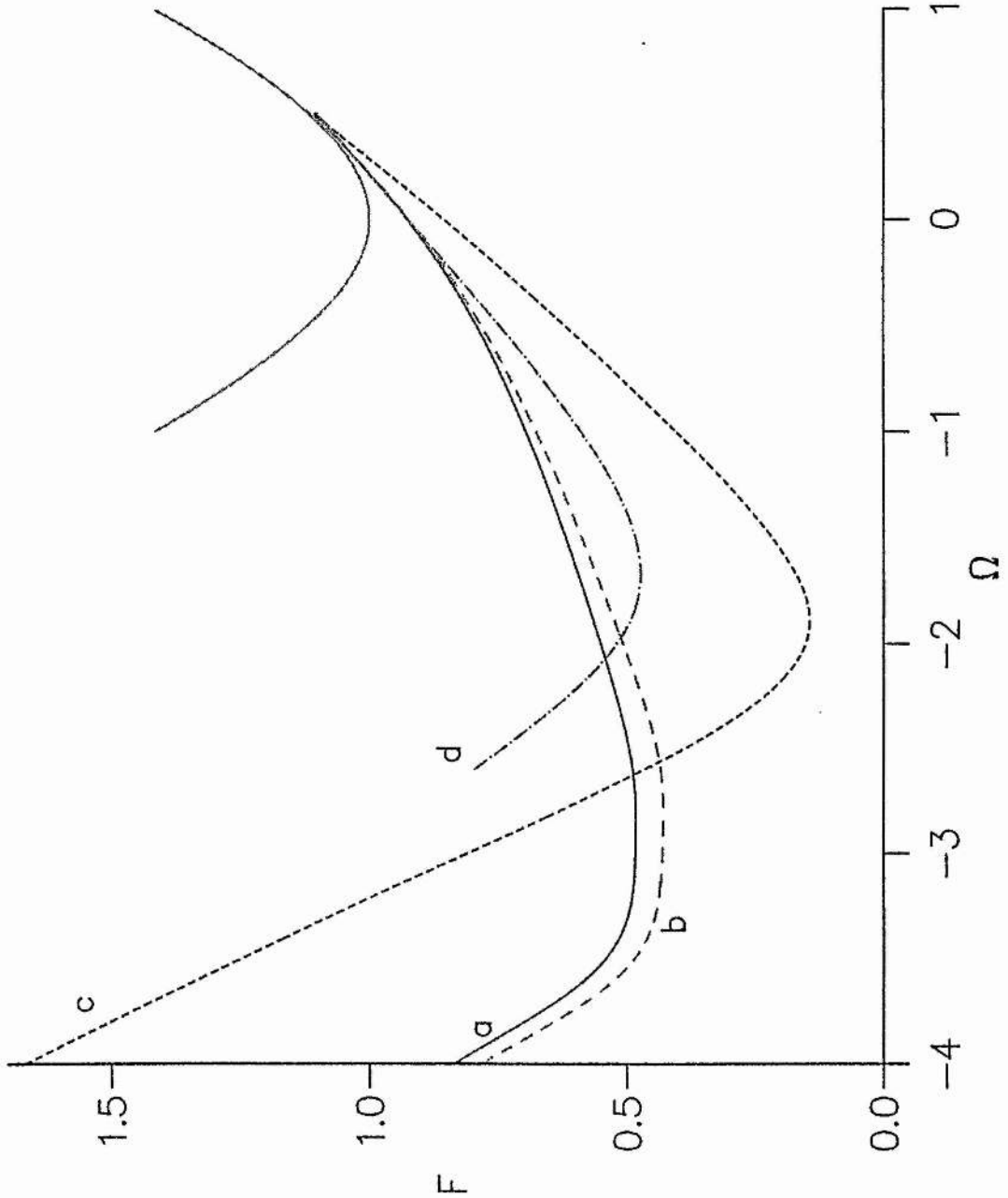

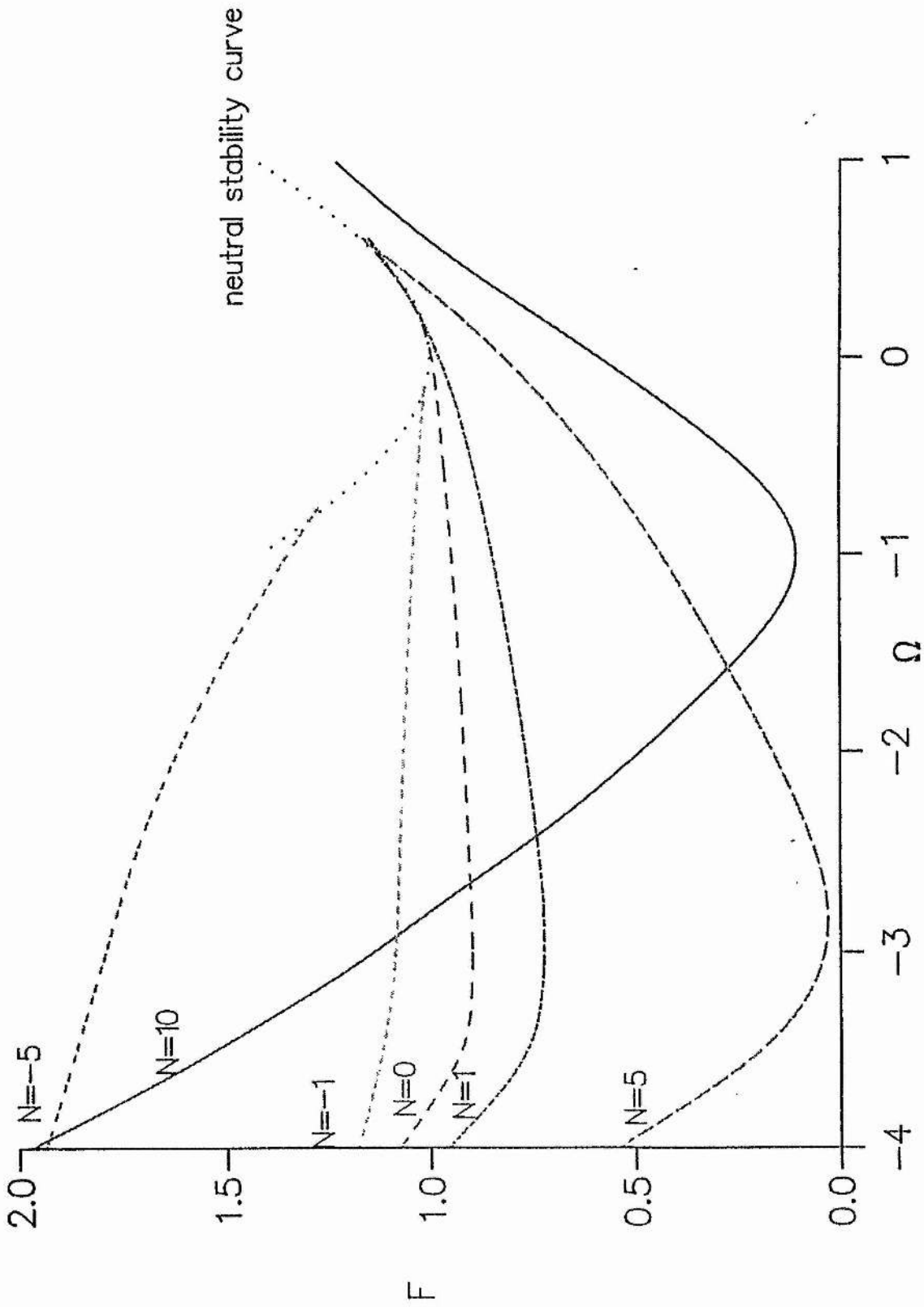

Figure 5. Existence of finite amplitude fixed points for six different values of N. Other parameters as in Figure 4.

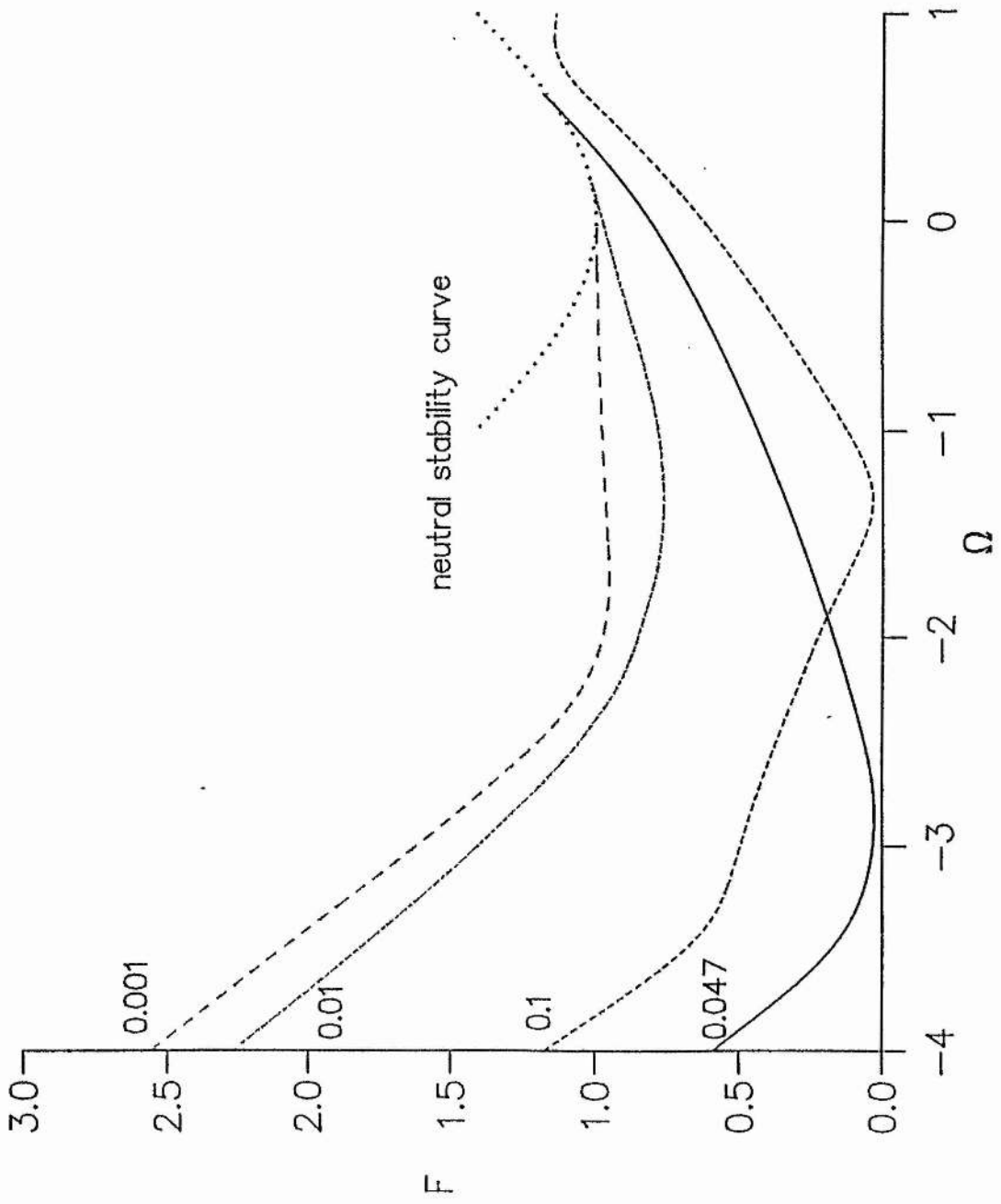

Figure 6. Existence of finite amplitude fixed points for four different values of ε^2. Other parameters as in Figure 4.

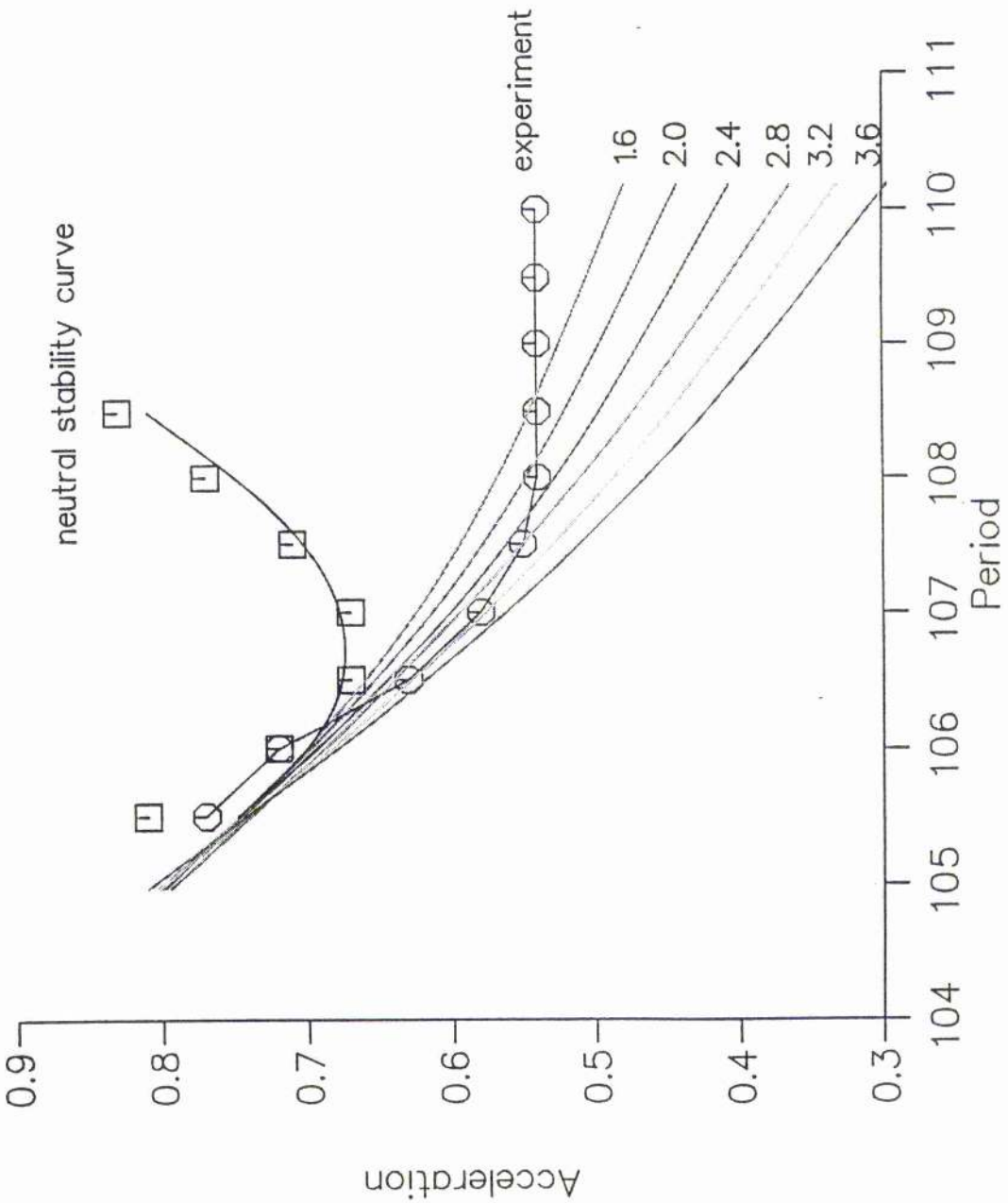

Figure 7. Lower hysteresis boundaries (calculated by considering the existence of fixed points) from our model (5.1) with $\tilde{F}_1$ for six different values of N, compared to equivalent experimental results.

Figure 8. Comparison between theoretical and experimental lower hysteresis boundaries for a water depth of 1cm, showing the boundaries predicted by our model (5.1) and by equation (1.3), as well as the experimental lower hysteresis boundary and neutral stability curve, for acceleration (ms^{-2}) against period (ms). Parameters are $N = -0.43$ (-0.68 for equation (1.3)), $\mu = 1$,

$h = -0.85, \Pi = -0.82, \Gamma = 2.7, \varepsilon^2 = 0.053$.

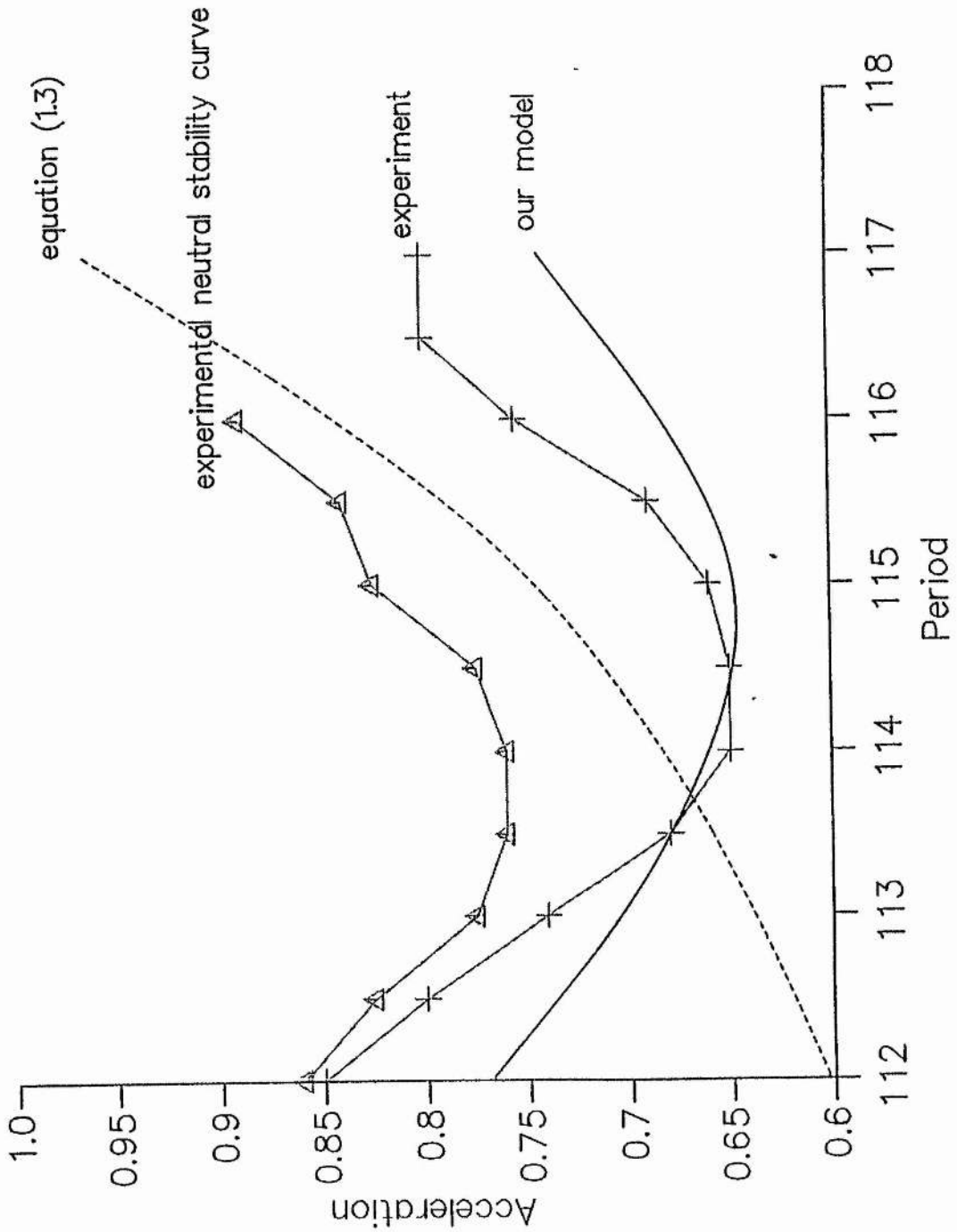

Figure 9. Stability diagrams for water depths of (a) 1.3cm (b) 2cm and (c) 2cm with $N = 3.7$. Parameters are $N = 2.43, \mu = 1, h = -2.1, \Pi = 0.25, \Gamma = 1.1, \varepsilon^2 = 0.047$, (b) and (c) $N = 6.4, \mu = 1, h = -2.1, \Pi = 0.42, \Gamma = 0.59, \varepsilon^2 = 0.047$.

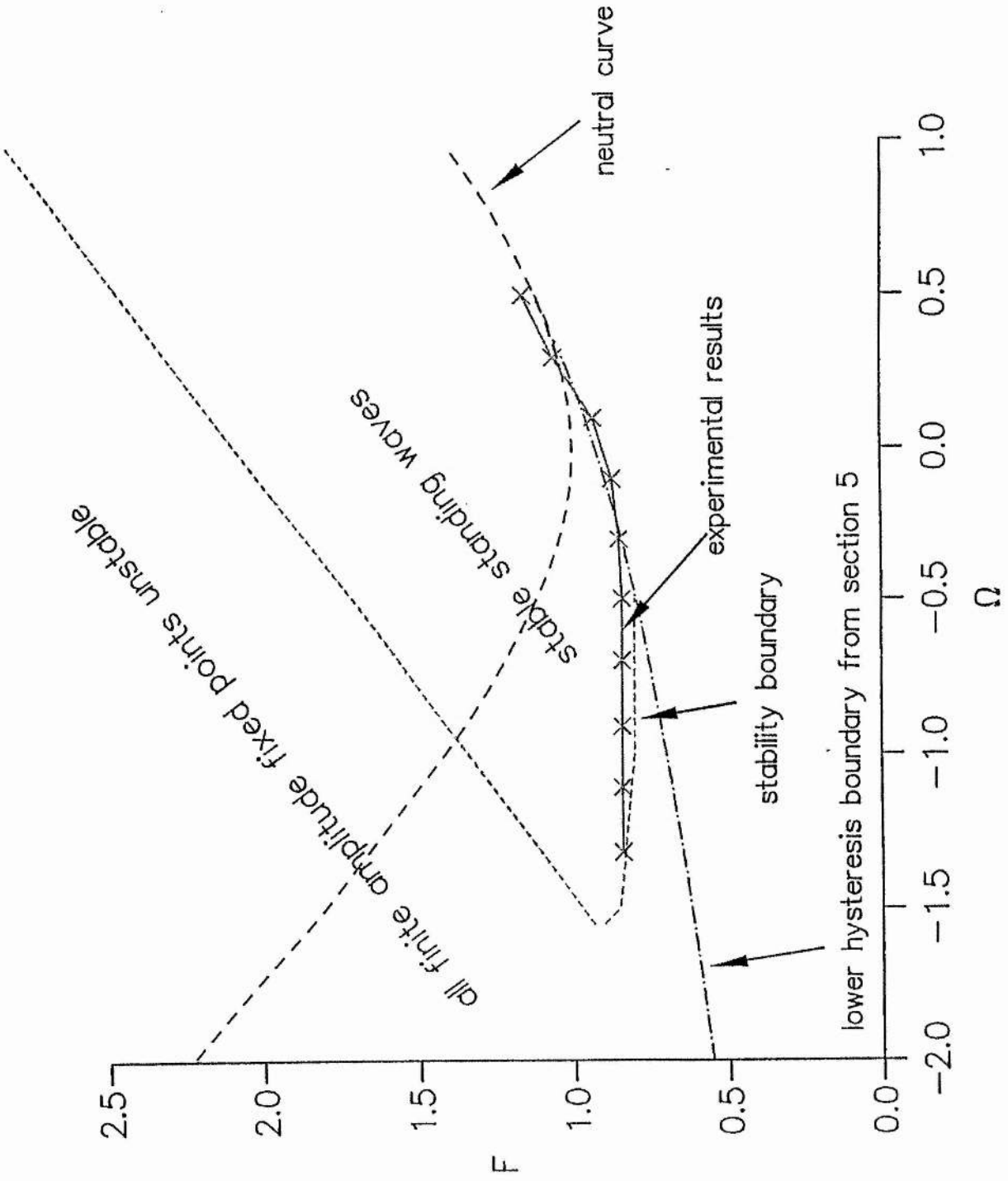

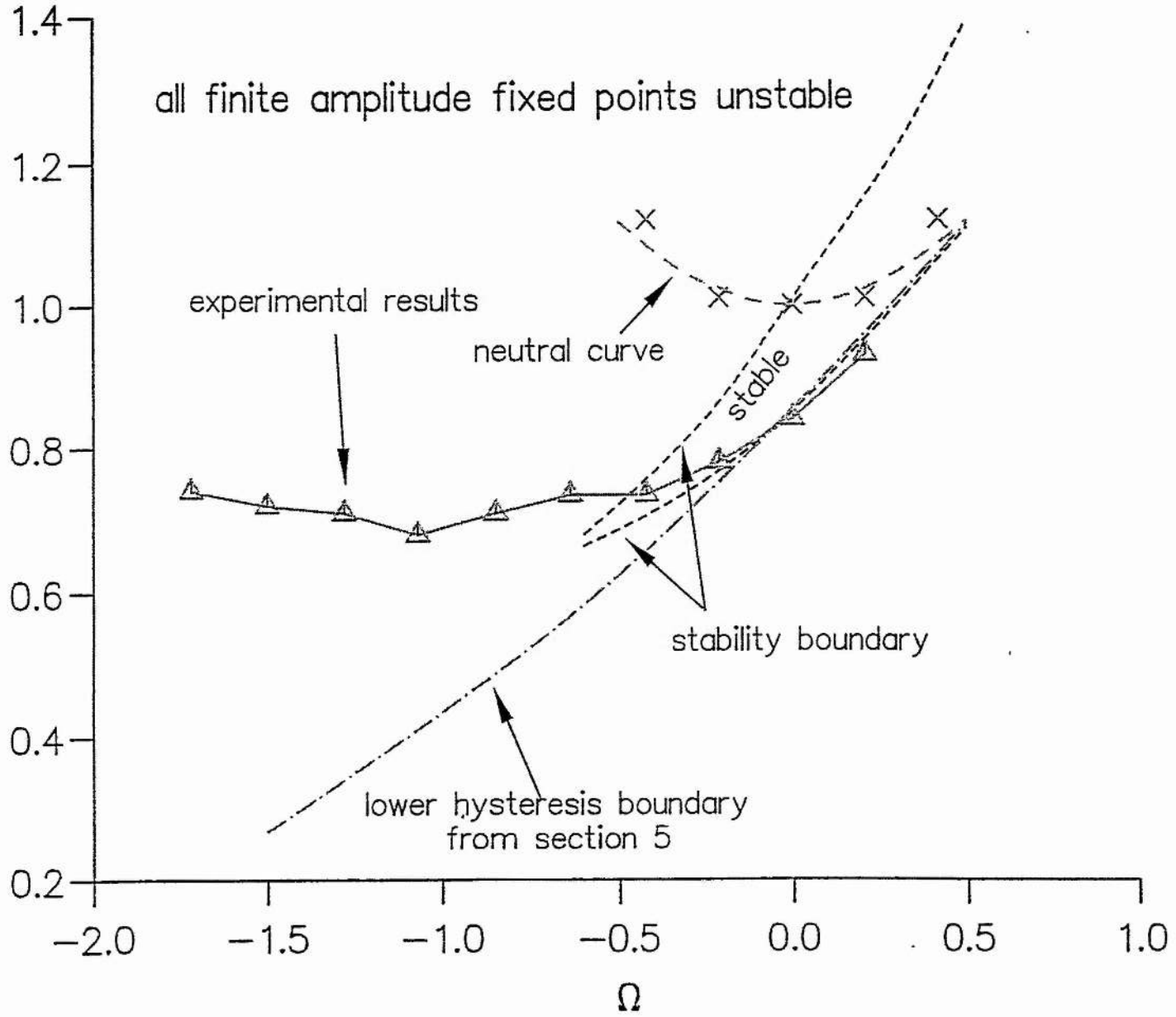
all finite amplitude fixed points unstable
experimental results
neutral curve
stable
stability boundary
lower hysteresis boundary
from section 5
F
Ω
1.4
1.2
1.0
0.8
0.6
0.4
0.2
−2.0
−1.5
−1.0
−0.5
0.0
0.5
1.0

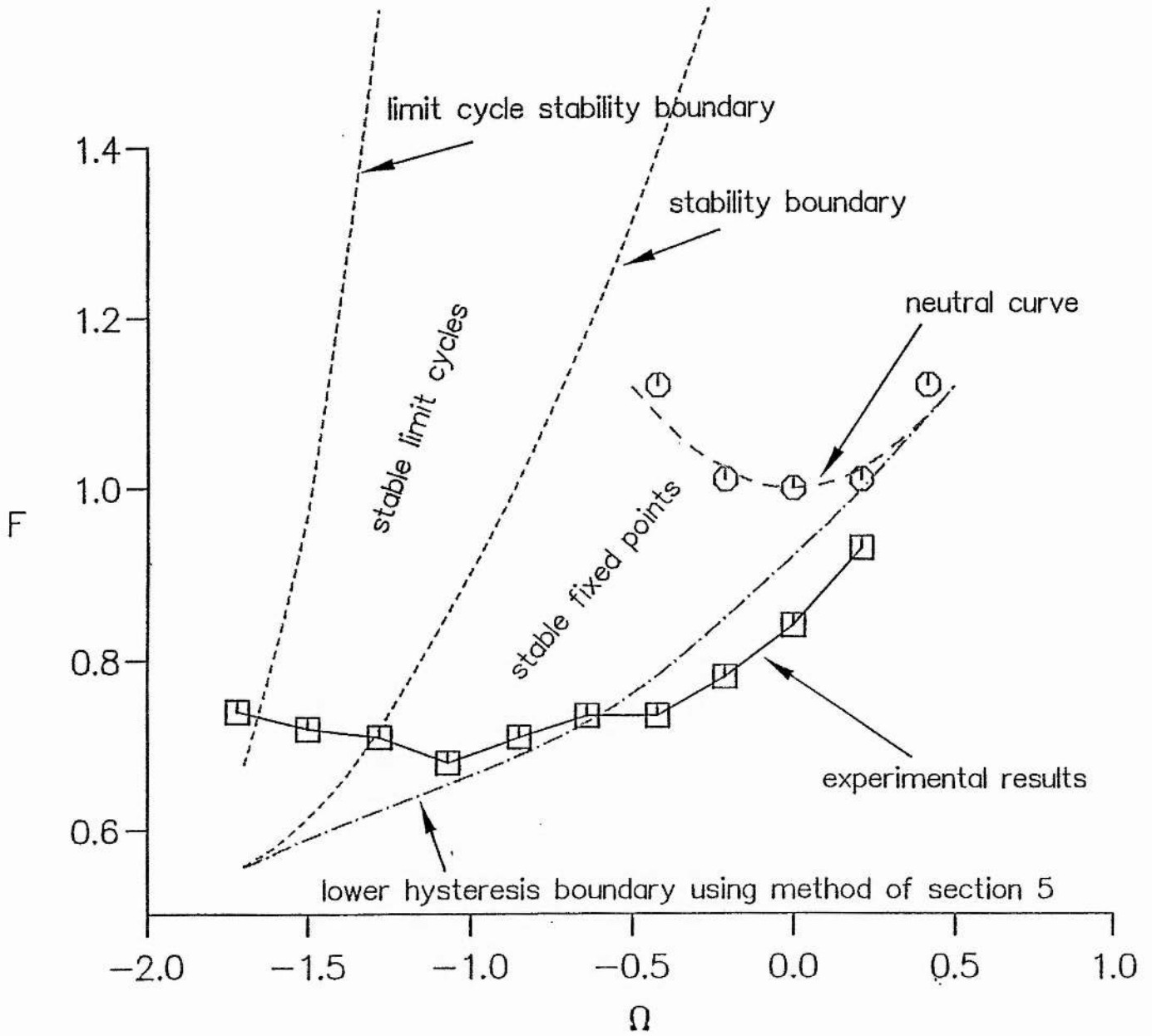
limit cycle stability boundary
stability boundary
neutral curve
stable limit cycles
stable fixed points
experimental results
lower hysteresis boundary using method of section 5
1.4
1.2
1.0
0.8
0.6
F
−2.0
−1.5
−1.0
−0.5
0.0
0.5
1.0
Ω

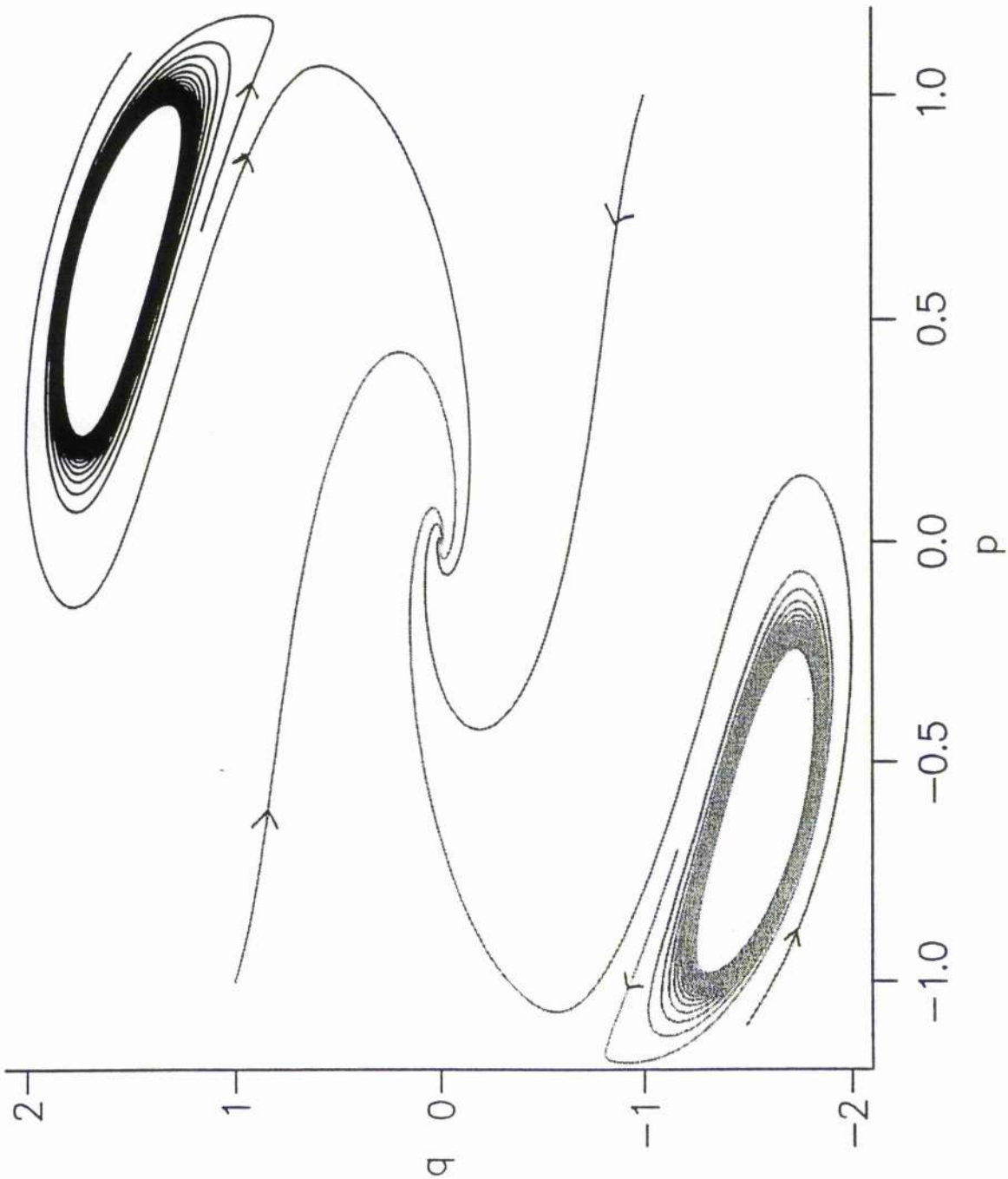

Figure 10. Phase plane diagram for Figure 9(c) at $\Omega = -1.5, F = 0.7$.

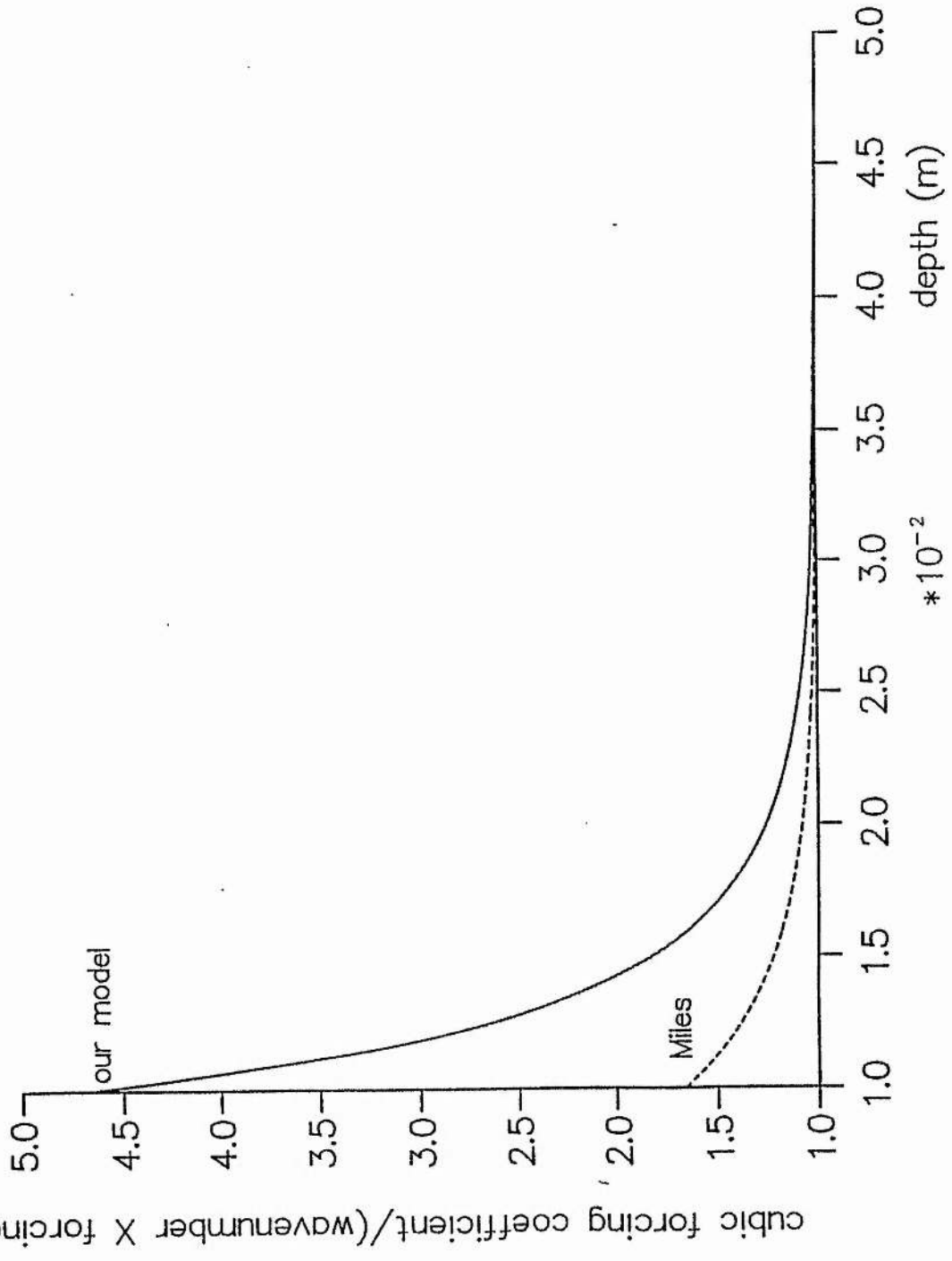

Figure 11. (a). Coefficient of cubic forcing given by (7.1) and (7.2). (b). Coefficient of cubic forcing given by (7.3) and (7.4).

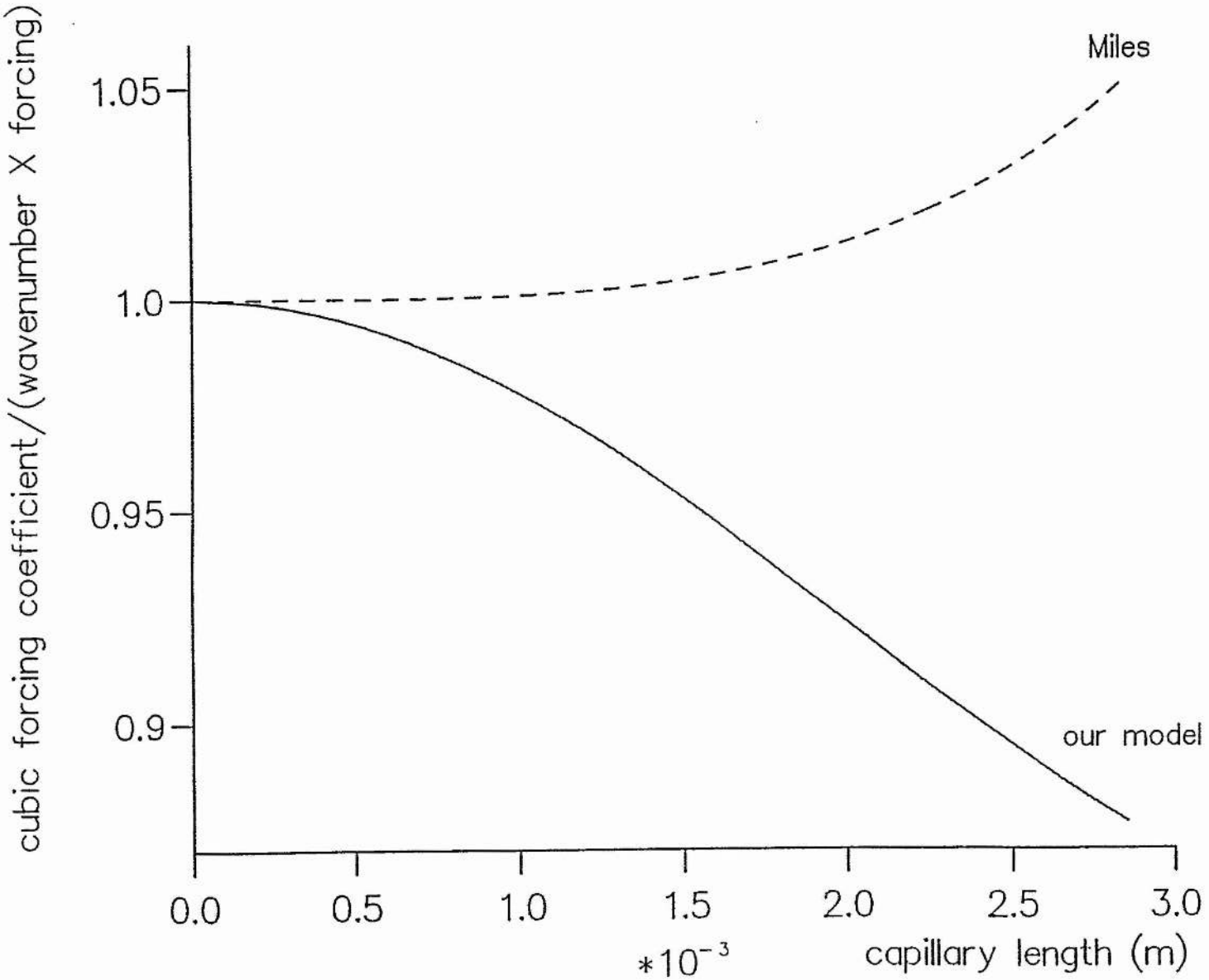
cubic forcing coefficient/(wavenumber X forcing)
1.05
1.0
0.95
0.9
Miles
our model
0.0
0.5
1.0
1.5
2.0
2.5
3.0
*10⁻³
capillary length (m)

CHAPTER IV

Limit cycles

1. Introduction

In this Chapter, we examine the evolution equation derived in the previous Chapter from a mathematical viewpoint, paying particular interest to the bifurcation structure of the equation. We abandon the scaling used in Chapter III and consider the composite evolution equation

$$\frac{dA}{dt} = -\mu A + i\Omega A + iFA^* + i\beta|A|^2 A + N|A|^2 A + iF\Gamma\left(A^3 + 3|A|^2 A^*\right) - ih|A|^4 A, \quad (1.1)$$

where now β is the real cubic conservative frequency shift coefficient. Comparing (1.1) with equation (5.1) from Chapter III, it can be seen that the coefficients in (1.1) are different to those used in Chapter III, with $\varepsilon^2\omega$ absorbed into μ, Ω, F and β, ε^2 absorbed into Γ, and $\varepsilon^4\omega$ absorbed into N and h. We now disregard the scaling assumptions used in Chapter III and examine equation (1.1) in its own right.

We will investigate the stable limit cycles which were seen in the previous Chapter to arise from equation (1.1). These limit cycles correspond to the amplitude and phase of the standing wave experiencing a slow periodic modulation, in addition to its fast basic periodicity. Several authors have reported stable limit cycles arising from the interaction of two modes (Ciliberto & Gollub 1985, Gu & Sethna 1987, Simonelli & Gollub 1989). As these stable limit cycles correspond to slow oscillation of the complex amplitudes of each of the two wave modes, the resultant phase space is four-dimensional. In contrast, here we have a single wave mode whose modulations describe a two-dimensional limit cycle.

A computational investigation of the limit cycles and bifurcations arising from (1.1) is described in section 2. It will be seen that stable limit cycles arise out of a Hopf

bifurcation, and this will be discussed in more detail in section 3. Section 4 employs a perturbation analysis to investigate the limit cycles arising out of the Hopf bifurcation. A further type of limit cycle, which is always unstable, is discussed analytically in section 5. Melnikov's method is used in section 6 to analyse global bifurcations. The results are summarised in section 7.

2. Computational results

In Chapter III, the existence and stability of stationary points corresponding to standing waves of constant amplitude were described, and the existence and stability of limit cycles was only briefly discussed. Here we describe the limit cycles in more detail, examing global and local bifurcations. Figure 1 shows the parameter space diagram corresponding to the 2cm water depth experiment of Craik & Armitage (1995), and we will discuss the limit cycles and bifurcations in terms of Figure 1. Stable finite-amplitude stationary points exist in the region between the lower hysteresis boundary and the line denoting Hopf bifurcations. Stable limit cycles exist in the region between the Hopf bifurcation curve and the lower homoclinic bifurcation curve (the stationary point within these stable limit cycles is of course unstable), while a larger stable limit cycle (with a doubled period) exists in the small region between the two homoclinic bifurcation curves and above the neutral curve . A large unstable limit cycle exists everywhere on Figure 1 *except* in the top left hand corner, above the two branches of the upper homoclinic bifurcation curve. Figure 1 was produced by solving (1.1) numerically and examining the character of solutions in phase space, over a fine grid in (F,Ω) space.

Figure 2(a) shows the (p,q) phase-plane diagram corresponding to point A on Figure 1. This shows a saddle point and two sinks, one at the origin and one at the centre of the spiral. A Hopf bifurcation occurs between points A and B on Figure 1 corresponding to a loss of stability of the non-zero stationary point (p_0,q_0). Figure

2(b) is the phase-plane diagram corresponding to point B, showing the stable limit cycle arising out of the Hopf bifurcation. (Only half of the phase-plane is shown in Figure 2 since the equations exhibit $(p,q) \leftrightarrow (-p,-q)$ symmetry. An identical limit cycle also arises from the stationary point at $(-p_0,-q_0)$). As the frequency detuning changes from point B to point C, the limit cycle grows. Figure 2(c) shows the limit cycle at point C. A homoclinic bifurcation occurs between C and D when the stable limit cycle collides with the unstable and stable manifolds of the saddle point. This destroys the stable limit cycle, so that the only remaining stable solution at D is the origin. Figure 2(d) shows the phase-plane at D.

The origin changes its stability between E and F, since they lie on either side of the linear neutral stability boundary $F = \left(\mu^2 + \Omega^2\right)^{1/2}$. At E the origin is a saddle, while at F it is a sink. This is demonstrated in Figures 3(a) and 3(b) which correspond to E and F respectively (both stable limit cycles are now shown). We can see from Figure 3(b) that two saddles (indicated by crosses) have been created at the bifurcation between E and F.

An unstable limit cycle can also be seen in both Figures 3(a) and 3(b), outside which all trajectories diverge to infinity, and inside which all trajectories end up on a stable limit cycle or (as at F) the sink at the origin. This limit cycle also exists for points like A, B, C and D, though it was not shown on the scale of Figure 2. The divergence of large amplitude solutions is due to the term in N in equation (1.1), which is a positive constant in this case (see section 7, where the limitations of this model are discussed). Figure 3(b) demonstrates sensitive dependence upon initial conditions near to the unstable limit cycle. All the trajectories shown on the Figure start near the point (1,-2), and some orbit the whole diagram before converging onto one of the two limit cycles or the origin.

Figure 4(a) shows the stable limit cycles that occur at point G on Figure 1. A homoclinic bifurcation occurs between G and H, when the two stable limit cycles collide with each other. Figure 4(b) shows the phase-plane at H, and the two stable limit cycles now form a single larger stable limit cycle, with a saddle at the origin. The

unstable limit cycle can still be detected outside the stable limit cycle. A further bifurcation occurs when the large stable limit cycle collides with the unstable limit cycle somewhere between H and I, and both are eliminated. Figure 4(c) shows the phase-plane at I: here all points diverge to infinity, but the vestiges of the two limit cycles can still be detected.

The phase-plane at J is shown in Figure 4(d). Here the origin is the only stable attractor, though most trajectories diverge to infinity. It can be seen that the basin of attraction of the origin is confined to two narrow tendrils (shaded), each spiralling away from a source.

3. Stationary points near the Hopf bifurcation

In this section we discuss the Hopf bifurcation that creates the stable limit cycles and in the next section we describe these limit cycles using a multiple-time-scale analysis. (In both this and the previous sections we have abandoned the scaling of Miles (1993, 1994) and the initial scaling of Chapter III, and treated all coefficients in (1.1) as *O(1)*: otherwise, the limit cycle behaviour is not evident - see Miles 1993 and section 7).

The *stable limit cycle* region shown in Figure 1 corresponds to stable limit cycles which have a single unstable stationary point inside them. At the Hopf bifurcation, this stationary point changes from a sink to a source. In Chapter III, section 6, we discussed the local stability of finite-amplitude stationary points of equation (1.1), and we will now use this approach to identify the Hopf bifurcation. A stationary point has $A_0 = ae^{i\theta}$ where a and θ are solutions of

$$-\mu + i\Omega + iFe^{-2i\theta} + (N + i\beta)a^2 + iF\Gamma a^2\left(e^{2i\theta} + 3e^{-2i\theta}\right) - iha^4 = 0 \qquad (3.1)$$

(which are best found numerically). For small disturbances about this stationary point, with $A = A_0 + Be^{\sigma t}$ where B is small, the eigenvalue equation for σ is found to be (see Chapter III, equation (6.3))

$$\sigma^2 + 2\sigma(\mu - 2Na^2) + G = 0$$
$$\text{where} \quad G \equiv \mu^2 + \Omega^2 - F^2 + 4(\beta\Omega - \mu N - 3\Gamma F^2)a^2$$
$$+2Fa^2\cos 2\theta(6\Omega\Gamma - \beta) - 2FNa^2\sin 2\theta$$
$$+3(N^2 + \beta^2 - 6\Gamma^2F^2)a^4 + 4Fa^4\cos 2\theta(h + 3\beta\Gamma) \qquad (3.2)$$
$$+18F^2\Gamma^2a^4\cos 4\theta - 12NF\Gamma a^4\sin 2\theta - 6\Omega ha^4$$
$$-12F\Gamma ha^6\cos 2\theta - 8\beta ha^6 + 5h^2a^8.$$

Therefore, when

$$\mu - 2Na^2 = 0 \text{ and } G > 0, \qquad (3.3)$$

there is a Hopf bifurcation. With the value of a^2 found from (3.1), result (3.3) yields a relation $\Omega = \Omega_{bif}(F)$ for the Hopf bifurcation. This relation will correspond to the Hopf bifurcation curve on Figure 1. Note that it is necessary that N is positive for the Hopf bifurcation to occur, since the coefficient of linear damping μ is always positive.

In the next section, we investigate the limit cycles that arise out of this Hopf bifurcation by using a multiple-time-scales asymptotic expansion. To describe a stationary point close to the Hopf bifurcation we first need to define a small positive scaling parameter ε by expanding

$$\Omega = \Omega_{bif} + \varepsilon^2\Omega_1 + O(\varepsilon^4), \qquad (3.4)$$

where $\Omega_{bif}(F)$ is the frequency detuning from resonance at the Hopf bifurcation for a given forcing F, as given by (3.1) and (3.3) and shown in Figure 1. Clearly, ε tends towards zero as the Hopf bifurcation is approached. (Note that ε is different from the scaling parameter used in Chapter III).

In view of (3.3), we initially substitute

$$A = ae^{i\phi} \equiv \left(\frac{\mu}{2N}\right)^{1/2} e^{i\theta} + \varepsilon^2(x + iy) + O(\varepsilon^4) \qquad (3.5)$$

into (1.1), where $ae^{i\phi}$ is a non-zero stationary point of (1.1) about which we may expect to find a limit cycle. At *O(1)*, equation (1.1) with (3.4) and (3.5) gives

$$-\frac{\mu}{2} + F\left(1 + \frac{\Gamma\mu}{N}\right)\sin 2\theta = 0,$$
$$\Omega_{bif} + \frac{\beta\mu}{2N} - \frac{h\mu^2}{4N^2} + F\left(1 + \frac{2\Gamma\mu}{N}\right)\cos 2\theta = 0. \qquad (3.6)$$

Therefore

$$\sin 2\theta = \frac{\mu N}{2F(N+\Gamma\mu)} \text{ and } \cos 2\theta = \frac{h\mu^2 - 2N\beta\mu - 4N^2\Omega_{bif}}{4NF(N+2\mu\Gamma)}, \tag{3.7}$$

and, for compatibility,

$$F = \left(\frac{\mu^2 N^2}{4(N+\mu\Gamma)^2} + \frac{\left(h\mu^2 - 2N\beta\mu - 4N^2\Omega_{bif}\right)^2}{16N^2(N+2\mu\Gamma)^2} \right)^{1/2}, \tag{3.8}$$

which is the curve in $\left(F, \Omega_{bif}\right)$ space upon which the Hopf bifurcation occurs. This analytical representation was found to coincide with the (numerically produced) Hopf bifurcation curve in Figure 1.

At $O(\varepsilon^2)$, we set $x + iy \equiv \tilde{a}e^{i\Phi}$ in (1.1), (3.4) and (3.5) to obtain

$$\begin{aligned} \Omega_1 \left(\frac{\mu}{2N}\right)^{1/2} \sin(\theta - \Phi) = \tilde{a}\Big\{ & -\frac{\mu}{2} + F\sin 2\Phi + \mu\cos^2(\theta - \Phi) \\ & + \frac{\mu}{2}\left(\frac{h\mu}{N^2} - \frac{\beta}{N}\right)\sin[2(\theta - \Phi)] + \frac{3\mu F\Gamma}{N}\sin 2\Phi \Big\} \end{aligned} \tag{3.9}$$

and

$$\begin{aligned} -\Omega_1 \left(\frac{\mu}{2N}\right)^{1/2} \cos(\theta - \Phi) = \tilde{a}\Big\{ & \Omega_{bif} + F\cos 2\Phi + \frac{\mu}{2}\sin[2(\theta - \Phi)] \\ & + \frac{\beta\mu}{2N}\left(1 + 2\cos^2(\theta - \Phi)\right) + \frac{3F\Gamma\mu}{N}(\cos 2\theta + \cos 2\Phi) \\ & - \frac{h\mu^2}{4N^2}\left(1 + 4\cos^2(\theta - \Phi)\right)\Big\}. \end{aligned} \tag{3.10}$$

Equations (3.9) and (3.10) can be solved explicitly to give $\tilde{a} / \Omega_1$ as functions of θ and hence, using (3.7) and (3.8), as functions of Ω_{bif} only. But the resulting expressions are rather long and are not printed here.

4. Limit cycles near the Hopf bifurcation

The limit cycles occurring near to the Hopf bifurcation may be estimated by a multiple-time-scales analysis of time-dependent disturbances applied to the stationary points found in the previous section. This method is equivalent to computing the normal form and using a theorem due to Hopf (1942) (see Guckenheimer & Holmes 1983 pp 150-156 for a description of the latter method). The multiple-time-scales approach is

preferred in this case since we wish to emphasise the two time scales that exist near to the Hopf bifurcation.

We add to the stationary points (3.5) a time-dependent perturbation $\tilde{p}+i\tilde{q}$ such that

$$\begin{aligned} &A(t)=ae^{i\phi}+\tilde{p}(t)+i\tilde{q}(t),\\ &\tilde{p}(t)+i\tilde{q}(t)\equiv\varepsilon\left(p_0(t,\tau)+iq_0(t,\tau)\right)\\ &+\varepsilon^2\left(p_1(t,\tau)+iq_1(t,\tau)\right)+\varepsilon^3\left(p_2(t,\tau)+iq_2(t,\tau)\right)+O\left(\varepsilon^4\right), \end{aligned} \tag{4.1}$$

where $\tau\equiv\varepsilon^2 t$ is a slow time scale.

Substituting (3.4) and (4.1) into equation (1.1) gives at $O(\varepsilon)$

$$\frac{\partial p_0}{\partial t}=\alpha_1 p_0+\alpha_2 q_0, \tag{4.2}$$

$$\frac{\partial q_0}{\partial t}=-\alpha_1 q_0+\alpha_3 p_0, \tag{4.3}$$

where

$$\alpha_1=\frac{\mu}{2N^2}\left(N^2\cos 2\theta-N\beta\sin 2\theta+h\mu\sin 2\theta\right), \tag{4.4}$$

$$\begin{aligned} \alpha_2=&(2\mu N^2\sin 2\theta+4FN^2-4\Omega_{bif}N^2+12F\Gamma\mu N\\ &-12F\Gamma\mu N\cos 2\theta-4\beta\mu N+2\beta\mu N\cos 2\theta\\ &+3h\mu^2-2h\mu^2\cos 2\theta)/(4N^2), \end{aligned} \tag{4.5}$$

$$\begin{aligned} \alpha_3=&(2\mu N^2\sin 2\theta+4FN^2+4\Omega_{bif}N^2+12F\Gamma\mu N\\ &+12F\Gamma\mu N\cos 2\theta+4\beta\mu N+2\beta\mu N\cos 2\theta\\ &-3h\mu^2-2h\mu^2\cos 2\theta)/(4N^2). \end{aligned} \tag{4.6}$$

Combining (4.2) to (4.6) gives

$$\frac{\partial^2 p_0}{\partial t^2}+\omega^2 p_0=0, \tag{4.7}$$

where

$$\begin{aligned} 16N^4\omega^2\equiv&\,16\Omega_{bif}^2N^4-4\mu^2N^4-16F^2N^4+32\Omega_{bif}\beta\mu N^3\\ &-96F^2\Gamma\mu N^3+12\beta^2\mu^2N^2-16\beta\mu^3hN-72F^2\Gamma^2\mu^2N^2\\ &-24\Omega_{bif}h\mu^2N^2+5h^2\mu^4-16F\beta\mu N^3\cos 2\theta+16Fh\mu^2N^2\cos 2\theta\\ &+96F\Gamma\mu\Omega_{bif}N^3\cos 2\theta+48F\Gamma\mu^2\beta N^2\cos 2\theta-24F\Gamma\mu^3hN\cos 2\theta\\ &+72F^2\Gamma^2\mu^2N^2\cos 4\theta-16\mu FN^4\sin 2\theta-48F\Gamma\mu^2N^3\sin 2\theta. \end{aligned} \tag{4.8}$$

Clearly whenever $\omega^2>0$, ω is the orbital frequency of small oscillations about (3.5), which will turn out to be close to that of stable limit cycles.

Combining (3.7) and (3.8) with (4.8) gives

$$2N^4\omega^2=\mu\left(4N^3\beta\Omega_{bif}-2\mu N^4+2\beta^2\mu N^2+\mu^3h^2-4N^2\mu\Omega_{bif}h-3N\mu^2h\beta\right) \tag{4.9}$$

for particular cases with $\Gamma = 0$. A corresponding, but rather lengthy expression for $\Gamma \neq 0$ can easily be obtained. Equation (4.9) is discussed later in this section.

Equation (4.7) gives

$$p_0 = \hat{B}(\tau)e^{i\omega t} + \hat{B}^*(\tau)e^{-i\omega t}, \tag{4.10}$$

where $\hat{B}$ is an as yet unknown complex function of the slow timescale τ, while q_0 follows by substituting (4.10) into (4.2).

From this point in the calculation, a symbolic manipulation computer package was used to carry out the necessary algebra, which would be formidable otherwise. Many of the resulting expressions are too lengthy to be published, and the outline given here concentrates on the method rather than the details. The final numerical results of the calculation will be summarised in a series of graphs.

At $O(\varepsilon^2)$, equations (1.1), (3.4) and (4.1) give

$$\frac{\partial p_1}{\partial t} = \alpha_1 p_1 + \alpha_2 q_1 + f_1 p_0^2 + f_2 q_0^2 + f_3 p_0 q_0 \tag{4.11}$$

and

$$\frac{\partial q_1}{\partial t} = -\alpha_1 q_1 + \alpha_3 p_1 + f_4 p_0^2 + f_5 q_0^2 + f_6 p_0 q_0, \tag{4.12}$$

where f_i $(i = 1,..,6)$ are known (but lengthy) *O(1)* real constants. Combining (4.11) and (4.12) and substituting the expressions for p_0 and q_0 gives

$$\frac{\partial^2 p_1}{\partial t^2} + \omega^2 p_1 = g_1(\tau)e^{2i\omega t} + g_1^*(\tau)e^{-2i\omega t} + g_2(\tau), \tag{4.13}$$

where g_1 and g_2 are known (but lengthy) *O(1)* functions of τ (g_1 is complex and g_2 is real). With this right-hand side, solutions of (4.13) are clearly non-secular, and take the form

$$p_1 = C(\tau)e^{i\omega t} + \kappa_1(\tau)e^{2i\omega t} + \kappa_2(\tau) + c.c., \tag{4.14}$$

where C is an unknown complex function of τ and κ_1 and κ_2 are known (but lengthy) *O(1)* functions of τ (κ_1 being complex and κ_2 real). A corresponding expression for q_1 can be deduced by substituting (4.14) into (4.11).

At $O(\varepsilon^3)$, equations (1.1), (3.4) and (4.1) give

$$\frac{\partial p_2}{\partial t} + \frac{\partial p_0}{\partial \tau} = \alpha_1 p_2 + \alpha_2 q_2 + u_1, \tag{4.15}$$

$$\frac{\partial q_2}{\partial t} + \frac{\partial q_0}{\partial \tau} = -\alpha_1 q_2 + \alpha_3 p_2 + u_2, \tag{4.16}$$

$$u_1 \equiv r_1 p_0^3 + r_2 q_0^3 + r_3 p_0^2 q_0 + r_4 p_0 q_0^2 + r_5 p_0 p_1 + r_6 p_0 q_1 + r_7 q_0 p_1 + r_8 q_0 q_1 + r_9 \tilde{a} p_0 + r_{10} \tilde{a} q_0 + r_{11} \Omega_1 p_0 + r_{12} \Omega_1 q_0, \tag{4.17}$$

$$u_2 \equiv r_{13} p_0^3 + r_{14} q_0^3 + r_{15} p_0^2 q_0 + r_{16} p_0 q_0^2 + r_{17} p_0 p_1 + r_{18} p_0 q_1 + r_{19} q_0 p_1 + r_{20} q_0 q_1 + r_{21} \tilde{a} p_0 + r_{22} \tilde{a} q_0 + r_{23} \Omega_1 p_0 + r_{24} \Omega_1 q_0, \tag{4.18}$$

where $r_i \ (i = 1,..,24)$ are known (but lengthy) *O(1)* real constants. Note that terms in $\tilde{a}$ (where $\tilde{a} e^{i\phi} = x + iy$) appear in the expansion for the first time in expressions (4.17) and (4.18). Combining (4.15) - (4.18) gives

$$\frac{\partial^2 p_2}{\partial t^2} + \omega^2 p_2 = \alpha_1 u_1 + \alpha_2 u_2 - \alpha_1 \frac{\partial p_0}{\partial \tau} - \alpha_2 \frac{\partial q_0}{\partial \tau} + \frac{\partial u_1}{\partial t} - \frac{\partial^2 p_0}{\partial t \partial \tau}, \tag{4.19}$$

and substituting the above expressions for p_0, q_0, p_1 and q_1 gives

$$\frac{\partial^2 p_2}{\partial t^2} + \omega^2 p_2 = e^{i\omega t}\left(-2i\omega \frac{d\hat{B}}{d\tau} + b_1 \Omega_1 \hat{B} + b_2 \hat{B}^2 \hat{B}^* \right) + c.c. + N.S.T. \tag{4.20}$$

where b_1 and b_2 are known (but lengthy) *O(1)* complex constants, and *N.S.T.* stands for non-secular terms. The $e^{i\omega t}\hat{B}$ terms arise from the $r_9, r_{10}, r_{11}, r_{12}, r_{21}, r_{22}, r_{23}$ and r_{24} terms in (4.17) and (4.18). The $e^{i\omega t}\hat{B}^2\hat{B}^*$ terms arise from (i) cubic interactions between the p_0, q_0 terms and (ii) quadratic interactions between p_0 (or q_0) and the particular integral part of p_1 (or q_1).

To suppress secular growth of (p_2, q_2), we must equate to zero the term in $e^{i\omega t}$ on the right-hand side of (4.20), i.e. we put $2i\omega \, d\hat{B}/d\tau = b_1 \Omega_1 \hat{B} + b_2 \hat{B}^2 \hat{B}^*$. Substituting $\hat{B} = R\, e^{i\psi}$ into this gives

$$\frac{dR}{d\tau} = -R\left(c_1 \Omega_1 + c_2 R^2\right), \quad \frac{d\psi}{d\tau} = c_3 \Omega_1 + c_4 R^2, \tag{4.21}$$

where

$$c_1 = -\frac{\mathrm{Im}(b_1)}{2\omega}, \ c_2 = -\frac{\mathrm{Im}(b_2)}{2\omega}, \ c_3 = -\frac{\mathrm{Re}(b_1)}{2\omega}, \ c_4 = -\frac{\mathrm{Re}(b_2)}{2\omega} \tag{4.22}$$

are real *O(1)* constants (provided $\omega^2 > 0$: compare with equations (3.4.9) in Guckenheimer & Holmes 1983). If we put $dR/d\tau = 0$ we get $R = 0$, or $\pm\left(-c_1\Omega_1/c_2\right)^{1/2}$, where only real non-negative roots are meaningful. When $c_1\Omega_1/c_2 < 0$ then

$$\hat{B} = \mathrm{R}e^{i\psi} = \left(-c_1\Omega_1/c_2\right)^{1/2} \exp\left\{ i\Omega_1\left(c_3 - c_1 c_4/c_2\right)\tau \right\}. \tag{4.23}$$

This fixes both the amplitude and frequency of the perturbation about the stationary point. Note that its frequency is close to ω of (4.7), but with an $O(\varepsilon^2)$ correction given by (4.23). Provided $\omega^2 > 0$, this corresponds to a limit cycle. By examining the sign of $dR/d\tau$ on either side of the Hopf bifurcation we see that the limit cycle will be stable if $c_2 > 0$ and unstable if $c_2 < 0$. As $\Omega_1 \to 0$ (i.e. as the Hopf bifurcation is approached) the size of the limit cycle tends towards zero, as it must.

The constants c_i $(i = 1,..,4)$ are very lengthy expressions that were calculated using the symbolic manipulation computer package MAPLE. Here, we present these expressions graphically for particular cases. To aid this, we use the fact that we can scale (1.1) to give $\mu = \beta = 1$ without loss of generality (see Craik & Armitage 1995). Figures 5 (a-d) show the dependence of the coefficients on N and h for $\Omega_{bif} = -1$, $\Gamma = 0$. Figure 5 (e) shows the dependence of the coefficients on Γ for $h = 0, N = 0.2, \Omega_{bif} = -1$. (In these Figures, we use the expression (3.8) for F).

Three things should be noted from these graphs. Firstly, the coefficients c_i $(i = 1,..,4)$ all diverge to infinity for $h = 0.2$ at $N \approx 0.13$ and $h = 0.3$ at $N \approx 0.23$, and it can be seen that the curves corresponding to $h = 0$ are also beginning to diverge to infinity on the right-hand sides of the diagrams. Such divergence corresponds to $\omega \to 0$ ($c_i \propto \frac{1}{\omega}$ for $i = 1,..,4$). For higher values of N, ω and c_i are imaginary. It appears that the value $N = N_0(h)$, at which the coefficients c_i $(i = 1,..,4)$ diverge, increases as $|h|$ increases when $h < 0$; but N_0 decreases as h decreases when $h > 0$.

Note also that ω becomes imaginary at $\Gamma = -\frac{N}{2\mu}$: this is where the graphs terminate and corresponds to a pole in equation (3.8) (see Figure 5(e)). Also, from Figure 5(b), it appears that $c_2 > 0$ whenever ω is real and therefore only stable limit cycles arise from the Hopf bifurcation for the parameter ranges studied here.

From (4.9), $\omega = 0$ when

$$\Omega_{bif} \equiv \hat{\Omega} = \frac{\mu\left(2N^4 + 3\mu N h\beta - 2\beta^2 N^2 - \mu^2 h^2\right)}{4N^2(N\beta - \mu h)} \tag{4.24}$$

for cases with $\Gamma = 0$. For $\Omega_{bif} > \hat{\Omega}$ (or $\Omega_{bif} < \hat{\Omega}$) ω is real, while for $\Omega_{bif} < \hat{\Omega}$ (or $\Omega_{bif} > \hat{\Omega}$) ω is imaginary. When ω becomes imaginary, equation (4.10)

has exponentially growing solutions and so the limit cycle is destroyed. This is what happens at the homoclinic bifurcation and we can deduce that (4.24) gives the frequency detuning at which the Hopf bifurcation and the homoclinic bifurcation occur simultaneously i.e. where the line on Figure 1 denoting the Hopf bifurcation intersects the line denoting the homoclinic bifurcation. The value of the forcing at this (single) point is given by (3.8) with $\Gamma = 0$. For the values of the parameters corresponding to Figure 1 (but with $\Gamma = 0$), equations (4.23) and (3.8) give a point of intersection at $(-1.92, 0.436)$ which can be seen to be in good agreement with the (numerically obtained) point of intersection shown on Figure 1. (Note that for Figure 1, $\Gamma = 0.02775 \approx 0$).

Finally we compare limit cycles predicted by this theory with one produced numerically from (1.1): this is shown in Figure 6 for $\Omega = -1.5, F = 0.7$. In calculating the asymptotic limit cycle in Figure 6, it is first necessary to find Ω_1. To do this we used equations (3.4) and (3.8), to arrive at $\varepsilon^2 \Omega_1 = \Omega - \Omega_{bif}\big|_{F=0.7} \approx -0.04$. Therefore we are free to choose $\varepsilon = 1$, $\Omega_1 = -0.04$ so that our small parameter in the expansion effectively becomes $(-\Omega_1)^{1/2}$ (and therefore is 0.2 here) instead of ε. The multiple-time-scales solutions are a plot of $\mathrm{Im}\, A(t) \equiv q$ against $\mathrm{Re}\, A(t) \equiv p$ where $A(t)$ is given by (4.1). We plot both the leading-order solution retaining terms only in p_0, q_0 and the second-order solution retaining terms up to p_1, q_1. The numerical solution corresponds to a Runge-Kutta solution of (1.1) using the initial conditions $p = 0.7, q = 1.16$. Figure 6 shows that even the leading-order asymptotic solution, which is an ellipse, is a good approximation to the numerical solution, while the second-order solution matches the numerical limit cycle almost exactly.

5. Large limit cycles

(a) Behaviour far from the origin

The dominant behaviour of equation (1.1) far from the origin is oscillatory (though there will generally be additional growth or contraction). Here, we reintroduce the scaling used in Chapter III, namely, that the coefficients of cubic damping N, the coefficient of cubic forcing Γ, and the coefficient of the fifth-order conservative term h are all much smaller than the other four coefficients μ, F, Ω and β. We therefore replace (N,h,Γ) with $\left(N\tilde{\varepsilon}^2, h\tilde{\varepsilon}^2, \Gamma\tilde{\varepsilon}^2\right)$ where $\tilde{\varepsilon}$ is small and positive (and identical to the scaling parameter used in Chapter III). We also apply

$$A(t) = \frac{1}{\tilde{\varepsilon}}\left(x_0(t) + iy_0(t)\right) + O(1) \tag{5.1}$$

to (1.1), and carry out a regular perturbation that is valid at large amplitudes.

At leading order, that is $O\left(\frac{1}{\tilde{\varepsilon}^3}\right)$, we obtain

$$\begin{aligned} \frac{dx_0}{dt} &= -\beta y_0\left(x_0^2 + y_0^2\right) + h y_0\left(x_0^2 + y_0^2\right)^2 \\ \frac{dy_0}{dt} &= \beta x_0\left(x_0^2 + y_0^2\right) - h x_0\left(x_0^2 + y_0^2\right)^2 \end{aligned} \tag{5.2}$$

which has the circular solution

$$\begin{aligned} x_0 &= r_0 \cos\left\{r_0^2\left(\beta - h r_0^2\right)t + \varphi_0\right\} \\ y_0 &= r_0 \sin\left\{r_0^2\left(\beta - h r_0^2\right)t + \varphi_0\right\} \end{aligned} \tag{5.3}$$

where r_0, φ_0 are constants of integration.

Since this leading-order solution is always oscillatory, the behaviour of equation (1.1) is dominated by oscillatory motion far from the origin. Higher order terms in $\tilde{\varepsilon}$ in this regular perturbation would determine whether nearly-circular trajectories spiral out to infinity, move inwards to a stable solution, or lie on a large limit cycle. We will not extend this regular perturbation to examine these higher order terms, but instead use the above result to apply an averaging method.

(b) Large unstable limit cycle

Substitution of $A(t) = r(t)\exp\{i\Theta(t)\}$ into (1.1) yields differential equations of the form $dr/dt = l_1(r,\Theta)$, $d\Theta/dt = l_2(r,\Theta)$. We can average out the oscillatory behaviour by applying the average operator $\langle\ \rangle \equiv \frac{1}{2\pi}\int_0^{2\pi}(\ )\ d\Theta$ to the right-hand side of each differential equation. This gives

$$\left\langle \frac{dr}{dt} \right\rangle = -\mu r + Nr^3, \quad \left\langle \frac{d\Theta}{dt} \right\rangle = \Omega + \beta r^2 - hr^4 \tag{5.4}$$

provided $\langle d\Theta/dt \rangle >> \langle dr/dt \rangle$ (otherwise the trajectories are not nearly-circular). Therefore, if $r^2 < \frac{\mu}{N}$, this 'dominant' behaviour tends towards zero as t tends towards infinity and the trajectory will spiral inwards towards some stable solution (with the terms here averaged out eventually becoming important). If $r^2 > \frac{\mu}{N}$ then (5.4) gives a trajectory which spirals out towards infinity. Therefore the unstable limit cycle will be near to the circle $r^2 = \frac{\mu}{N}$. (In fact, if $r^2 > \frac{\mu}{N}$, the total dissipation in the system is negative and our model is physically unrealistic: see section 7).

In Figures 3(a) and 3(b) the large unstable limit cycle can be seen. This section predicts that its average radius will be $\left(\frac{\mu}{N}\right)^{1/2} \approx 2.398$. It can be seen that the vertical height of the unstable limit cycles in Figure 3 is approximately 5.2, while the horizontal width is approximately 3.8. These average out to 4.5, giving an approximate average radius of 2.25. Our estimate is therefore reasonably accurate. Improvements could be made, but do not seem worthwhile, because of the breakdown of the model at such large amplitudes.

6. Global bifurcations

Here we further discuss two global bifurcations briefly described in section 2, exemplified by the points C, D and G, H on Figure 1. The first of these is a saddle-connection bifurcation as described in section 6.1 of Guckenheimer & Holmes (1983).

Their theorem (6.1.1) can be applied here to show that the limit cycle destroyed in going from point C to D is stable. It is necessary to show that at the homoclinic bifurcation $\frac{\partial \dot{p}}{\partial p}+\frac{\partial \dot{q}}{\partial q}<0$ (evaluated at the hyperbolic saddle point associated with the homoclinic orbit), where $A=p+iq$. A straight-forward calculation gives

$$\frac{\partial \dot{p}}{\partial p}+\frac{\partial \dot{q}}{\partial q}=-2\mu+4N\left(p^2+q^2\right)=-2\left(\mu-2N|A|^2\right). \tag{6.1}$$

It is difficult to evaluate this expression at the hyperbolic saddle point in general because there is no explicit formula for the saddle and $|A|$ must be evaluated numerically (see Chapter III). In Figure 2(c), it can be seen that $|A|\approx 1.42$ for the saddle point. The right-hand side of (6.1) is then -0.607 and so negative, confirming that the limit cycle destroyed in the bifurcation is stable in this case.

We will now examine these global bifurcations using Melnikov's method (see for example Guckenheimer & Holmes 1983). It is necessary to have the equations in the form $\dot{x}=f(x)+\varepsilon g(x)$ where $\dot{x}=f(x)$ has a homoclinic orbit and $\varepsilon g(x)$ forms a small perturbation to it. It is easier if f is Hamiltonian, so we will examine the equation

$$\frac{dA}{dt}=i\Omega A+iFA^*+i\beta|A|^2A+\hat{\varepsilon}\left(-\mu A+N|A|^2A+iF\Gamma\left(A^3+3|A|^2A^*\right)-ih|A|^4A\right). \tag{6.2}$$

This imposes the additional assumption that the linear damping term is small, replacing μ with $\hat{\varepsilon}\mu$, where $\hat{\varepsilon}$ is a small parameter: the leading-order terms are then conservative. Firstly, it is necessary to locate the homoclinic orbits in the leading-order equation (i.e. for $\hat{\varepsilon}=0$). Miles (1984) showed that this equation has three different types of global behaviour: (i) for $F^2>\Omega^2$ the origin is a saddle and there are two homoclinic orbits (Figure 7a), (ii) for $F^2<\Omega^2$ and $\Omega<0$ the origin is a centre and there are heteroclinic orbits (Figure 7b), (iii) for $F^2<\Omega^2$ and $\Omega>0$ the origin is a centre and the phase diagram consists of concentric circles around the origin. The homoclinic orbits in Figure 7(a) resemble the global bifurcation that occurs when the two stable limit cycles collide forming a single larger stable limit cycle between points G and H on Figure 1. The heteroclinic orbits in Figure 7(b) correspond to a global bifurcation below the neutral stability curve, which could correspond to the bifurcation

that occurs between points C and D on Figure 1, or the bifurcation between points D and J. We consider the two cases separately.

(i) Above the neutral curve

Here there are two centres at $p=0,\ q=\pm\left(\frac{F-\Omega}{\beta}\right)^{1/2}$, where $A=p+iq$. The Hamiltonian is

$$H=-\frac{\Omega}{2}\left(p^2+q^2\right)-\frac{F}{2}\left(p^2-q^2\right)-\frac{\beta}{4}\left(p^2+q^2\right)^2 \tag{6.3}$$

so each homoclinic orbit is given by $H=0$.

The Melnikov function is

$$M=\int_{-\infty}^{\infty}\left\{f_1[\chi(t)]g_2[\chi(t)]-f_2[\chi(t)]g_1[\chi(t)]\right\}dt, \tag{6.4}$$

where

$$\begin{aligned} f_1&=-\Omega q+Fq-\beta q\left(p^2+q^2\right),\\ f_2&=\Omega p+Fp+\beta p\left(p^2+q^2\right),\\ g_1&=-\mu p+Np\left(p^2+q^2\right)+4F\Gamma q^3+hq\left(p^2+q^2\right)^2,\\ g_2&=-\mu q+Nq\left(p^2+q^2\right)+4F\Gamma p^3-hp\left(p^2+q^2\right)^2 \end{aligned} \tag{6.5}$$

and $\chi(t)$ is one of the two homoclinic orbits. The function M will have zeros at parameter values corresponding to homoclinic bifurcations.

From Guckenheimer and Holmes (1983 equation 4.5.15) we have

$$M=\int_{\chi}\left(g_2dp-g_1dq\right)=2\iint_{\text{int }\chi}\left(\mu-2N\left(p^2+q^2\right)\right)dpdq \tag{6.6}$$

using Green's theorem, where int χ denotes the region enclosed by χ.

Changing to polar coordinates $p=r\cos\theta,\ q=r\sin\theta$, the homoclinic orbit χ becomes

$$r^2=-\frac{2}{\beta}(\Omega+F\cos 2\theta) \tag{6.7}$$

since here $H=0$. The homoclinic orbit passes through $p=0,\ q^2=\frac{2}{\beta}(F-\Omega)$ which is equivalent to $r^2=\frac{2}{\beta}(F-\Omega),\ \theta=\frac{\pi}{2}$, while the homoclinic orbit leaves the saddle at

$r=0,\ \theta=\frac{1}{2}\arccos\left(-\frac{\Omega}{F}\right)$. We can use these two points on the homoclinic orbit to arrive at

$$M=4\int_{\Psi}^{\frac{\pi}{2}}\int_{0}^{\Xi(\theta)}\left(\mu-2Nr^2\right)rdrd\theta$$
$$\text{with } \Xi(\theta)\equiv\left(-\frac{2}{\beta}(\Omega+F\cos 2\theta)\right)^{1/2},\ \Psi\equiv\frac{1}{2}\arccos\left(-\frac{\Omega}{F}\right). \tag{6.8}$$

This gives

$$M=\frac{2}{\beta}\left\{\left(\mu+\frac{3N\Omega}{\beta}\right)\left(F^2-\Omega^2\right)^{1/2}-\left(\mu\Omega+\frac{2N\Omega^2}{\beta}+\frac{NF^2}{\beta}\right)\arccos\left(\frac{\Omega}{F}\right)\right\} \tag{6.9}$$

for the homoclinic cycle in the upper half of the plane. The result is identical for the other cycle.

Remarkably, (6.9) is independent of h and Γ. Also, note that the result is only valid when the origin is a saddle (i.e. when $F^2>\Omega^2$), and that $M=0$ when $F=\Omega$, as it should. We will discuss (6.9) further at the end of the following subsection.

(ii) Below the neutral curve

Here there are centres at the origin and $p=0,\ q=\pm\left(\frac{F-\Omega}{\beta}\right)^{1/2}$ and saddles at $p=\pm\left(\frac{-(\Omega+F)}{\beta}\right)^{1/2},\ q=0$. The heteroclinic orbits are given by $H=\frac{(\Omega+F)^2}{4\beta}$.

If we label the four separatrices $\zeta_i(t), i=1,..4$, with $\zeta_1(t)$ denoting the uppermost separatrix and $\zeta_4(t)$ the lowermost separatrix, as in Figure 7(b), where each portion $\zeta_i(t)$ is transversed anticlockwise about the origin, then the four heteroclinic orbits are given by $\zeta_1-\zeta_2, -\zeta_3+\zeta_4, \zeta_1+\zeta_4$ and $-\zeta_2-\zeta_3$. We now derive the Melnikov function for each of these.

Transforming to polar coordinates gives

$$r^2=\frac{-(\Omega+F\cos 2\theta)\pm\left(F^2\left(\cos^2 2\theta-1\right)+2\Omega F(\cos 2\theta-1)\right)^{1/2}}{\beta}\equiv\xi_{\pm}^2 \tag{6.10}$$

for the heteroclinic orbits. At the two saddles, $r^2=-\frac{\Omega+F}{\beta},\theta=0,\pi$. Therefore

$$M(\zeta_1-\zeta_2)=2\int_0^{\pi}\int_{\xi_-}^{\xi_+}(\mu-2Nr^2)rdrd\theta, \tag{6.11}$$

using the same method as in the previous subsection.

Therefore

$$\begin{aligned} M(\zeta_1-\zeta_2)&=\frac{2}{\beta}\int_0^{\pi}\left(\mu+\frac{2N}{\beta}(\Omega+F\cos 2\theta)\right)\varphi(\theta)d\theta, \\ \text{where } \varphi(\theta)&\equiv\left(F^2(\cos^2 2\theta-1)+2\Omega F(\cos 2\theta-1)\right)^{1/2}, \end{aligned} \tag{6.12}$$

which can be solved numerically. By symmetry, $M(-\zeta_3+\zeta_4)=-M(\zeta_1-\zeta_2)$, so these global bifurcations, having $M=0$, occur simultaneously as expected. The other two orbits give

$$\begin{aligned} M(-\zeta_2-\zeta_3)&=4\int_0^{\pi}\int_0^{\xi_-}(\mu-2Nr^2)rdrd\theta \\ &=-\frac{2\pi\Omega}{\beta}\left(\mu+\frac{N\Omega}{\beta}-\frac{2NF}{\beta}\right)-\frac{2}{\beta}\int_0^{\pi}\left(\mu-\frac{2N}{\beta}(\Omega+F\cos 2\theta)\right)\varphi(\theta)d\theta \end{aligned} \tag{6.13}$$

and

$$\begin{aligned} M(\zeta_1+\zeta_4)&=4\int_0^{\pi}\int_0^{\xi_+}(\mu-2Nr^2)rdrd\theta \\ &=-\frac{2\pi\Omega}{\beta}\left(\mu+\frac{N\Omega}{\beta}-\frac{2NF}{\beta}\right)+\frac{2}{\beta}\int_0^{\pi}\left(\mu+\frac{2N}{\beta}(\Omega+F\cos 2\theta)\right)\varphi(\theta)d\theta \end{aligned} \tag{6.14}$$

which also have to be investigated numerically. Again, these expressions for the Melnikov function are independent of h and Γ.

We find solutions of $M=0$ numerically as follows. We choose $\beta=\mu=1, N=0.1$ (these values are purely for illustration: it is impossible to choose values corresponding to an existing experiment since we have made the assumption that the linear damping term is so small) and find $F=F(\Omega)$ for which $M=0$ for a range of Ω. Figure 8 shows the homoclinic bifurcation curves resulting from (6.9), (6.12), (6.13) and (6.14). The neutral curve is $F^2=\Omega^2$ (with zero damping) and the Hopf bifurcation curve was found from equation (3.8) using $\beta=\mu=1, N=0.1$ and $h=\Gamma=0$. The dashed line above the neutral curve results from equation (6.9). The three (unlabelled) curves below the neutral curve result from the Melnikov calculations from this subsection: with (6.14) corresponding to the uppermost (dotted-dashed) curve, (6.12)

giving the (dotted-dashed) curve below it and (6.13) giving the (dashed) curve just above the horizontal axis.

It can be seen that three of the four homoclinic bifurcation curves meet up on the neutral curve at a single point. Examination of various time-dependent solutions (produced by a Runge-Kutta scheme) reveals that the curves produced by (6.12) and (6.14) are equivalent to the two homoclinic bifurcation curves below the neutral curve in Figure 1. Therefore, below the neutral curve, stable limit cycles exist between the Hopf boundary and the boundary given by (6.12). The curve produced by (6.13) is found to be equivalent to the lower hysteresis boundary, with stable stationary points existing only above this boundary. Above the neutral curve, stable limit cycles exist between the Hopf curve and the dashed homoclinic boundary. Above the dashed homoclinic boundary all solutions diverge to infinity. The only qualitative difference between Figure 1 and Figure 8 is that there is not a second homoclinic boundary above the neutral curve in Figure 8. In fact, the two homoclinic boundaries above the neutral curve in Figure 1 are found to coincide in Figure 8. Therefore, the region of period-doubled limit cycles (see Figure 4(b)) degenerates, in Figure 8, onto the homoclinic boundary itself.

A quantitative comparison is not appropriate since it was necessary to assume in this section that the linear damping is very weak, which is not the case in Figure 1. Nevertheless, the clear qualitative similarities between the present analytical results for weak damping and our computations in Figure 1 have helped explain the latter.

7. Discussion and Conclusions

Miles (1993) asserts that if $\mu - 2N|A|^2 < 0$ for all $|A|$ then limit cycles are impossible. This is so under the scaling assumptions of Miles (1984, 1993, 1994), namely that the coefficient of cubic damping N is much smaller than the coefficient of linear damping μ, and that the real and imaginary parts of A are *O(1)*. These scalings

were also used at first in Chapter III, but later abandoned in favour of (1.1). The theory is certainly valid with the $\tilde{\varepsilon}$ scaling: but must be regarded as an approximate model otherwise. Yet the experimental hysteresis results described in Chapter II and Craik & Armitage (1995) support the model equation (1.1) stated here (see Chapter III) and this certainly exhibits limit cycles. (However, the growth to infinity at sufficiently large amplitudes is unphysical because the total damping $\mu - N|A|^2 < 0$).

For (1.1) to be valid, it is necessary that the terms in the equation are larger than those terms neglected in its derivation. We will now evaluate the size of the terms in (1.1) at parameter values which correspond to the stable limit cycle of Figure 6, and we estimate the magnitude of the largest terms neglected from (1.1). These parameter values are

$$\mu = 1, F = 0.7, \Omega = -1.5, \beta = 0.4179, N = 0.1739, h = -0.09726, \Gamma = 0.02775 \qquad (7.1)$$

and the maximum value of $|A|^2$ on the limit cycle is approximately $1.75^2 + 0.7^2 = 3.5525$. The terms in equation (1.1) are therefore

$$\begin{aligned} &\mu = 1,\ \Omega = -1.5,\ F = 0.7,\ \beta|A|^2 = 1.485, \\ &N|A|^2 = 0.6178,\ F\Gamma|A|^2 = 0.09858,\ h|A|^4 = -1.2274, \end{aligned} \qquad (7.2)$$

where the numbers represent the largest numerical values of the terms on the limit cycle.

The three largest terms neglected in the derivation of (1.1) will be of the form

$$D|A|^4 A,\ iF\gamma|A|^4 A^*,\ iH|A|^6 A \qquad (7.3)$$

plus various other fifth-order forcing terms of the same magnitude. The three coefficients D, γ and H are unknown but will be *O(1)* quantities multiplied by the square of the scaling parameter used in the derivation of (1.1) (see Miles 1984, 1993, 1994, Umeki 1991). In Chapter III, we estimated the scaling parameter $\tilde{\varepsilon}^2$ to be *0.047* for the experimental depth of 1.3cm: then $(D, \gamma, H) = 0.047^2(\hat{D}, \hat{\gamma}, \hat{H})$ where $\hat{D}, \hat{\gamma}, \hat{H}$ are undetermined *O(1)* quantities. Therefore the three largest neglected terms will be

$$D|A|^4 = 0.0279\hat{D},\ F\gamma|A|^4 = 0.01951\hat{\gamma},\ H|A|^6 = 0.09904\hat{H}. \qquad (7.4)$$

On comparing these values to those in (7.2), it appears that these terms are likely to be acceptably small compared to those retained. The exception is the cubic forcing term in

$F\Gamma$, which may well also be negligible in this case (supporting the $\Gamma = 0$ approximation in section 4).

We have considered the structure of solutions of equation (1.1), which models Faraday waves. We have discussed the Hopf bifurcation that causes the family of stable (smaller) limit cycles to appear. We have estimated their size and analytically calculated their shape in excellent agreement with our computations. We have also demonstrated that the Hopf bifurcation gives rise only to stable limit cycles in the parameter ranges studied here. Our analytical result (3.8) giving the relationship between forcing and frequency detuning at the Hopf bifurcation is in precise agreement with our numerical computations. We have examined the large unstable limit cycle by using a regular perturbation expansion and an averaging method, which succesfully predicts its approximate size. We have used Melnikov's method in the weak damping limit to describe the homoclinic bifurcations that occur in (1.1): this gives a greater qualitative understanding and is broadly in line with our computations for stronger damping.

It is certain that stable single-mode limit cycles exist for appropriate parameter values, though they have not yet been observed experimentally. From this Chapter, it is unclear whether interference from neighbouring modes might disrupt the single mode limit cycle; however, in Chapter VI we find a region in the forcing-frequency plane in which the limit cycles are stable to sideband perturbations. The best chance of observing the stable limit cycles would probably be for parameter values not too far beyond the Hopf bifurcation. [3]

[3] There has recently been a (tentative) experimental sighting of a stable single-mode limit cycle by Sterratt (1995), though the results are preliminary.

Figure 1. Parameter space diagram showing the locations of Hopf and homoclinic bifurcations for $\mu = 1, \beta = 0.4179, N = 0.1739, h = -0.09726, \Gamma = 0.02775$. The coordinates of the points are: A (-1.2,0.8), B (-1.4, 0.8), C (-1.5, 0.8), D (-1.7, 0.8), E (-0.75, 1.4), F (-0.9, 1.3), G (-1.2, 1.8), H (-1.3, 1.8), I (-1.5, 1.9) and J (-1.6, 1.9).

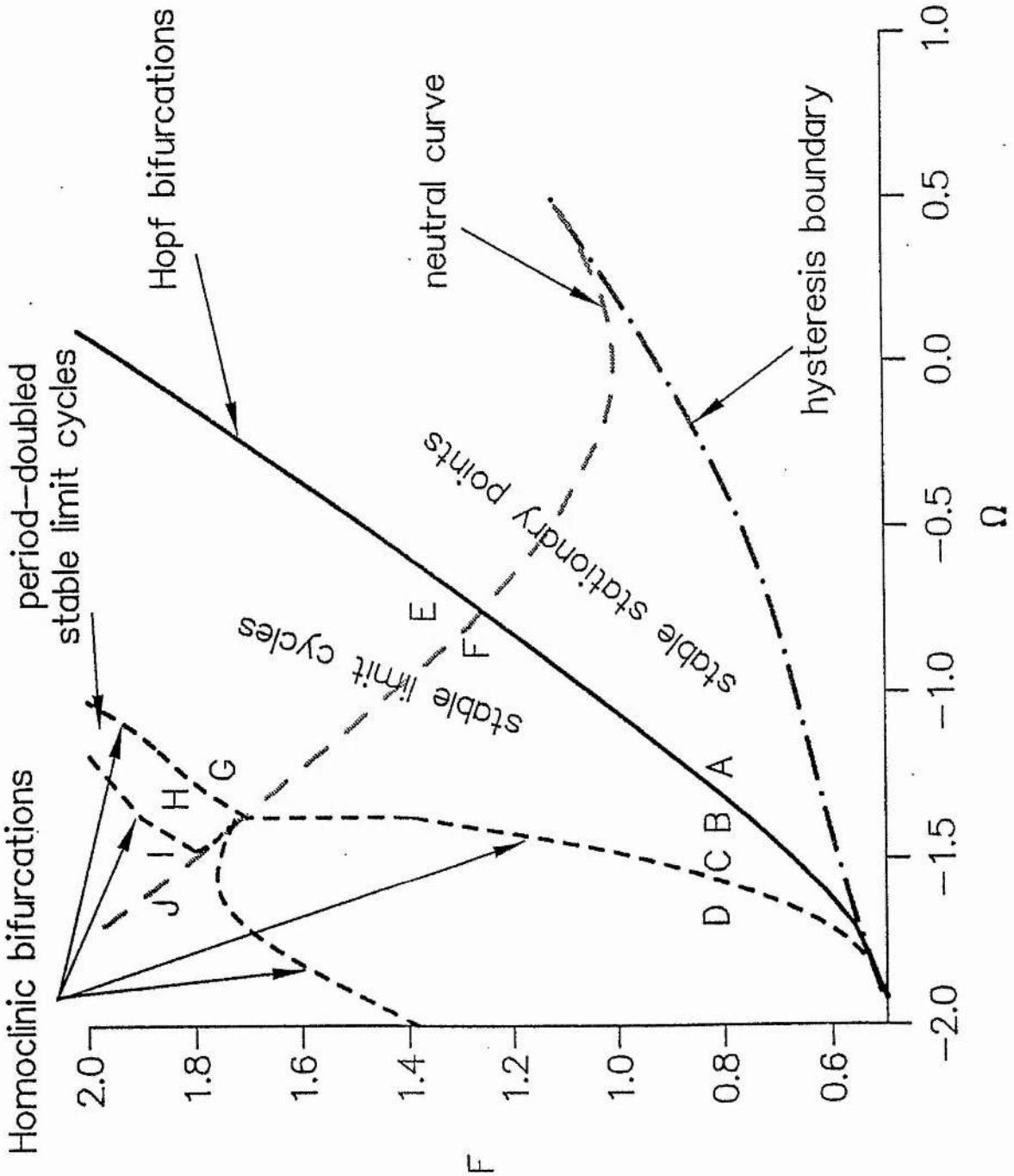

Figure 2. The phase plane for points A, B, C and D on Figure 1, showing a Hopf bifurcation followed by a homoclinic bifurcation.

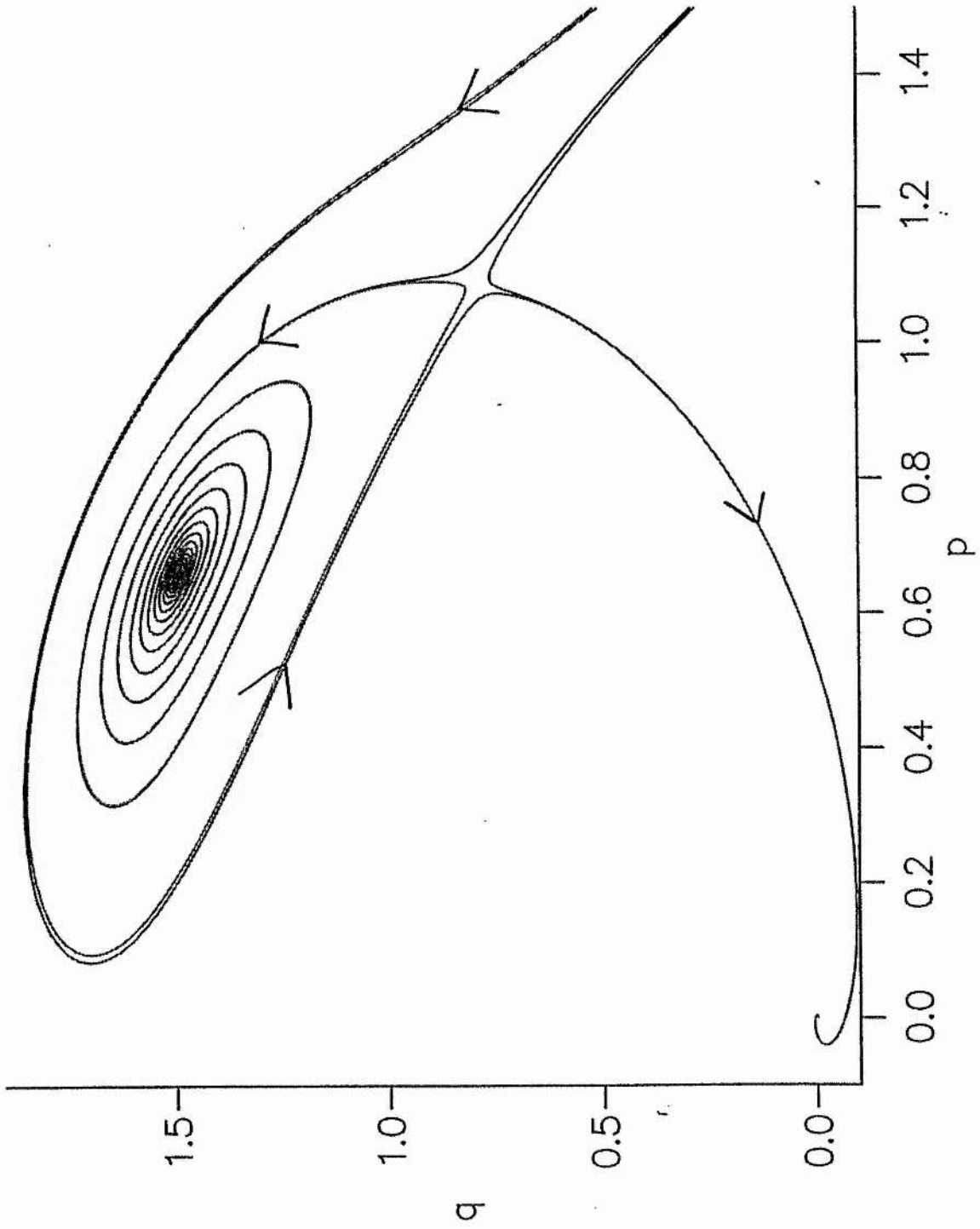

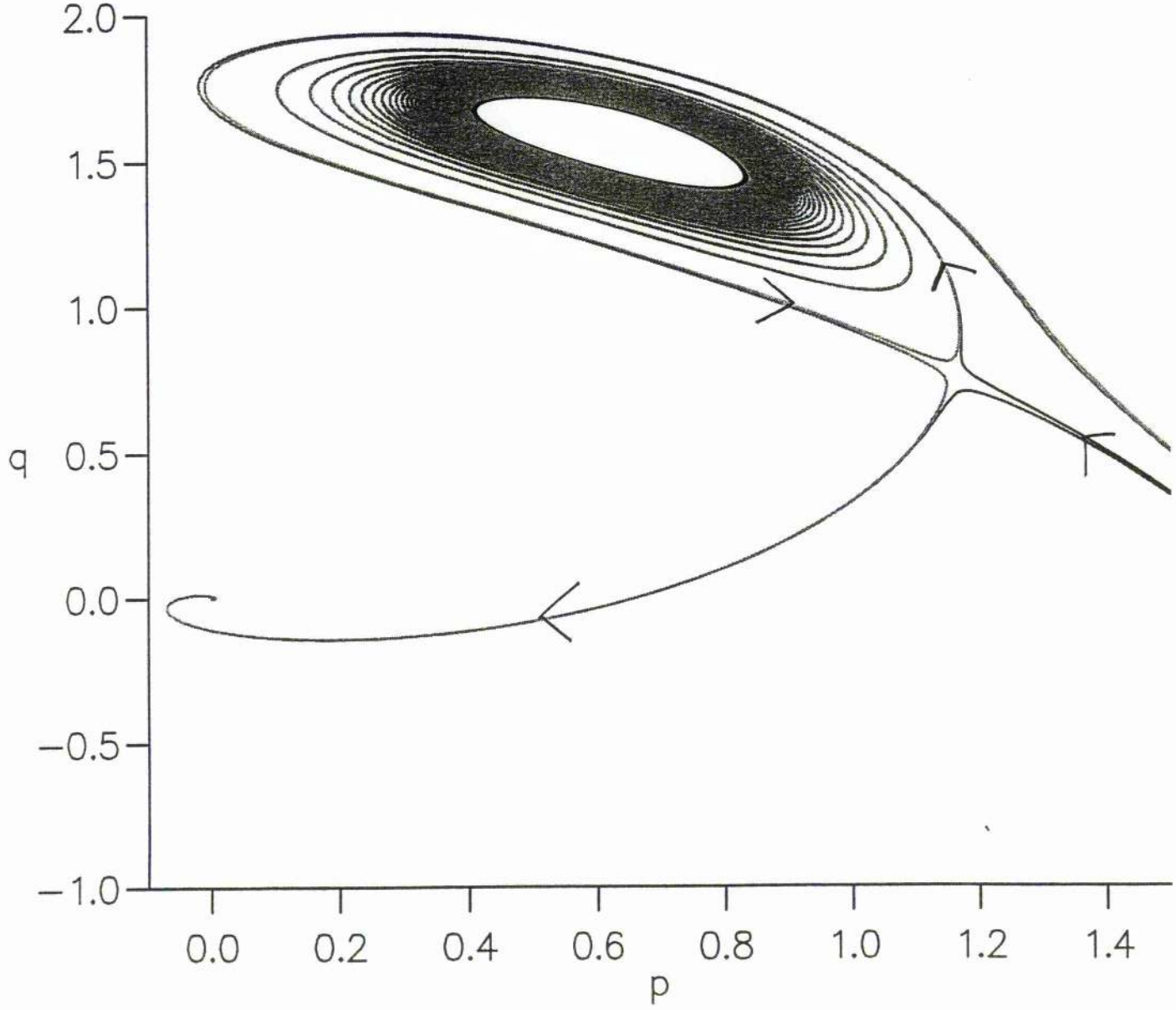
2.0
1.5
1.0
0.5
0.0
−0.5
−1.0
q
0.0
0.2
0.4
0.6
0.8
1.0
1.2
1.4
p

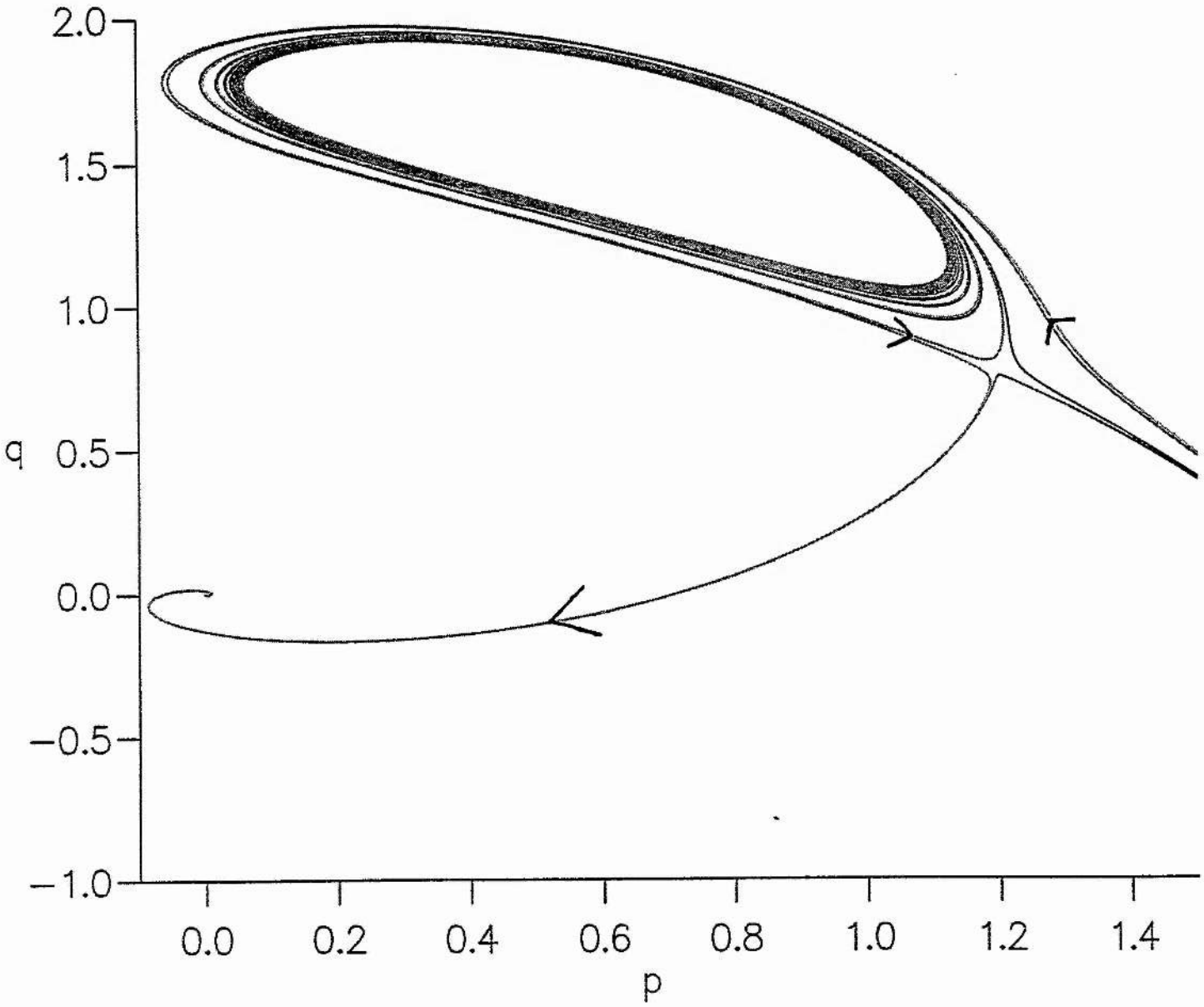
2.0
1.5
1.0
q 0.5
0.0
−0.5
−1.0
0.0
0.2
0.4
0.6
0.8
1.0
1.2
1.4
p

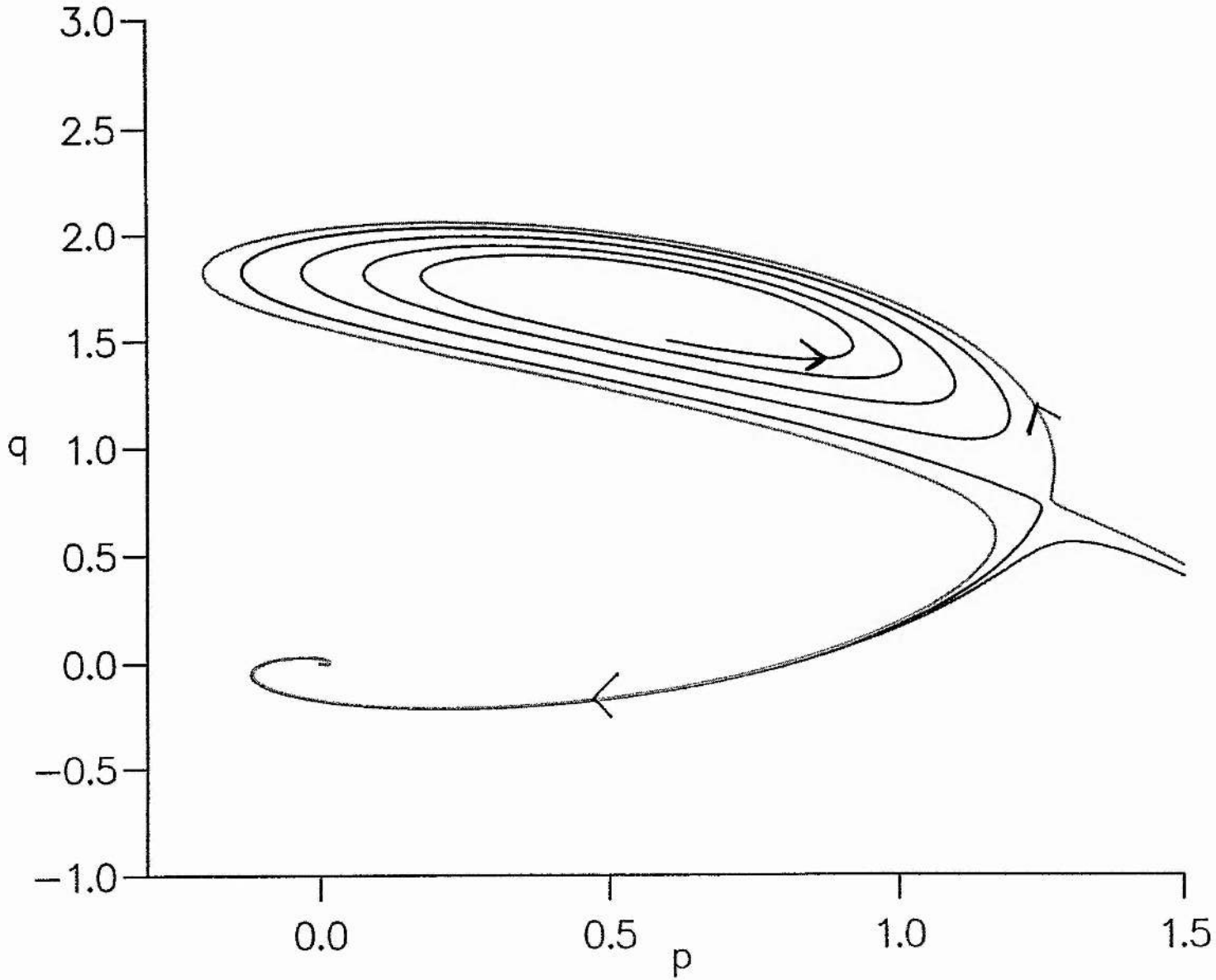
3.0
2.5
2.0
1.5
1.0
0.5
0.0
−0.5
−1.0
q
0.0
0.5
1.0
1.5
p

Figure 3. The phase plane for points E and F on Figure 1, showing a change of stability of the origin. The large unstable limit cycle is also shown. (Crosses denote saddles and a dot denotes a sink).

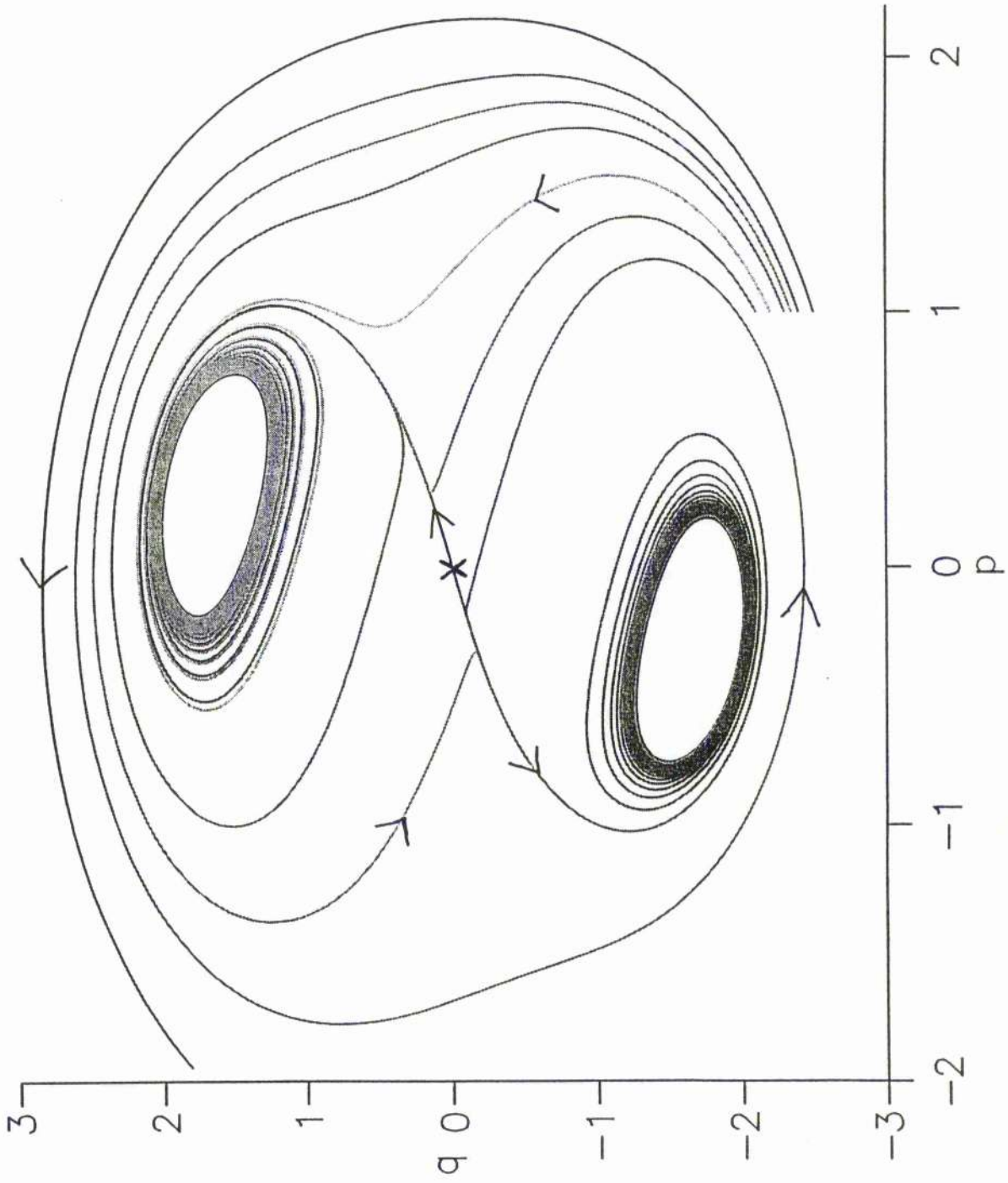

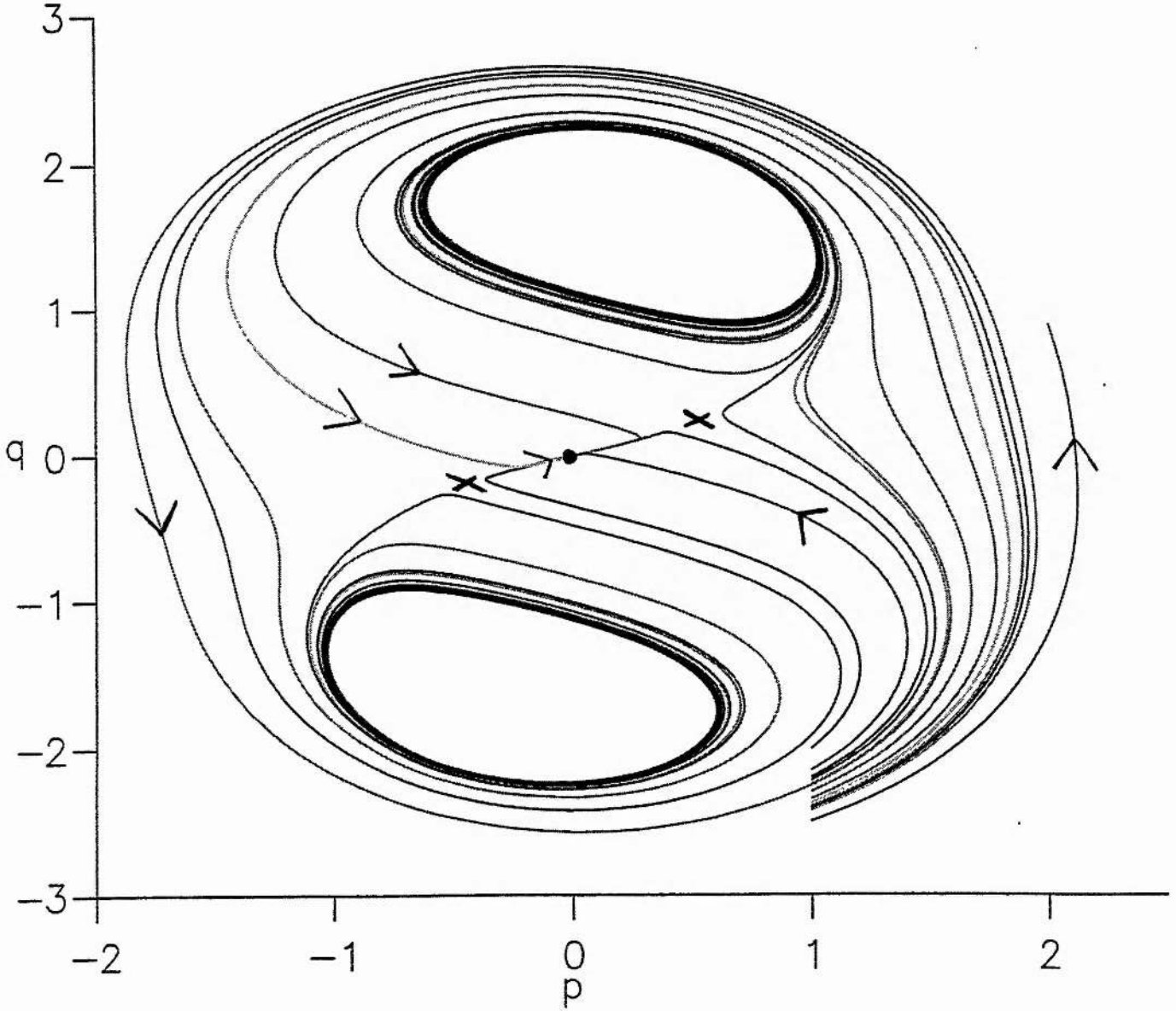
3
2
1
0
−1
−2
−3
q
−2
−1
0
1
2
p

Figure 4. The phase plane for points G, H, I and J on Figure 1, showing two limit cycles colliding to form a single limit cycle and then touching the outer unstable limit cycle, before undergoing yet another homoclinic bifurcation. (Crosses denote saddles and a dot denotes a sink).

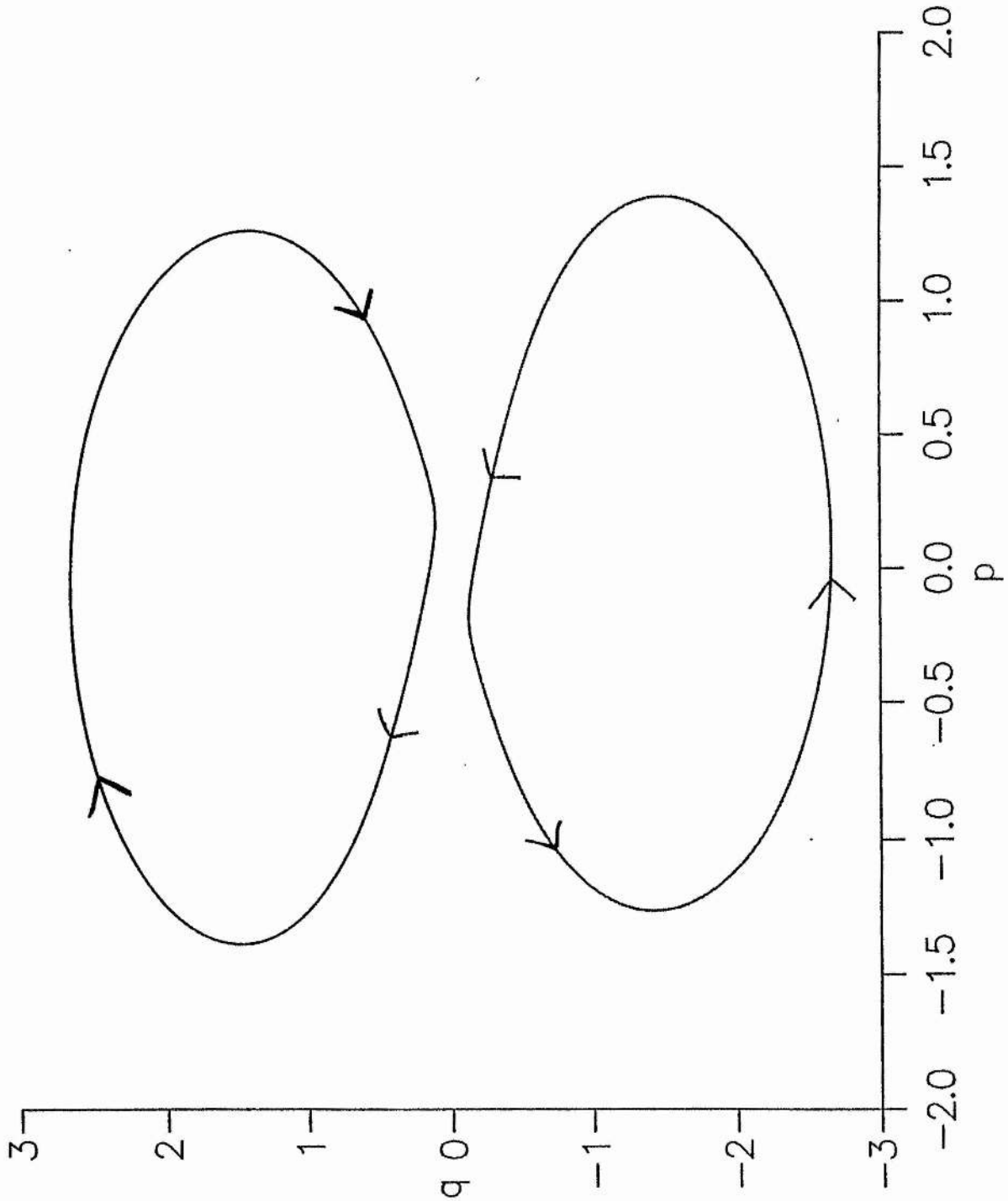

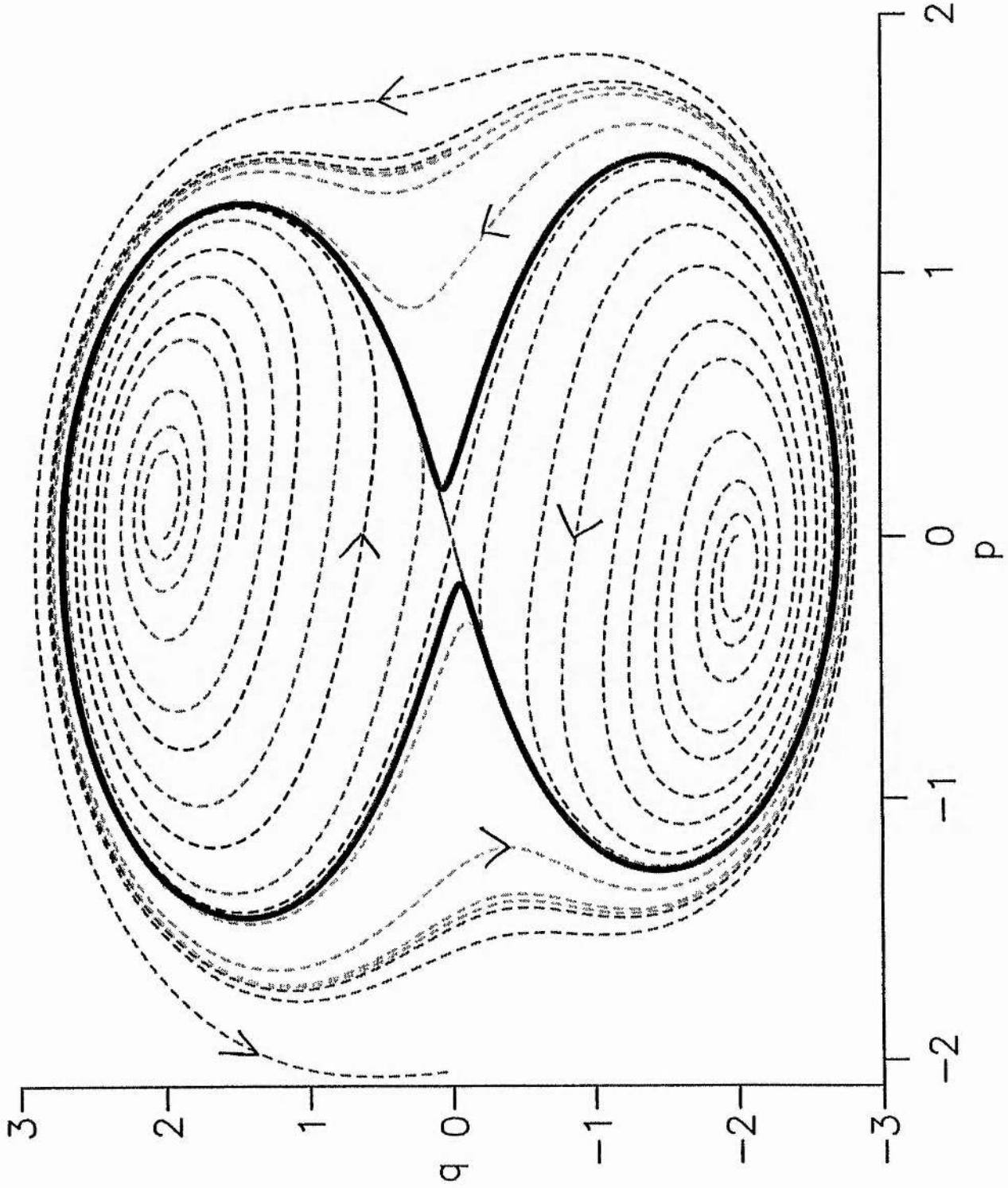
3
2
1
q 0
−1
−2
−3
−2
−1
0
1
2
p

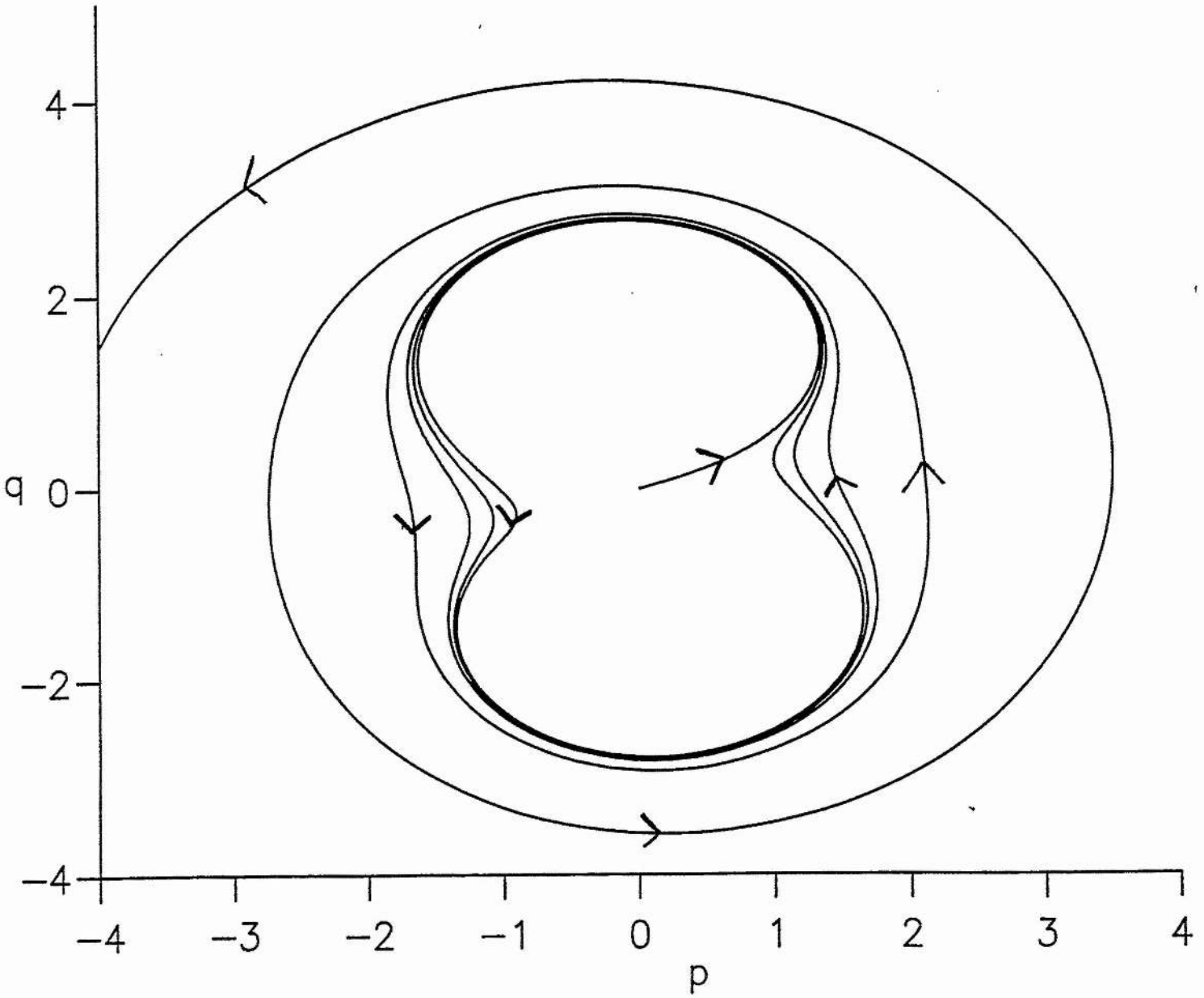

[76]

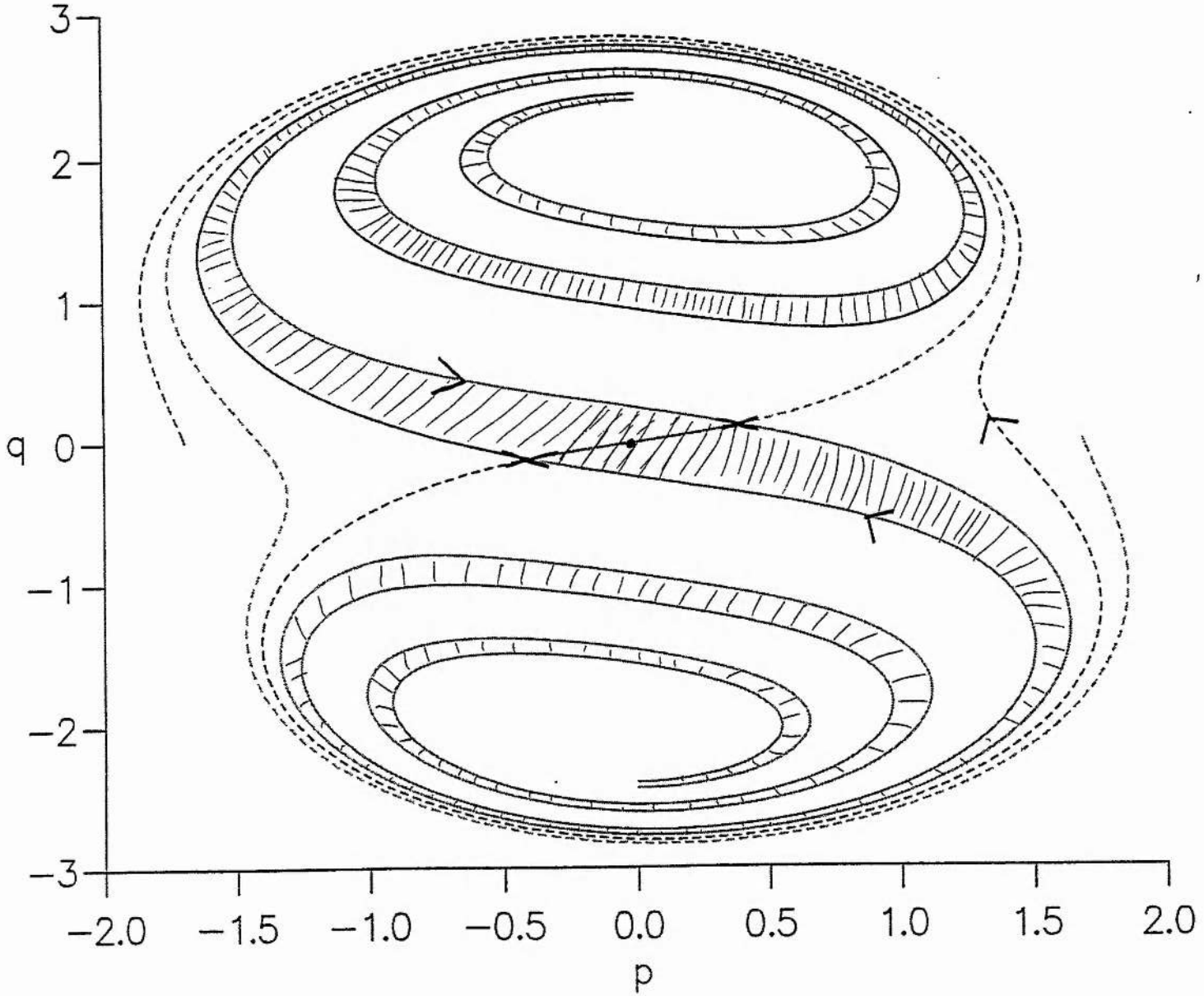
3
2
1
q 0
−1
−2
−3
−2.0
−1.5
−1.0
−0.5
0.0
0.5
1.0
1.5
2.0
p

Figure 5. The variation of $c_i (i = 1,..,4)$ with N, h and Γ for $\beta = \mu = 1, \Omega_{bif} = -1$.

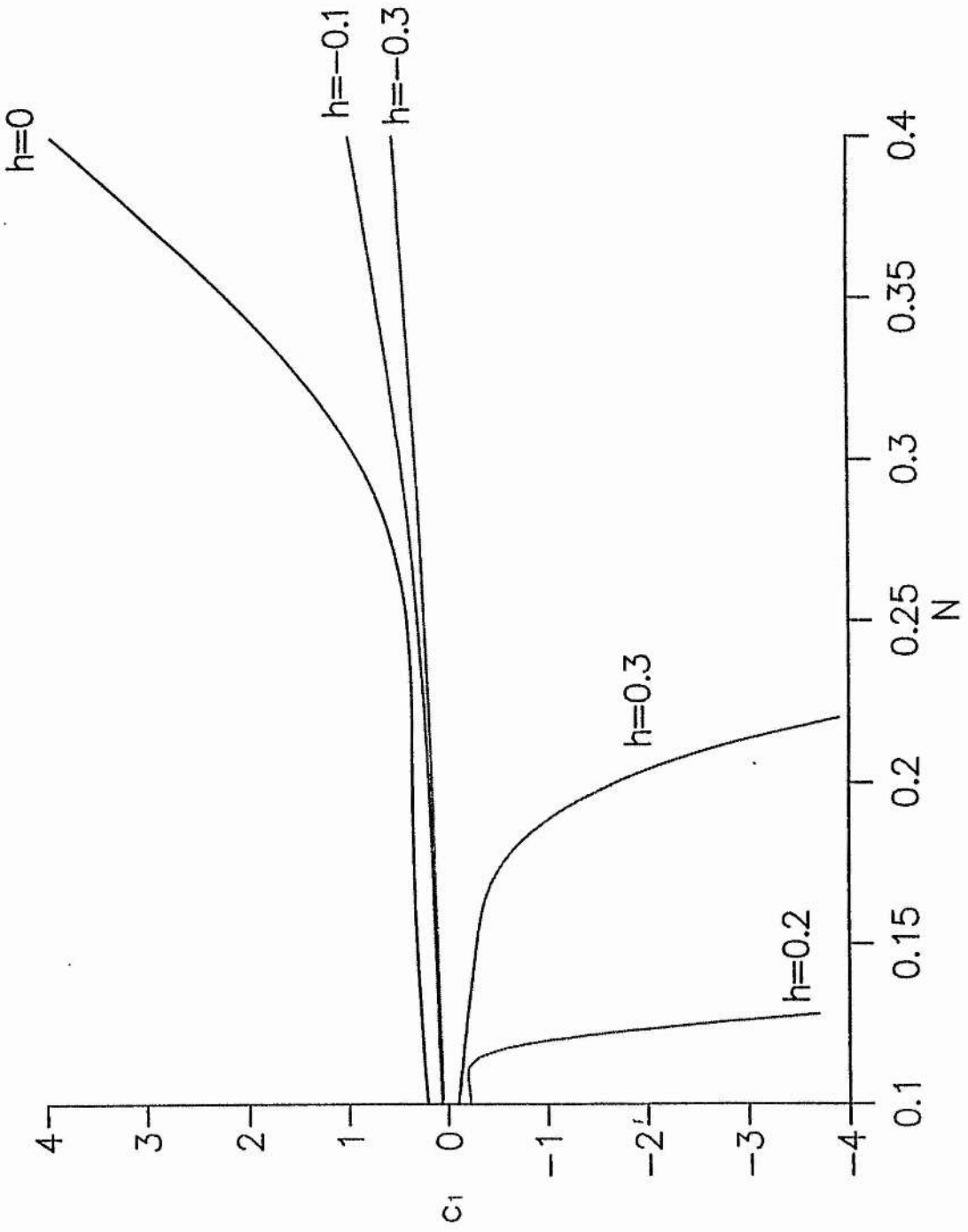

h=0
h=0.3
h=0.2
h=−0.1
h=−0.3
15
10
5
0
c_2
0.1
0.15
0.2
0.25
0.3
0.35
0.4
N

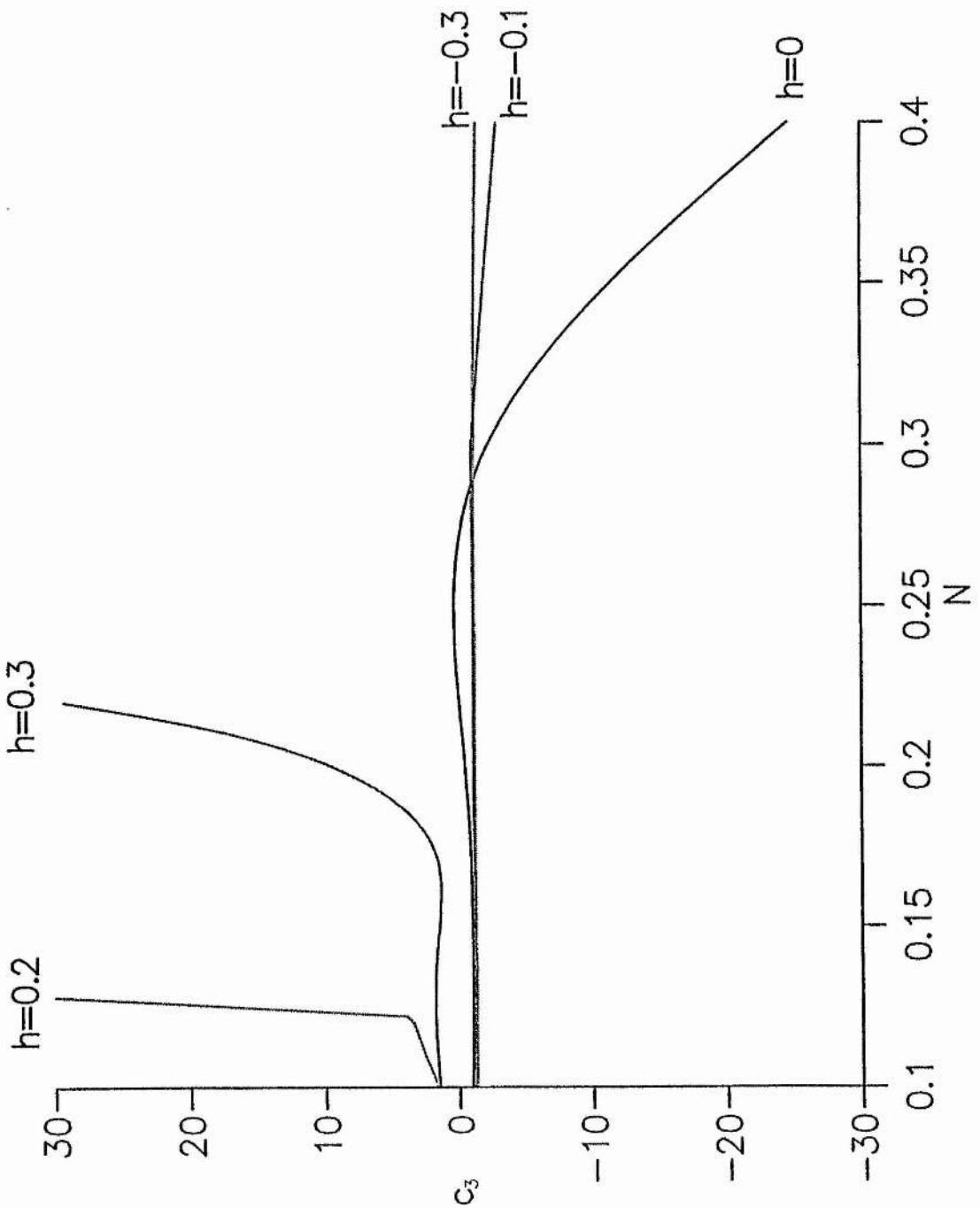
h=0.3
h=0.2
h=−0.3
h=−0.1
h=0
30
20
10
0
−10
−20
−30
c_3
0.1
0.15
0.2
0.25
0.3
0.35
0.4
N

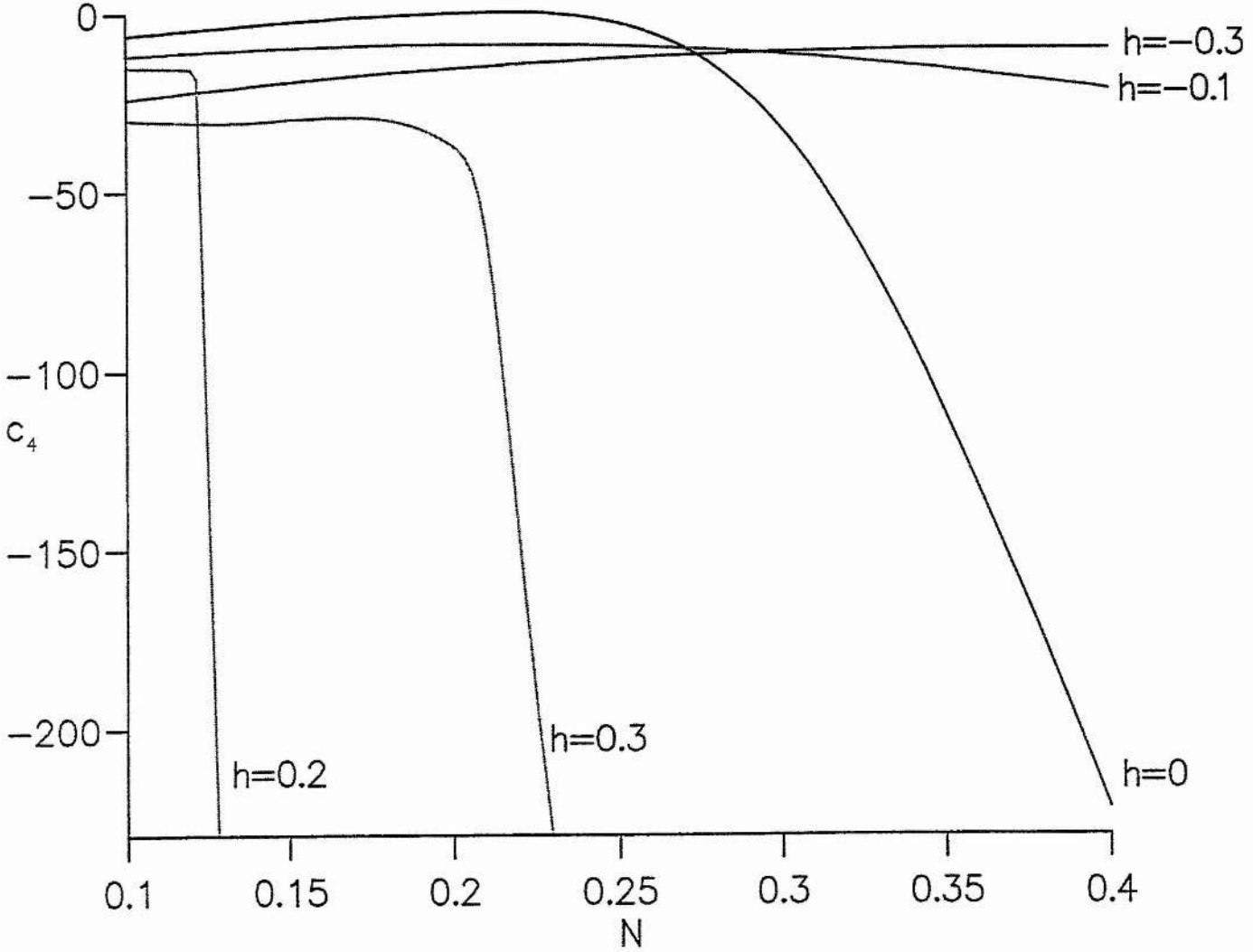
0
−50
−100
−150
−200
c_4
h=−0.3
h=−0.1
h=0
h=0.3
h=0.2
0.1
0.15
0.2
0.25
0.3
0.35
0.4
N

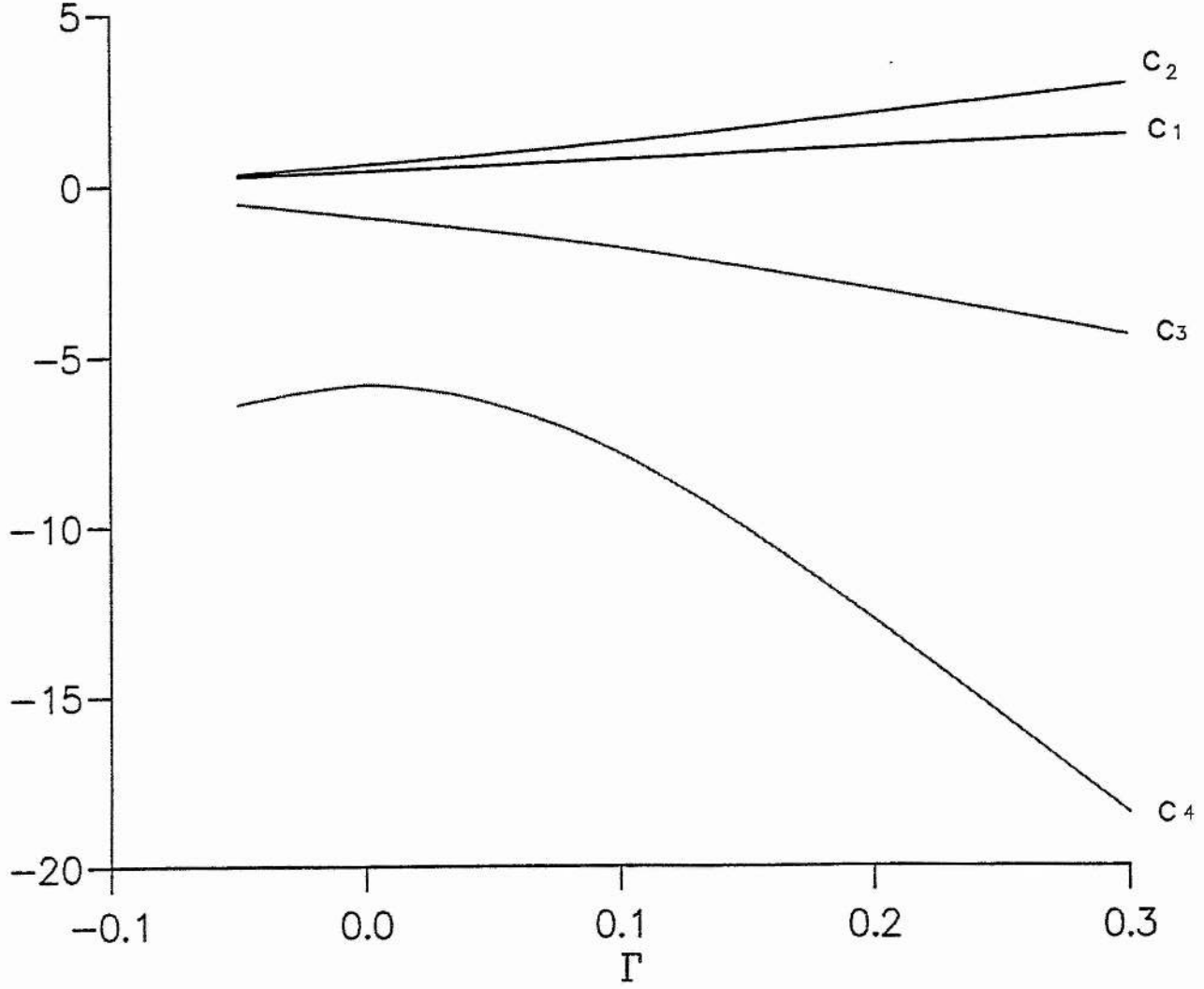
5
0
−5
−10
−15
−20
−0.1
0.0
0.1
0.2
0.3
Γ
c2
c1
c3
c4

Figure 6. Comparison of the analytical approximation for the limit cycle with the numerical results. Parameters as in Figure 1 and $\Omega = -1.5, F = 0.7$.

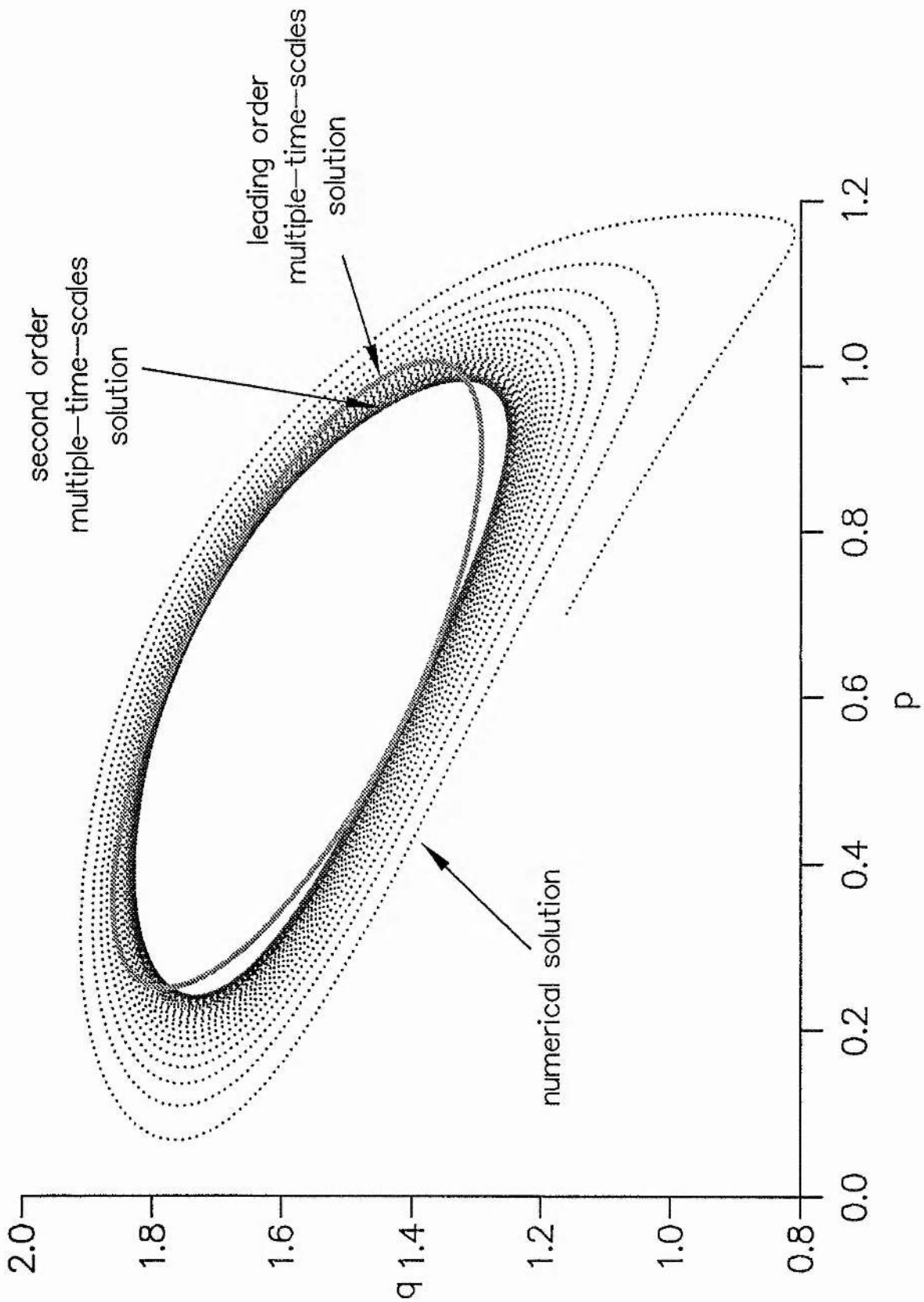

Figure 7. Homoclinic and heteroclinic orbits for equation (6.3). Parameters (a) $\beta = F = 1, \Omega = 0$ (b) $\beta = 1, \Omega = -1, F = 0.5$.

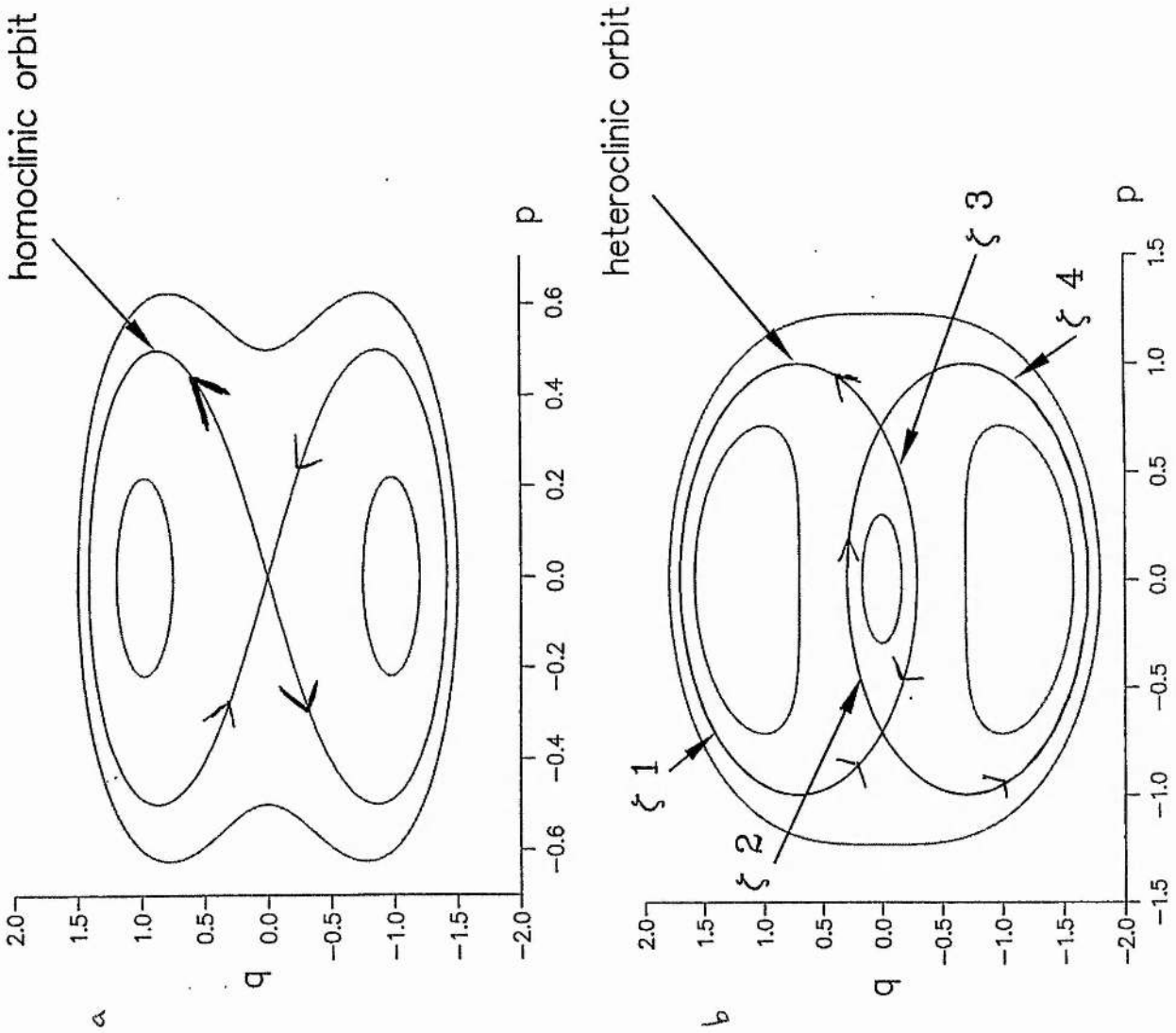

Figure 8. Homoclinic bifurcation curves predicted by Melnikov's method. The Hopf bifurcation curve predicted by (3.8) and the neutral curve $F^2 = \Omega^2$ are also shown. The parameters used were $\beta = \mu = 1, N = 0.1, h = \Gamma = 0$.

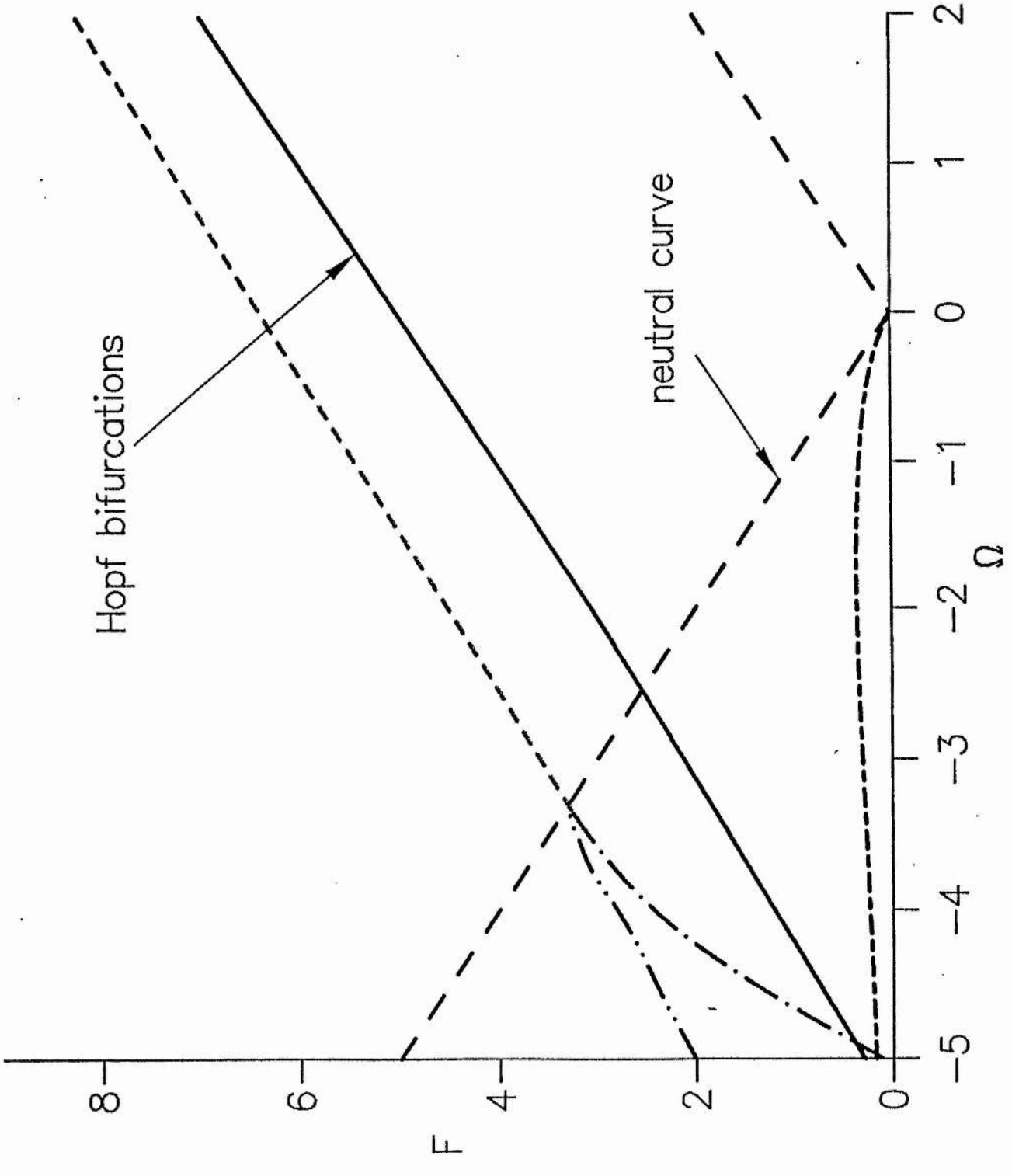

CHAPTER V

Theoretical determination of the damping coefficients

1. Introduction

The linear theory of the damping of surface waves in closed containers is described by Miles (1967). He calculated the linear damping coefficient for a liquid of finite depth due to (i) dissipation in the main body of the fluid, (ii) dissipation in the boundary layers at the sidewalls and at the bottom of the container, (iii) dissipation resulting from surface contamination, and (iv) capillary hysteresis resulting from the meniscus surrounding the free surface. He found that all effects contribute significantly to the damping and went on to show that there is good agreement between his theoretical results and experimental data. Keulegan (1959) considered the boundary layers at the sidewalls and at the bottom of the container.

Surface contamination due to the presence of a thin viscoelastic surface film creates a boundary layer at the surface which causes enhanced dissipation. Lamb (1895, 1932) and Levich (1941, 1962) carried out pioneering studies of surface contamination. Tempel & Riet (1965) calculated the linear damping due to a surface film on an unbounded body of water.

It is well known that a second-order mean velocity field in a boundary layer can drive a second-order mean velocity field in the bulk fluid (otherwise known as streaming: see Longuet-Higgins 1953). The effect of surface contamination on streaming for travelling waves has been studied by Dore (1972, 1975), Craik (1982) and Riley (1984), but (to our knowledge) the effect of surface contamination on streaming resulting from standing waves has not previously been studied.

In Chapter III, we derived a composite evolution equation for the amplitude of a single two-dimensional mode in a rectangular container, which here we rewrite as

$$\begin{aligned}\frac{dA}{dt} &= \varepsilon^2\omega\left\{-\frac{\mu}{2\pi\varepsilon^2}A + i\Omega A + iFA^* + i\Pi|A|^2A\right\}\\ &+\varepsilon^4\omega\left\{\frac{N}{2\pi\varepsilon^2}|A|^2A + iF\Gamma\left(A^3 + 3|A|^2A^*\right) - ih|A|^4A\right\}\end{aligned} \tag{1.1}$$

where * denotes complex conjugate, A is the time-dependent complex wave amplitude, ε is a small parameter (the same small parameter as the one used in Chapter III), ω is half the frequency of the forcing, F is the amplitude of the forcing, Ω is the frequency detuning from linear parametric resonance, μ and N are real linear and cubic damping coefficients, Π and h are real cubic and quintic conservative frequency shift coefficients and Γ is the real coefficient of cubic forcing. We here consider the values to be assigned to μ and N. Note that we have redefined μ and N from their form in equation (5.1) of Chapter III, so that they do not depend upon ε here: this accords with the notation of Miles (1967).

(i) The linear damping coefficient μ

The linear damping coefficient μ for a rectangular tank is calculated in Miles (1967) (Miles also determines μ in an arbitrary geometry) to be

$$\begin{aligned}\mu &= \frac{1}{2lB}(B+l)(2\nu\omega)^{1/2} + \frac{k}{2}\left(1-\frac{2d}{l}\right)(2\nu\omega)^{1/2}\operatorname{cosech}(2kd)\\ &+\frac{1}{4}k(C_r - C_i)(2\nu\omega)^{1/2}\coth(kd) + O(\nu),\end{aligned} \tag{1.2}$$

where l is the tank length, B is the width, ν is the kinematic viscosity, k is the wavenumber, d is the ambient water depth and C is a surface contamination parameter (C_r and C_i denote the real and imaginary parts of C). (Note that the first term in (1.2) results from the boundary layers at the sidewalls, the second term results from the boundary layer at the bottom of the container, and the third term represents the boundary layer at the surface.) Miles (1967) showed that, for gravity waves,

$$C \approx \frac{\xi}{\xi - 1 + i(1+\eta)}, \tag{1.3}$$

where ξ and η are dimensionless measures of the surface compressional modulus and solubility respectively, and η vanishes for an insoluble surfactant[4]. For an uncontaminated surface $C = \xi = 0$, and for an inextensible surface film $C = 1$, $\xi = \infty$. The surface boundary layer is therefore negligible for an uncontaminated surface. Note that capillary hysteresis is neglected in (1.2), though Miles also calculates this.

Figure 1 shows, for large depth d, the dependence of the coefficient of linear damping μ upon the surface contamination parameters: the compressional modulus ξ and the solubility η of the surface film. The other parameters are

$$l = 0.7,\ B = 0.025,\ \nu = 10^{-6}, \tag{1.4}$$

(in s.i. units) depth $d = \infty$ and wavenumber $k = 22\pi / l$. (Note that (1.4) corresponds to the experiments of Craik & Armitage 1995, described in Chapter II.) It can be seen that surface contamination has a large effect upon μ.

Figure 2 shows μ plotted against ambient water depth d, for parameter values (1.4) and $k = 22\pi / l$. Three lines are shown: one for the uncontaminated surface, one for the inextensible film (for which $\xi = \infty$), and one for the maximum linear damping attained when the surface compressional modulus $\xi = 2$ and the surfactant is insoluble. The crosses mark three points inferred from the experiments described in Chapter II. The three points were calculated by comparing the theoretical and experimental values of the r.m.s. acceleration required to destablize the flat surface at resonance (this calculation is carried out in Chapters III and VI). It can be seen that the experimental points lie between the uncontaminated surface line and the inextensible film line. (Note that in Chapters III and IV, the evolution equation was normalised, setting the linear

---

[4] Miles (1967) defines ξ and η as follows. As in Levich (1962), the surface tension γ is assumed to be uniquely specified by the superficial concentration of the film ϑ, and that the relaxation time for equilibrium between the material in the film and the dissolved material in the underlying liquid is negligible compared with $2\pi / \omega$. Small perturbations in γ, ϑ and the bulk concentration c are related according to $\nabla\gamma = \left(\frac{d\gamma}{d\vartheta}\right)_0 \nabla\left(\vartheta - \vartheta_0\right)$ and $\vartheta - \vartheta_0 = \left(\frac{d\gamma}{dc}\right)_0 \left(c - c_0\right)_{z=0}$. The surface compressional modulus and solubility can then be defined as $\xi = -\frac{\sqrt{2}k^2\vartheta_0}{\rho\sqrt{\nu\omega^3}}\left(\frac{d\gamma}{d\vartheta}\right)_0$ and $\eta = \sqrt{\frac{2\hat{D}}{\omega}}\left(\frac{d\vartheta}{dc}\right)_0^{-1}$ where ρ is the density and $\hat{D}$ is the bulk diffusion coefficient.

damping coefficient to unity; the experimental points show the values of the linear damping coefficient if this normalisation is not applied.)

(ii) The cubic damping coefficient N

The cubic damping coefficient N greatly effects the behaviour of Faraday waves. Douady (1990), Milner (1991) and Chapter III demonstrate the effects of N upon hysteresis. Miles (1994) and Chapter VI demonstrate the effects of N upon mode competition. The stable limit cycles described in Chapter IV only exist when $N > 0$. It should be emphasised that $N > 0$ is counter-intuitive, since the local modulus of decay decreases as the wave amplitude increases. Appendix A discusses the effect of the sign of N upon two-mode competition, extending Nagata (1989, 1991).

The cubic damping coefficient N is difficult to determine theoretically. Milner (1991) and Miles (1993, 1994) derived formulae for N under rather limiting assumptions. This included assuming that dissipation in the boundary layers (at the container walls and at the surface) is negligible, which is appropriate only when the surface is uncontaminated and the wavelength is small compared to the dimensions of the tank. In Chapter III, we determined N/μ experimentally in our long rectangular tank by comparing experimental hysteresis measurements with theoretical results. For an ambient water depth of $d = 1\text{cm}$ we found $N/\mu = -0.43$, and for an ambient water depth of $d = 1.3\text{cm}$ we found $N/\mu = 2.43$. For $d = 2\text{cm}$, two values were obtained (using two different criteria for the comparison between theory and experiment), namely $N/\mu = 3.7$ and 6.4, giving an average value of 5.05 (the value 6.4 was produced by comparing the theoretical and experimental lower hysteresis boundaries beneath the minimum of the linear onset curve, and the value 3.7 was obtained by comparing the lower hysteresis boundaries for frequencies far from the minimum of the linear onset curve: see Chapter III). Further experimental and theoretical methods for determining N need to be developed, and this Chapter goes some way towards fulfilling the latter.

(iii) Summary of scalings and analysis

In this Chapter we extend the calculations of Keulegan (1959) and Miles (1967) to calculate μ and N by considering the energy dissipated in the main body of the fluid and in the boundary layers at the sidewalls and at the surface, for water with infinite depth. Keulegan (1959) and Miles (1967) retained only leading-order terms in their calculations and obtained the coefficient of linear damping μ (for finite depth, see (1.2)) but not N. Firstly, in this subsection, we summarise the scalings and detailed analysis contained in the rest of the Chapter.

In calculating the coefficient of cubic damping it is necessary to determine the size of the terms to be retained in the calculation. We choose our scaling parameter to be ε, which is the small parameter defined in Chapter III, though we will additionally use the inverse wave Reynolds number $R^{-1} \equiv \frac{\nu k^2}{\omega}$. We calculate the leading-order (that is $O(\varepsilon^2)$) dissipation due to the boundary layers at the sidewalls and at the surface (the contribution of the boundary layer at the surface is found to be negligible if the surface is uncontaminated). We also calculate the $O(\varepsilon^2)$ dissipation in the bulk, which is due to the potential flow. These together give the linear damping coefficient μ, as in Miles (1967) (see equation (1.2)).

To derive the cubic damping coefficient N, we calculate the $O(\varepsilon^4)$ dissipation due to the boundary layers and the bulk. We will find that the largest contribution to the $O(\varepsilon^4)$ dissipation can be from the streaming driven by a contaminated surface (we find that this contribution is independent of R); however, for both an uncontaminated surface and for an inextensible surface film, we find that there is no streaming, of this order, driven by the surface boundary layer. We find that the second largest contribution to the $O(\varepsilon^4)$ dissipation comes from the boundary layers at the sidewalls (this contribution is proportional to $R^{-1/2}$), and the smallest contribution to the $O(\varepsilon^4)$ dissipation is from the streaming driven by the sidewalls (this contribution is proportional to R^{-1}). We neglect this third contribution since $R^{-1} << R^{-1/2} << 1$.

The $O(\varepsilon^4)$ dissipation due to the surface boundary layer is negligible for an uncontaminated surface (see Miles 1967, 1993, 1994). For a contaminated surface, it

will be proportional to $R^{-1/2}$, and is therefore of a similar size to the $O(\varepsilon^4)$ dissipation in the boundary layers at the sidewalls. However, it is very difficult to determine this contribution to the dissipation, and we leave it uncalculated (this is discussed in more detail in section 4); therefore, for a contaminated surface, our calculation of the coefficient of cubic damping N is only an estimate.

We consider three situations: (i) a standing wave on a contaminated surface in a rectangular tank where the length and breadth of the tank are large compared with the wavelength of the standing wave, so that the boundary layers at the sidewalls can be neglected; (ii) an uncontaminated surface in a rectangular tank, so that the surface boundary layer can be neglected; (iii) a contaminated surface in a rectangular tank with sidewalls incorporated into the model, which is a combination of cases (i) and (ii). We will produce estimates in cases (i) and (iii) (where the surface is contaminated), and derive an exact formula in the second case (where the surface is uncontaminated). We neglect capillary hysteresis in all three situations.

We present strong evidence that N is positive (giving reduced dissipation) for infinite depth, for a variety of sizes of the tank and for a variety of surface films. This is especially relevant since equation (1.1) has very different types of behaviour for positive and negative N.

In situations (i) and (iii) we find the second-order streaming due to standing waves on a contaminated surface, which so far as we are aware, is a new result. From this we demonstrate that N is highly dependent on the compressional modulus of the surface film ξ, especially for an insoluble film. We also find cases where the (rotational) streaming induced by the surface boundary layer has unexpectedly high velocity fields. In these cases, the assumption of irrotational motion (which has been adopted in most work to date in Faraday waves) breaks down.

In the following section the potential flow is determined. In section 3 the modulus of decay is defined and the energy of the waves due to the potential flow is calculated. Section 4 considers the surface boundary layer, and sections 5 and 6 consider the boundary layers at the sidewalls. In section 7 the dissipation in the bulk fluid is

calculated, as well as the rotational contribution to the kinetic energy of the waves. The coefficients of cubic damping are calculated in each of the three scenarios in section 8, and the results are discussed in section 9. In section 10, we briefly discuss the implications of our results to (1.1) for water with infinite depth. In Appendix A, we discuss the implications of our results to the two mode equations derived by Nagata (1989), but here with cubic damping terms added. We show that changes in the coefficient of cubic damping can cause large changes in the behaviour of the system, which highlights the importance of accurately determining the coefficient of cubic damping.

2. Irrotational motion in the main body of the liquid

We consider irrotational fluid motion in a rectangular container of length l, width B and infinite ambient water depth. We assume that the surface waves are two-dimensional, along the length l of the tank. As the inviscid motion is assumed irrotational, the velocity $(u_0, v_0, w_0) = (\phi_x, 0, \phi_z)$ where the velocity potential $\phi(x,z,t)$ satisfies Laplace's equation $\nabla^2\phi = 0$, $0 < x < l$, $-\infty < z < \tilde{\eta}$, and $z = \tilde{\eta}(x,t)$ is the liquid's surface. The width of the tank is described by the co-ordinate y, where $0 < y < B$; but, since the waves are two-dimensional in x and z, ϕ does not depend upon y. In this Chapter, we use the perturbation method (Nagata 1989) rather than the variational method used in Chapters III and VI. This is because we are determining the velocity fields rather than the evolution equations.

The boundary conditions at the sidewalls are

$$\left.\frac{\partial\phi}{\partial x}\right|_{x=0,l} = 0, \tag{2.1}$$

and the boundary conditions at the free surface $z = \tilde{\eta}$ are

$$\frac{\partial\tilde{\eta}}{\partial t} + \frac{\partial\phi}{\partial x}\frac{\partial\tilde{\eta}}{\partial x} = \frac{\partial\phi}{\partial z}, \tag{2.2}$$

$$\frac{\partial\phi}{\partial t}+(g-f\cos 2\omega t)\tilde{\eta}=-\frac{1}{2}(\nabla\phi)^2. \tag{2.3}$$

The $f\cos 2\omega t$ term in (2.3) represents the vertical oscillation of the container. However $|f|<<g$, so the coefficients μ and N will not depend upon f at leading-order.

Following Nagata (1989), we expand

$$\phi=\varepsilon\phi_1+\varepsilon^2\phi_2+\varepsilon^3\phi_3+\ldots,\quad \tilde{\eta}=\varepsilon\eta_1+\varepsilon^2\eta_2+\varepsilon^3\eta_3+\ldots \tag{2.4}$$

as series in a small parameter ε where $f=O(\varepsilon^2)$, $|\omega^2-\omega_1^2|=O(\varepsilon^2)$ and $\omega_1=(gk)^{1/2}$ is the frequency of the primary mode. Nagata (1989) calculated the first two terms in the velocity-potential expansion, and at infinite depth these are

$$\phi_1=\cos kx e^{kz}A(\tau)e^{i\omega t}+c.c. \tag{2.5}$$

and

$$\phi_2=\tilde{B}e^{2i\omega t}+c.c., \tag{2.6}$$

where

$$\tilde{B}=\frac{ik^2A^2}{2\omega}, \tag{2.7}$$

A is the time-dependent complex wave amplitude, $\tau=\varepsilon^2\omega t$ is a slow time-scale and $k=\frac{m\pi}{l}$ (where m is the number of half-wavelengths across the tank). The coefficient of the $\cos 2kx e^{2kz\pm 2i\omega t}$ contribution to (2.6) tends towards zero for infinite depth (see Nagata 1989), and so does not appear here.

On extending this method, the next term in the expansion is found to be

$$\phi_3=D\cos kx e^{kz+3i\omega t}+c.c., \tag{2.8}$$

where

$$D=\frac{5A^3k^3}{8g}. \tag{2.9}$$

Note that (2.8) would be more complicated if the depth were not infinite.

At $O(\varepsilon^3)$, the conservative evolution equation (compare with equation (1.1))

$$\frac{dA}{d\tau}=i\Omega A+iFA^*+i\Pi|A|^2A \tag{2.10}$$

also results from the analysis, where

$$\Pi=\frac{k^4}{2\omega}, \tag{2.11}$$

(see Nagata 1989). The higher-order conservative terms in (1.1) result from a continuation of the expansion (2.4). However, no further terms in the (2.4) series expansion are required to calculate the coefficient of cubic damping.

The first three terms in the expansion of the surface elevation $\tilde{\eta}$ can be found using the method of Mei (1983, pp 607-616). The surface $\tilde{\eta}$ is expanded in a Taylor series about $z=0$ and then (2.4) is substituted into equation (2.3). This gives three equations at $O(\varepsilon)$, $O(\varepsilon^2)$ and $O(\varepsilon^3)$: the first two can be solved to give

$$\eta_1 = -\frac{i\omega\cos(kx)}{g}\left(Ae^{i\omega t} - A^* e^{-i\omega t}\right) \tag{2.12}$$

and

$$\frac{g}{k^2}\eta_2 = |A|^2\cos 2kx - \frac{1}{2}A^2\cos 2kx e^{2i\omega t} + c.c.. \tag{2.13}$$

Both (2.12) and (2.13) are in agreement with Keulegan (1959). The third equation gives a similar expression for η_3, but is too lengthy to display here.

3. The modulus of decay and the energy of the waves

Following Keulegan (1959), the exponential modulus of decay of wave amplitudes is measured by

$$\alpha = \frac{1}{2n}\int_0^n \frac{\chi}{E}dn \tag{3.1}$$

where n is a chosen number of oscillations of the wave, χ is the energy loss during a single oscillation and E is the energy of the waves. This can be approximated by

$$\alpha \approx \frac{\langle\chi\rangle}{2\langle E\rangle} \tag{3.2}$$

where $\langle\ \rangle$ denotes a time average over a single oscillation. The modulus of decay is identified with

$$\alpha = \mu - \varepsilon^2 N|A|^2 + \ldots, \tag{3.3}$$

if $|A|$ is assumed constant.

We now calculate the average energy of the wave motion $\langle E \rangle$. Mei (1983) gives the expression

$$E = \frac{1}{2}\rho g \int_0^B \int_0^l \tilde{\eta}^2 dx dy + \frac{1}{2}\rho \int_o^B \int_0^l \int_{-\infty}^{\tilde{\eta}} (\nabla\phi)^2 dz\, dx\, dy \tag{3.4}$$

for the energy of the waves, where the first integral represents the potential energy and the second integral represents the kinetic energy. (In the following section we will find a rotational flow in the main body of the fluid driven by the surface boundary layer. This will contribute to the kinetic energy of the waves, and this contribution will be added to (3.4): see section 7.) Using the results of section 2, equation (3.4) may be evaluated, giving

$$\begin{aligned} \langle E \rangle &= \int_0^{\frac{2\pi}{\omega}} E dt = \frac{2\varepsilon^2 \pi \rho B k l}{\omega} |A|^2 \left(1 + \varepsilon^2 \frac{\Omega}{\omega}\right) \\ &+ \frac{\varepsilon^4 \pi \rho B l F}{g}\left(A^2 + A^{*2}\right) + \varepsilon^4 \frac{9\pi\rho B l k^4}{2g\omega}|A|^4 + O\left(\varepsilon^6\right) \end{aligned} \tag{3.5}$$

for the time-averaged energy of the waves. Note that Keulegan (1959) only retained the leading-order contribution of (3.5).

4. The surface boundary layer

The equations governing the motion of the fluid in the boundary layer at the surface are (see Schlichting 1960)

$$\begin{aligned} &\frac{\partial u}{\partial t} + u\frac{\partial u}{\partial x} + w\frac{\partial u}{\partial z} - \nu\frac{\partial^2 u}{\partial z^2} = \frac{\partial u_0}{\partial t} + u_0\frac{\partial u_0}{\partial x} + w_0\frac{\partial u_0}{\partial z}, \\ &\frac{\partial u}{\partial x} + \frac{\partial w}{\partial z} = 0, \end{aligned} \tag{4.1}$$

where u and w are the velocities in the boundary layer in the x and z directions respectively, u_0 and w_0 are the irrotational velocities in the main body of the fluid in the x and z directions, and ν is the kinematic viscosity.

The boundary conditions at the surface $z = \eta(x,t)$ are that (i) the component of the stress tensor normal to the surface of the liquid is equal to the sum of the hydrostatic

pressure in the gas phase and the Laplace pressure due to curvature of the surface in the presence of the wave, and (ii) the tangential stress component at the surface is equal to the surface tension gradient (see Tempel & Riet 1965). If the motion in the bulk is purely irrotational then the boundary condition at the bottom of the boundary layer is

$$\frac{\partial u}{\partial z} = \frac{\partial u_0}{\partial z} \text{ as } \beta z \to -\infty, \tag{4.2}$$

where β is a large parameter given by (4.9). It will be seen that in certain circumstances (4.2) does not hold, in which case there is rotational streaming in the bulk. (In such cases, $\frac{\partial u}{\partial z}$ tends towards the sum of $\frac{\partial u_0}{\partial z}$ and the equivalent rotational component in the bulk as $\beta z \to -\infty$.) Note that we distinguish z which varies with the depth of the tank, from βz which varies across the boundary layer such that $z \approx 0$ when $\beta z = -\infty$.

Since the thickness of the boundary layer will normally be much smaller than the wave amplitude, the surface boundary conditions must be applied at the liquid's surface $z = \tilde{\eta}(x,t)$ rather than at the mean level $z = 0$. This is usually achieved by a transformation to curvilinear coordinates (see Benjamin 1959, Phillips 1977 and Craik 1982). This is straight-forward at leading-order, but is difficult at higher-order. However, the leading-order time-periodic velocity field and the second-order mean velocity field can be determined without transforming to curvilinear coordinates (see Craik 1982). These velocity fields will be determined and we will show that the second-order mean field in the surface boundary layer drives a second-order mean rotational (streaming) velocity field in the bulk fluid. However, since we do not transform to curvilinear coordinates, we will not be able to calculate the second-order time-periodic and the third-order velocity fields in the surface boundary layer, which means we are not able to determine the $O(\varepsilon^4)$ dissipation in the surface boundary layer (which contributes to N); this calculation would involve a substantial amount of algebraic manipulation, and the task appears intimidating and of questionable significance (it will be seen that in most cases this contribution will be much smaller than the contribution from the streaming). Therefore, our results for the cubic damping

coefficient N are approximate for a contaminated surface, though exact for an uncontaminated surface. (Note that our calculation of the linear damping coefficient μ is not affected by neglecting these velocity fields.)

The linearized tangential surface boundary condition is proposed by Miles (1967) to be

$$u = \varepsilon k(C-1)A\sin kx e^{i\omega t} + c.c. \text{ at } z = 0, \tag{4.3}$$

where C is given by (1.3) for gravity waves. This is found by equating the viscous shearing stress in the liquid and the tangential stress in the surface film.

The method of Lin (1957) (described in Schlichting 1960) can be used, where the velocities, in the boundary layer and in the bulk, are decomposed into mean flow and time-periodic components:

$$\begin{aligned} u(x,y,z,t) &= \overline{u}(x,y,z) + u_1(x,y,z,t), \\ w(x,y,z,t) &= \overline{w}(x,y,z) + w_1(x,y,z,t), \\ u_0(x,y,z,t) &= \overline{u}_0(x,y,z) + u_{01}(x,y,z,t), \\ w_0(x,y,z,t) &= \overline{w}_0(x,y,z) + w_{01}(x,y,z,t), \end{aligned} \tag{4.4}$$

where the bar denotes an average with respect to time over one period, and $\overline{u}_1 = \overline{w}_1 = \overline{u}_{01} = \overline{w}_{01} = 0$.

We also expand the above velocity components as ε series:

$$\begin{aligned} \overline{u} &= \varepsilon^2\overline{u}_b + \varepsilon^3\overline{u}_c + \ldots., \\ \overline{w} &= \varepsilon^2\overline{w}_b + \varepsilon^3\overline{w}_c + \ldots., \\ u_1 &= \varepsilon u_{1a} + \varepsilon^2 u_{1b} + \varepsilon^3 u_{1c} + \ldots., \\ w_1 &= \varepsilon w_{1a} + \varepsilon^2 w_{1b} + \varepsilon^3 w_{1c} + \ldots., \\ \overline{u}_0 &= \varepsilon^2\overline{u}_{0b} + \varepsilon^3\overline{u}_{0c} + \ldots., \\ u_{01} &= \varepsilon u_{01a} + \varepsilon^2 u_{01b} + \varepsilon^3 u_{01c} + \ldots., \\ \overline{w}_0 &= \varepsilon^2\overline{w}_{0b} + \varepsilon^3\overline{w}_{0c} + \ldots., \\ w_{01} &= \varepsilon w_{01a} + \varepsilon^2 w_{01b} + \varepsilon^3 w_{01c} + \ldots. \end{aligned} \tag{4.5}$$

Subsituting (4.4) and (4.5) into (4.1) gives the leading-order time-periodic equations

$$\begin{aligned} \frac{\partial u_{1a}}{\partial t} - \nu\frac{\partial^2 u_{1a}}{\partial z^2} &= \frac{\partial u_{01a}}{\partial t}, \\ \frac{\partial u_{1a}}{\partial x} + \frac{\partial w_{1a}}{\partial z} &= 0, \end{aligned} \tag{4.6}$$

and the second-order mean flow velocity equations

$$-\nu\frac{\partial^2\overline{u}_b}{\partial z^2} = \overline{u_{01a}\frac{\partial u_{01a}}{\partial x}} + \overline{w_{01a}\frac{\partial u_{01a}}{\partial z}} - \overline{u_{1a}\frac{\partial u_{1a}}{\partial x}} - \overline{w_{1a}\frac{\partial u_{1a}}{\partial z}},$$
$$\frac{\partial\overline{u}_b}{\partial x} + \frac{\partial\overline{w}_b}{\partial z} = 0. \tag{4.7}$$

The leading-order time-periodic velocity field can be found by solving (4.6) with the boundary conditions (4.2) and (4.3). This has the solution

$$u_{1a} - u_{01a} = \varepsilon k\sin(kx)CA\exp(\beta z + i\beta z + i\omega t) + c.c.,$$
$$w_{1a} = -\int_0^z \frac{\partial u_{1a}}{\partial x}dz, \tag{4.8}$$

where

$$\beta^2 = \frac{\omega}{2\nu}. \tag{4.9}$$

Note that $u_{01a} = \dfrac{\partial\phi_1}{\partial x}$ from section 2.

The second-order mean velocity field in the boundary layer can be calculated by solving (4.7). The boundary condition at the surface is that the mean tangential stress is zero, namely

$$\frac{\partial\overline{u}_b}{\partial z} + \frac{\partial\overline{w}_b}{\partial x} = 0 \text{ at } z = 0 \tag{4.10}$$

(see Craik 1982, equation (4.9)). Solving (4.7) subject to (4.10) gives a rather complicated formula for the velocity field which we do not display here. However, it is found that the boundary condition at the bottom of the boundary layer (4.2) can only be satisfied for an uncontaminated surface and for an inextensible surface film: in both these cases there is no streaming in the bulk (the latter result was unexpected). For any other surface film, the boundary condition (4.2) cannot be satisfied, which results in streaming in the bulk: as $\beta z \to -\infty$ we find that

$$\frac{\partial\overline{u}_b}{\partial z} \to \varepsilon^2|A|^2k^3\sqrt{\frac{2}{\nu\omega}}\sin(2kx)\left\{\{C_r + C_i\} - |C|^2\right\} \equiv U\sin(2kx),$$
$$\overline{w}_b \to 0, \tag{4.11}$$

for $z \approx 0$, where $C = C_r + iC_i$. (Note that $\dfrac{\partial\overline{u}_b}{\partial z} \to 0$ as $\beta z \to -\infty$ for $C = 0$, corresponding to an uncontaminated surface, in agreement with Longuet-Higgins

(1953), and for $C=1$, corresponding to an inextensible surface film; in both these cases there is no streaming, of this order, in the bulk.)

The energy dissipated in the boundary layer at the surface due to the leading-order time-periodic terms was calculated by Miles (1967). Converting his expression (4.12b in his paper) to the scalings and variables used here gives

$$\Delta E_1 = 2\pi\varepsilon^2\rho Blk^2\left(\frac{\nu}{2\omega}\right)^{1/2}(C_r - C_i)|A|^2, \tag{4.12}$$

which corresponds to the third term of (1.2).

Before we calculate the streaming resulting from (4.11), it is beneficial to summarise the work of Longuet-Higgins (1953), who derived the streaming resulting from the boundary layer at the bottom of the container (for finite depth) for standing waves on an uncontaminated surface. He identified two types of solution: (i) the conduction solution and (ii) the convective solution. The steady-state two-dimensional conduction solution in the bulk can be described by a stream function satisfying

$$\nabla^4\Psi = 0, \tag{4.13}$$

(see Longuet-Higgins 1953) for sufficiently small amplitude waves. This solution may be attained after a time sufficiently long for vorticity to diffuse from the boundary layer throughout the bulk (see Craik 1982). A steady-state inviscid convection solution can be described by

$$\left(\nabla^2 + r^2\right)\Psi = 0, \tag{4.14}$$

where r is a constant to be determined, and the streaming is assumed to be two-dimensional (see Longuet-Higgins 1953). However, Haddon & Riley (1983) claim that the appropriate steady convection equation is not (4.14), but instead

$$\nabla^2\Psi = \omega_0, \tag{4.15}$$

where ω_0 is an unknown piecewise-constant vorticity. However, we will solve the steady conduction equation (4.13) here, which will give the final state of the streaming after a sufficiently long period of time and for sufficiently small amplitude waves.

We define

$$\tilde{u} = \frac{\partial\Psi}{\partial z},\ \tilde{w} = -\frac{\partial\Psi}{\partial x}, \tag{4.16}$$

where $\tilde{u}$ and $\tilde{w}$ are the second-order mean flow velocities in the bulk. We solve the conduction equation (4.13), subject to the boundary conditions

$$\frac{\partial^2\Psi}{\partial z^2} = \varepsilon^2|A|^2k^3\sqrt{\frac{2}{\nu\omega}}\sin(2kx)\left\{\{C_r + C_i\} - |C|^2\right\} \equiv U\sin(2kx),$$
$$\frac{\partial\Psi}{\partial x} = 0, \tag{4.17}$$

at $z = 0$. The solution is found to be

$$\Psi = \frac{U}{4k}z\exp(2kz)\sin(2kx), \tag{4.18}$$

which consists of counter-rotating cells. (Equation (4.18) is similar to the streaming found by Rayleigh 1883 c.)

The energy dissipation due to this streaming will be calculated in section 7.

5. The boundary layers at the sidewalls $y = 0$ and $y = B$

Here we derive the dissipation due to the boundary layers at the sidewalls $y = 0$ and $y = B$. The three-dimensional time-dependent equations governing the motion of the fluid in the boundary layers adjacent to the sidewalls $y = 0$ and $y = B$ (see Schlichting 1960) are

$$\frac{\partial u}{\partial t} + u\frac{\partial u}{\partial x} + v\frac{\partial u}{\partial y} + w\frac{\partial u}{\partial z} - \nu\frac{\partial^2 u}{\partial y^2} = \frac{\partial u_0}{\partial t} + u_0\frac{\partial u_0}{\partial x} + w_0\frac{\partial u_0}{\partial z}$$
$$\frac{\partial w}{\partial t} + u\frac{\partial w}{\partial x} + v\frac{\partial w}{\partial y} + w\frac{\partial w}{\partial z} - \nu\frac{\partial^2 w}{\partial y^2} = \frac{\partial w_0}{\partial t} + u_0\frac{\partial w_0}{\partial x} + w_0\frac{\partial w_0}{\partial z} \tag{5.1}$$
$$\frac{\partial u}{\partial x} + \frac{\partial v}{\partial y} + \frac{\partial w}{\partial z} = 0$$

where v is the velocity in the boundary layer in the y direction.

The boundary conditions are

$$u = v = w = 0 \text{ at } \beta y = 0,$$
$$u = u_0,\ w = w_0 \text{ as } \beta y \to \infty. \tag{5.2}$$

We again substitute (4.4) and (4.5) into our equations. At leading-order, (5.1) gives

$$\frac{\partial u_{1a}}{\partial t} - \nu\frac{\partial^2 u_{1a}}{\partial y^2} = \frac{\partial u_{01a}}{\partial t},$$
$$\frac{\partial w_{1a}}{\partial t} - \nu\frac{\partial^2 w_{1a}}{\partial y^2} = \frac{\partial w_{01a}}{\partial t}, \tag{5.3}$$
$$\frac{\partial u_{1a}}{\partial x} + \frac{\partial v_{1a}}{\partial y} + \frac{\partial w_{1a}}{\partial z} = 0.$$

The solution to (5.3), subject to the boundary conditions, is

$$u_{1a} - u_{01a} = k\sin(kx)e^{kz}f(t,y),$$
$$v_{1a} = 0, \tag{5.4}$$
$$w_{1a} - w_{01a} = -k\cos(kx)e^{kz}f(t,y),$$

where

$$f(t,y) = A\exp(-\beta y - i\beta y + i\omega t) + c.c.. \tag{5.5}$$

At $O(\varepsilon^2)$, the mean flow equations are

$$-\nu\frac{\partial^2 \overline{u}_b}{\partial y^2} = 0,$$
$$-\nu\frac{\partial^2 \overline{w}_b}{\partial y^2} = \overline{u_{01a}\frac{\partial w_{01a}}{\partial x}} + \overline{w_{01a}\frac{\partial w_{01a}}{\partial z}} - \overline{u_{1a}\frac{\partial w_{1a}}{\partial x}} - \overline{w_{1a}\frac{\partial w_{1a}}{\partial z}}, \tag{5.6}$$
$$\frac{\partial \overline{u}_b}{\partial x} + \frac{\partial \overline{v}_b}{\partial y} + \frac{\partial \overline{w}_b}{\partial z} = 0,$$

where the right-hand side of the first expression in (5.6) has simplified to zero.

The $O(\varepsilon^2)$ time-dependent equations are

$$\frac{\partial u_{1b}}{\partial t} - \nu\frac{\partial^2 u_{1b}}{\partial y^2} = 0,$$
$$\frac{\partial w_{1b}}{\partial t} - \nu\frac{\partial^2 w_{1b}}{\partial y^2} = u_{01a}\frac{\partial w_{01a}}{\partial x} + w_{01a}\frac{\partial w_{01a}}{\partial z} - \overline{u_{01a}\frac{\partial w_{01a}}{\partial x}} - \overline{w_{01a}\frac{\partial w_{01a}}{\partial z}}$$
$$-u_{1a}\frac{\partial w_{1a}}{\partial x} - w_{1a}\frac{\partial w_{1a}}{\partial z} + \overline{u_{1a}\frac{\partial w_{1a}}{\partial x}} + \overline{w_{1a}\frac{\partial w_{1a}}{\partial z}}, \tag{5.7}$$
$$\frac{\partial u_{1b}}{\partial x} + \frac{\partial v_{1b}}{\partial y} + \frac{\partial w_{1b}}{\partial z} = 0.$$

The right-hand side of the first expression in (5.7) has also simplified to zero.

Solving (5.6) and (5.7) subject to the boundary conditions at $\beta y = 0$ gives

$$
\begin{aligned}
&\overline{u}_b + u_{1b} = 0, \\
&\overline{w}_b + w_{1b} = \frac{k^3}{\omega}|A|^2 \exp(2kz)\left\{-1+\exp(-2\beta y)+2i\exp(-\beta y - i\beta y)\right\} \\
&+\frac{k^3}{2\omega}A^2\exp(2kz+2i\omega t) \\
&\times\left\{5\exp(-\beta_3 y)-\exp(-2\beta y-2i\beta y)-4\exp(-\beta y - i\beta y)\right\}+c.c., \\
&\overline{v}_b + v_{1b} = -\int_0^y \frac{\partial(\overline{w}_b + w_{1b})}{\partial z}dy,
\end{aligned}
\tag{5.8}
$$

where

$$
\beta_3^2 = \frac{2i\omega}{\nu}. \tag{5.9}
$$

The time-dependent component w_{1b} satisfies both boundary conditions, but the mean flow component $\overline{w}_b$ does not satisfy the boundary condition (5.2) at $\beta y \to \infty$, which requires that it connects to an irrotational flow in the bulk. In fact,

$$
\overline{w}_b \to -\frac{k^3}{\omega}|A|^2\exp(2kz) \text{ as } \beta y \to \infty, \tag{5.10}
$$

which gives rise to rotational streaming in the bulk. This streaming would be very difficult to determine, especially since (5.10) appears to imply that there is downwards flow between the surface boundary layer and the bulk, near to the sidewalls $y = 0, B$. It seems likely that the overlap between the surface boundary layer and the boundary layers at the sidewalls is significant, and this overlap would probably have to be incorporated into the model if the streaming were to be determined in this situation. This is a very difficult task, and is not attempted here. However, in the case studied in section 4, the induced streaming (so long as $C \neq 0$ or 1) was $\Psi = O\left(\varepsilon^2 R^{1/2}\right)$ (see equation (4.18)) giving dissipation due to the streaming of $O\left(\varepsilon^4\right)$, which is independent of R (see equation (7.2)); remember, $R = O\left(\nu^{-1}\right)$. In this section, the streaming in the bulk may be expected to be $\Psi = O\left(\varepsilon^2\right)$ (see equation (5.10)), giving dissipation due to the streaming of $O\left(\varepsilon^4 R^{-1}\right)$. But the dissipation in the boundary layers at the sidewalls (see (5.13)) is $O\left(\varepsilon^4 R^{-1/2}\right)$. Since $\varepsilon^4 R^{-1} << \varepsilon^4 R^{-1/2} << \varepsilon^4$, the bulk dissipation due to the streaming induced by the sidewalls is small compared to *both* the dissipation within the boundary layers at the sidewalls *and* the bulk dissipation due to the streaming driven by the surface boundary layer. Therefore, the dissipation

due to the streaming induced by the sidewalls is expected to be negligible and we leave this streaming uncalculated.

We now return to the flow in the boundary layer at the sidewalls $y = 0, B$ to calculate the $O(\varepsilon^3)$ velocities there. At $O(\varepsilon^3)$, (5.1) is

$$\begin{aligned}
&\frac{\partial u_c}{\partial t} - \nu\frac{\partial^2 u_c}{\partial y^2} = \frac{\partial u_{01c}}{\partial t} + w_{01b}\frac{\partial u_{01a}}{\partial z} - v_b\frac{\partial u_{1a}}{\partial y} - w_b\frac{\partial u_{1a}}{\partial z},\\
&\frac{\partial w_c}{\partial t} - \nu\frac{\partial^2 w_c}{\partial y^2} = \frac{\partial w_{01c}}{\partial t} + u_{01a}\frac{\partial w_{01b}}{\partial x} + w_{01a}\frac{\partial w_{01b}}{\partial z} + w_{01b}\frac{\partial w_{01a}}{\partial z}\\
&-u_{1a}\frac{\partial w_b}{\partial x} - v_b\frac{\partial w_{1a}}{\partial y} - w_{1a}\frac{\partial w_b}{\partial z} - w_b\frac{\partial w_{1a}}{\partial z},\\
&\frac{\partial u_c}{\partial x} + \frac{\partial v_c}{\partial y} + \frac{\partial w_c}{\partial z} = 0,
\end{aligned} \tag{5.11}$$

where

$$\begin{aligned}
u_i &= \overline{u}_i + u_{1i},\\
v_i &= \overline{v}_i + v_{1i},\\
w_i &= \overline{w}_i + w_{1i}, \text{ for } i = a,b,c.
\end{aligned} \tag{5.12}$$

We have solved equation (5.11) subject to the boundary conditions (5.2), though the result is too lengthy to be shown here.

Following Keulegan (1959), the energy dissipated in the boundary layer at the wall $y = 0$ during one oscillation of the wave can be calculated from (5.4), (5.8) and the solution to (5.11). This gives

$$\begin{aligned}
\Delta E_2 &= \nu\rho\int_{-\infty}^{0}\int_{0}^{l}\int_{0}^{\infty}\int_{0}^{\frac{2\pi}{\omega}}\left[\left(\frac{\partial u}{\partial y}\right)^2 + \left(\frac{\partial w}{\partial y}\right)^2\right]dt\,dy\,dx\,dz\\
&= \frac{\varepsilon^2\pi\rho k l(2\nu)^{1/2}|A|^2}{\omega^{1/2}} - 0.66108\frac{\varepsilon^4\rho k^4 l\nu^{1/2}|A|^4}{g\omega^{1/2}}.
\end{aligned} \tag{5.13}$$

Note that the number 0.66108 in (5.13) is dimensionless and that A has the units $m^2 s^{-1}$. (We later apply the transformation (9.3) to form a non-dimensional $\hat{A}$.)

Keulegan (1959) only obtained the first term in (5.13).

6. The boundary layers at the sidewalls $x = 0$ and l

Here we derive the dissipation within the boundary layers at the sidewalls $x = 0$ and l. The equations governing the motion of the fluid in the boundary layer adjacent to the wall $x = 0$ are

$$\begin{aligned}
&\frac{\partial v}{\partial t} + u\frac{\partial v}{\partial x} + v\frac{\partial v}{\partial y} + w\frac{\partial v}{\partial z} - \nu\frac{\partial^2 v}{\partial x^2} = 0,\\
&\frac{\partial w}{\partial t} + u\frac{\partial w}{\partial x} + v\frac{\partial w}{\partial y} + w\frac{\partial w}{\partial z} - \nu\frac{\partial^2 w}{\partial x^2} = \frac{\partial w_0}{\partial t} + w_0\frac{\partial w_0}{\partial z},\\
&\frac{\partial u}{\partial x} + \frac{\partial v}{\partial y} + \frac{\partial w}{\partial z} = 0,
\end{aligned} \tag{6.1}$$

and the boundary conditions are

$$\begin{aligned}
&u = v = w = 0 \text{ at } \beta x = 0,\\
&v = 0, w = w_0 \text{ as } \beta x \to \infty.
\end{aligned} \tag{6.2}$$

We see immediately that $v = 0$. Note that we distinguish x, which varies along the length of the tank, from βx which varies across the boundary layer such that $x \approx 0$ when $\beta x = \infty$.

At leading-order, the time-periodic equations are

$$\begin{aligned}
&\frac{\partial w_{1a}}{\partial t} - \nu\frac{\partial^2 w_{1a}}{\partial x^2} = \frac{\partial w_{01a}}{\partial t},\\
&\frac{\partial u_{1a}}{\partial x} + \frac{\partial w_{1a}}{\partial z} = 0,
\end{aligned} \tag{6.3}$$

which, subject to the boundary conditions, has the solution

$$\begin{aligned}
&u_{1a} = -\int_0^x \frac{\partial w_1}{\partial z}dx,\\
&w_{1a} - w_{01a} = -\varepsilon Ak\exp(-\beta x - i\beta x + i\omega t + kz) + c.c.,
\end{aligned} \tag{6.4}$$

where β is defined by (4.9).

The $O(\varepsilon^2)$ time-dependent terms satisfy

$$\begin{aligned}
&\frac{\partial w_{1b}}{\partial t} - \nu\frac{\partial^2 w_{1b}}{\partial x^2} = -u_{1a}\frac{\partial w_{1a}}{\partial x} - w_{1a}\frac{\partial w_{1a}}{\partial z}\\
&+\overline{u_{1a}\frac{\partial w_{1a}}{\partial x}} + \overline{w_{1a}\frac{\partial w_{1a}}{\partial z}} + w_{01a}\frac{\partial w_{01a}}{\partial z} - \overline{w_{01a}\frac{\partial w_{01a}}{\partial z}},\\
&\frac{\partial u_{1b}}{\partial x} + \frac{\partial w_{1b}}{\partial z} = 0.
\end{aligned} \tag{6.5}$$

The second-order mean flow velocity components satisfy

$$
\begin{aligned}
&-\nu\frac{\partial^2\overline{w}_b}{\partial x^2} = \overline{w_{01a}\frac{\partial w_{01a}}{\partial z}} - \overline{u_{1a}\frac{\partial w_{1a}}{\partial x}} - \overline{w_{1a}\frac{\partial w_{1a}}{\partial z}},\\
&\frac{\partial\overline{u}_b}{\partial x} + \frac{\partial\overline{w}_b}{\partial z} = 0.
\end{aligned}
\tag{6.6}
$$

Solving (6.5) and (6.6), subject to the boundary conditions at $\beta x = 0$, gives

$$
\begin{aligned}
&u_{1b} + \overline{u}_b = -\int_0^x \frac{\partial(w_{1b} + \overline{w}_b)}{\partial z}dx,\\
&w_{1b} + \overline{w}_b = \frac{|A|^2k^3}{\omega}\exp(2kz)\{-3 + \exp(-2\beta x) + (1+2i)\exp(-\beta x - i\beta x)\}\\
&+\frac{iA^2k^3}{\omega}\exp(2i\omega t + 2kz)\{\exp(-\beta_3 x) - \exp(-\beta x - i\beta x)\} + c.c..
\end{aligned}
\tag{6.7}
$$

We find that it is not possible to satisfy the boundary condition at $\beta x \to \infty$. Therefore, the boundary layer at the sidewall $x = 0$ drives streaming in the bulk: as $\beta x \to \infty$,

$$
\overline{w}_b \to -\frac{3|A|^2k^3\exp(2kz)}{\omega}
\tag{6.8}
$$

at $x \approx 0$. This streaming is negligible here, as discussed in the previous section, since it will give rise to dissipation much smaller than the $O(\varepsilon^4)$ dissipation within the boundary layers.

At $O(\varepsilon^3)$, equation (6.1) is

$$
\begin{aligned}
&\frac{\partial w_c}{\partial t} - \nu\frac{\partial^2 w_c}{\partial x^2} = \frac{\partial w_{01c}}{\partial t} - u_b\frac{\partial w_{1a}}{\partial x} - w_b\frac{\partial w_{1a}}{\partial z}\\
&-u_{1a}\frac{\partial w_b}{\partial x} - w_{1a}\frac{\partial w_b}{\partial z}\\
&+\overline{w}_{0b}\frac{\partial w_{01a}}{\partial z} + w_{01a}\frac{\partial\overline{w}_{0b}}{\partial z},\\
&\frac{\partial u_{1c}}{\partial x} + \frac{\partial w_{1c}}{\partial z} = 0.
\end{aligned}
\tag{6.9}
$$

The solution of (6.9), subject to the boundary conditions, is a lengthy expression which is not displayed here.

The energy dissipated in the boundary layer at the sidewall $x = 0$ during one oscillation of the wave, calculated from (6.4), (6.7) and the solution to (6.9), is given by

$$\Delta E_3 = \nu\rho \int_0^B \int_{-\infty}^0 \int_0^\infty \int_0^{\frac{2\pi}{\omega}} \left(\frac{\partial w}{\partial x}\right)^2 dt\, dx\, dz\, dy$$
$$= \frac{\pi\varepsilon^2\rho k B (2\nu)^{1/2}|A|^2}{\omega^{1/2}} - 4.1840\frac{\varepsilon^4|A|^4 B\rho\nu^{1/2}k^4}{g\omega^{1/2}}. \tag{6.10}$$

Again, the constant 4.1840 is non-dimensional.

Keulegan (1959) only calculated the first term in (6.10).

7. The bulk fluid

The velocity field in the bulk consists of (i) the potential flow given by (2.5) - (2.9), and (ii) the streaming driven by the surface boundary layer, which is zero if $C = 0$ or 1 (other streaming effects being neglected). Each will contribute to the dissipation in the bulk.

The energy dissipated in the bulk due to the potential flow during one oscillation of the wave is given by (Lamb 1932, Miles 1993, 1994)

$$\Delta E_4 = \nu\rho \int_0^B \int_0^l \int_{-\infty}^0 \int_0^{\frac{2\pi}{\omega}} \left\{\left(\frac{\partial^2\phi}{\partial x^2}\right)^2 + \left(\frac{\partial^2\phi}{\partial z^2}\right)^2 + 2\left(\frac{\partial^2\phi}{\partial x\partial z}\right)^2\right\} dt\, dz\, dx\, dy$$
$$= \frac{4\pi\varepsilon^2\nu\rho l B k^3|A|^2}{\omega} + O(\varepsilon^6). \tag{7.1}$$

Note that there is no $O(\varepsilon^4)$ contribution to (7.1).

Following Miles (1967), the dissipation due to the streaming flow (4.18) is given by

$$\Delta E_{1s} = \frac{2\pi\nu\rho}{\omega} \int_0^B \int_0^l \int_{-\infty}^0 \left|curl(\tilde{u}\mathbf{i} + \tilde{w}\mathbf{k})\right|^2 dz\, dx\, dy$$
$$= \frac{lU^2\pi B\rho\nu}{4\omega k}, \tag{7.2}$$

where U is defined in (4.17). The streaming (4.18) also contributes to the average kinetic energy of the waves. This contribution is given by

$$\langle E_{KE1}\rangle = \frac{\pi\rho}{\omega} \int_0^B \int_0^l \int_{-\infty}^{\tilde{\eta}} (\tilde{u}^2 + \tilde{w}^2) dz\, dx\, dy$$
$$= \frac{lU^2\pi B\rho}{128\omega k^3}. \tag{7.3}$$

8. Coefficients of cubic damping

We can now proceed to determine the coefficients of cubic damping in the three scenarios studied here.

(i) The contaminated surface without sidewalls

Here we consider a standing wave in a rectangular container where the length and breadth of the tank are so large compared with the wavelength, that the boundary layers at the sidewalls can be neglected. We retain the dissipation in the bulk, due to the potential flow and the surface-induced streaming, and the leading-order dissipation in the surface boundary layer, giving an estimate of the coefficient of cubic damping.

The energy of the waves is given by the sum of (3.5) and (7.3). The leading-order energy dissipation in the surface boundary layer is given by (4.12). The energy dissipated in the bulk is given by the sum of (7.1) and (7.2). Therefore, the total energy dissipated during one oscillation of the waves is

$$\langle \chi \rangle \approx \Delta E_1 + \Delta E_{1s} + \Delta E_4 . \tag{8.1}$$

Substituting the total energy dissipation and the total wave energy into (3.2) and applying the expansion (3.3) gives the coefficients of linear and cubic damping in this case. The linear damping coefficient μ is found to be in agreement with the equivalent expression derived by Miles (1967), and was discussed in section 1. The cubic damping coefficient, in this case, is

$$\begin{aligned} N &= \frac{9k^5\nu}{4g} - \frac{15u^2\nu}{256k^2} + \frac{(2\omega\nu)^{1/2}(C_r - C_i)\left(576k^7 + gu^2\right)}{1024gk^3} \\ &\approx -\frac{15u^2\nu}{256k^2} + \frac{(2\omega\nu)^{1/2}(C_r - C_i)\left(576k^7 + gu^2\right)}{1024gk^3} \text{ for } C \neq 0, \text{ since } \nu << 1. \end{aligned} \tag{8.2}$$

In (8.2), $u \equiv k^3\sqrt{\frac{2}{\nu\omega}}\left\{(C_r + C_i) - |C|^2\right\}$ (from (4.17)), and so the terms in u will dominate N so long as $(C_r + C_i) - |C|^2$ is not small. Note that (8.2) is not explicitly dependent on the length l or breadth B of the tank, since sidewalls are not built into this

model. Also, note that $N \to \frac{9k^5\nu}{4g}$ as $C \to 0$, which is the contribution from the potential flow in the bulk.

For an inextensible surface film, which real films often approximate (see Craik 1982), $C = 1$ and $u = 0$, which gives

$$N \approx \frac{9(2\nu\omega)^{1/2}k^4}{16g}. \tag{8.3}$$

(ii) The rectangular tank with an uncontaminated surface

Here we assume an uncontaminated surface and therefore we neglect the surface boundary layer. In this case, the streaming is negligible. The total energy of the waves is given by (3.5). The total energy dissipated during one oscillation of the waves is given by

$$\langle \chi \rangle = 2\Delta E_2 + 2\Delta E_3 + \Delta E_4. \tag{8.4}$$

Equations (3.2) and (3.3) give the linear damping coefficient μ for an uncontaminated surface (as described in section 1) and the cubic damping coefficient N, which is

$$N = \frac{(\nu\omega)^{1/2}k^3}{gBl}(1.696l + 2.257B) + \frac{9\nu k^5}{4g}. \tag{8.5}$$

Note that the last term in (8.5) is identical to the first term in (8.2) (this term results from the dissipation due to the potential flow) and will be negligible for short or narrow tanks. The other terms in (8.5) represent the dissipation due to the boundary layers at the sidewalls.

(iii) The contaminated surface with sidewalls

Here we derive an approximate model, combining the previous two situations, incorporating the boundary layers at the sidewalls, the boundary layer at the surface, the potential flow and the streaming in the bulk (driven by the surface film). The total energy of the waves is given by the sum of (3.5) and (7.3). The total energy dissipated during one oscillation of the waves is

$$\langle \chi \rangle \approx \Delta E_1 + \Delta E_{1s} + 2\Delta E_2 + 2\Delta E_3 + \Delta E_4. \tag{8.6}$$

Equations (3.2) and (3.3) give the linear damping coefficient μ (equation (1.2)) and the cubic damping coefficient N, namely

$$N = \frac{9k^5\nu}{4g} - \frac{15u^2\nu}{256k^2} + \frac{(2\omega\nu)^{1/2}(C_r - C_i)(576k^7 + gu^2)}{1024gk^3} + \frac{(\nu\omega)^{1/2}k^3}{gBl}(1.696l + 2.257B) + 0.002762\frac{(\nu\omega)^{1/2}u^2(l+B)}{k^4Bl}, \tag{8.7}$$

which for an inextensible film is

$$N = \frac{9(2\omega\nu)^{1/2}k^4}{16g} + \frac{(\nu\omega)^{1/2}k^3}{gBl}(1.696l + 2.257B) + \frac{9k^5\nu}{4g}. \tag{8.8}$$

Note that the first term in (8.8) is identical to (8.3), and the second term is identical to the first term in (8.5). Remember, in calculating (8.8), that we neglected the $O(\varepsilon^4)$ dissipation in the surface boundary layer.

9. Discussion of the results

Firstly, we redefine A to be the same here as in Chapters III, IV and VI, and Miles (1976, 1984, 1993, 1994). From Miles (1976) and Chapter III,

$$\phi = \frac{2^{1/2}\varepsilon\omega}{k^2}\cos(kx)\exp(kz)(-p\sin\omega t + q\cos\omega t) + \ldots \tag{9.1}$$

at leading-order, and the A used elsewhere in this thesis (we shall denote this as $\hat{A}$ for the rest of this Chapter) was defined as

$$\hat{A} = p + iq. \tag{9.2}$$

Comparing (9.1) with (2.5) gives

$$A = \frac{2^{1/2}\omega}{k^2}\hat{A}, \tag{9.3}$$

which is the formula relating A here with the $\hat{A}$ in Chapters III, IV and VI, and Miles (1976, 1984, 1993, 1994). Note that $\hat{A}$ is dimensionless. Incorporating (9.3) into (8.2), (8.3), (8.5), (8.7) and (8.8) rescales our results for the coefficient of cubic damping N, and it is these modified results that we shall discuss in this section.

Figure 3 shows N given by (8.2) (with (9.3)) plotted against the compressional modulus ξ for three values of the solubility η. The parameters used were

$\nu = 10^{-6}$, $l = 0.7$ and $k = 22\pi / l$ in s.i. units (it is not necessary to specify the breadth B). It can be seen that N is extremely dependent upon ξ for an insoluble film. Note that, in Figure 3, $N = 0.0439$ for $\xi = 0$, and $N = 0.9202$ for $\xi = \infty$, for any η. Also, N is positive except for small values of the surface compressional modulus ξ. Real surface films tend to have a fairly high value for ξ (see Craik 1982), and so the right-hand side of Figure 3 is most likely to give the behaviour of N in the presence of a typical surface film.

Figure 4 shows N given by (8.3), (8.5) and (8.8) (with (9.3)) plotted against k, for the parameters shown in (1.4). Equation (8.3) corresponds to an inextensible film without sidewalls, (8.5) to an uncontaminated surface with sidewalls, and (8.8) to an inextensible surface film with sidewalls. Again, N is positive in all three cases.

The only experimental data that we are aware of which can be compared with these theoretical results comes from Chapter III, in which we measured the ratio of the cubic damping coefficient N to the linear damping coefficient μ in our narrow rectangular tank, with a contaminated surface. In fact, surface contamination was deliberately introduced into the experiments described in Chapter II, since it is extremely difficult to maintain an uncontaminated surface in the laboratory. For an ambient water depth of 2cm, two different values of $\frac{N}{\mu}$ were obtained, using two different types of comparison between theory and experiment: namely, 3.7 and 6.4, giving an average value of 5.05. For the 2cm depth observations $\tanh(kd) = 0.96 \approx 1$. Therefore, this depth approximates infinite depth, which means that our theory can be compared with this experimental result. (The measurements of $\frac{N}{\mu}$ for depths of 1cm and 1.3cm cannot sensibly be compared to the theoretical results given here since these depths do not approximate infinite depth.)

The parameters appropriate to this experiment are those shown in (1.4) with $k = 22\pi / l$. For the first case studied here, the contaminated surface without sidewalls, the linear damping coefficient $\mu = 0.1947$, and coefficient (8.3), with the substitution (9.3), gives $N = 0.9202$ (for an inextensible film). For the second case, the

uncontaminated surface with sidewalls, $\mu = 0.1634$, and the coefficient (8.5), with the substitution (9.3), gives $N = 0.8368$. For the third case, the contaminated surface with sidewalls, $\mu = 0.3582$, and the coefficient (8.8), with the substitution (9.3), gives $N = 1.7131$ (for an inextensible surface film). This gives $N/\mu = 4.725$ in the first case, $N/\mu = 5.120$ in the second case and $N/\mu = 4.783$ in the third case, which are all fairly close to our experimental estimate of 5.05. We chose an inextensible film (for the first and third case) since this usually approximates real surface films (see Craik 1982). (However, in Figure 2, which shows the linear damping, the experimental points are found to be between the uncontaminated surface and the inextensible film curves.) The first and third models are approximate (neglecting $O(\varepsilon^4)$ dissipation in the surface boundary layer) and the second model is exact (though only valid for an uncontaminated surface). All three models, however, give approximately the same results. As capillary hysteresis is neglected in all three models, such good agreement between the theoretical and experimental results suggests that its effect was unimportant.

The ratio between the cubic and linear damping coefficients can be found analytically in all three cases. Applying the transformation (9.3) to each of (8.3), (8.5) and (8.8), and then dividing by the appropriate linear damping in each case gives (in s.i. units)

$$\frac{N}{\mu} = \begin{cases} \dfrac{9}{2} + O(R^{-1/2}), \text{ for (8.3)}, \\ \dfrac{\sqrt{2}(3.392l + 4.514B)}{l+B} + O(R^{-1/2}), \text{ for (8.5)}, \\ \dfrac{9.594l + 12.77B + 4.5klB}{2l + 2B + klB} + O(R^{-1/2}), \text{ for (8.8)}, \end{cases} \tag{9.4}$$

where $R^{-1} \equiv \dfrac{\nu k^2}{\omega}$ is the inverse wave Reynolds number. Only the last formula depends on the wavenumber at leading-order, and all are positive.

In summary, we have found that our estimates of N are almost always positive. This is the most significant result of this Chapter since Faraday waves behave very differently for N negative and N positive (both for hysteresis and mode competition).

We have also demonstrated that N can be very sensitive to changes in the surface compressional modulus, especially for a highly elastic insoluble film. We have compared our theoretical results with an experimental result from Chapter III, and found good agreement. However, it must be remembered that this is only a single experimental result and that the theories were approximate.

10. Faraday waves in deep water

Finally, we examine the dependence of Faraday waves on the coefficient of cubic damping N for infinite depth, as was done in Chapters III and IV for finite depths. Figure 5 shows the forcing F - frequency detuning Ω parameter space diagram for $N/\mu = 4.2$, and Figure 6 shows the equivalent diagram for $N/\mu = 6.9$, for parameter values (1.4), with $k = 22\pi/l$ and $\mu = 0.5$. These values of the cubic damping coefficient were chosen with no special meaning, except that they cover a plausible range. As in Chapter IV, the diagrams were produced by solving equation (1.1) numerically for various values of F and Ω. Each diagram shows regions where stable stationary points and stable limit cycles exist. The neutral curve (shown as a dashed line) denotes the stability of the flat surface: it is stable beneath the line and unstable above it. It can be seen that there are significant differences between Figures 5 and 6, especially in relation to the size and shape of the *stable stationary points* and *stable limit cycles* regions. Also, the lower hysteresis boundary, which is the lowest solid curve in both diagrams, is different: it has a minimum in Figure 5 but not in Figure 6. For equation (1.1), stable limit cycles do not exist at all for $N \leq 0$ (see Chapter IV). These results may be useful for comparison with a future experiment using greater water depths than those of Craik & Armitage (1995).

Figure 1. Graph of the linear damping coefficient μ against the compressional modulus of the surface film ξ for various values of the solubility η of the surface film. Parameters are $l = 0.7, B = 0.025, \nu = 10^{-6}, d = \infty, k = 22\pi / l$.

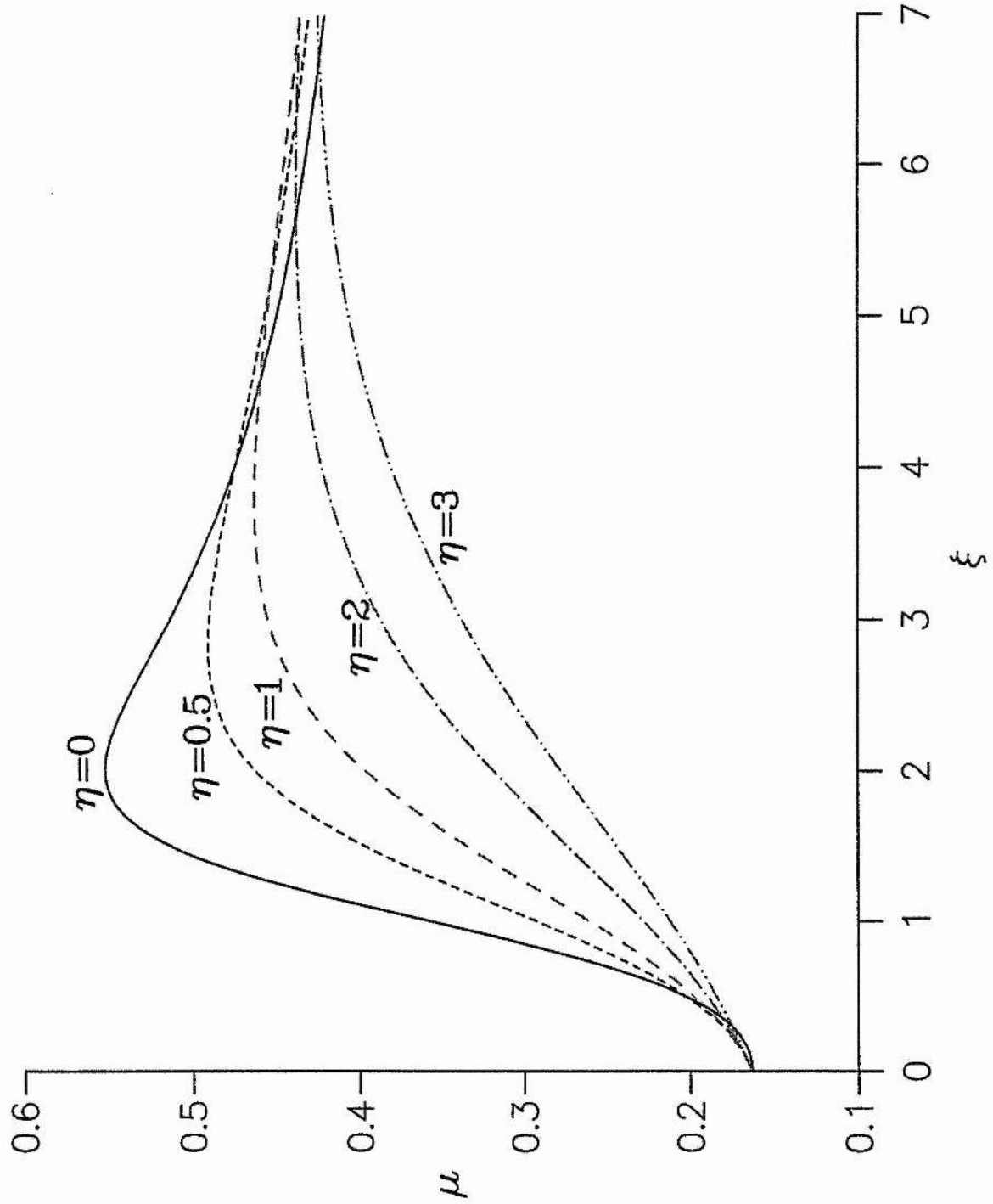

Figure 2. Graph of the linear damping coefficient μ against the ambient water depth d, for an uncontaminated surface, an inextensible surface film and an insoluble surfactant with surface compressional modulus ξ equal to 2. The crosses mark experimental data points inferred from Chapter II. The parameters used were $l = 0.7, B = 0.025, \nu = 10^{-6}, k = 22\pi / l$.

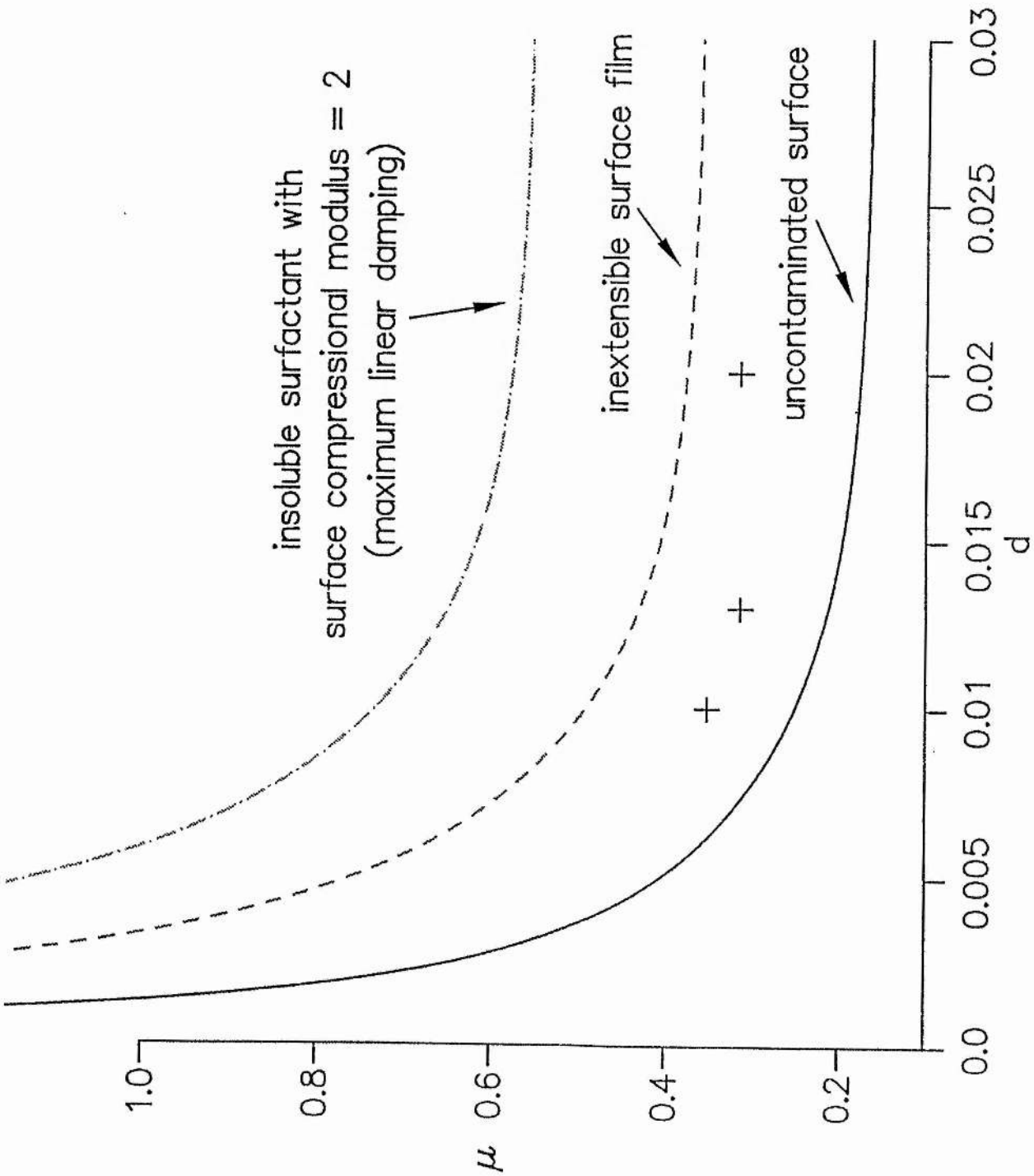

Figure 3. Graph of the coefficient of cubic damping N given by (8.2) with (9.3) against the surface compressional modulus ξ for various values of the solubility η of the surfactant. The parameters used were those of Figure 1.

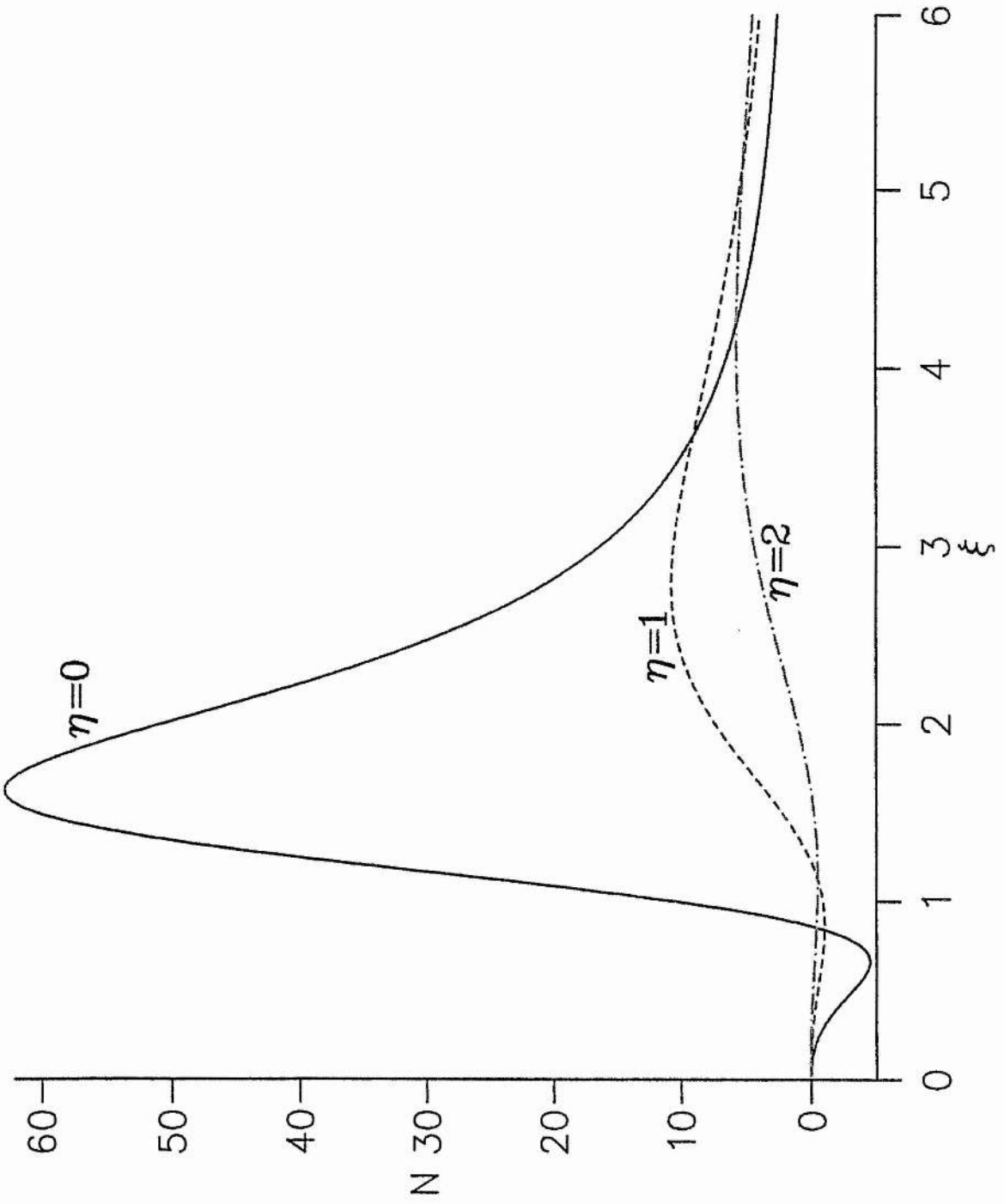

Figure 4. Graph of the coefficient of cubic damping N given by (8.3), (8.5) and (8.8) (all with (9.3)) against k. Parameters used were $l = 0.7, B = 0.025, \nu = 10^{-6}$.

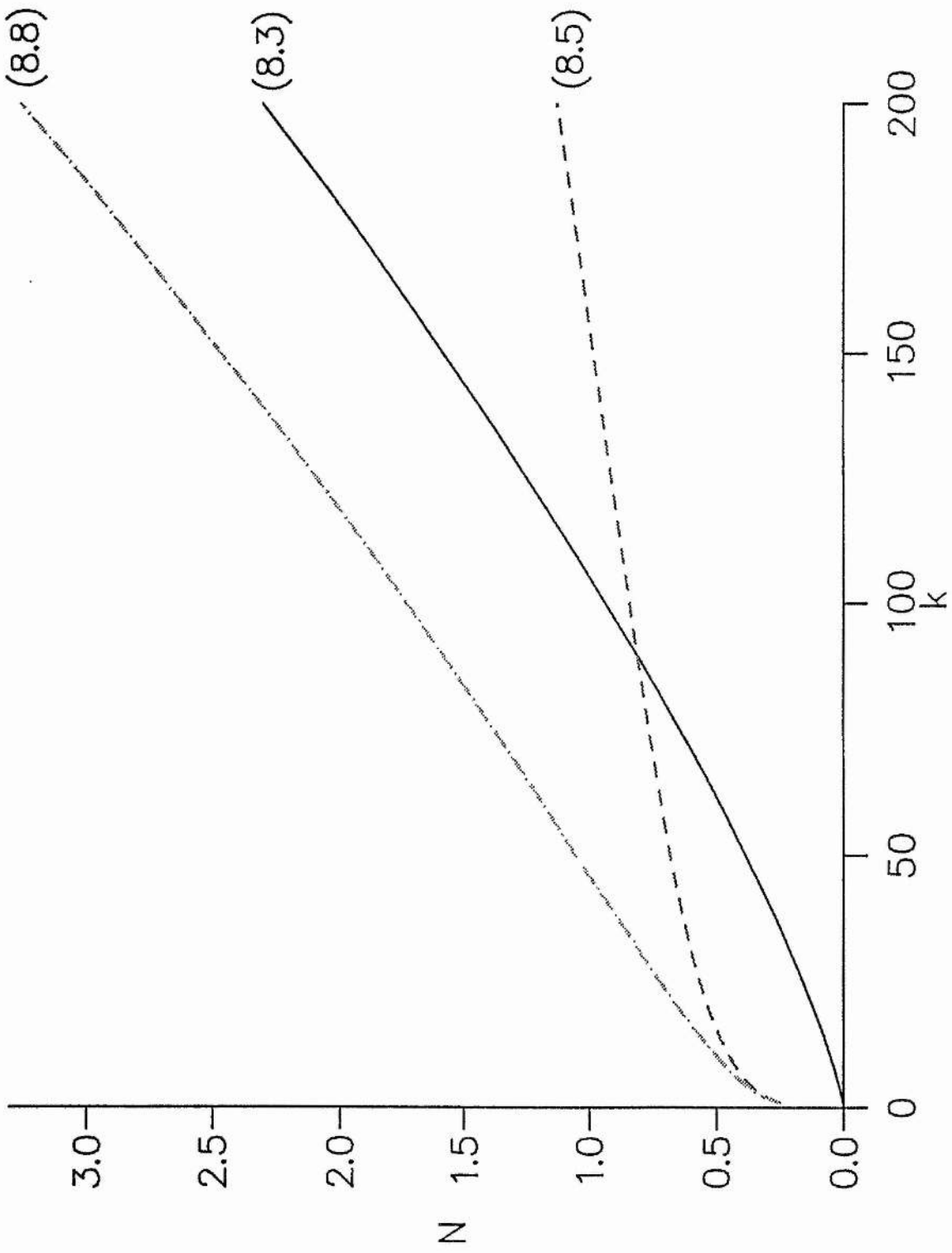

Figure 5. Forcing F frequency detuning Ω space diagram showing the behaviour of (1.1). Parameters used were $l=0.7, B=0.025, \nu=10^{-6}, d=\infty, k=22\pi/l$ which gives $\Pi=\Gamma=0.5, h=-243/128, N/\mu=4.2, \mu=0.5$.

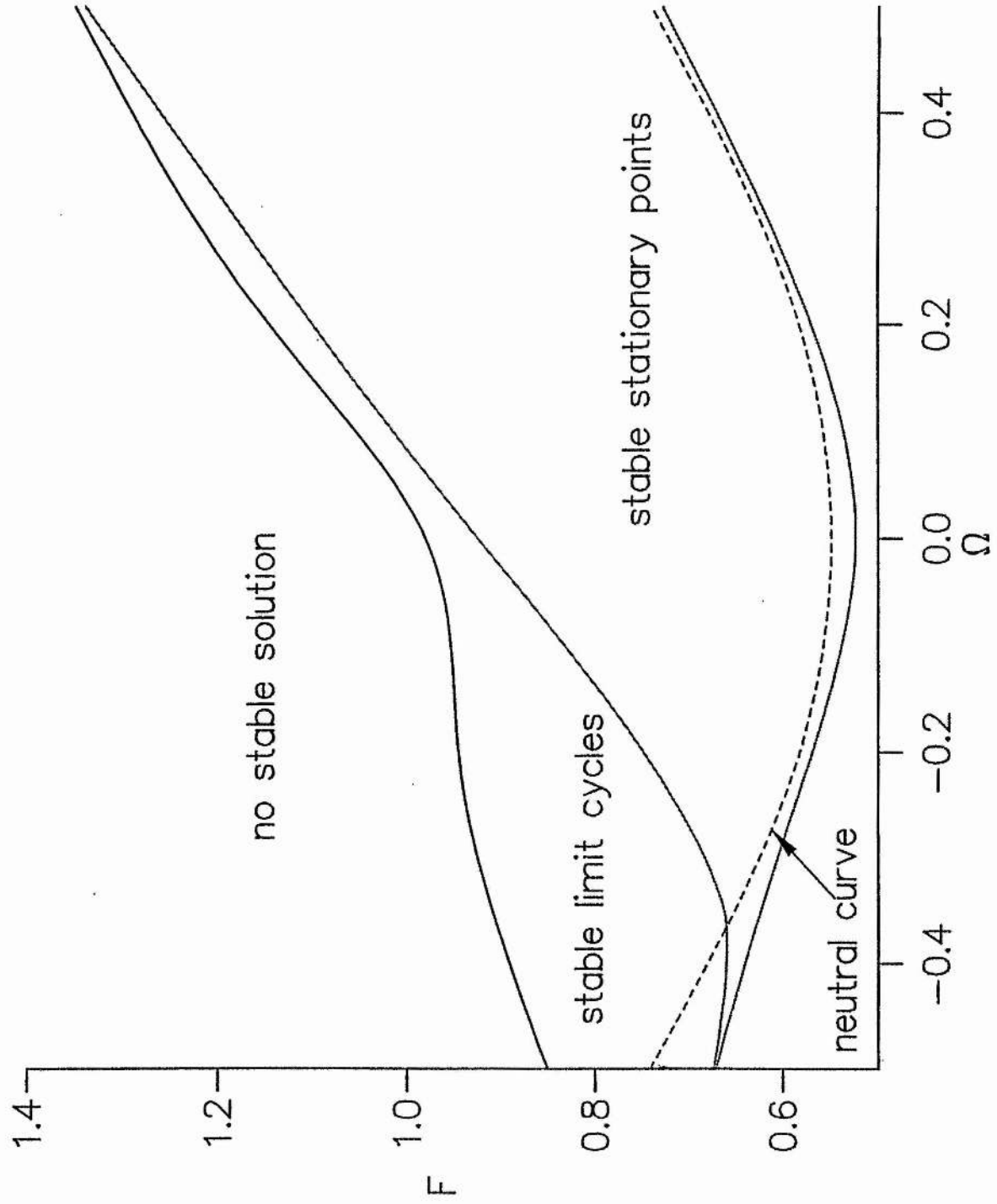

Figure 6. Forcing F frequency detuning Ω space diagram showing the behaviour of (1.1). Parameters used were $l = 0.7, B = 0.025, \nu = 10^{-6}, d = \infty, k = 22\pi / l$ which gives $\Pi = \Gamma = 0.5, h = -243/128, N/\mu = 6.9, \mu = 0.5$.

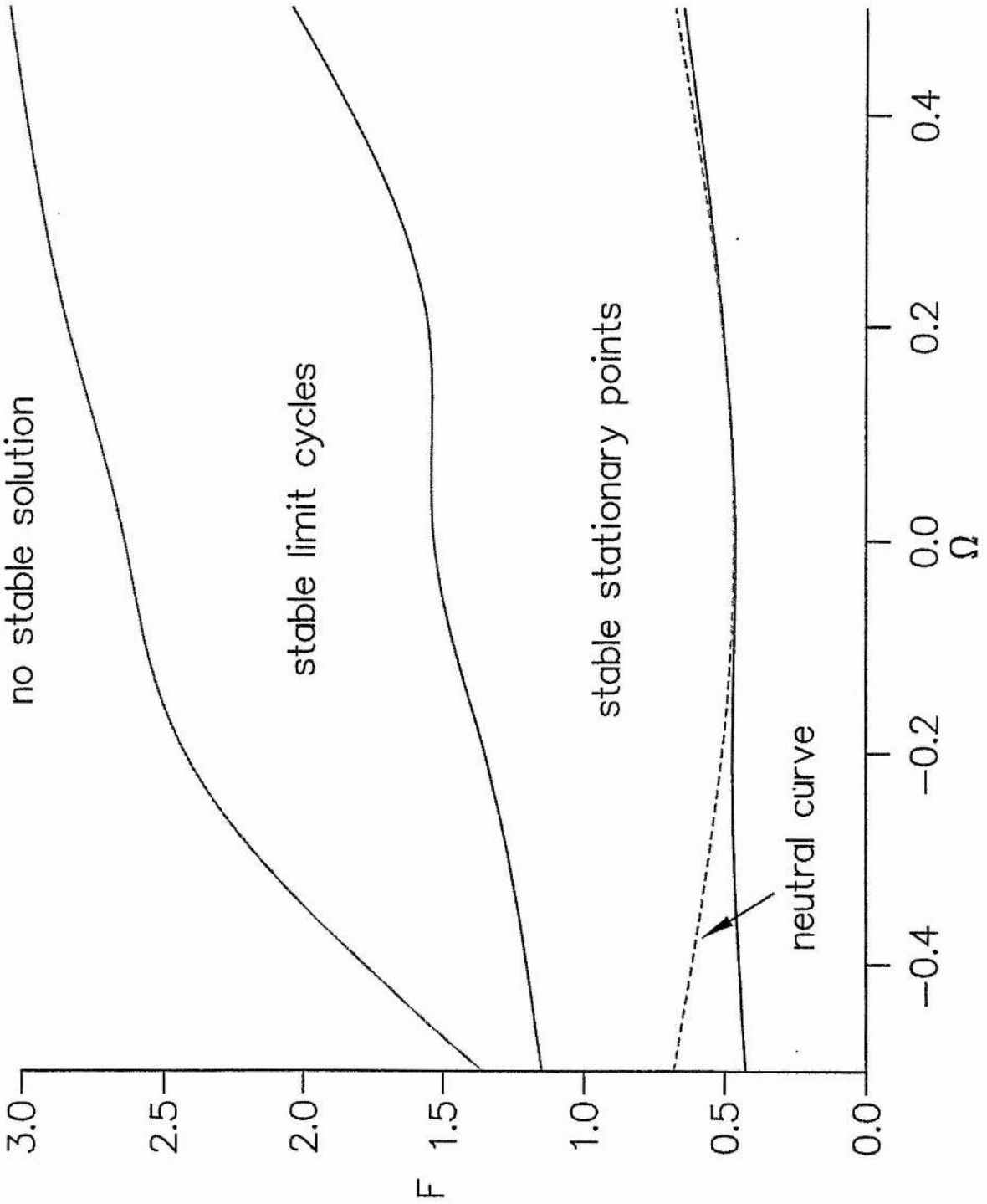

CHAPTER VI

Modulations and intermittency arising from sideband instabilities

1. Introduction

In Chapter II we described experiments carried out by Craik & Armitage (1995). We described strong wave modulations, where a standing wave would lose stability to other wave modes. This was also observed in the experiments of Feng & Sethna (1989) in a slightly rectangular container (by this we mean a rectangle where the length and breadth are approximately equal). Craik & Armitage (1995) also observed intermittency: long periods of calm (lasting for typically 30 seconds or more) with almost no surface waves, were followed by periods of wave activity, which were followed again by long periods of calm (also observed in the experiments of Simonelli & Gollub (1989) in their slightly rectangular basin). Modulations and intermittency were found to be common for the experimental observations of Craik & Armitage (1995) at an ambient water depth of 1cm; for their 2cm depth observations the modulations were less common and intermittency was not observed at all. We propose a scenario for the modulations and intermittency found by Craik & Armitage in their long rectangular tank as essentially due to a sideband instability mechanism (Eckhaus (1963) and Benjamin & Feir (1967)), but modified by the forcing and by tank geometry. This is quite unlike the situation studied by Feng & Sethna (1989) and Simonelli & Gollub (1989), in a slightly rectangular tank, where modulations and intermittency are due to two mode competition, rather than the three mode competition which results from the sideband instability in the long tank described here.

The mode competition observations of Craik & Armitage (1995) have not previously been modelled theoretically (aside from a preliminary study by Craik (1993) where the evolution equations used were simpler than those proposed here and the coefficients were left undetermined). We derive evolution equations for three two-dimensional modes which describe a standing wave and its two sideband modes. Such three-mode interaction equations, incorporating finite depth and surface tension, have not been derived previously. Our theoretical results are found to agree qualitatively, but not quantitatively, with the experimental results of Craik & Armitage (1995) described in Chapter II.

We consider the effects of cubic damping, cubic forcing and fifth-order conservative terms on the model equations, and show that it is essential to retain these higher-order terms for the 2cm water depth model. At this depth, we also study the stability of the single-mode limit cycle described in Chapters III and IV. A parameter regime is found in which the single-mode limit cycle is stable to disturbances from neighbouring modes.

The following section contains the derivation of our nonlinear model, retaining cubic conservative terms. The sideband instability mechanism is discussed in section 3 and time-dependent solutions of this model are described in section 4. Cubic damping, cubic forcing and fifth-order conservative terms are derived in section 5, and this improved model is investigated numerically in section 6. Section 7 contains a discussion of the conclusions of this Chapter.

2. Derivation of model

We use the variational method due to Miles (1976, 1984, 1993, 1994), Umeki & Kambe (1989) and Umeki (1991) to derive our three-mode interaction equations. We consider two-dimensional waves on the surface of an inviscid liquid (introducing

damping at a later stage) with ambient water depth d in a rectangular container of length l. The container experiences a small vertical displacement with frequency 2ω given by

$$z_0 = \varepsilon^2 f \cos 2\omega\tilde{t} \tag{2.1}$$

where $0 < \varepsilon << 1$ is a small parameter and $\tilde{t}$ is time. Following Umeki (1991) and Miles (1994) (as in section 2, Chapter III), the velocity potential (assuming irrotational flow) can be expressed as

$$\phi\left(x,z,\tilde{t}\right) = \sum_n \phi_n\left(\tilde{t}\right)\psi_n(x)\sec h\left(k_n d\right)\cosh\left[k_n(z+d)\right] \tag{2.2}$$

and the free surface as

$$z = \eta\left(x,\tilde{t}\right) = \sum_n \eta_n\left(\tilde{t}\right)\psi_n(x), \tag{2.3}$$

where

$$\psi_n(x) = \sqrt{2}\cos\frac{n\pi x}{l} \tag{2.4}$$

for $0 < x < l$, and

$$k_n = \frac{n\pi}{l}. \tag{2.5}$$

The natural (linear) frequency of each mode is

$$\omega_n^2 = g k_n \tanh\left(k_n d\right)\left(1+\lambda^2 k_n^2\right) \tag{2.6}$$

where $\lambda = (\hat{T}/g)^{1/2}$ is the capillary length, $\hat{T}$ is the kinematic surface tension and g is the acceleration due to gravity.

We assume that the slowly modulated amplitude of the nth mode is

$$\begin{aligned}\eta_n\left(\tilde{t}\right) &= \varepsilon a_n\left\{p_n(t)\cos\omega\tilde{t} + q_n(t)\sin\omega\tilde{t}\right\} \\ &+\varepsilon^2 a_n\left\{A_n(t)\cos 2\omega\tilde{t} + B_n(t)\sin 2\omega\tilde{t} + C_n(t)\right\} + O(\varepsilon^3)\end{aligned} \tag{2.7}$$

where $a_n = \sec h\left(k_n d\right)/k_n$ and $p_n = q_n = 0$ except for the three primary near-resonant modes. The slow time is defined as $t = \varepsilon^2\omega\tilde{t}$. For the three-mode equations, the primary modes correspond to $n = M-1,\ M,\ M+1$, and the second harmonics appearing at $O\left(\varepsilon^2\right)$ correspond to $n = 2(M-1),\ 2M,\ 2(M+1),\ 2M-1,\ 2M+1,\ 1$ and 2, and these are the ten modes that should be summed over in equations (2.2) and (2.3). Note that the modes $n = 1,2$, which are long wave modes, are very different in character from the other 5 second harmonics, which all have approximately the same wavelength; in fact, we will see that the modes $n = 1,2$ are negligible, unless the

frequency of excitation is close to that which gives a long-short wave resonance (this is discussed in more detail at the end of this section). Hereinafter, we shall label $p_{M-1} \equiv p_1$, $q_{M-1} \equiv q_1$, $p_M \equiv p_2$, $q_M \equiv q_2$, $p_{M+1} \equiv p_3$, $q_{M+1} \equiv q_3$, without risk of confusion.

The Lagrangian function is derived in Miles (1976, 1984), Umeki & Kambe (1989) and in Chapter III. As we initially retain only terms up to cubic order, we need use only the $O(\varepsilon^4)$ Lagrangian derived in Miles (1976, 1984) and Umeki & Kambe (1989), rather than the higher-order Lagrangian derived in Chapter III which retains terms up to $O(\varepsilon^6)$. Substituting (2.1) and (2.7) into this function, averaging $\tilde{t}$ over the period $\frac{2\pi}{\omega}$ and neglecting terms of $O(\varepsilon^6)$ gives the averaged Lagrangian $\langle L \rangle$.

Solving $\frac{\partial \langle L \rangle}{\partial A_n} = 0$ for A_n, $\frac{\partial \langle L \rangle}{\partial B_n} = 0$ for B_n, and $\frac{\partial \langle L \rangle}{\partial C_n} = 0$ for C_n, for each n, and substituting back the expressions for A_n, B_n and C_n, gives $\langle L \rangle$ in terms of p's and q's only. Now solving $\frac{\partial \langle L \rangle}{\partial p_i} = \frac{\partial \langle L \rangle}{\partial q_i} = 0$ for $\frac{dp_i}{dt}, \frac{dq_i}{dt}$, for $i = 1,2,3$, gives the evolution equations. The above process is well documented (see Miles 1976, 1984, 1993, 1994, Umeki 1991 and Chapter III) and it is unnecessary to expand on this further.

Substituting $A = p_1 + iq_1, B = p_2 + iq_2, C = p_3 + iq_3$ (not to be confused with the second-order expressions A_n, B_n and C_n) into the evolution equations for p_j, q_j gives the complex forms

$$\begin{aligned} \dot{A} = &-\mu_1 A + i(\Omega + 1)A + iF_1 A^* + i\alpha_1 |A|^2 A + i\alpha_2 |B|^2 A \\ &+ i\alpha_3 B^2 A^* + i\alpha_4 |C|^2 A + i\alpha_5 C^2 A^* + i\alpha_6 |B|^2 C + i\alpha_7 B^2 C^* \end{aligned} \tag{2.8a}$$

$$\begin{aligned} \dot{B} = &-\mu_2 B + i\Omega B + iF_2 B^* + i\alpha_8 |B|^2 B + i\alpha_9 |A|^2 B + i\alpha_{10} A^2 B^* \\ &+ i\alpha_{11} |C|^2 B + i\alpha_{12} C^2 B^* + i\alpha_{13} (ABC^* + A^* BC) + i\alpha_{14} AB^* C \end{aligned} \tag{2.8b}$$

$$\begin{aligned} \dot{C} = &-\mu_3 C + i(\Omega - 1)C + iF_3 C^* + i\alpha_{15} |C|^2 C + i\alpha_{16} |B|^2 C \\ &+ i\alpha_{17} B^2 C^* + i\alpha_{18} |A|^2 C + i\alpha_{19} A^2 C^* + i\alpha_{20} |B|^2 A + i\alpha_{21} B^2 A^* \end{aligned} \tag{2.8c}$$

where

$$F_i = \frac{2f}{a_i}, \quad i = 1,2,3, \tag{2.9}$$

$$\Omega = \frac{\omega^2 - \omega_2^2}{\varepsilon^2 \omega^2}, \tag{2.10}$$

and the dot represents differentiation with respect to t. (Note that choosing the frequency detuning terms in Ω to be in their above form, so that the natural frequencies correspond to $\Omega = 0, \pm 1$, fixes the scaling parameter ε: this is discussed further in the following section). The coefficients α_1, α_8 and α_{15} are well known (see Miles 1976, 1984, Umeki 1991 and Chapter III). These are given by

$$\alpha_i = -\frac{1}{4}a_j^2 k_j^2 + a_j^3 k_j^4 \hat{a}_j + \frac{a_j \omega^2}{8\hat{a}_j \hat{\omega}_j^2}\left\{1 + a_j^2 \omega^2\right\}^2 + \frac{9\lambda^2 a_j g k_j^4}{16\omega^2}$$

$$-\frac{a_j}{4\hat{a}_j}\left(1 - \frac{\hat{\omega}_j^2}{4\omega^2}\right)^{-1}\left\{\frac{3}{4} - 2a_j \hat{a}_j k_j^2 - \frac{1}{4}a_j^2 k_j^2\right\}^2 \text{ for } j = \begin{cases} 1, & i = 1 \\ 2, & i = 8 \\ 3, & i = 15 \end{cases} \tag{2.11}$$

where $\hat{a}_1 = a_4$, $\hat{a}_2 = a_5$, $\hat{a}_3 = a_6$, $\hat{\omega}_1 = \omega_4$, $\hat{\omega}_2 = \omega_5$ and $\hat{\omega}_3 = \omega_6$.

The other nonlinear coefficients are shown graphically in Figures 1 (a-c), since to show all 21 coefficients explicitly would be rather lengthy. Figures 1 (a-c) show their variation with depth for $M = 22$, $l = 0.7$ and $\lambda = 0.002\text{m}$ (the numbers on the curves denote j for each α_j). (It is found that the coefficients do not vary significantly with surface tension.) Also note that $\alpha_5 = \alpha_6$ and $\alpha_{19} = \alpha_{20}$.

For simplicity we redefine $f = \frac{a_2 F}{2}$. The linear damping terms in μ_i have been arbitrarily introduced at this stage, in line with Miles (1984, 1993, 1994), Umeki (1991), Umeki & Kambe (1989) and Chapter III. (Note that we could introduce the damping terms by using a dissipation function: see Miles 1993, 1994). We put $\mu = \mu_1 = \mu_2 = \mu_3$ since

$$\mu_i = \mu\left(1 + O(M^{-1})\right) \text{ for } M >> 1, \tag{2.12}$$

(wavelengths are comparable) which is in agreement with the experimental observations of Craik & Armitage (1995). The value of μ is determined in section 3 through a comparison with experimental data. (Theoretical estimates of μ were derived in the previous Chapter.) Numerical computations with slightly different μ_i's reveal no noticeable changes to the results presented here, and if calculated separately,

μ_1, μ_2 and μ_3 are found to be very similar. Equations (2.8) agree with the two-mode equations derived by Umeki (1991) if B is set to zero.

It is found that, if the above calculations are repeated without including the secondary long-wavelength modes $n=1$ and $n=2$, then the coefficients $\alpha_j \ (j=1,..,21)$ remain approximately unchanged (agreeing to two decimal places). However, our scalings have excluded the possibility of long-short wave resonance. This resonance occurs when

$$\begin{aligned} \omega_1 &= \omega_{M+1} - \omega_M, \\ k_1 &= k_{M+1} - k_M, \end{aligned} \tag{2.13}$$

as described, for example, in Craik (1985). For parameters appropriate to the experiments of Craik & Armitage (1995), namely $M=22$, $\lambda = 0.002$m and $l=0.7$, this resonance occurs at a water depth of about 0.0035 m. Near to this resonance, equations (2.8) are no longer valid. Also, there is second-harmonic resonance in equations (2.8), where the cubic coefficients become infinite. For example, the 21, 22 and 23 half-wavelength modes resonate with the 42, 43, 44, 45 and 46 half-wavelength second-harmonics: these resonances occur at water depths of 0.0006 m, 0.0025 m, 0.0035 m, 0.0043 m and 0.0050 m respectively, for the above parameter values. (Note that the second-harmonic resonance between the primary modes and the 44 half-wavelength mode occurs at the same water depth as the long-short wave resonance here.) Equations (2.8) are no longer valid near to these resonances, as other scalings are then required.

For pure gravity waves in deep water, $d \to \infty$ for $\lambda = 0$, $\alpha_{13} + \alpha_{14} \to 0$. Also, for short capillary-gravity waves,

$$\alpha_i \to \begin{matrix} 0 \text{ for } i = 7,14,21 \\ 1 \qquad \text{otherwise} \end{matrix} \quad \text{as } M \to \infty \text{ for } \lambda \neq 0. \tag{2.14}$$

3. Sideband instability

Here we consider the stability of a standing wave to its sidebands using an approach similar to that of Eckhaus (1963) and Benjamin & Feir (1967). In their experiment, Craik & Armitage (1995) (see Chapter II) observed standing waves that lost stability to neighbouring wave modes: this resulted in modulations.

We consider a finite-amplitude standing wave corresponding to the B-mode in equations (2.8). We consider A and C to be sidebands which are initially small. Here, we determine the conditions for standing wave B to cause A and C to grow exponentially. We therefore linearize equations (2.8) in A and C to give

$$\dot{A} = -\mu A + i(\Omega+1)A + iF_1A^* + i\alpha_2|B|^2A + i\alpha_3B^2A^* + i\alpha_6|B|^2C + i\alpha_7B^2C^* \tag{3.1a}$$

$$\dot{B} = -\mu B + i\Omega B + iF_2B^* + i\alpha_8|B|^2B \tag{3.1b}$$

$$\dot{C} = -\mu C + i(\Omega-1)C + iF_3C^* + i\alpha_{16}|B|^2C + i\alpha_{17}B^2C^* + i\alpha_{20}|B|^2A + i\alpha_{21}B^2A^*. \tag{3.1c}$$

Since we are considering a standing wave, we make equation (3.1b) stationary. This then has stationary points $B = re^{i\theta}$ where

$$r^2 = \frac{-\Omega \pm \left(F_2^2 - \mu^2\right)^{1/2}}{\alpha_8} \tag{3.2}$$

and

$$\cos 2\theta = -\frac{\pm\left(F_2^2 - \mu^2\right)^{1/2}}{F_2}, \quad \sin 2\theta = \frac{\mu}{F_2}. \tag{3.3}$$

Therefore, there are zero, two or four stationary points, depending on the values of μ, F_2, Ω and α_8 (see Chapter II section 3, and Chapter III section 3).

Substituting (3.2) and (3.3) into (3.1a and c) gives two linear differential equations in A and C, for each stationary point. Rewriting these equations in the real form

$$\begin{pmatrix} \dot{p}_1 \\ \dot{q}_1 \\ \dot{p}_3 \\ \dot{q}_3 \end{pmatrix} = \begin{pmatrix} -\mu-\gamma_1 & \beta_1 & -\alpha_7 r^2\sin 2\theta & \beta_3 \\ \beta_2 & -\mu+\gamma_1 & \beta_4 & \alpha_7 r^2\sin 2\theta \\ -\alpha_{21}r^2\sin 2\theta & \beta_5 & -\mu-\gamma_2 & \beta_7 \\ \beta_6 & \alpha_{21}r^2\sin 2\theta & \beta_8 & -\mu+\gamma_2 \end{pmatrix} \begin{pmatrix} p_1 \\ q_1 \\ p_3 \\ q_3 \end{pmatrix} \tag{3.4}$$

where

$$
\begin{aligned}
\beta_1 &= F_1 - \Omega - 1 - \alpha_2 r^2 + \alpha_3 r^2 \cos 2\theta, \\
\beta_2 &= F_1 + \Omega + 1 + \alpha_2 r^2 + \alpha_3 r^2 \cos 2\theta, \\
\beta_3 &= -\alpha_6 r^2 + \alpha_7 r^2 \cos 2\theta, \\
\beta_4 &= \alpha_6 r^2 + \alpha_7 r^2 \cos 2\theta, \\
\beta_5 &= -\alpha_{20} r^2 + \alpha_{21} r^2 \cos 2\theta, \\
\beta_6 &= \alpha_{20} r^2 + \alpha_{21} r^2 \cos 2\theta, \\
\beta_7 &= F_3 - \Omega + 1 - \alpha_{16} r^2 + \alpha_{17} r^2 \cos 2\theta, \\
\beta_8 &= F_3 + \Omega - 1 + \alpha_{16} r^2 + \alpha_{17} r^2 \cos 2\theta, \\
\gamma_1 &= \alpha_3 r^2 \sin 2\theta, \\
\gamma_2 &= \alpha_{17} r^2 \sin 2\theta,
\end{aligned}
\tag{3.5}
$$

gives rise to a matrix from which eigenvalues can be found. If any of these eigenvalues has a positive real part then the standing wave will be unstable to its sidebands. We will examine two cases: namely, the 1cm and 2cm depth cases of Craik & Armitage (1995). For each case, we will solve the characteristic equation at each point in a fine grid of points in $F - \Omega$ space, therefore determining the region of instability. (Equations (3.2) and (3.3) give saddles and sinks of the *B*-wave evolution equation without sidebands. Since only the sinks correspond to a self-stable standing wave, it is only necessary to consider these in the calculation.)

Before calculating the regions of instability, it is necessary to estimate the value of the linear damping parameter μ for each depth. This is done by comparing the r.m.s. acceleration of forcing required in the experiments of Craik & Armitage (1995) to achieve onset of wave motion at resonance with the minimum theoretical value of $F = \mu$. This gives the formula (derived in Chapter III)

$$
\mu = \frac{\Psi}{\sqrt{2} a_2 \omega_2^2 \varepsilon^2} \tag{3.6}
$$

where Ψ is the observed acceleration of forcing. Also, the value of ε can be calculated by comparing (2.10) with the known experimental values for the separation of resonant frequencies of each mode, since these are taken to be a unit distance apart on the Ω-line. This gives a value of $\varepsilon^2 = 0.07$ for the 1cm depth case and $\varepsilon^2 = 0.05$ for the 2cm depth experiment. Using (3.6), this gives the approximate values $\mu = 0.8$ for the lesser depth and $\mu = 1.0$ for the greater depth. This is at first sight

rather surprising, since the r.m.s. forcing required to destablize the flat surface in the experiments of Craik & Armitage (1995) is larger for the 1cm depth than the 2cm depth: but the fact that μ is smaller for the lesser depth is due to the dimensionless scalings imposed in section 2, the actual mode frequencies being closer for the smaller depth than for the larger depth. (Note that this calculation gives the values of the experimental points marked on Figure 2 in Chapter V: however, in Chapter V, the linear damping coefficient is defined differently to here, and so the experimental values shown on Figure 2, Chapter V, are different to the values quoted above.)

The results are shown in Figures 2 and 3, for the 1cm and 2cm depths respectively. In Figure 2, the standing wave is stable in the shaded region, and unstable above this region (the standing wave does not exist below the shaded region). The hyperbolic dashed line denotes the linear stability (neutral) curve of equation (2.8b). Non-zero stationary points of equation (3.1b) exist above the horizontal dashed line for $\Omega > 0$, and above the dashed neutral curve for $\Omega < 0$. The dotted curves show the neutral curve for equations (3.1a) and (3.1c). (We will discuss this diagram in more detail in the following section.)

In the experiment of Craik & Armitage (1995), modulations were found to be common for this depth, with stable standing waves a rarity. This is in general agreement with our theoretical result, though details differ.

Craik (1993) reported that Benjamin-Feir instability in Faraday waves can give rise to purely exponential or exponential-oscillatory growth in A and C depending on whether the unstable eigenvalue has a zero or non-zero imaginary component. For the parameter values examined here, all unstable eigenvalues had zero imaginary part (at the bifurcation), and therefore the growth is purely exponential.

There is considerably less instability for the 2cm water depth diagram, shown in Figure 3 (here the *unstable* area is shaded). The three neutral curves plus the horizontal lower hysteresis boundary are also shown. Again unstable eigenvalues were found to have zero imaginary part giving purely exponential growth in A and C.

In their experiments, Craik & Armitage (1995) found stable standing waves to be more common for this depth than for the lesser depth, a result in broad agreement with our theoretical results, but details differ greatly. We shall return to Figures 2 and 3 in the next section.

4. Time-dependent solutions

Here we solve equations (2.8) computationally to investigate the nature of solutions in the unstable regions of Figures 2 and 3. The approach was to solve (2.8) numerically at each point in a fine grid of points in $F-\Omega$ space. The initial conditions used were $p_1 = q_1 = p_3 = q_3 = 0.001$ and p_2, q_2 equal to the values given by (3.2) and (3.3), therefore simulating a standing wave with two small sidebands. We expect the sidebands to grow in the unstable regions of Figures 2 and 3.

(i) 1 cm ambient water depth

Figure 2 shows the different behaviours of solutions of the initial-value problem. In the region immediately above the shaded stable region, a generalised stationary point was found: this is a six-dimensional stationary point in $(p_1, q_1, p_2, q_2, p_3, q_3)$ space, corresponding to a standing wave with complex spatial structure (it is interesting to note that this standing wave will not pass through the flat surface during its oscillation). Figure 4 shows the variation of the wave amplitude over a short time interval at $x = 0,\ l/2,\ l$: the solid line shows the wave amplitude at the left-hand side of the tank, the dotted-dashed line shows the amplitude at the centre of the tank and the dashed line shows the amplitude at the right-hand side of the tank. It can be seen that the left and right hand sides are out of phase, and differ in their peak amplitude. Note that the left-right symmetry of the tank has been broken here. Further investigation reveals a pair of stationary solutions: $(p_1, q_1, p_2, q_2, p_3, q_3)$ and $(-p_1, -q_1, p_2, q_2, -p_3, -q_3)$. Slightly different initial conditions to those described above, for example by choosing

$p_1 = p_3 = 0.001$, $q_1 = q_3 = -0.001$, will give the other solution. In this case, the curves showing the left and right hand sides of the tank in Figure 4 are swapped around. Therefore, there are two solutions: one where the peak amplitude of the standing wave over a single period is greater at the left of the tank than at the right of the tank, and another solution where the peak amplitude is greater at the right of the tank than at the left.

The periodic/chaotic region in Figure 2 denotes a six-dimensional periodic or chaotic solution in $(p_1, q_1, p_2, q_2, p_3, q_3)$ space. Figures 5 (a-g) show the variation of the six variables at points A, B, C, D, E, F and G in Figure 2 respectively. Figure 5 (g) appears to be chaotic, while the other six graphs show periodic behaviour. (Note that the time t is a non-dimensional time given by $t = \varepsilon^2 \omega \tilde{t}$, where $\tilde{t}$ is the time in seconds; therefore, at this depth, a time length of 200 on the Figures corresponds to 105.57 seconds. Remember, also, that the fast time scale was averaged out in section 2, and is not shown in Figure 5). Again, there are two similar solutions: (A, B, C) and $(-A, B, -C)$, with the initial conditions choosing which is selected (one of the solutions corresponds to the travelling wave going from left to right in the tank initially, and the other solution corresponds to the travelling wave going from right to left initially). The r.m.s. wave amplitude at $x = 0, l$ is shown in Figures 6 (a-c) for points A, B and G respectively (the solid line gives the r.m.s. amplitude at the left of the tank and the dashed line at the right of the tank). Again, left-right symmetry in the tank is broken. It can be seen that the behaviour at point A, for example, resembles the strong modulations observed by Craik & Armitage (1995): Figure 6 (a) shows evidence of travelling waves, along the length of the tank, periodically reversing direction. Also, note that Figures 6 (a-c) are progressively more peaked.

In Figures 5 (b) and 5 (c), there are quite long periods of relative calm where all six variables are approximately zero, followed by periods of intense wave activity. (Figure 5(c) shows calm periods lasting for about 22 seconds). This resembles the intermittency found in the experiments of Craik & Armitage (1995) at the 1cm water depth. In both cases, it can be seen that a standing wave (in $B = p_2 + iq_2$) grows from

the flat surface, because the flat surface is unstable. Then, because of the Benjamin-Feir instability mechanism, the standing wave becomes unstable to its sidebands, resulting in modulations. Then interaction with the sidebands causes the central of the three modes to die away, and this in turns destroys the sidebands since their energy comes from the central mode. Therefore near calm is restored.

Craik & Armitage (1995) observed that the length of the calm period varied, depending upon the frequency and acceleration of forcing, finding periods of calm lasting for anything up to several minutes. They also found one example in which the length of the calm period varied during a single time-series (see Chapter II). The length of the calm periods found in equations (2.8) also vary with F and Ω; though only periods of calm lasting up to about 25 seconds have been found here.

The uppermost region in Figure 2 can support a single stationary point in the A mode, which corresponds to a standing wave. Here other modes will become significant since this mode is itself unstable to its sidebands, though these have not been examined.

The circles marked on Figure 2 denote experimental points from Craik & Armitage (1995) for the onset of standing waves from a flat surface. The squares mark the subsequent onset of modulations, or the onset of modulations from a flat surface, depending on whether there was an intermediate region of stable standing waves. It can be seen that the agreement is not good. The only data points which seem to agree with the theory are the points at $\Omega \approx 0.2$. Therefore, equations (2.8) give qualitative agreement with experimental results for this depth, but not quantitative agreement. We shall discuss this depth further in the following sections.

(ii) 2 cm ambient water depth

We now turn to the 2cm depth experiment. In the wedge shaped instability region on the right-hand side of Figure 3, the solutions were always found to tend towards a six-dimensional stationary point, corresponding to a standing wave with complex spatial structure. No modulating solutions were found here for the chosen initial data. In the experiments of Craik & Armitage (1995), stable standing waves were found to be

common for this depth, with modulations only appearing for values of the forcing F above those needed to drive stable standing waves. However, we now see that equations (2.8) predict no modulations at all for this depth. We therefore conclude that higher-order nonlinear terms in the evolution equations are needed here, and these will be derived in the following section.

5. Higher-order nonlinear terms

We now turn our attention to the cubic forcing, cubic damping and the fifth-order conservative terms, which, as discussed in Chapter III, all appear at the next level in the evolution equations. Here we calculate these terms, though we do not determine the complete set of fifth-order conservative terms. As a result of this, our equations are valid for considering the onset of the sideband instability, but rather limited for considering the resulting time-dependent modulations. It would be desirable to derive all the fifth-order conservative terms, but this is an intimidating prospect.

It was seen in Chapter III that third harmonics in both space and time contribute to the cubic forcing terms (as well as the fifth-order conservative terms). However, we demonstrated that as the depth $d \to \infty$ and capillary length $\lambda \to 0$ then the coefficient of cubic forcing for a single mode derived considering first, second and third harmonics tends towards the coefficient of cubic forcing derived considering only the first and second harmonics (as in Miles 1993, 1994). Also, we showed that for the Craik & Armitage (1995) experiment, for a water depth of about 2cm and for a coefficient of surface tension typical for water, the two methods produce approximately the same values for the coefficient of cubic forcing (though there are significant differences for the 1cm depth experiment). We shall therefore assume, for simplicity, that the same will apply for all cubic forcing coefficients in the three-mode equations, and derive approximate coefficients using only the first and second harmonics in the model, as in Miles (1993, 1994).

We extend the derivation of section 2. Taking the averaged Lagrangian and substituting in the expressions derived for A_n, B_n and C_n, we retain forcing terms of $O(\varepsilon^6)$ in addition to those $O(\varepsilon^4)$ terms retained in section 2. As before, solving $\frac{\partial\langle L\rangle}{\partial p_i} = \frac{\partial\langle L\rangle}{\partial q_i} = 0$ for $\frac{dp_i}{d\tau}, \frac{dq_i}{d\tau}$, for $i = 1,2,3$, gives the evolution equations, including cubic forcing terms. The evolution equations now become the old equations (2.8) plus some new terms:

$$\begin{aligned}
\dot{A} &= \text{terms in (2.8)} + \varepsilon^2 iF\left\{\begin{matrix}\Gamma_1\left(q_1^3 + ip_1^3\right) + \Gamma_2\left(q_1q_2^2 + ip_1p_2^2\right) \\ +\Gamma_3\left(q_2^2q_3 + ip_2^2p_3\right) + \Gamma_4\left(q_1q_3^2 + ip_1p_3^2\right)\end{matrix}\right\} \\
\dot{B} &= \text{terms in (2.8)} + \varepsilon^2 iF\left\{\begin{matrix}\Gamma_5\left(q_2^3 + ip_2^3\right) + \Gamma_6\left(q_1^2q_2 + ip_1^2p_2\right) \\ +\Gamma_7\left(q_2q_3^2 + ip_2p_3^2\right) + \Gamma_8\left(q_1q_2q_3 + ip_1p_2p_3\right)\end{matrix}\right\} \\
\dot{C} &= \text{terms in (2.8)} + \varepsilon^2 iF\left\{\begin{matrix}\Gamma_9\left(q_3^3 + ip_3^3\right) + \Gamma_{10}\left(q_2^2q_3 + ip_2^2p_3\right) \\ +\Gamma_{11}\left(q_1q_2^2 + ip_1p_2^2\right) + \Gamma_{12}\left(q_1^2q_3 + ip_1^2p_3\right)\end{matrix}\right\}.
\end{aligned} \tag{5.1}$$

The cubic forcing coefficients are given in Table 1.

The cubic damping terms might be derived from an extension of the dissipation function proposed by Miles (1994), namely

$$D = \mu\left(e_1 + e_2 + e_3\right) + \sum_{m=1,2,3}\sum_{n=1,2,3}\tilde{A}_{mn}e_me_n \tag{5.2}$$

(assuming equal μ_i's) where $e_n \equiv \frac{1}{2}\left(p_n^2 + q_n^2\right)$. The first part of this function gives the linear damping already in equation (2.8). The coefficients $\tilde{A}_{mn}$ $(m \neq n)$ are all unknown, and are difficult to calculate, either theoretically or experimentally; approximate formulae for the diagonal coefficients A_{mn} were derived in the previous Chapter. Since we have no better information, we will assume, for purpose of illustration, that all the cubic damping coefficients in the evolution equations are equal.

The damping terms on the right-hand side of the evolution equation for the $p_n + iq_n$ mode are given by $-\frac{\partial D}{\partial p_n} - i\frac{\partial D}{\partial q_n}$. Therefore we postulate the evolution equations to be

$$\begin{aligned}
\dot{A} &= \text{r.h.s. of (5.1)} + \varepsilon^2 NA\left\{|A|^2 + |B|^2 + |C|^2\right\} \\
\dot{B} &= \text{r.h.s. of (5.1)} + \varepsilon^2 NB\left\{|A|^2 + |B|^2 + |C|^2\right\} \\
\dot{C} &= \text{r.h.s. of (5.1)} + \varepsilon^2 NC\left\{|A|^2 + |B|^2 + |C|^2\right\},
\end{aligned} \tag{5.3}$$

Table 1 Coefficients of cubic forcing

Coefficient of cubic forcing for $M = 22$ and $\hat{T} = 0.00004$.

	depth 2.075cm	infinite depth
$\frac{F\Gamma_1}{f}$	231.26	188.99
$\frac{F\Gamma_2}{f}$	433.04	362.53
$\frac{F\Gamma_3}{f}$	203.86	174.40
$\frac{F\Gamma_4}{f}$	409.55	349.52
$\frac{F\Gamma_5}{f}$	238.15	200.10
$\frac{F\Gamma_6}{f}$	508.17	416.82
$\frac{F\Gamma_7}{f}$	451.06	386.33
$\frac{F\Gamma_8}{f}$	478.44	401.04
$\frac{F\Gamma_9}{f}$	248.62	213.38
$\frac{F\Gamma_{10}}{f}$	524.22	441.44
$\frac{F\Gamma_{11}}{f}$	278.02	229.12
$\frac{F\Gamma_{12}}{f}$	558.55	459.19

where N is a single cubic damping coefficient. In Chapter III we estimated N for water depths of 1 cm, 1.3 cm and 2cm from experimental data using hysteresis results. We will use these estimates of the value of this coefficient: $N = 3.7$ for an ambient water depth of 2cm, and $N = -0.4$ for a water depth of 1cm.

In Chapter III we also derived the fifth-order conservative term, along with its coefficient, for the single mode equation. If we only consider the onset of the sideband instability, and not the subsequent time-dependent motion, then we can assume that $|A|,|C| << |B| \leq O(1)$. In this case, all fifth-order conservative terms apart from $-i\varepsilon^2 h|B|^4 B$ (which appears on the right-hand side of the $\dot{B}$ equation) and linear terms in A and C such as $i\varepsilon^2|B|^4 A, i\varepsilon^2|B|^4 C, i\varepsilon^2 B^4 A^*, i\varepsilon^2 B^4 C^*$ (which appear on the right-hand side of the $\dot{A}$ and $\dot{C}$ equations) will be negligible. (Moreover, $-i\varepsilon^2 h|B|^4 B$ will be large compared with terms of the form $i\varepsilon^2|B|^4 A, i\varepsilon^2|B|^4 C, i\varepsilon^2 B^4 A^*, i\varepsilon^2 B^4 C^*$.) We shall initially include all these fifth-order conservative terms in our evolution equations, though we later conclude that only $-i\varepsilon^2 h|B|^4 B$ is important; we will then additionally neglect linear terms in A and C such as $i\varepsilon^2|B|^4 A, i\varepsilon^2|B|^4 C, i\varepsilon^2 B^4 A^*, i\varepsilon^2 B^4 C^*$. The values of h were computed in Chapter III for various depths, surface tensions etc. For the 2cm depth experiment we calculated h to be -2.1, and for a water depth of 1cm we calculated h to be -0.9. We shall initially assume, for simplicity, that the fifth-order conservative terms which are linear in A and C are also multiplied by this coefficient h (which is not unreasonable given similar mode shapes).

The equations proposed in this section are therefore

$$\begin{aligned}
\dot{A} &= \text{r.h.s. of (5.3)} - i\varepsilon^2 h\left(|B|^4 A + |B|^4 C + B^4 A^* + B^4 C^*\right) \\
\dot{B} &= \text{r.h.s. of (5.3)} - i\varepsilon^2 h|B|^4 B \qquad (5.4) \\
\dot{C} &= \text{r.h.s. of (5.3)} - i\varepsilon^2 h\left(|B|^4 A + |B|^4 C + B^4 A^* + B^4 C^*\right),
\end{aligned}$$

which, though over-simplified, provide an illustrative model for determining the onset of the sideband instability. Also, so long as $|A|,|C| << |B| \leq O(1)$ i.e. the motion is dominated by the standing wave (central mode), then time-dependent behaviour can be (tentatively) examined.

For the 1cm depth experiment, the cubic forcing coefficients calculated here are not reliable (as explained above). However, since cubic forcing tends to be the least significant of the three higher-order effects (see Chapter III), we shall proceed with the higher-order calculation in this case without the cubic forcing terms in the equations, though retaining the cubic damping terms (5.3) and the fifth-order conservative terms (5.4).

6. The effects of higher-order terms on the sideband instability

The higher-order terms derived in the previous section give a more realistic description of the single-mode hysteresis region, and transform the lower hysteresis boundary, formerly a horizontal line in the previous model (see Figures 2 and 3), into a curve. We examine the nature of the behaviour in the $F-\Omega$ plane by solving the higher-order equations at each point over a fine grid, and investigate the stability of the standing wave in the central B-mode to sideband disturbances. We adopt initial conditions similar to those used in section 4, except now p_2 and q_2 are solutions of the fifth-order amplitude equation in B, discussed in Chapters III and IV.

(i) Water depth of 2 cm

Here we examine the higher-order equations for parameter values (in s.i. units) $M=22,\ l=0.7,\ \lambda=0.002$ and $d=0.02$. For this depth we retain the cubic forcing, cubic damping and the fifth-order conservative terms proposed in the previous section. We carried out several numerical investigations both with and without the fifth-order conservative terms which are linear in A and C, namely $i\varepsilon^2|B|^4A, i\varepsilon^2|B|^4C, i\varepsilon^2B^4A^*, i\varepsilon^2B^4C^*$, and we found very similar results in the two cases. However, we found that the fifth-order conservative term $-i\varepsilon^2h|B|^4B$ has significant effects upon the results, through its modification of the standing wave. Here we present our results for the equations

$$\begin{aligned}
\dot{A} &= \text{r.h.s. of (5.3)} \\
\dot{B} &= \text{r.h.s. of (5.3)} - i\varepsilon^2 h|B|^4 B \\
\dot{C} &= \text{r.h.s. of (5.3).}
\end{aligned} \tag{6.1}$$

Figure 7 shows the stability diagram produced using (6.1); comparing Figures 3 and 7, we see that the stability diagram has changed considerably from the one previously determined using the cubic equations (2.8). Because of the higher-order terms, the horizontal lower hysteresis boundary from Figure 3 has been transformed into a curve in Figure 7 (labelled the hysteresis boundary). The stable standing wave region corresponds to a stable stationary point of the B mode, with the small A and C modes tending towards zero. The stable limit cycle region corresponds to a periodic solution in the B mode, the A and C waves again tending towards zero. Figure 8 shows a typical solution in this region. The B mode solution can be seen to be periodic, with the two sideband perturbations decaying to zero. We have therefore shown that the limit cycle of a single mode (discussed in Chapter IV) is (here) stable to sideband disturbances.

The large three-wave modulation region at the top left corner of Figure 7 corresponds to very complex solutions of the three mode equations. Within this region, A and C can grow considerably, and so the validity of the evolution equations (to describe the time-dependent behaviour after the sideband instability has occurred) is doubtful, as discussed in the previous section. But there is no doubt that the equations satisfactorily predict a sideband instability here. We (tentatively) examine the nature of the time-dependent behaviour, so long as the condition $|A|,|C| << |B| \leq O(1)$ is approximately true. Figure 9 (a) shows one such solution at point A on Figure 7, and Figure 9 (b) shows the corresponding r.m.s amplitude variation at both ends of the tank. Comparing Figure 9 (a) with Figures 5 (a-g), and comparing Figure 9 (b) with Figures 6 (a-c), reveal that the modulations at the greater depth have a short modulating time scale which is absent at the lesser depth. (Note, once more, that t is the slow time, given by the expression $t = \varepsilon^2 \omega \tilde{t}$). In the 3 wave-modulation region on the right side of Figure 7, we found that solutions with our chosen initial data always tended towards a six-dimensional stationary point, and so do not display time-periodic behaviour.

There is also a region in the bottom-left corner of Figure 7 where all six variables tend towards zero, resulting in a flat surface. The dashed line cannot be continued further on Figure 7 because A and C become very large (before tending towards zero), and so violate our assumptions.

The squares on Figure 7 show experimental data points from Craik & Armitage (1995) for the onset of modulations and the circles show data points for experimental measurements of the neutral curve. There is good agreement between theory and experiment for the neutral curve data, but results for the onset of modulations do not match nearly so well.

The above calculations were repeated for the cubic damping coefficient N equal to 5.5 (rather than 3.7, as before). It was found that the sideband instability curve, the lower hysteresis boundary and the stable limit cycle region all moved considerably. The regions of stable limit cycles and stable standing waves were found to be much smaller than in Figure 7, with almost no stable solutions being found outside of the neutral curve. Agreement between theory and experiment for the data points within the neutral curve was improved, but overall, the agreement was found to be worse than before. It therefore appears that the unsatisfactory quantitative agreement between theory and experiment is not due to a poor choice of the cubic damping coefficient N. It seems likely that even higher-order terms (fifth-order damping, fifth-order forcing and seventh-order conservative terms) are needed in the evolution equations to achieve quantitative agreement between theory and experiment. In short, equations (6.1) give only qualitative agreement between theory and experiment for this depth. But this is an improvement over equations (2.8), which failed to predict modulations at all for this depth.

(ii) Water depth of 1cm

Here we examine equations (6.1) for a water depth of 1cm, though neglecting cubic forcing terms, since we do not have an estimate available for the cubic forcing coefficients in this case. The results of this investigation are shown in Figure 10.

Comparing this with Figure 2, it can be seen that the higher-order nonlinear terms now included have shifted the sideband instability curve upwards, and have significantly altered the lower hysteresis boundary (as in Chapter III). In Figure 10 we do not investigate the periodic/chaotic region (as we did in Figure 2) since the assumptions used in the derivation of (6.1) are violated within this region of Figure 10. The squares and circles mark experimental results from Craik & Armitage (1995) showing the onset of modulations and standing waves respectively. Unfortunately, there is poor quantitative agreement between theory and experiment for the onset of modulations here.

7. Conclusions

It has been shown that the higher-order terms completely alter the stability diagram for the larger depth (compare Figure 3 with Figure 7), though they leave the stability diagram largely unchanged for the smaller depth, except with regard to the location of the lower hysteresis boundary. It seems likely that the change in sign of the cubic damping coefficient N between water depths of 1cm and 2cm is the reason why the higher-order nonlinear terms have so much effect at the larger depth, but so little at the smaller depth. (Note that the cubic damping terms are destablizing for the greater depth and stablizing for the lesser depth.)

Arguably, the general character of the experimental observations of Craik & Armitage (1995) (see Chapter II) have been captured theoretically, though agreement is qualitative rather than quantitative. Our model for the ambient water depth of 1cm gives rise to strong modulations and intermittency, much as seen in Craik & Armitage's experiment. We have identified strong modulations in equations (2.8) (see Figures 5 (a) and 6 (a)), which corresponds to travelling waves moving along the length of the tank, periodically reversing direction every few seconds, as seen by Craik & Armitage. We have also found intermittency, with long periods of calm separated by wave activity.

We also identified a six dimensional stationary point which corresponds to a standing wave with complex spatial structure. Quantitative agreement for the onset of modulations is poor. This may be due to the fact that the depth is near to that required for second-harmonic resonance. We anticipate that the inclusion of second-harmonic resonance into the model would give better quantitative agreement. As cubic forcing was not included in the higher-order model for this depth, this may also have contributed to the poor quantitative agreement.

For the 2cm depth case, we find that the cubic equations (2.8) are completely inadequate for describing the experimental observations of Craik & Armitage (1995). However, the higher-order equations (6.1) predict a large region where standing waves are stable to sideband perturbations, as well as predicting modulations for larger values of F; this gives good qualitative agreement with Craik & Armitage. We also find very complicated modulations at this depth which exhibit two slow time scales: comparing Figure 9 (a) with Figures 5 (a-g), and comparing Figure 9 (b) with Figures 6 (a-c), we see that the modulations at the greater depth have a short modulating time scale which is absent at the lesser depth. The higher-order 2cm depth model also gives a parameter regime in which the single-mode limit cycle, discussed in Chapters III and IV, is stable to sideband perturbations.

Despite qualitative agreement between theory and experiment for the greater depth, quantitative agreement for the onset of modulations is not good: we speculate that it would be necessary to retain even more higher-order nonlinear terms (quintic damping and forcing, and seventh-order conservative terms) to achieve quantitative agreement between theory and experiment.

In summary, we have attempted to model, with some success, the modulations and intermittency observed by Craik & Armitage (1995), in terms of the Benjamin & Feir (1967) and Eckhaus (1963) instability mechanism. We have emphasised the significance of higher-order nonlinear terms, especially for the greater depth of 2 cm.

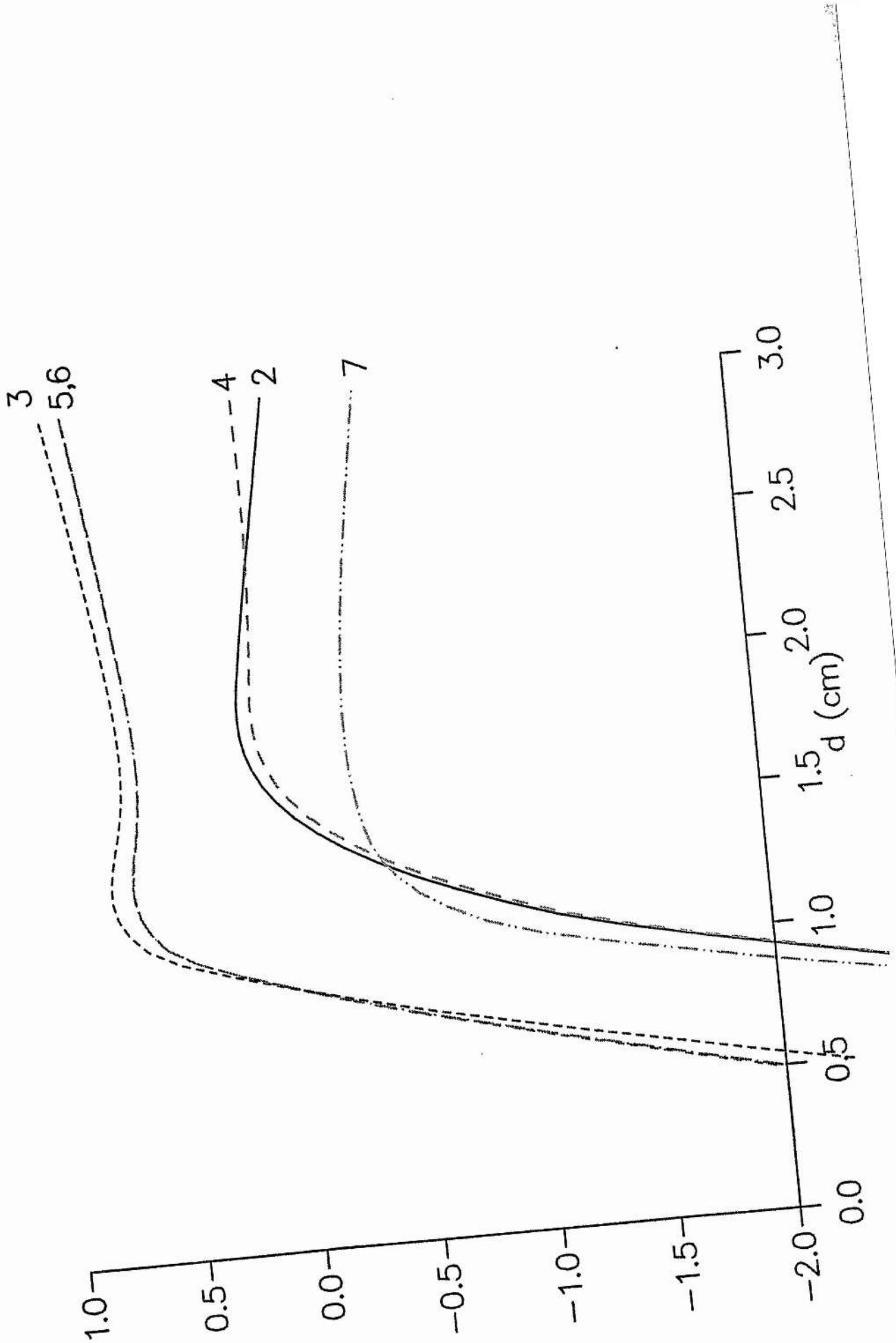

Figure 1. The variation of nonlinear coefficients with depth (a-c).

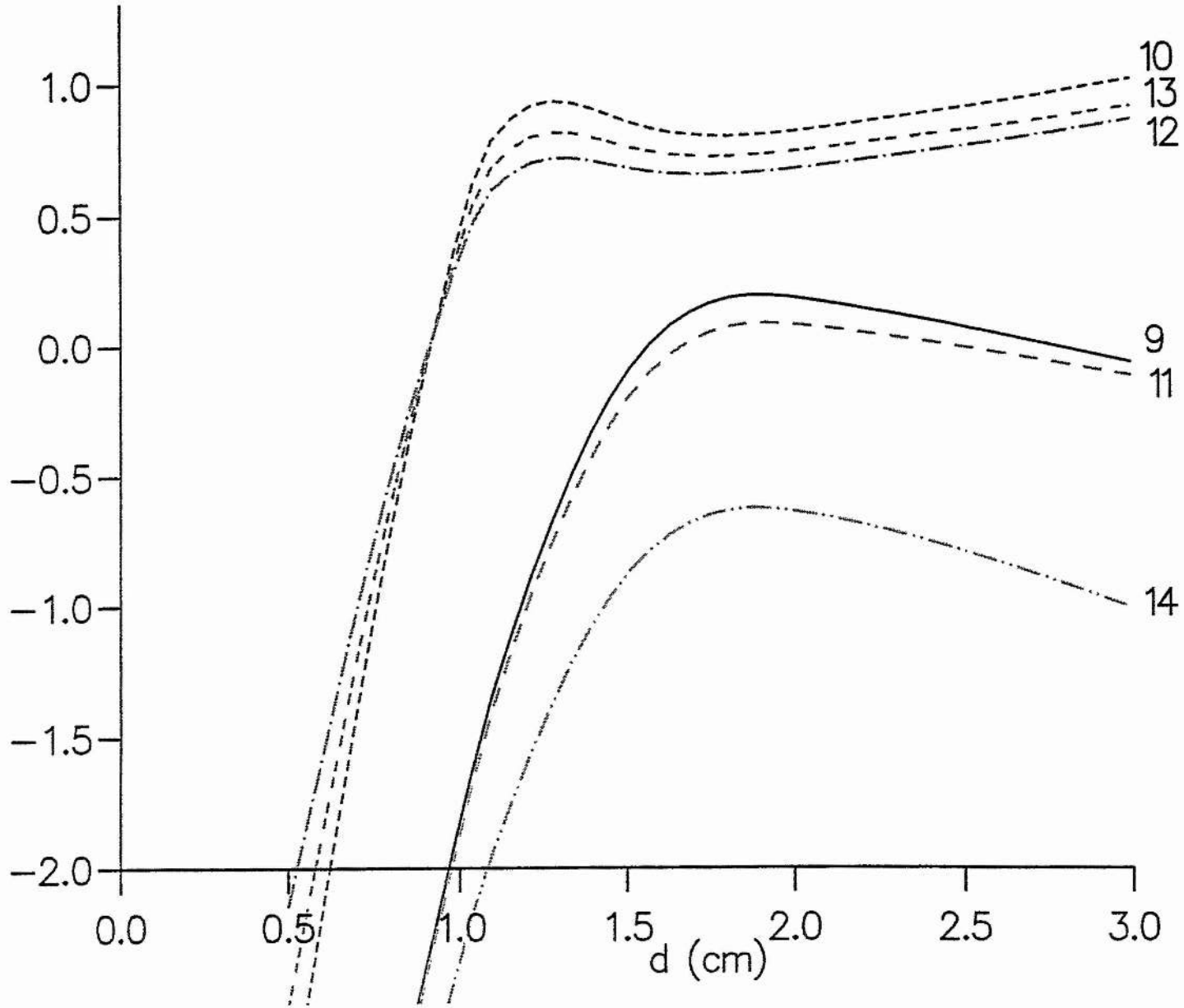

124 b

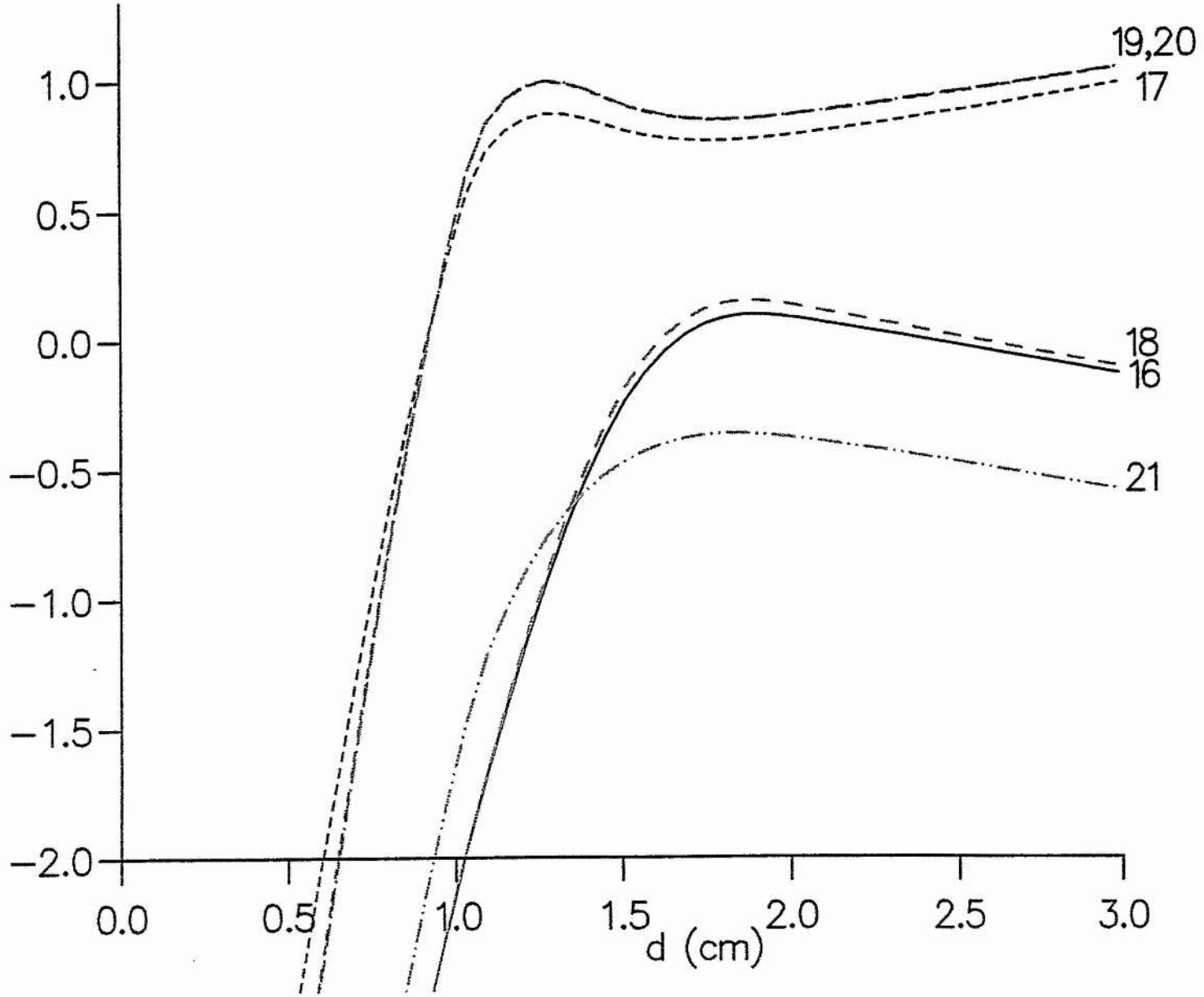
19,20
17
18
16
21
1.0
0.5
0.0
−0.5
−1.0
−1.5
−2.0
0.0
0.5
1.0
1.5
2.0
2.5
3.0
d (cm)

Figure 2. Stability diagram for water depth of 1cm, surface tension $\hat{T} = 0.00004$, tank length $l = 0.7$ and wave mode $M = 22$. The circles denote experimental data points from Craik & Armitage (1995), for the onset of standing waves from the flat surface. The squares denote experimental data points for the onset of modulations from either the flat surface or standing waves.

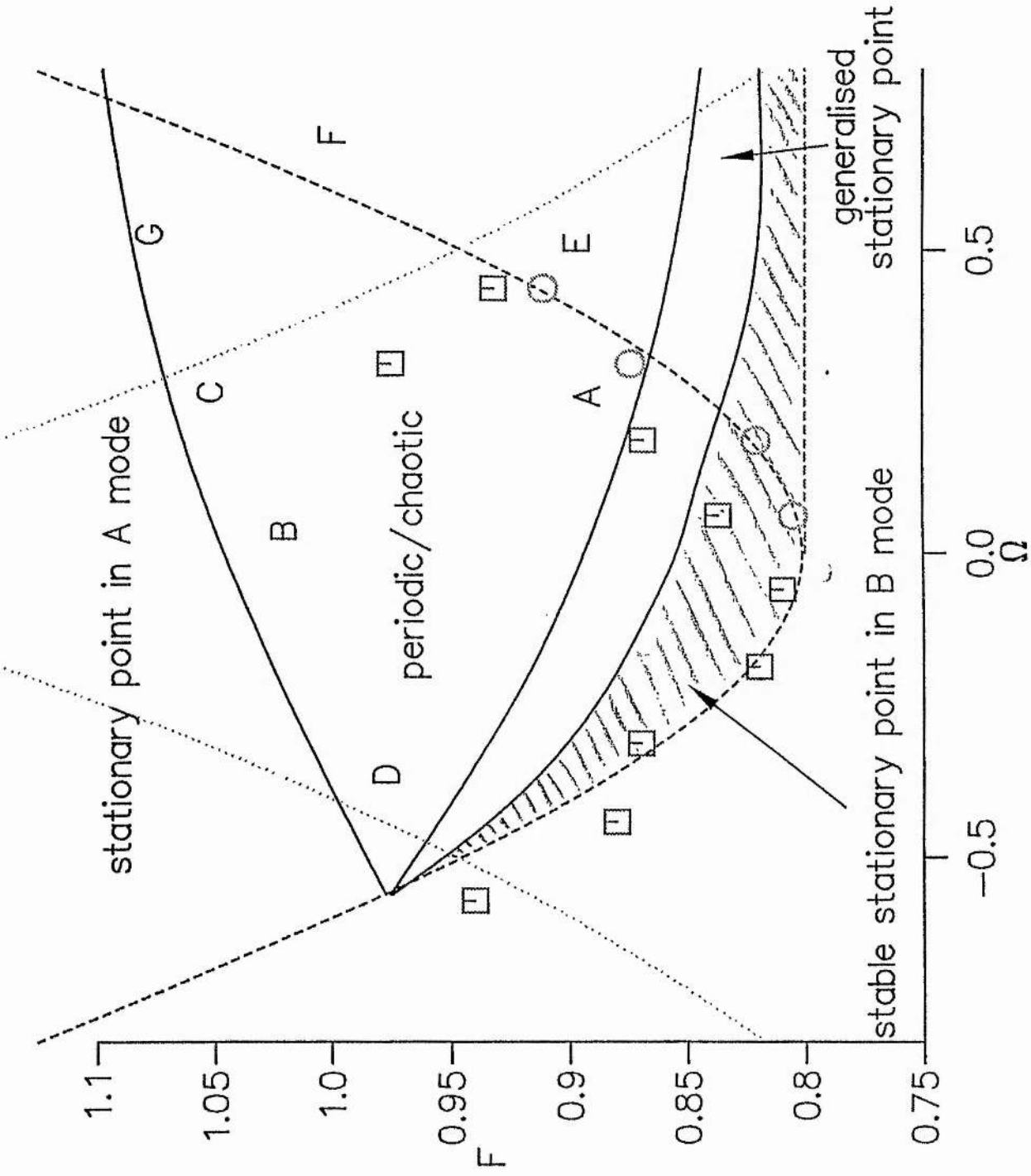

Figure 3. Stability diagram for water depth of 2cm, surface tension $\hat{T} = 0.00004$, tank length $l = 0.7$ and wave mode $M = 22$.

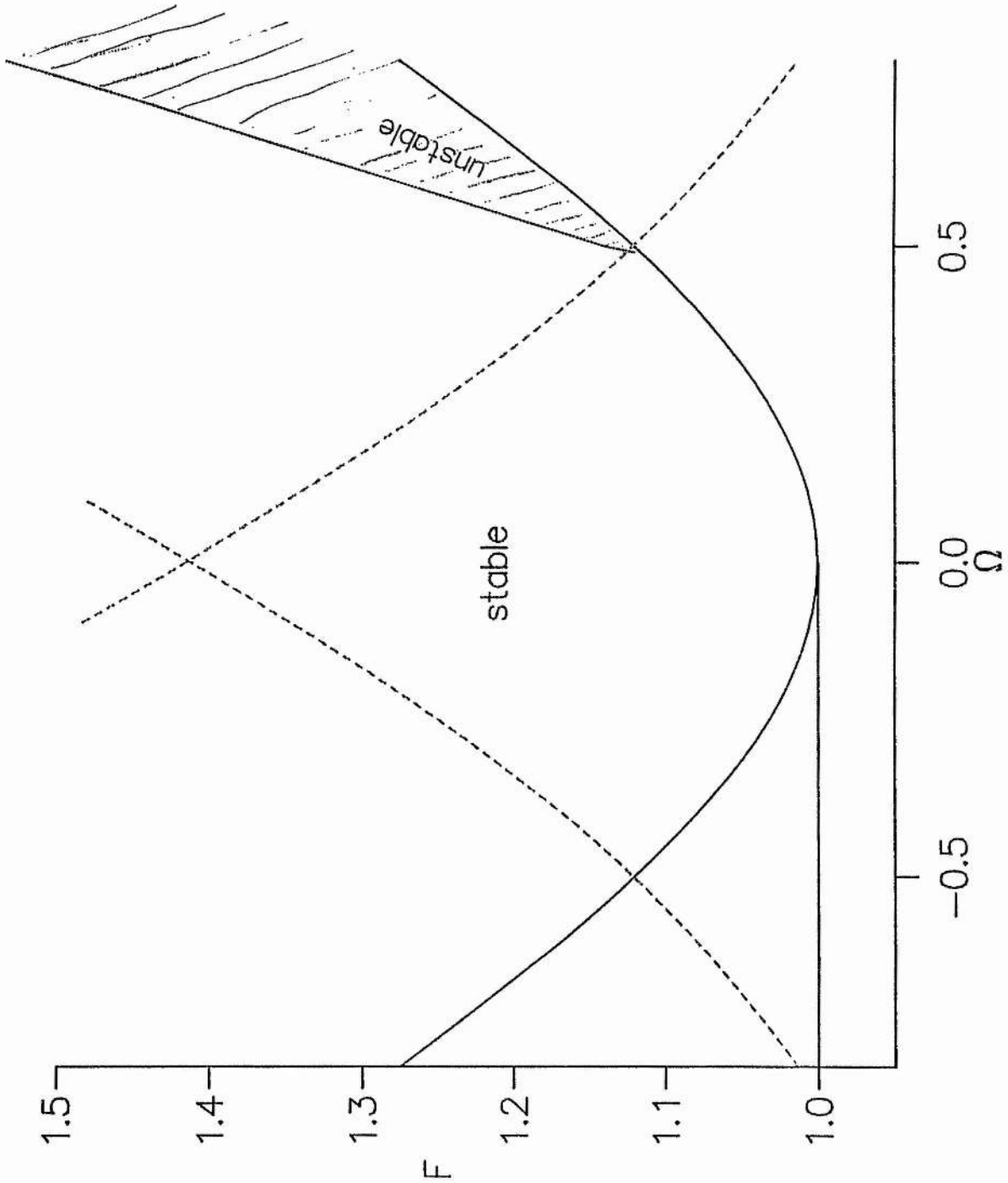

Figure 4. Wave oscillations for an example from the six-dimensional stationary point region on Figure 2. The solid line shows the variation at the far left of the tank, the dotted-dashed line shows the centre of the tank and the dashed line shows the far right of the tank.

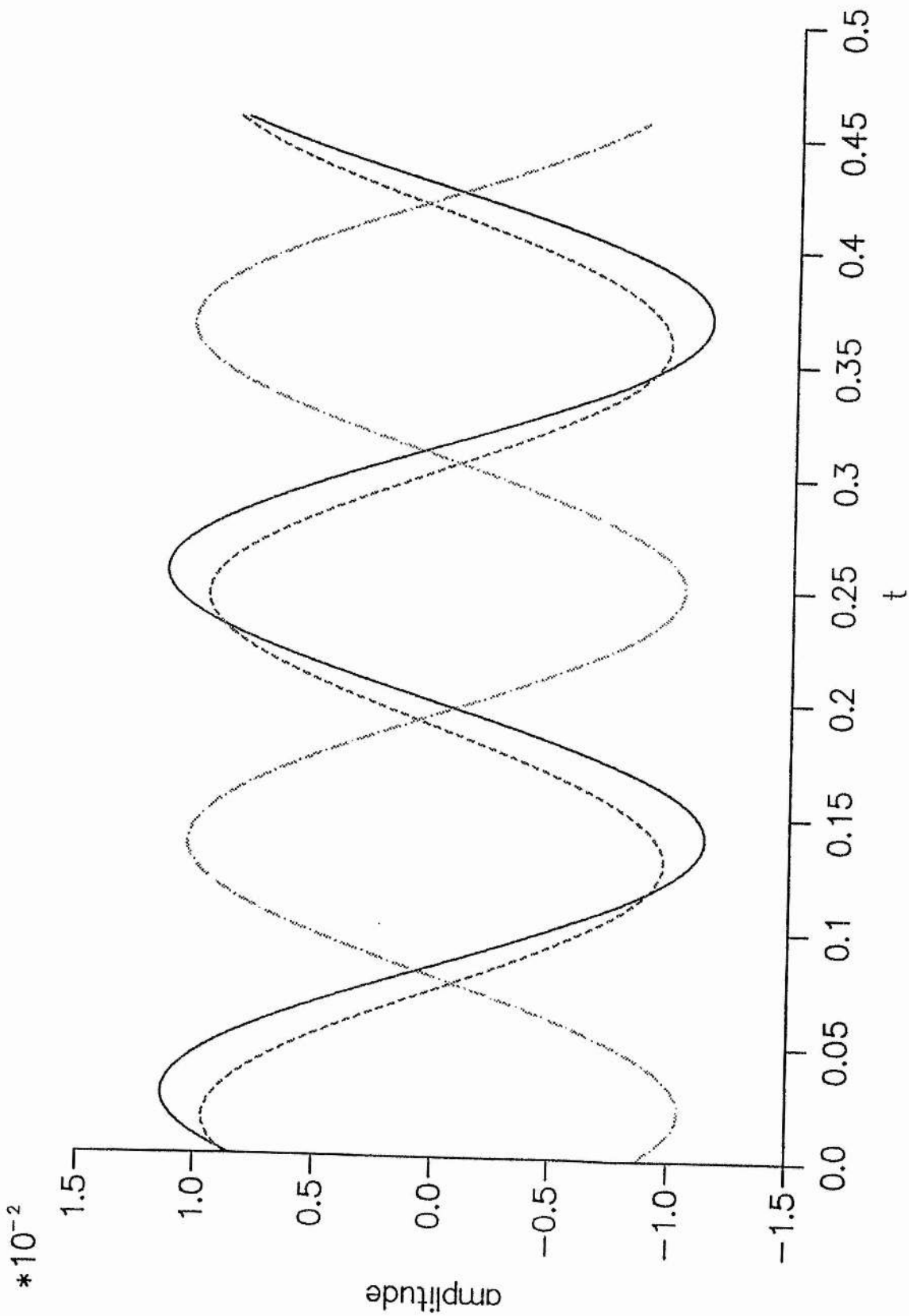

Figure 5. Time evolution of the three modes at points A, B, C, D, E, F and G on Figure 2 respectively. In each case, the top graph shows the *A* mode, the middle graph shows the *B* mode and the bottom graph shows the *C* mode. The solid lines show their real parts and the dashed lines show their imaginary parts. The coordinates of the points on Figure 2 are: A (0.25, 0.89), B (0, 1.02), C (0.25, 1.05), D (-0.4, 0.975), E (0.5, 0.9), F (0.7, 1) and G (0.5, 1.075).

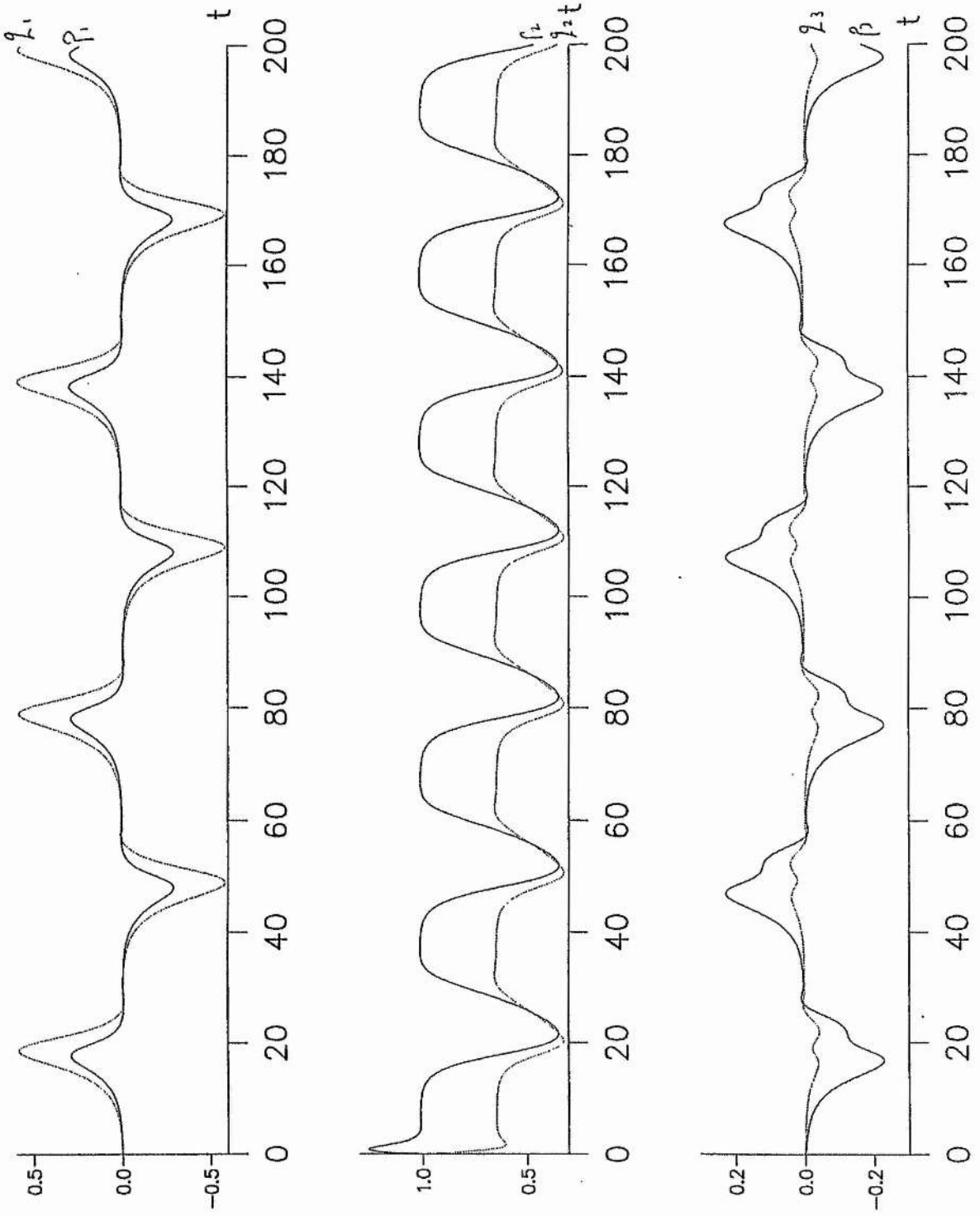

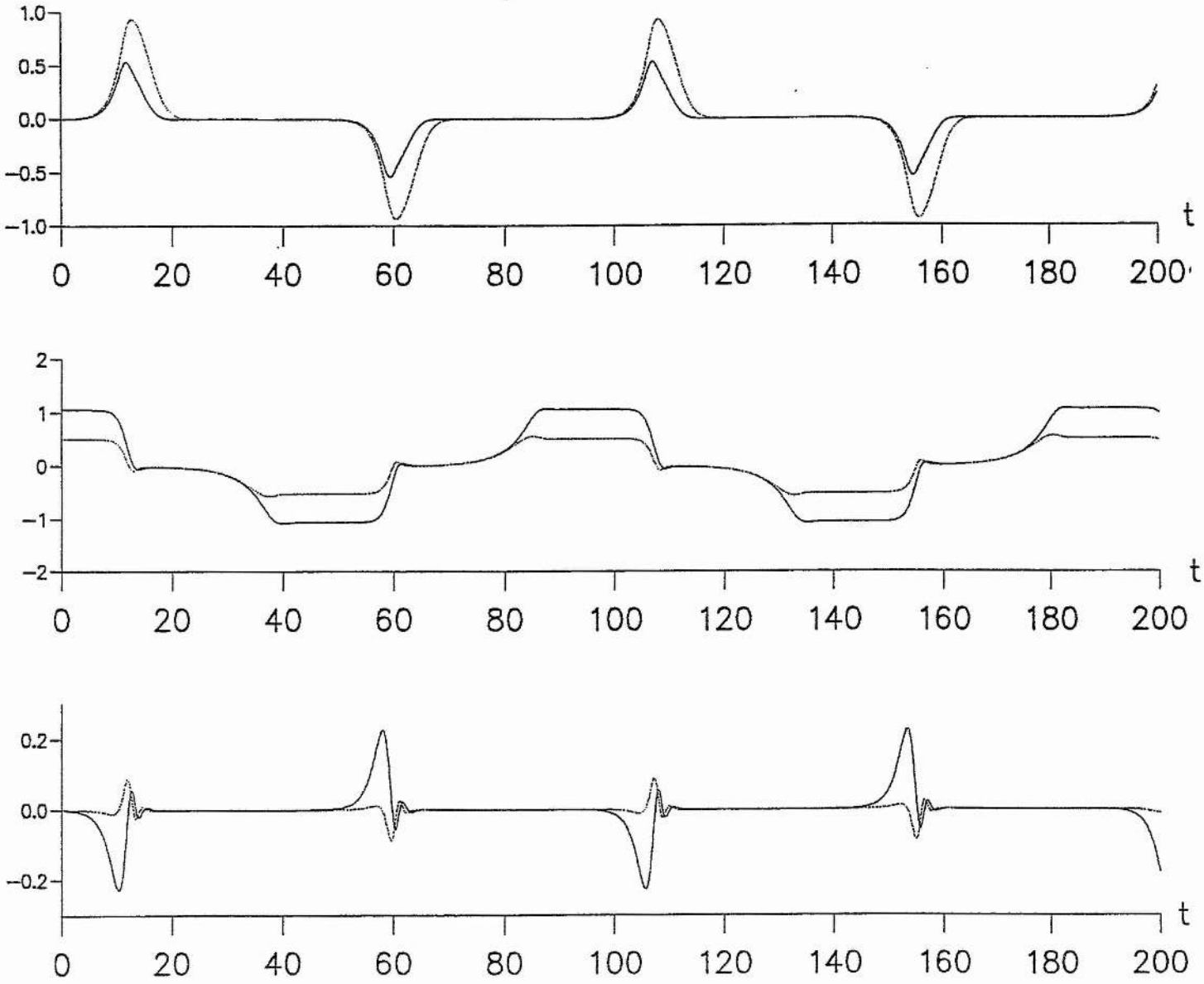
1.0
0.5
0.0
−0.5
−1.0
t
0
20
40
60
80
100
120
140
160
180
200
2
1
0
−1
−2
t
0
20
40
60
80
100
120
140
160
180
200
0.2
0.0
−0.2
t
0
20
40
60
80
100
120
140
160
180
200

124 h

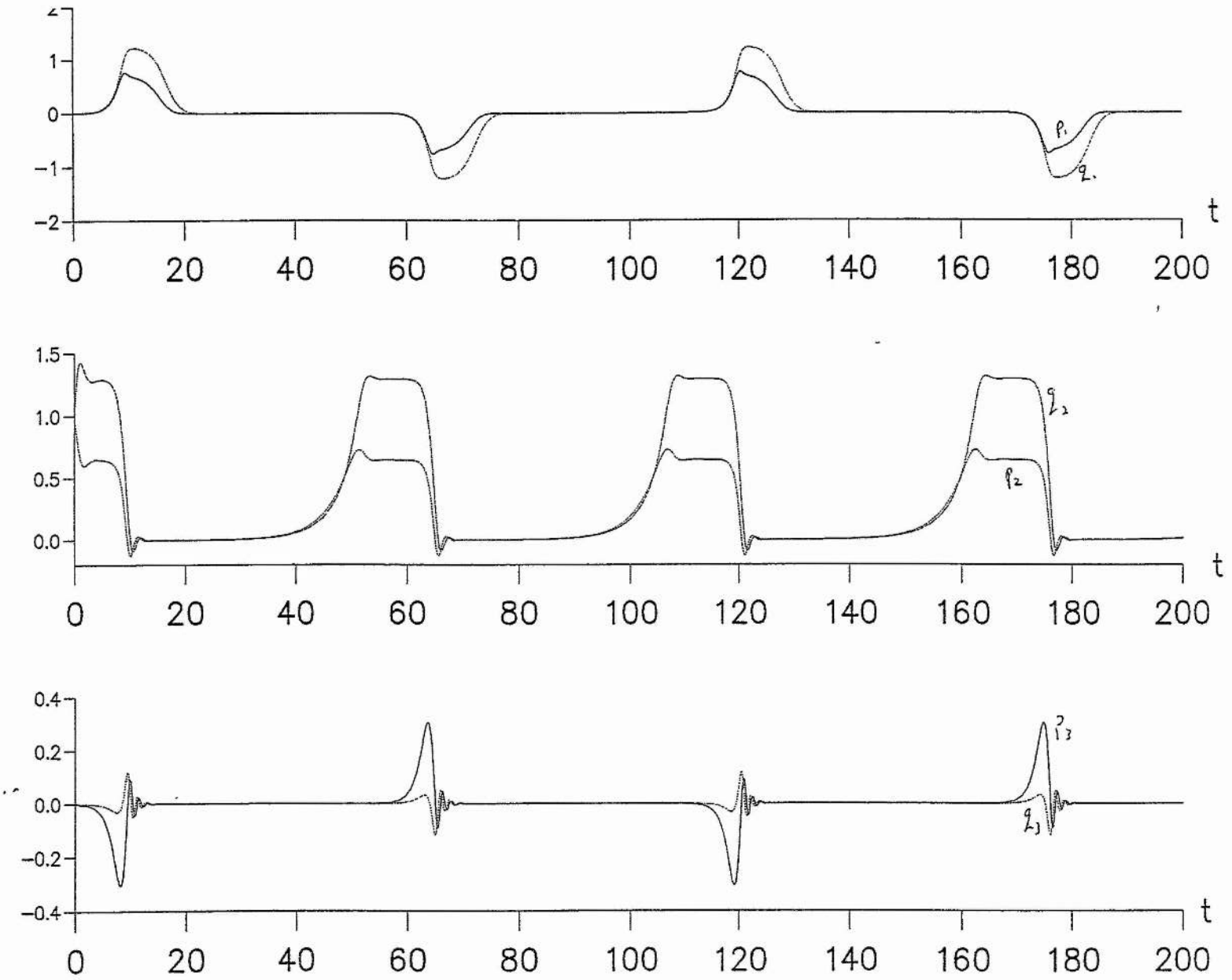
2
1
0
−1
−2
p1
q1
t
0
20
40
60
80
100
120
140
160
180
200
1.5
1.0
0.5
0.0
q2
p2
t
0
20
40
60
80
100
120
140
160
180
200
0.4
0.2
0.0
−0.2
−0.4
p3
q3
t
0
20
40
60
80
100
120
140
160
180
200

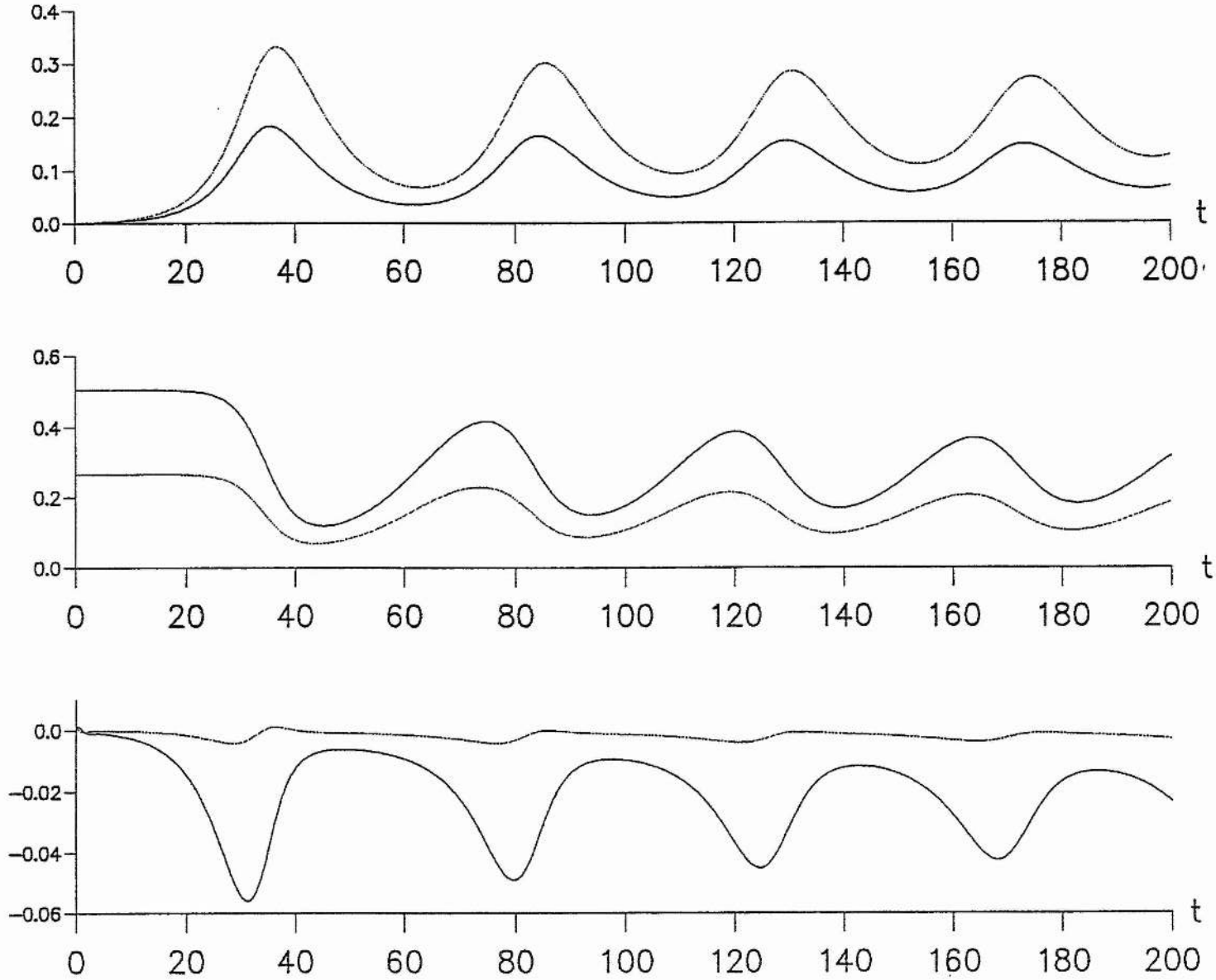
0.4
0.3
0.2
0.1
0.0
t
0 20 40 60 80 100 120 140 160 180 200
0.6
0.4
0.2
0.0
t
0 20 40 60 80 100 120 140 160 180 200
0.0
−0.02
−0.04
−0.06
t
0 20 40 60 80 100 120 140 160 180 200

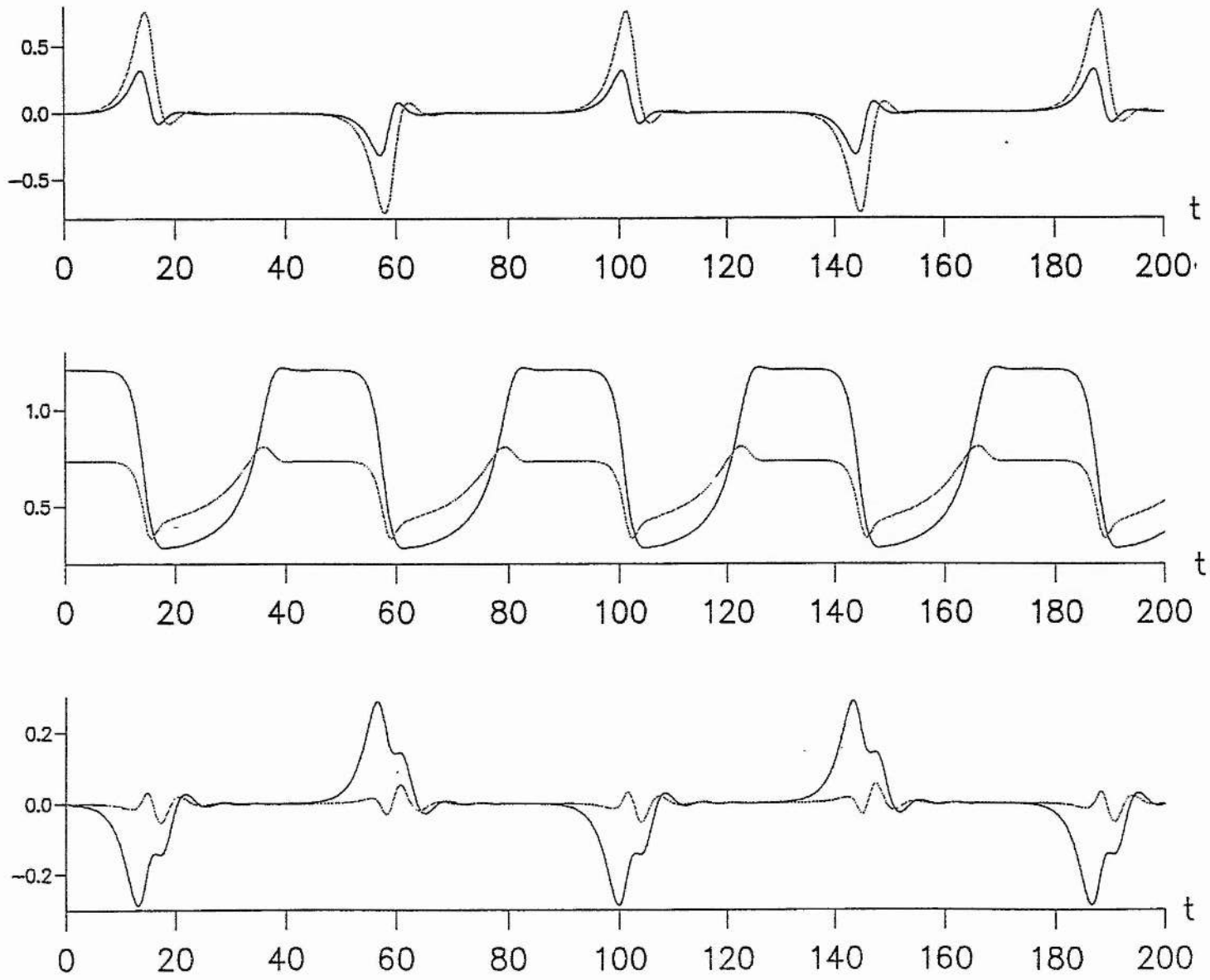
0.5
0.0
−0.5
t
0
20
40
60
80
100
120
140
160
180
200
1.0
0.5
t
0
20
40
60
80
100
120
140
160
180
200
0.2
0.0
−0.2
t
0
20
40
60
80
100
120
140
160
180
200

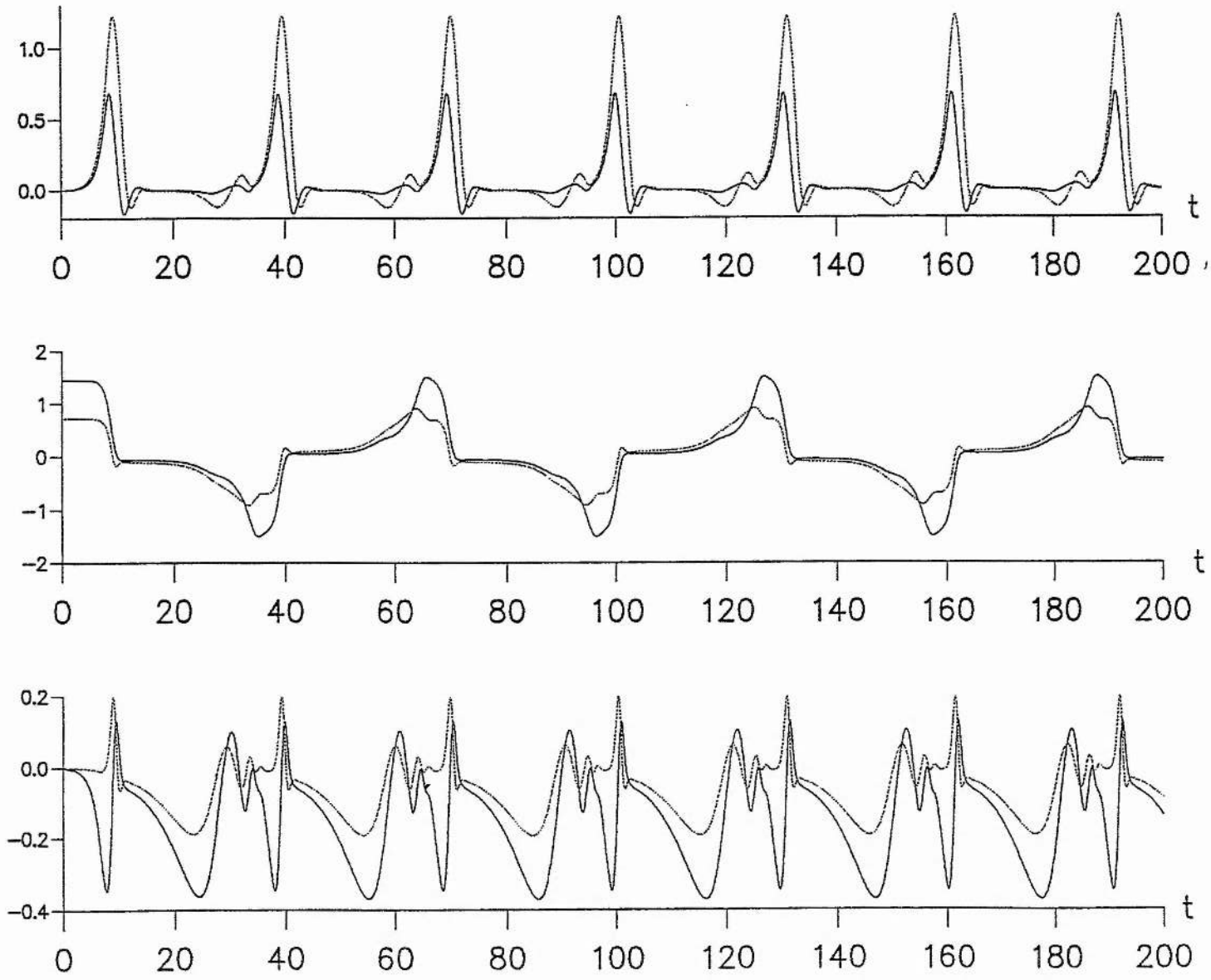
1.0
0.5
0.0
t
0
20
40
60
80
100
120
140
160
180
200
2
1
0
−1
−2
t
0
20
40
60
80
100
120
140
160
180
200
0.2
0.0
−0.2
−0.4
t
0
20
40
60
80
100
120
140
160
180
200

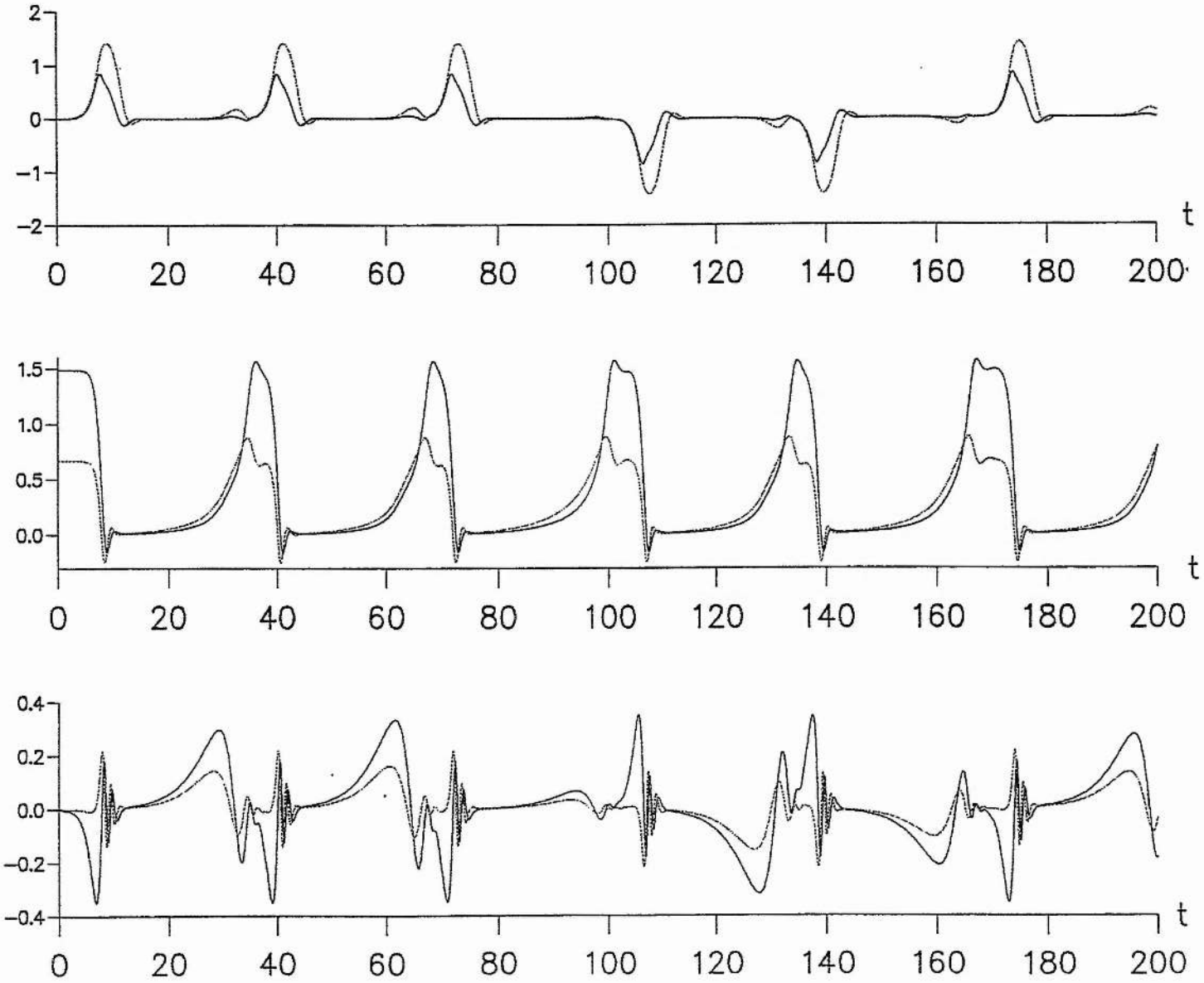
2
1
0
−1
−2
t
0
20
40
60
80
100
120
140
160
180
200
1.5
1.0
0.5
0.0
t
0
20
40
60
80
100
120
140
160
180
200
0.4
0.2
0.0
−0.2
−0.4
t
0
20
40
60
80
100
120
140
160
180
200

Figure 6. The r.m.s. wave amplitude at $x = 0$ and l for points (a) A, (b) B and (c) G in Figure 2. The solid lines show the r.m.s. amplitude at the left hand end of the tank and the dashed lines show the r.m.s. amplitude at the right hand end of the tank.

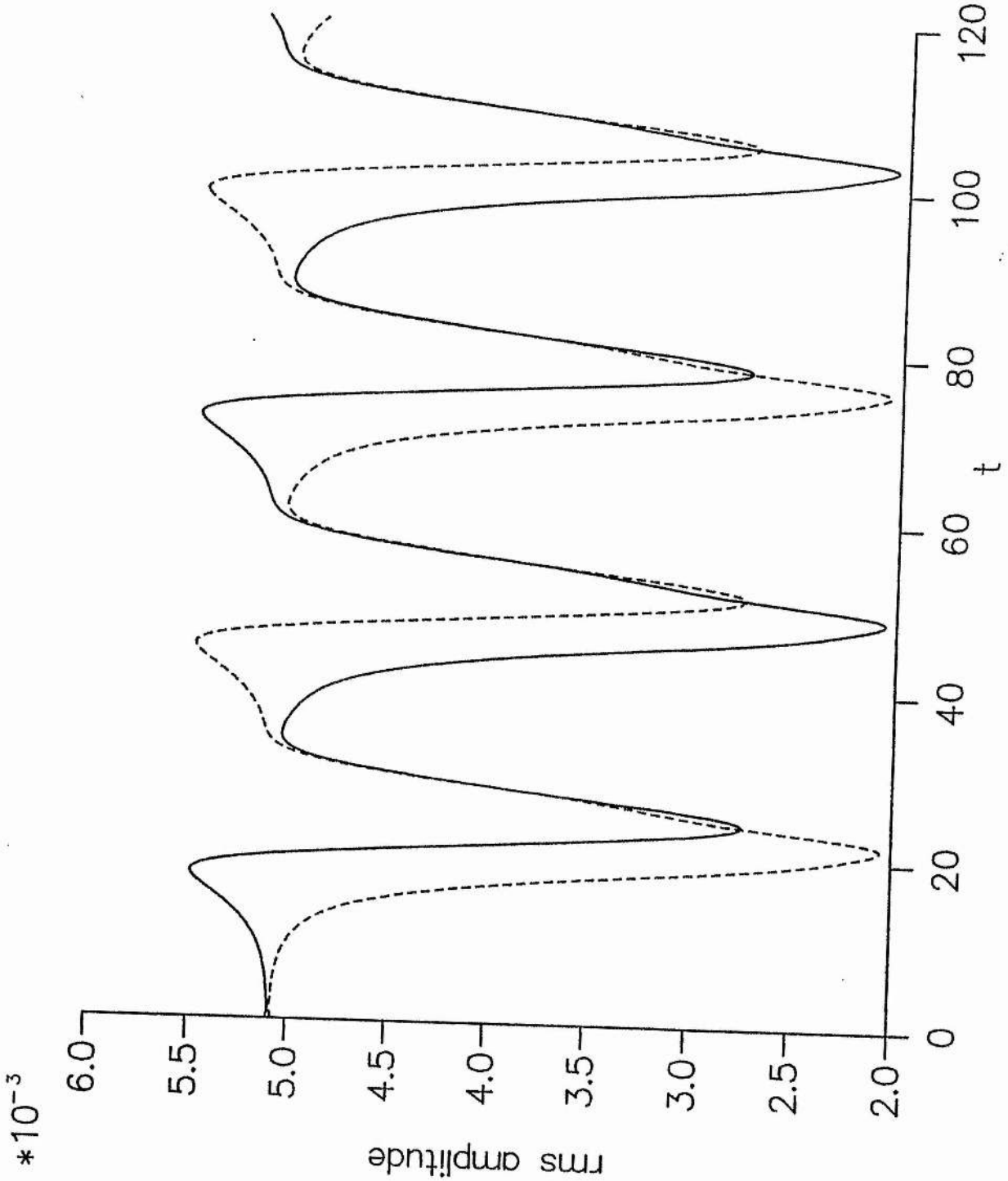

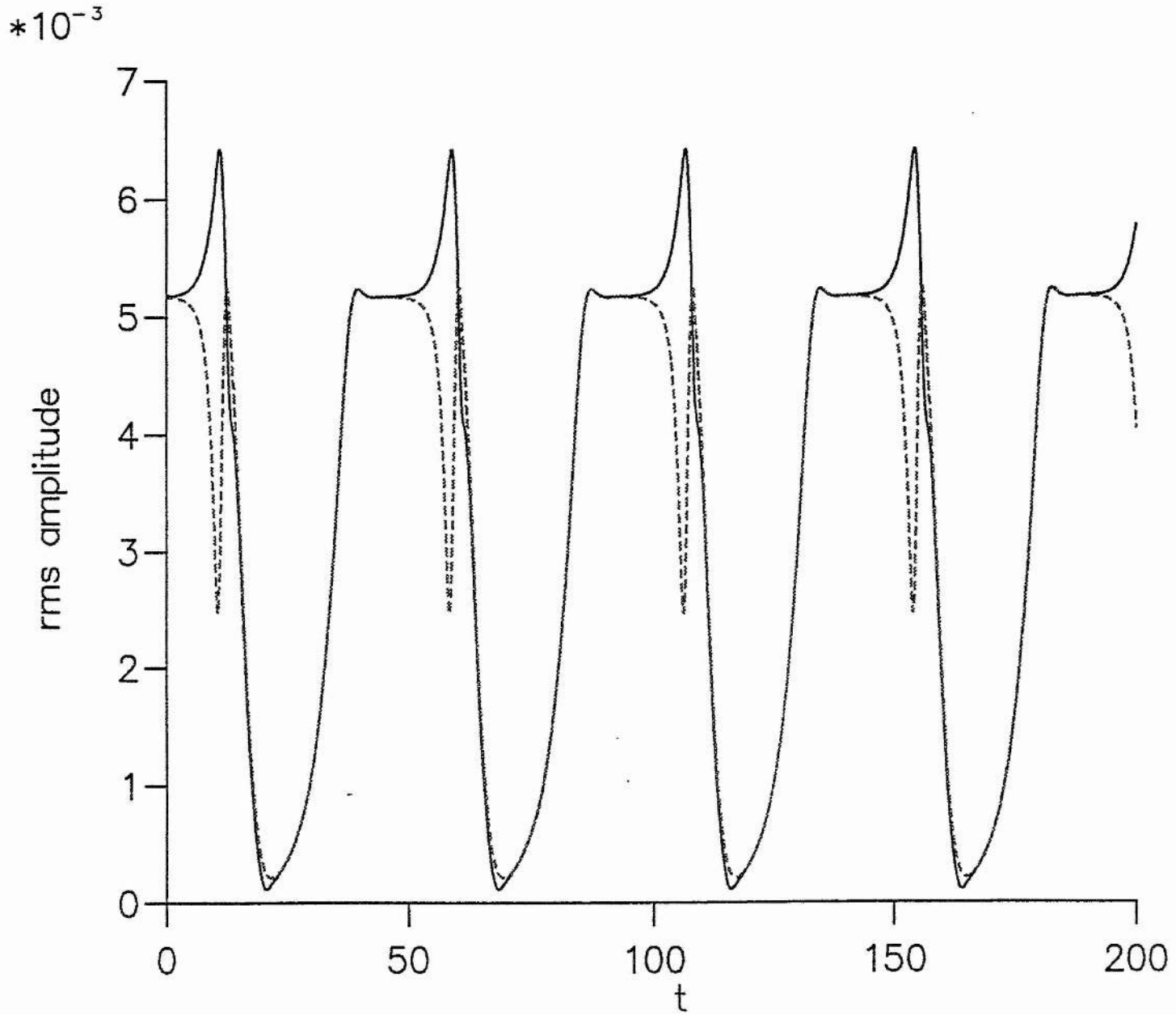
*10^-3
7
6
5
4
3
2
1
0
rms amplitude
0
50
100
150
200
t

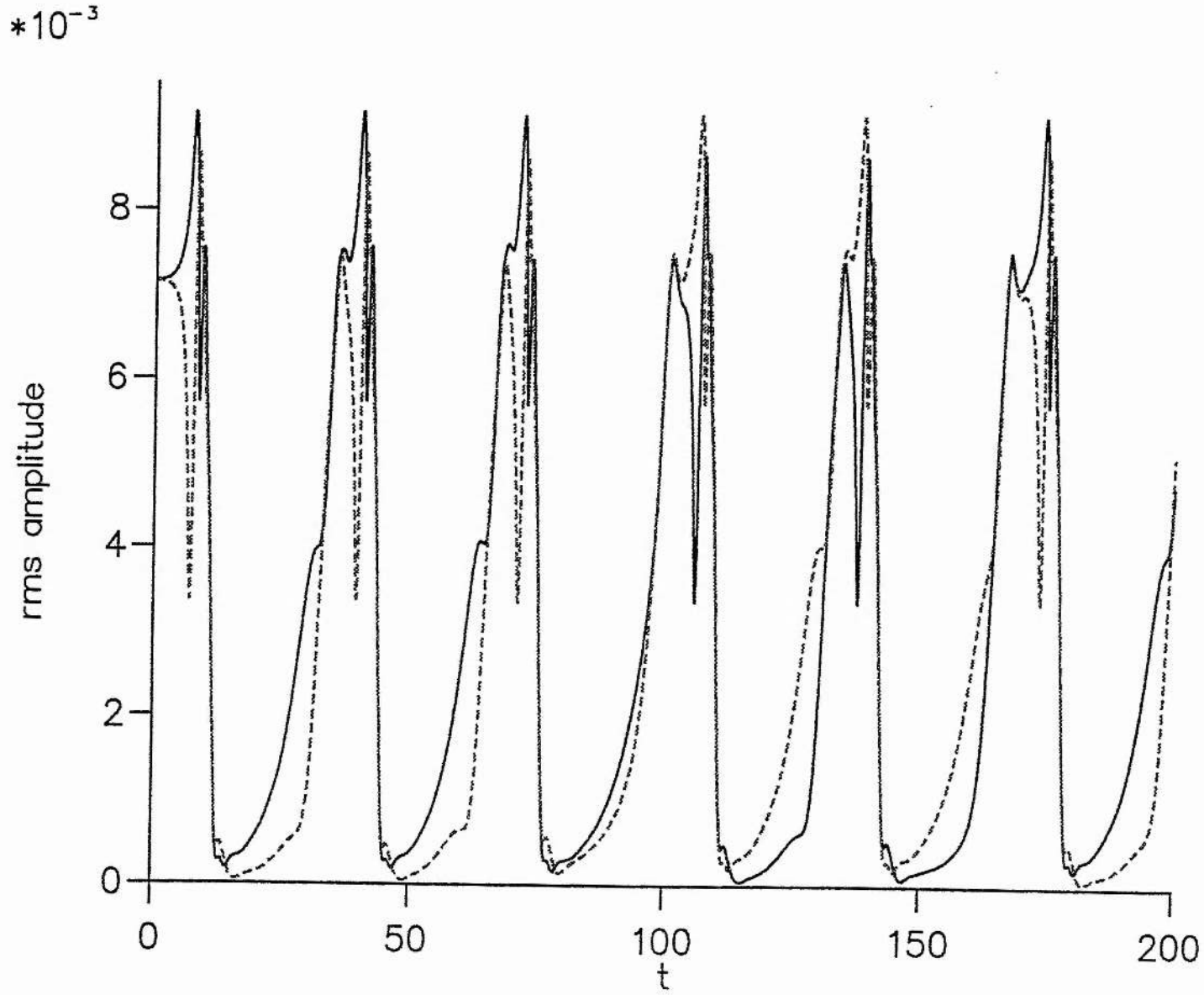
*10⁻³
rms amplitude
8
6
4
2
0
0
50
100
150
200
t

Figure 7. Stability diagram for a water depth of 2cm for the higher-order model, showing a region of stable standing waves, stable limit cycles (in a single mode) and three wave modulations. The circles show experimental data points from Craik & Amitage (1995) for the neutral curve and the squares show data points for the onset of modulations. Parameters are as for Figure 3.

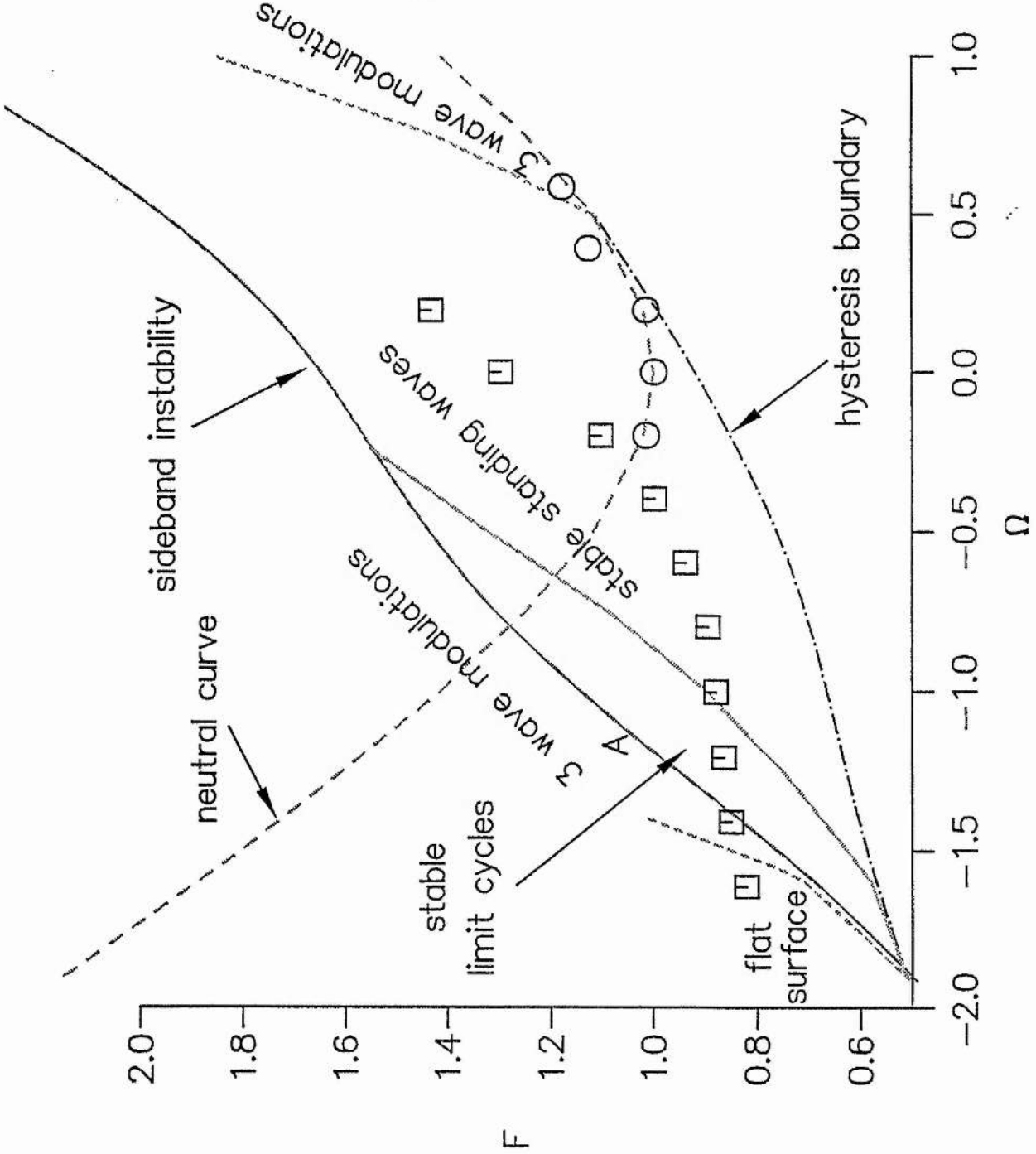

Figure 8. Time evolution of the three modes at the point (-1,1) in the *stable limit cycles* region of Figure 7. The central graph shows a periodic solution and the other two graphs show the sidebands decaying to zero. Therefore, this limit cycle is stable to sideband perturbations.

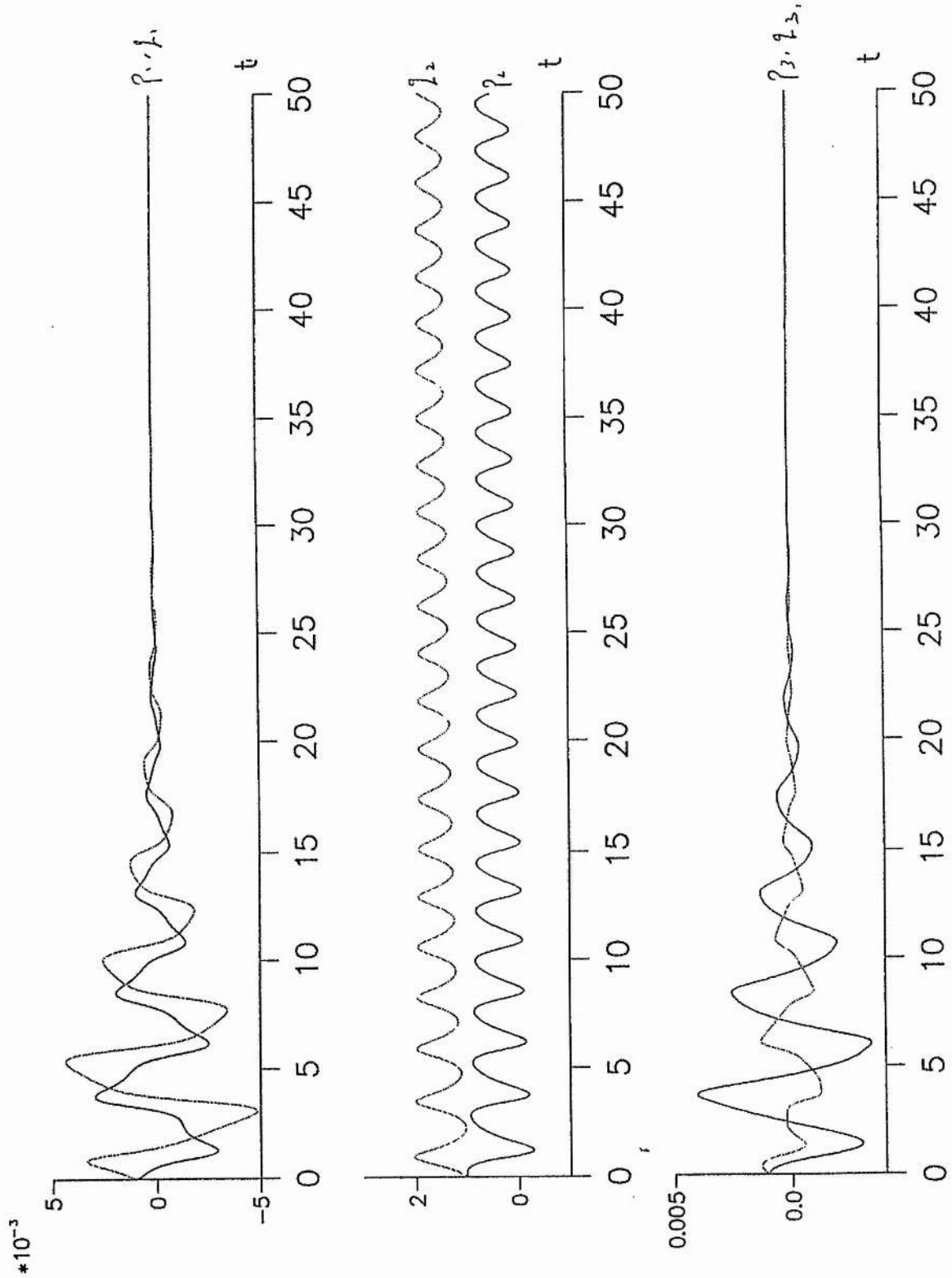

Figure 9. (a) Time evolution of the three modes at point A on Figure 7, showing complex wave interactions. (b) The r.m.s. wave amplitude at the left (solid) and right (dashed) ends of the tank for point A on Figure 7.

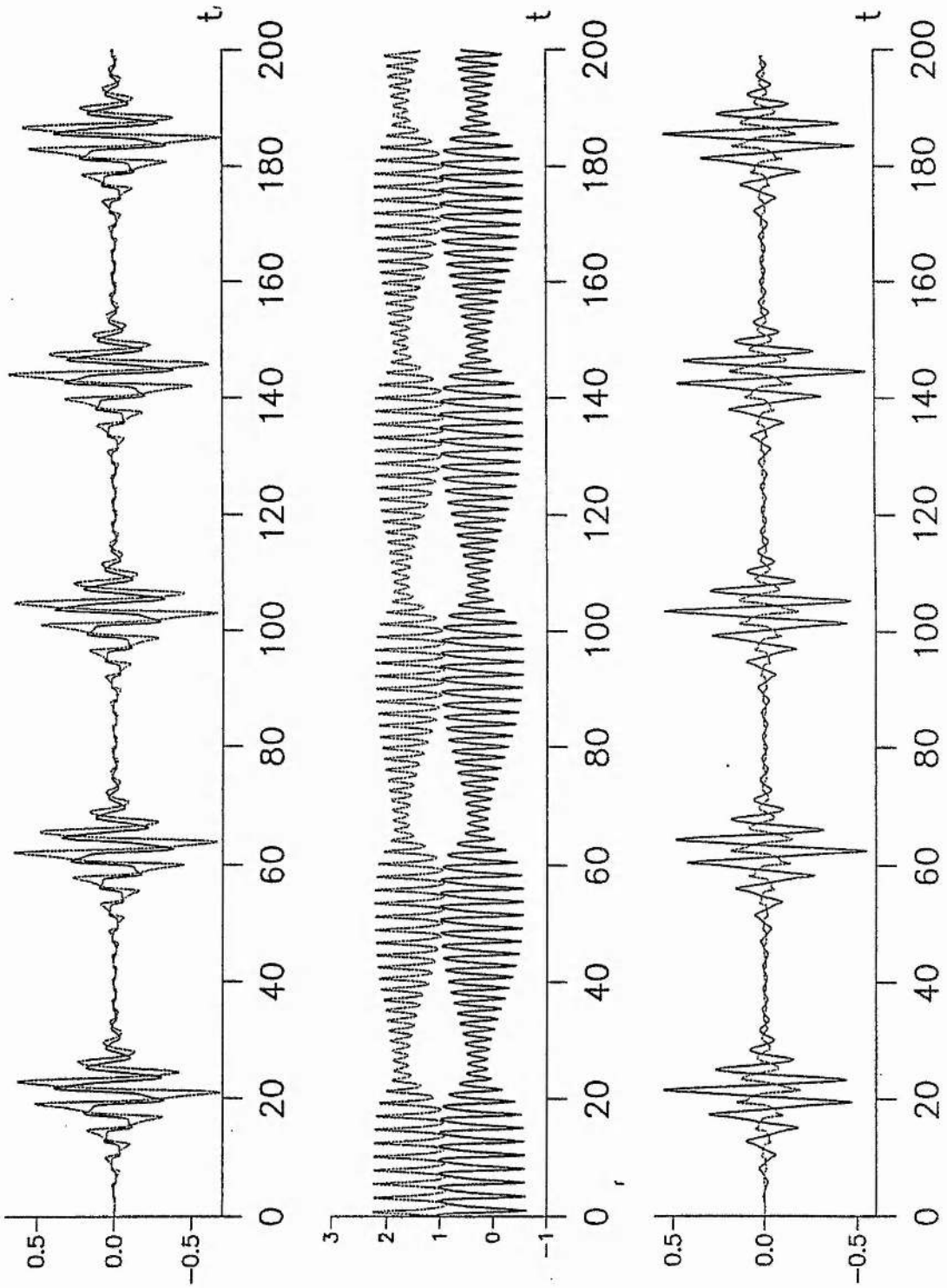

124 s

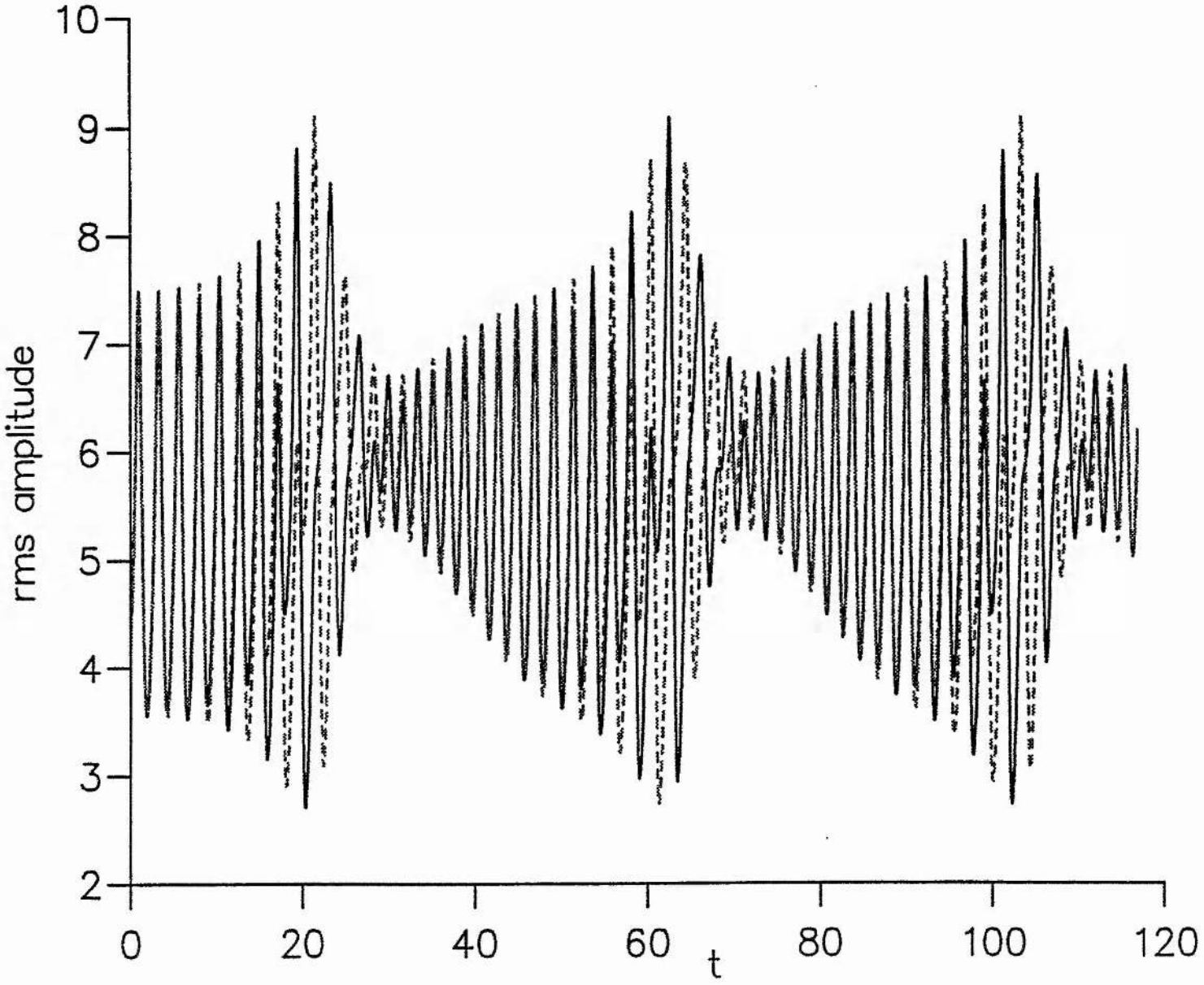
10
9
8
7
6
5
4
3
2
rms amplitude
0
20
40
60
80
100
120
t

Figure 10. Stability diagram for a water depth of 1cm for the higher-order model. The circles denote experimental data points from Craik & Armitage (1995), for the onset of standing waves from the flat surface. The squares denote experimental data points for the onset of modulations from either the flat surface or standing waves. Parameters are as for Figure 2.

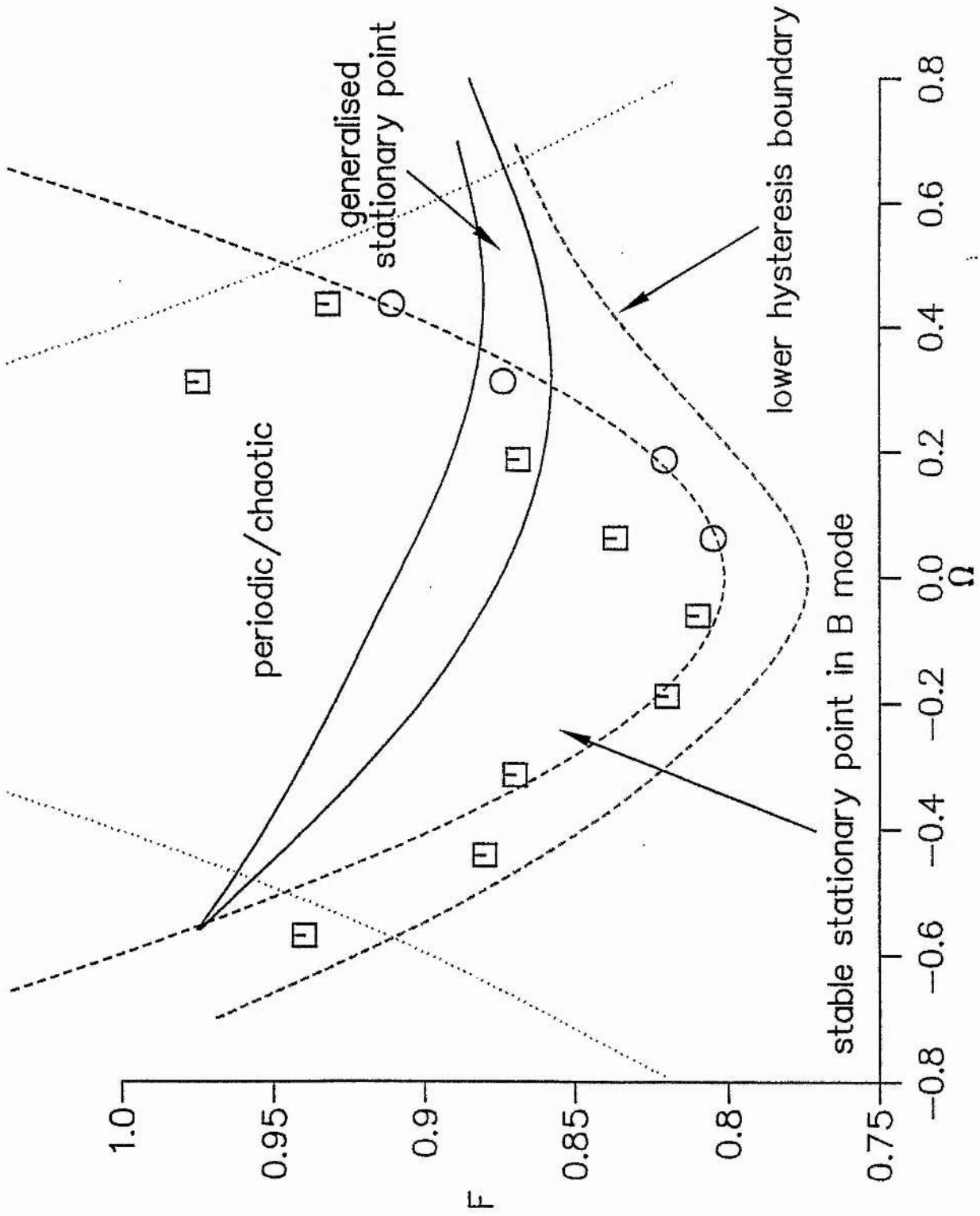

CHAPTER VII

Conclusions

Two-dimensional Faraday waves have been extensively studied in a long rectangular container. A clear advantage of considering two-dimensional waves has been to simplify the derivation of the models (the derivations would be even more complicated for three-dimensional waves!). This has allowed us to examine the role of nonlinear terms not before retained in theoretical studies of Faraday waves, particularly the fifth-order conservative terms.

It has been found that these nonlinear terms have been very influential in both hysteresis and mode competition in Faraday waves. In Chapter III, a single mode was studied and the cubic conservative, forcing and damping terms were derived, as well as the fifth-order conservative term. The coefficients of the conservative and forcing terms were calculated in terms of the depth, surface tension, wavenumber and tank length, and the coefficients of the damping terms were estimated from experimental data. The cubic forcing coefficient was found to be different to that calculated by Miles (1993, 1994) since Miles neglected third harmonics. Also, the fifth-order conservative term is a new feature, not retained in previous work. Hysteresis was investigated both analytically and numerically by studying the existence and stability of stationary points and limit cycles. It was found that the fifth-order conservative term bends the lower hysteresis boundary. Theoretical hysteresis predictions were found to agree well with experimental data. [5]

The stable limit cycles found in Chapter III were investigated further in Chapter IV. This included a study of the local and global bifurcations that occur in the single mode equations. A multiple time-scales analysis was used to obtain formulae for the

[5] Chapter III is published in Decent & Craik (1995 a).

position, size, shape and frequency of oscillation of the limit cycles, which were found to agree excellently with numerical results. The global bifurcations were modelled using Melnikov theory, assuming weak linear damping. It was found that the stable limit cycles only exist for positive values of the cubic damping coefficient N. [6]

In Chapter V, the coefficient of cubic damping N was estimated theoretically in three different scenarios, incorporating dissipation due to the boundary layers at the sidewalls and at the surface, and the dissipation due to the streaming resulting from surface contamination. Second-order dissipation in the surface boundary layer and dissipation due to the streaming induced by the sidewalls were neglected, and the obstacles to further progress were highlighted. Despite approximations, encouraging agreement was obtained between theoretical and experimental results, and insight was obtained into the relative importance of the sidewalls and the surface film on the cubic damping coefficient. In particular, Chapter V presents strong theoretical evidence that the cubic damping coefficient is positive for deep water, as was found experimentally in Chapter III. The significance of this result is discussed. [7]

In Chapter VI, mode competition between three two-dimensional modes was studied. Evolution equations for three neighbouring modes were derived, initially incorporating terms up to the cubic conservative terms; then later, including cubic damping, forcing and fifth-order conservative terms. It was found that a Benjamin-Feir (1967) instability mechanism can be responsible for the modulations and intermittency observed in the experiments of Craik & Armitage (1995) (described in Chapter II). The effects on the sideband instability of cubic forcing, cubic damping and the fifth-order conservative terms were discussed. Qualitative agreement between theoretical and experimental results was established, though detailed quantitative agreement was generally poor. It was found that the higher-order nonlinear terms are

---

[6] Chapter IV has been submitted for publication as Decent & Craik (1995 b).

[7] Chapter V will be submitted for publication as Decent (1995).

essential for even a qualitative comparison between theory and experiment for the 2cm depth case. [8]

The stable limit cycles found in Chapter III correspond to the amplitude and phase of the standing wave experiencing a slow periodic modulation, in addition to its fast basic periodicity. These limit cycles in a single-mode are a new solution. In Chapter VI we found a region of the forcing-frequency plane in which the limit cycles are stable to sideband disturbances. Another novel solution is the six-dimensional stationary point found in Chapter VI, corresponding to a standing wave with complex spatial structure: this standing wave has the interesting property that it will not pass through the flat surface during its oscillation.

The importance of nonlinear terms has been seen throughout this thesis. But the problem of determining the many coefficients of these terms is not a trivial task. However, much can be accomplished without detailed knowledge of all the coefficients. In Chapter VI, we derived a nonlinear model of three modes, with cubic damping, cubic forcing and a single fifth-order conservative term. Here we assumed that the 9 cubic damping coefficients were all equal, and chose their value to be the cubic damping coefficient for a single mode. We also neglected all but one of the fifth-order conservative terms. The resulting model gave qualitative agreement between theory and experiment.

Computing the coefficients of the fifth-order conservative terms requires only patience and a lot of computer time; but calculating the cubic damping coefficients is a more problematic task, as seen in Chapter V. There are several theoretical obstacles to be overcome just to calculate the coefficient of cubic damping for a single mode, quite apart from additional computing problems. To extend Chapter V to a full derivation for a multimode system appears completely out of reach presently.

There are many unsolved problems in the field of Faraday waves. The model presented here could be extended to describe three-dimensional waves in square and rectangular containers, which will be a higher-order extension of the work of Miles

---

[8] Chapter VI will be submitted for publication as Decent & Craik (1995 c).

(1993, 1994). In three dimensions, the surface waves can have fascinating and complex geometrical properties, including hexagonal 'honeycomb' type patterns (see for example Edwards & Fauve 1994). The higher-order nonlinear terms included in our two dimensional models will also be very important in these three dimensional situations. The derivation of fifth-order terms in three dimensions is an intimidating task, which will involve symbolic manipulation and substantial computer time; but the rewards of such an exercise look promising. Once the equations are known, it will be possible to examine the stability of various wave patterns. These equations will probably also have chaotic solutions, providing many mathematical challenges.

Knobloch & De Luca (1990) describe waves which have frequencies very close to each other, using partial differential equations. They found spatio-temporal 'blinking states', in which the direction of propagation of a travelling wave reverses more or less periodically in time. These resemble the rapid modulations observed in Craik & Armitage (1995), though Knobloch & De Luca did not incorporate parametric forcing into their model. It would be interesting to investigate the relationship between these 'blinking states' arising from partial differential equations and the rapid modulations found in Chapter VI, in the amplitude expansion model, consisting of ordinary differential equations.

Hughes & Proctor (1990 a, b) investigated the dynamics of three-wave resonant coupling (without parametric forcing), and found behaviour resembling the intermittency described here. Their solution trajectory is found to be very sensitive to noise since it lingers close to the saddle at the origin. It would be interesting to study the effects of noise on the equations described in Chapter VI.

Normal forms provide an alternative method of determining the bifurcation structure of Faraday waves (see Crawford, Knobloch & Riecke 1990; Crawford 1991; Crawford, Gollub & Lane 1993), which derive from symmetry considerations. The relationship between the hydrodynamical methodologies (including those described here in Chapters III and VI) and the normal form approach deserves further study.

Standing solitary waves are also a feature of Faraday resonance, and have received comparatively little theoretical attention (see Wu et al. 1984, Larraza & Putterman 1984 and Wu & Rudnick 1985). It would be profitable to investigate the mode competition processes involving parametrically driven solitary waves.

There is plenty of further work possible using the experimental apparatus described in Chapter II. There have recently been modifications to the equipment carried out by Mr. D. Sterratt, along with some further experimental observations (see Sterratt 1995). It is hoped that the modifications will eventually enable the phase-space of several interacting waves to be reconstructed experimentally. Also, it is hoped that the modifications will result in the single-mode limit cycle described in Chapter IV being observed experimentally.

APPENDIX A

Two-mode competition

We will now briefly discuss the dependence of two-mode competition in Faraday waves on the cubic damping coefficients. Nagata (1989) derived evolution equations for two modes in a square container, namely

$$\begin{aligned}\frac{dA}{dt} &= -\mu A + i\Omega A + iFA^* + iA\left(\Pi|A|^2 + \hat{\Pi}|B|^2\right) + i\tilde{\Pi}B^2A^*,\\ \frac{dB}{dt} &= -\mu B + i\Omega B + iFB^* + iB\left(\Pi|B|^2 + \hat{\Pi}|A|^2\right) + i\tilde{\Pi}A^2B^*,\end{aligned} \tag{A.1}$$

where A and B are the complex wave amplitudes of the two modes, and Π, $\hat{\Pi}$ and $\tilde{\Pi}$ are real cubic conservative coefficients. The two modes correspond to a mode along the length of the tank and an identical mode along the breadth of the tank. Nagata (1991) described chaotic behaviour in (A.1).

We propose the equations

$$\begin{aligned}\frac{dA}{dt} &= \text{terms on r.h.s. of (A.1)} + NA\left(|A|^2 + |B|^2\right),\\ \frac{dB}{dt} &= \text{terms on r.h.s. of (A.1)} + NB\left(|A|^2 + |B|^2\right),\end{aligned} \tag{A.2}$$

which retain cubic damping terms. The form of these terms is as in Miles (1993, 1994), though we have assumed that all four of the coefficients of cubic damping are equal, for simplicity. We also neglect the cubic forcing and quintic conservative terms. Though this assumption is not realistic, it allows us to easily determine if the behaviour of (A.1) is robust to the inclusion of cubic damping terms.

We examine the case

$$\Omega = 0,\ \mu = 0.9,\ k = 1.0,\ \sigma = 0.5,\ \Pi = -0.65,\ \hat{\Pi} = -0.055,\ \tilde{\Pi} = 0.063 \tag{A.3}$$

by solving equations (A.2) numerically for various initial conditions, for various values of the forcing F and for various values of N. For $N = 0$ (that is, the equations examined by Nagata 1989, 1991) we find non-zero stable stationary points for all

$F > \mu$, and for $0 \leq F < \mu$ we find that all trajectories tend towards the origin. Therefore, we are examining a situation in which Nagata (1989, 1991) did not find chaos. (Note that Nagata 1989, 1991 found chaos in (A.1) for parameters similar to those of (A.3), though for different values of the frequency detuning Ω.)

For $N < 0$ we find the same qualitative behaviour as described for $N = 0$. However, for $N > 0$ we find limit cycles, chaos and divergence to infinity for various values of the forcing F. For example, for $N = 0.1$ we examined the behaviour of the system for several different values of F and the results are shown in Table 1 (we did not examine the bifurcation structure in detail). Figure 1 shows the phase portrait for A and B for $F = 1.95$, which is very similar to Figure 2 from Nagata (1991). (The almost straight line from bottom left to top right on Figure 1(a) is transient motion).

Therefore, it can be seen that the addition of small cubic damping terms (with $N > 0$) can completely change the behaviour of (A.1). Moreover, the evidence of this thesis suggests that it is common for N to be positive.

Table 1

F	behaviour
1.4	stationary point
1.5	limit cycle
1.6	limit cycle
1.7	quasi-periodic
1.8	quasi-periodic
1.85	chaotic
1.9	chaotic
1.95	chaotic
2	divergence to infinity

Figure 1. Phase portrait for A and B for equation (A.2). The parameters used were $\Omega = 0, \mu = 0.9, k = 1, \tanh(kd) = 0.5, \Pi = -0.65, \hat{\Pi} = -0.055, \tilde{\Pi} = 0.063, N = 0.1$.

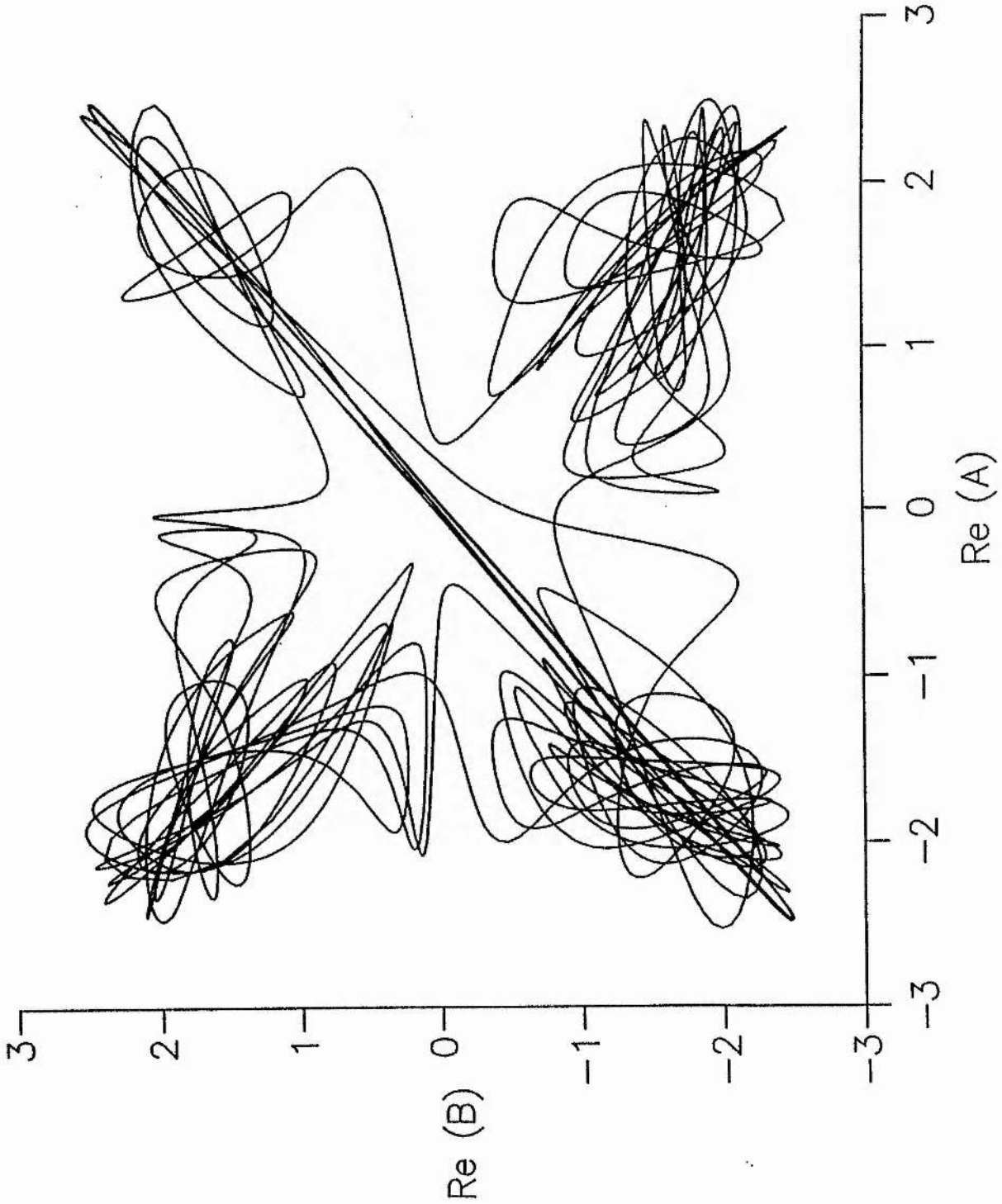

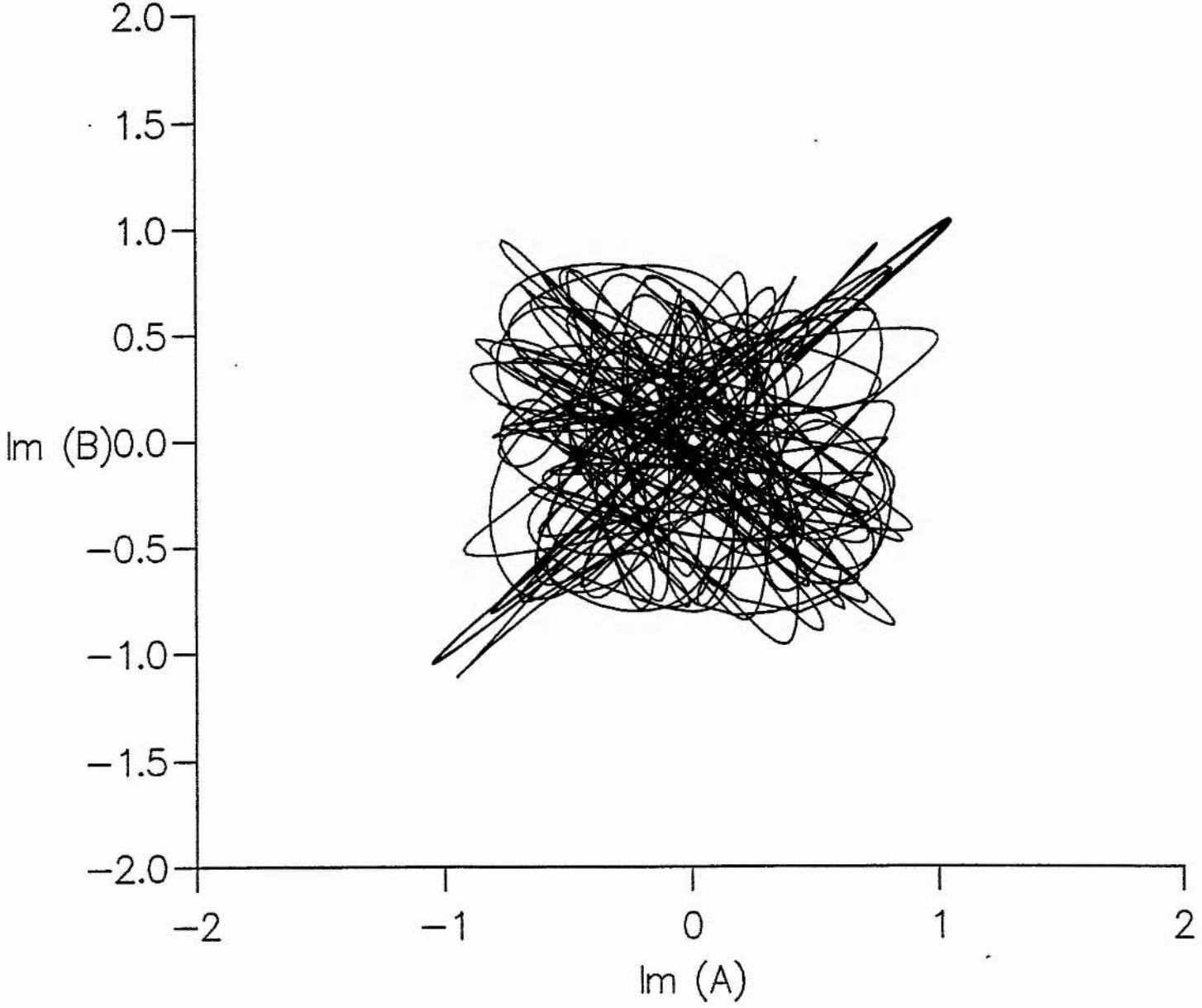

131 b

APPENDIX B

An example of the derivation of (3.22) in Chapter III

The derivation of (3.22) (Chapter III) is very algebraically demanding. (Note that all equation numbers referred to in this appendix correspond to Chapter III.) It has been performed using the symbolic manipulation package MAPLE and the algebra covers several hundred pages. The average Lagrangian (3.4) has not been given fully in this text and the h coefficient in (3.22) has not been given except for two limiting cases. Here we will show the derivation in more detail by choosing a particular numerical example. The parameters chosen for this are $m = 23$ half wavelengths in a channel length of $l = 0.7\text{m}$ and depth $d = 0.01352\text{m}$. The capillary length is taken to be $\lambda = 0.002\text{m}$.. Taking (2.30) and (3.14) gives the natural frequencies and the wavenumbers of the primary mode and its harmonics. These can be used to calculate (2.20) to (2.23). Substituting (3.1), (3.2) and (3.3) into (2.31), averaging over a $\frac{2\pi}{\omega}$ interval of t and using (3.5) gives

$\langle L \rangle =$ Terms in ε^4 already given in (3.4)

$$
\begin{aligned}
&+\varepsilon^6 10^{-3}\left\{0.614\left(\frac{\partial p}{\partial \tau_2}q-\frac{\partial q}{\partial \tau_2}p\right)+0.635\left(p^2+q^2\right)^3\right.\\
&+0.307\left(\left(\frac{\partial p}{\partial \tau_1}\right)^2+\left(\frac{\partial q}{\partial \tau_1}\right)^2\right)-0.614F_1^2-0.137F_2^2-0.0712F_3^2\\
&+56.1f_1\left(p^2-q^2\right)+61.2f_0\left(p^4-q^4\right)+112f_0\left(pD_1+qE_1\right)\\
&+p\left(1.30D_1-0.189D_3\right)\left(p^2-3q^2\right)\\
&+q\left(1.30E_1-0.189E_3\right)\left(3p^2-q^2\right)\\
&+2.46\left(D_1^2+E_1^2\right)+0.176\left(D_2^2+E_2^2\right)+0.0353\left(D_3^2+E_3^2\right) \qquad \text{(B.1)}\\
&\left.+0.563\left(p^2+q^2\right)\left(\frac{\partial p}{\partial \tau_1}q-\frac{\partial q}{\partial \tau_1}p\right)\right\}\\
&+O(\varepsilon^8).
\end{aligned}
$$

This corresponds to (3.4) with (3.5) substituted into it.

Note that $\omega = \omega_1$ in (B.1) since it is not necessary to have the h coefficient dependent upon ω. We are interested only in stationary solutions here so put $\partial p / \partial \tau_1 = \partial q / \partial \tau_1 = 0$. The average Lagrangian can now be made stationary with respect to variations in D_n, E_n and F_n. When these expressions are substituted back into the Lagrangian it becomes

$$\begin{aligned}\langle L \rangle &= \text{terms in } \varepsilon^4 \\ &+\varepsilon^6 10^{-3}\left\{0.614\left(\frac{\partial p}{\partial \tau_2}q - \frac{\partial q}{\partial \tau_2}p\right) + 31.7 f_0\left(p^4 - q^4\right)\right. \\ &\left. -0.211\left(p^2+q^2\right)^3 - 0.0384\mu^2\left(p^2+q^2\right) + 56.1\frac{f_1}{\varepsilon^2}\left(p^2 - q^2\right)\right\} \\ &+ O(\varepsilon^8).\end{aligned} \tag{B.2}$$

This gives the evolution equation (i.e. (3.22) and (3.23))

$$\begin{aligned}\frac{\partial p}{\partial \tau_2} &= 183 f_1 q + 206 f_0 q^3 - 2.07 q\left(p^2+q^2\right)^2 + 0.125\mu^2 q \\ \frac{\partial q}{\partial \tau_2} &= 183 f_1 p + 206 f_0 p^3 + 2.07 p\left(p^2+q^2\right)^2 - 0.125\mu^2 p\end{aligned} \tag{B.3}$$

which therefore gives $h = -2.07$ in this case. The last term in each equation in (B.3) is a small frequency shift term. This type of term has already appeared in (3.6) and it can be absorbed into $i\Omega A$ to cause a shift in the origin on the hysteresis diagram. (Since the coefficient is very small this shift will be negligible). Note that the dependence upon the coefficient of linear damping comes from (3.8b) and (3.12).

REFERENCES

ARNEODO, A., COULLET, P. & TRESSER, C. 1981 *Phys. Lett.* **81A**, *197.*

BENJAMIN, T.B. 1959 Shearing flow over a wavy boundary. *J. Fluid Mech.* **6**, *161-205.*

BENJAMIN, T.B. & FEIR, J.E. 1967 The disintegration of wave trains on deep water. *J. Fluid Mech.* **27**, *417-430.*

BENJAMIN, T.B. & URSELL, F. 1954 The stability of the plane free surface of a liquid in vertical periodic motion. *Proc. R. Soc. Lond. A* **225**, *505-517.*

BUSSE, F.H. 1981 Transition to turbulence in Rayleigh-Benard convection. *In 'Hydrodynamic instabilities and the transition to turbulence' eds. H.L. Swinney & J.P. Gollub, 97-137. Springer.*

CHEN, Y.Y. 1992 Boundary conditions and linear analysis of finite-cell Rayleigh-Benard convection. *J. Fluid Mech.* **241**, *549-585.*

CILIBERTO, S. & GOLLUB, J.P. 1985 Chaotic mode competition in parametrically forced surface waves. *J. Fluid Mech.* **158**, *381-398.*

CRAIK, A.D.D. 1982 The drift velocity of water waves. *J. Fluid Mech.* **116**, *187-205.*

CRAIK, A.D.D. 1985 Wave interactions and fluid flows. *Cambridge Univ. Press.*

CRAIK, A.D.D. 1993 The stability of some three-dimensional and time-dependent flows. *Proc. IUTAM Symp., Potsdam, N.Y.*

CRAIK, A.D.D. & ARMITAGE, J. 1995 Faraday excitation, hysteresis and wave instability in a narrow rectangular wave tank. *Fluid Dyn. Res.* **15**, *129-143.*

CRAWFORD, J.D. 1991 Normal forms for driven waves: Boundary conditions, symmetry and genericity. *Physica D* **52**, *429-457.*

CRAWFORD, J.D., GOLLUB, J.P. & LANE, D. 1993 Hidden symmetries of parametrically forced waves. *Nonlinearity* **6**, *119-164.*

CRAWFORD, J.D., KNOBLOCH, E. & RIECKE, H. 1990 Period-doubling mode interactions with circular symmetry. *Physica D* **44**, *340-396.*

DECENT, S.P. 1995 On the damping of Faraday waves in a rectangular container. *In preparation.*

DECENT, S.P. & CRAIK, A.D.D. 1995 a Hysteresis in Faraday resonance. *J. Fluid Mech.* **293**, *237-268.*

DECENT, S.P. & CRAIK, A.D.D. 1995 b On limit cycles arising from the parametric excitation of standing waves. *Nonlinearity (submitted).*

DECENT, S.P. & CRAIK, A.D.D. 1995 c Intermittency and modulations arising from sideband instabilities in Faraday waves. *In preparation.*

DEVANEY, R.L. 1989 An introduction to chaotic dynamical systems. *Addison-Wesley.*

DODGE, F.T., KANA D.D. & ABRAMSON, N. 1965 Liquid surface oscillations in longitudinally excited rigid cylindrical containers. *AIAA J.* **3**, *685-695.*

DORE, B.D. 1975 Wave-induced vorticity in free-surface boundary layers: application to mass transport in edge waves. *J. Fluid Mech.* **70**, *257-266.*

DORE, B.D. 1972 A study of mass transport in boundary layers at oscillating free surfaces and interfaces. *Proc. IUTAM Symp. Unsteady Boundary Layers VII. Laural Univ. Press.*

DOUADY, S. 1990 Experimental study of the Faraday instability. *J. Fluid Mech.* **221**, *383-409.*

DOUADY, S. & FAUVE, S. 1988 Parametric selection in Faraday instability. *Europhys. Lett.* **6**, *221-226.*

ECKHAUS, W. 1963 Problèmes non-linéaires de stabilité dans un espace à deux dimensions. Deuxième partie: Stabilité des solutions périodiques. *J. Méchanique* **2**, *153-172.*

EDWARDS, W.S. & FAUVE, S. 1992 *C.R. Acad. Sci. Paris* **315**, *no. 2 p 417.*

EDWARDS, W.S. & FAUVE, S. 1993 *Phys. Rev. E* **47**, *R788.*

EDWARDS, W.S. & FAUVE, S. 1994 Patterns and quasi-patterns in the Faraday experiment. *J. Fluid Mech.* **278**, *123-148.*

EZERSKII, A.B., RABINOVICH, M.I., REUTOV, V.P. & STAROBINETS, I.M. 1986 Spatiotemporal chaos in the parametric excitation of a capillary ripple. *Sov. Phys. JETP* **64**, *1228-1236.*

FARADAY, M. 1831 On the forms and states of fluids on vibrating elastic surfaces. *Phil. Trans. R. Soc. Lond.* **52**, *319-340.*

FAUVE, S., KUMAR, K. & LAROCHE, C. 1992 Parametric instability of a liquid-vapour interface close to the critical point. *Phys. Rev. Lett.* **68**, *no. 21.*

FENG, Z.C. & SETHNA, P.R. 1989 Symmetry breaking bifurcations in resonant surface waves. *J. Fluid Mech.* **199**, *495-518.*

FUNAKOSHI, M. & INOUE, S. 1988 Surface waves due to resonant horizontal oscillation. *J. Fluid Mech.* **192**, *219-247.*

FUNAKOSHI, M. & INOUE, S. 1992 a Bifurcations and chaos in resonantly forced water waves. *Nonlinear dispersive wave systems 635-666. World Scientific.*

FUNAKOSHI, M. & INOUE, S. 1992 b Stable periodic orbits of equations for resonantly forced water waves. *J. Phys. Soc. Japan* **61**, *no. 9 3411-3412.*

GAMBAUDO, J.M., PROCACCIA, I., THOMAE, S. & TRESSER, C. 1986 *Phys. Rev. Lett.* **57**, *925.*

GENERALIS, S.C. & NAGATA, M. 1995 Faraday resonance in a two-liquid layer system. *Fluid Dyn. Res.* **15**, *145-165.*

GLEICK, J. 1988 Chaos, making a new science. *William Heinemann.*

GOLLUB, J.P., MEYER, C.W. 1983 Symmetry breaking instabilites on a fluid surface. *Physica D* **6**, *337-346.*

GOLUBITSKY, M. & STEWART, I. 1985 Hopf bifurcations in the presence of symmetry. *Arch. Rat. Mech. Anal.* **87**, *107-165.*

GOLUBITSKY, M. & STEWART, I. 1986 Hopf bifurcations with dihedral group symmetry: coupled nonlinear oscillator. *In multiparameter bifurcation theory,. Contemporary Mathematics* **56**, *131-173. American Mathematical Society.*

GU, X.M. & SETHNA, P.R. 1987 Resonant surface waves and chaotic phenomena. *J. Fluid Mech.* **183**, *543-565.*

GU, X.M., SETHNA, P.R. & NARAIN, A. 1988 On three-dimensional nonlinear subharmonic resonant surface waves in a fluid: part 1 - theory. *J. Appl. Mech.* **55**, *213-219.*

GUCKENHEIMER, J. & HOLMES, P. 1983. Nonlinear oscillations, dynamical systems, and bifurcations of vector fields. *Springer-Verlag.*

HADDON, E.W. & RILEY, N. 1983 A note on the mean circulation in standing waves. *Wave motion* **5**, *43-48.*

HAMMACK, J.L. & HENDERSON, D.M. 1993 Resonant interactions among surface water waves. *Ann. Rev. Fluid Mech.* **25**, *55-92.*

HAO BAI-LIN. 1982 Elementary symbolic dynamics and chaos in dissipative systems. *World Scientific.*

HENDERSON, D.M. & MILES, J.W. 1990 Single-mode Faraday waves in small cyclinders. *J. Fluid Mech.* **213**, *95-109.*

HENSTOCK, W. & SANI, R.L. 1974 On the stability of the free-surface of a cylindrical layer of fluid in vertical motion. *Lett. Heat Mass Trans.* **1**, *95-102.*

HOLMES, P. 1986 Chaotic motions in a weakly nonlinear model for surface waves. *J. Fluid Mech.* **162**, *365-388.*

HOPF, E. 1942 Abzweigung einer periodischen Lösung von einer stationären Lösung eines Differentialsystems. *Ber. Verh. Sächs. Akad. Wiss. Leipzig. Math.-phys. Kl.* **94**, *1-22.* Translated in The Hopf bifurcation and its applications (1976), *163-193, eds. J. E. Marsden & M. McCracken. New York: Springer-Verlag.*

HUGHES, D.W. & PROCTOR, M.R.E. 1990 a A low-order model of the shear instability of convection: chaos and the effect of noise. *Nonlinearity* **3**, *127-153.*

HUGHES, D.W. & PROCTOR, M.R.E. 1990 b Chaos and the effect of noise in a model of three-wave mode coupling. *Physica D* **46**, *163-176.*

JONES, C.A. & PROCTOR, M.R.E. 1987 Strong spatial resonance and travelling waves in Benard convection. *Phys. Lett. A* **121**, *224-227.*

KAMBE, T. & UMEKI, M. 1990 Nonlinear dynamics of two-mode interactions in parametric excitation of surface waves. *J. Fluid Mech.* **212**, *373-393.*

KEOLIAN, R., TURKEVICH, L.A., PUTTERMAN, S.J., RUDNICK, I. & RUDNICK J.A. 1981 Subharmonic sequences in the Faraday experiment: departures from period doubling. *Phys. Rev. Lett.* **47**, *1133-1136.*

KEULEGAN, G.H. 1959 Energy dissipation in standing waves in rectangular basins. *J. Fluid Mech.* **6**, *33-50.*

KNOBLOCH, E. & DE LUCA, J. 1990 Amplitude equations for travelling wave convection. *Nonlinearity* **3**, *975-980.*

KUMAR, K. & TUCKERMAN, L.S. 1994 Parametric instability at the interface of two fluids. *J. Fluid Mech.* **279**, *49-68.*

LAMB, H. 1895, 1932 Hydrodynamics. 6th edn., *Cambridge Univ. Press.*

LANDAU, L.D. & LIFSHITZ, E.M. 1987 Fluid Mechanics. *Pergamon Press.*

LARRAZA, A. & PUTTERMAN, S. 1984 Theory of non-propagating surface waves solitons. *J. Fluid Mech.* **148**, *443-449.*

LEVICH, V.G. 1941 Acta Physicochim. *URSS* **14**, *308-321.*

LEVICH, V.G. 1962 Physicochemical hydrodynamics. *New York: Prentice-Hall, Inc.*

LIN, C.C. 1957 Motion in the boundary layer with a rapidly oscillating external flow. *Proc. 9th Intern. Congress Appl. Mech. Brussels.* **4**, *155.*

LOCHERER, K.H. & BRANDT, C.D. 1982 Parametric electronics. *Springer, New York.*

LONGUET-HIGGINS, M.S. 1953 Mass transport in water waves. *Phil. Trans. R. Soc. Lond. A* **245**, *535-581.*

LUKE, J.C. 1967 A variational principle for a fluid with a free-surface. *J. Fluid Mech.* **27**, *no. 2 395-397.*

MACKAY, R.S. & MEISS, J.D. 1987 Hamiltonian dynamical systems. *Adam Hilger, Bristol and Philadelphia.*

MATTHIESSEN, L. 1868 Akustische versuche, die kleinsten transversal wellen der flussigskeiten betressend. *Ann. Phys. (Leipzig)* **134**, *107-117.*

MEI, C.C. 1983 The applied dynamics of ocean surface waves. *John Wiley & Sons.*

MERON, E. 1987 Parametric excitation of multimode dissipative systems. *Phys. Rev. A* **35**, *no. 11 4892-4895.*

MERON, E. & PROCACCIA, I. 1986 Low-dimensional chaos in surface waves: Theoretical analysis of an experiment. *Phys. Rev. A* **34**, *3221-3237.*

MERON, E. & PROCACCIA, I. 1987 Gluing bifurcations in critical flows: The route to chaos in parametrically excited surface waves. *Phys. Rev. A* **35**, *no. 9 4008-4011.*

MERON, E. & PROCACCIA, I. 1989 Reply to Miles. *Phys. Rev. Lett.* **63**, *p. 1437.*

MILDER, D.M. 1977. A note regarding 'On Hamilton's principle for surface waves'. *J. Fluid Mech.* **83**, *no. 1 159-161.*

MILES, J.W. 1967 Surface-wave damping in closed basins. *Proc. R. Soc. Lond. A* **297**, *459-475.*

MILES, J.W. 1976 Nonlinear surface waves in closed basins. *J. Fluid Mech.* **75**, *part 3, 419-448.*

MILES, J.W. 1977 On Hamilton's principle for surface waves. *J. Fluid Mech.* **83**, *no. 1 153-158.*

MILES, J.W. 1984 Nonlinear Faraday resonance. *J. Fluid Mech.* **146**, *285-302.*

MILES, J.W. 1985 Resonantly forced, nonlinear gravity waves in a shallow rectangular tank. *Wave motion* **7**, *291-297.*

MILES, J.W. 1989 Symmetries of internally resonant, parametrically excited surface waves. *Phys. Rev. Lett.* **63**, *1436.*

MILES, J.W. 1993 On Faraday waves. *J. Fluid Mech.* **248**, *671-683.* (and Corrigendum, **269**, 1994,. *372*).

MILES, J.W. 1994 Faraday waves: rolls vs squares. *J. Fluid Mech.* **269**, *353-371.*

MILES, J.W. & HENDERSON, D. 1990 Parametrically forced surface waves. *Ann. Rev. Fluid Mech.*, **22**, *143-165.*

MILNER, S.T. 1991 Square patterns and secondary instabilities in driven capillary waves.*J. Fluid Mech.*, **225**, *81-100.*

NAGATA, M. 1989 Nonlinear Faraday resonance in a box with a square base. *J. Fluid Mech.* **209**, *265-284.*

NAGATA, M. 1991 Chaotic behaviour of parametrically excited surface waves in square geometry. *Eur. J. Mech. B/Fluids* **10**, *no. 2 61-66.*

NAYFEH, A.H. & MOOK, D.T. 1979 Nonlinear oscillations. *Wiley, New York..*

NOBILI, S., CILIBERTO, S., COCCIARO, B., FAETTI, S. & FRONZONI, L. 1988 Time-dependent surface waves in a horizontally oscillating container. *Europhys. Lett.* **7**, *no. 7 587-592.*

OCKENDON, J.R. & OCKENDON, H. 1973 Resonant surface waves. *J. Fluid Mech.* **59**, *397-413.*

PERKO, L. 1991 Differential equations and dynamical systems. *Springer-Verlag.*

PHILLIPS, O.M. 1960 On the dynamics of unsteady gravity waves of finite amplitude. Part 1. The elementary interactions. *J. Fluid Mech.* **9**, *193-217.*

PHILLIPS, O.M. 1977 The dynamics of the upper ocean. *Cambridge Univ. Press.*

PHILLIPS, O.M. 1981 Wave interactions - the evolution of an idea. *J. Fluid Mech.* **106**, *215-227.*

PIERCE, R.D. & KNOBLOCH, E. 1994 On the modulational stability of travelling and standing water waves. *Phys. Fluids* **6**, *no. 3 1177-1190.*

PROCACCIA, I., THOMAE, S. & TRESSER, C. 1987 *Phys. Rev. A* **35**, *1884.*

RAYLEIGH, LORD 1883 a On maintained vibrations. *Phil. Mag.* **15**, *229-235. (Scientific papers* **2**, *188-193).*

RAYLEIGH, LORD 1883 b On the crispations of a fluid resting on a vibrating support. *Phil. Mag.* **16**, *50-58. (Scientific papers* **2**, *212-219).*

RAYLEIGH, LORD 1883 c *Phil. Trans. A,* **175**, *1.*

RAYLEIGH, LORD 1896 The theory of sound. *Macmillan, London. (reprinted Dover, New York, 1945).*

RIECKE, H. 1990 Stable wavenumber kinks in parametrically excited standing waves. *Europhysics Lett.* **11**, *no. 3 213-218.*

RILEY, N. 1984 Progressive surface waves on a liquid of non-uniform depth. *Wave motion* **6**, *15-22.*

SCHLICHTING, H. 1960 Boundary layer theory. *McGraw-Hill.*

SILBER, M. & KNOBLOCH, E. 1989 Parametrically excited surface waves in square geometry. *Phys. Lett.* **137**, *349-354.*

SILNIKOV, L.P. 1970 A contribution to the problem of the structure of an extended neighbourhood of a rough equilibrium state of saddle-focus type. *Math. USSR Sbornik* **10**, *91-102.*

SIMMONS, W.F. 1969 A variational method for weak resonant wave interactions. *Proc. Roy. Soc. A* **309**, *551-575.*

SIMONELLI, F. & GOLLUB, J.P. 1989 Surface wave mode interactions: effects of symmetry and degeneracy. *J. Fluid Mech.* **199**, *471-494.*

STERRATT, D. 1995 Mode competition in Faraday excitation: an experimental study. *Undergraduate Physics dissertation, University of St. Andrews.*

STEWART, I. 1989 Does God play dice? *Penguin.*

STOKES, G.G. 1847 On the theory of oscillatory waves. *Trans. Camb. Phil. Soc.* **8**, *441-455.*

TEMPEL, M. & RIET. R.P. 1965 Damping of waves by surface-active materials. *J. Chem. Phys.* **42**, *no. 8 2769-2777.*

TUCKERMAN, L.S., KUMAR, K. & EDWARDS, W.S. 1994. *In preparation.*

UMEKI, M. 1989 Nonlinear dynamics and chaos in Faraday resonance. *J. Japan Soc. Fluid Mech.* **8**, *157-164.*

UMEKI M. 1991 Faraday resonance in rectangular geometry. *J. Fluid Mech.* **227**, *161-192.*

UMEKI M. & KAMBE T. 1989 Nonlinear Dynamics and Chaos in Parametrically Excited Surface Waves. *Journal of the Physical Society of Japan.* **58**, *no. 1, 140-154.*

VELHULST, F. 1979 Discrete symmetric dynamical system at the main resonances with applications to axi-symmetric galaxies. *Phil. Trans. R. Soc. Lond.* **290**, *435-465.*

VIRNIG, J.C., BERMAN, A.S. & SETHNA, P.R. 1988 On three-dimensional nonlinear subharmonic resonant surface waves in a fluid: Part 2 - experiment. *J. Appl. Mech.* **55**, *220-224.*

WHITHAM, G.B. 1965 A general approach to linear and non-linear dispersive waves using a Lagrangian. *J. Fluid Mech.* **22**, *no. 2 273-283.*

WHITHAM, G.B. 1967 Variational methods and applications to water waves. *Proc. Roy. Soc. A* **299**, *6-25.*

WHITHAM, G.B. 1970 Two-timing, variational principles and waves. *J. Fluid Mech.* **44**, *no. 2 373-395.*

WU, J., KEOLIAN, R. & RUDNICK, I. 1984 Observation of a non-propagating hydrodynamic soliton. *Phys. Rev. Lett.* **52**, *1421-1424.*

WU, J. & RUDNICK, I. 1985 Amplitude-dependent properties of a hydrodynamic soliton. *Phys. Rev. Lett.* **55**, *no. 2 204-207.*

YUEN, H.C. & LAKE, B.M. 1980 Instabilities of waves on deep water. *Ann. Rev. Fluid Mech.* **12**, *303-334.*